CO_2 Conversion to Syngas and Hydrocarbons over Transition Metal-Based Catalysts Synthesized via Reverse Microemulsion Method

by

Yue Yu

A thesis

presented to the University of Waterloo

in fulfilment of the

thesis requirement for the degree of

Doctor of Philosophy

in

Chemical Engineering

Waterloo, Ontario, Canada, 2024

Examining Committee Membership

The following served on the Examining Committee for this thesis. The decision of the Examining Committee is by majority vote.

External Examiner	Nicolas Abatzoglou Professor
Supervisor(s)	David Simakov Associate Professor
	Luis Ricardez-Sandoval Associate Professor
Internal Member	Xianshe Feng University Research Chair & Professor
	Michael Pope Associate Professor
	Aiping Yu Professor
Internal-external Member	XiaoYu Wu Assistant Professor

Author's Declaration

This thesis consists of material all of which I authored or co-authored: see Statement of Contributions included in the thesis. This is a true copy of the thesis, including any required final revisions, as accepted by my examiners. I understand that my thesis may be made electronically available to the public.

Statement of Contribution

This manuscript was written by Yue Yu and revised by Prof. David Simakov and Prof. Luis Ricardez-Sandoval. The contributions of all authors are listed below.

Chapter 4 of this thesis was co-authored by Yue Yu, Yue Yu's supervisors (Prof. David Simakov and Prof. Aiping Yu). Note that the first 5 terms of Yue Yu's PhD program (Jan 2020 – Aug 2021) was supervised by Prof. David Simakov and Prof. Aiping Yu, and starting from Sep 2021, Yue Yu's supervisors was switched to Prof. David Simakov and Prof. Luis Ricardez-Sandoval because of the corporation program.

Yue Yu devised the idea and carried out the experiments and analyses; Prof. David Simakov and Prof. Aiping Yu directed the research.

Chapter 5 of this thesis was co-authored by Yue Yu, Yue Yu's supervisors (Prof. David Simakov and Prof. Aiping Yu), two collaborators (Arunchander Asokan and Matthew E. Suss).

Yue Yu devised the idea and carried out the experiments and data analyses; Arunchander Asokan and Matthew E. Suss collected the TME spectra; Prof. David Simakov and Prof. Aiping Yu directed the research.

Chapter 6 of this thesis consists of the following contribution that was co-authored by Yue Yu, Yue Yu's supervisors (Prof. David Simakov and Prof. Luis Ricardez-Sandoval), two collaborators (Kishore Kandasamy and Muhammad Waqas Iqbal).

The contribution of Yue Yu includes performing experiments and results analysis. Kishore Kandasamy and Muhammad Waqas Iqbal performed material synthesis and characterization and

revision of the manuscript. Prof. David Simakov, Prof. Luis Ricardez-Sandoval and Prof. Aiping Yu directed the research.

Chapter 7 of this thesis was co-authored by Yue Yu, Yue Yu's supervisors (Prof. David Simakov and Prof. Luis Ricardez-Sandoval), one collaborator.

The contribution of Yue Yu includes devised the idea, performing DFT simulation, and analysis of the results. Wenxuan Xia performed material synthesis and characterization. Prof. David Simakov and Prof. Luis Ricardez-Sandoval directed the research.

Abstract

This thesis offers a comprehensive exploration into the development, exploration, and practical implications of various catalysts, with a particular focus on their performance and critical roles in the efficient and sustainable conversion of CO_2 through thermo-catalytic processes. In particular, this thesis focused on the exploration of potential catalysts for CO_2 conversion and hydrogenation processes including various catalyst systems such as Co-Mo carbides and oxides, Fe/Al_2O_3, and CeO_2-based materials. The study combines experimental and theoretical approaches to discover new insights and avenues for catalysis development. In the study of Cobalt-Molybdenum oxide and carbide catalysts for the reverse water gas shift (RWGS) reaction, the studies conducted in this thesis identified promising activity at specific conditions but also highlighted the need for further improvements in carburization and synthesis processes. The investigation into Al_2O_3-supported iron catalysts for CO_2 hydrogenation reveals that the RME Fe/Al_2O_3 catalysts, prepared through the RME method, exhibit superior performance, particularly in terms of CO_2 conversion rate and selectivity towards C2+ hydrocarbons. This finding underscores the importance of synthesis methods and reaction conditions in catalytic performance. Moreover, the study conducted on CeO_2-based catalysts for RWGS showed that Cu/CeO_2 and Fe/CeO_2 catalysts synthesized by reverse microemulsion method are favored in CO_2 reduction to CO, maintaining high selectivity to CO across a broad temperature range. This is attributed to the effective doping with transition metals like Cu and Fe, which enhances CO_2 adsorption on CeO_2 surfaces, also underscoring the significant role of oxygen vacancies generated by doping in CO_2 adsorption and activation. These insights paved the way for a more nuanced understanding of the factors influencing adsorption and subsequent catalytic activity. These findings contribute

significantly to the field of catalysis, providing a robust foundation for developing more efficient and resilient catalysts for RWGS reactions and CO_2 conversion. The novel integration of experimental and computational methods in this thesis offers a comprehensive understanding of the catalytic processes, setting new benchmarks for catalyst design and advancing sustainable energy initiatives. This thesis integrates theoretical research with practical application, providing insights and guidelines that hold substantial promise for the future of environmental sustainability and efficient, selective CO_2 conversion processes.

Acknowledgements

I would like to express my heartfelt gratitude to my supervisors, Prof. David Simakov, Prof. Aiping Yu and Prof. Luis Ricardez-Sandoval for their exceptional mentorship, professional support, invaluable guidance, and constructive feedback throughout my research process. My thanks also go to my friends, for the late-night discussions and moral support, especially during the hard time of pandemic. I must also express my heartful appreciation to my parents, whose unwavering support and belief in my abilities have been a constant source of motivation.

This thesis would not have been possible without the contributions and support of all mentioned above, along with many others whose names I cannot list but whose help was just as significant. Thank you.

Table of Contents

List of figures

List of tables

List of abbreviations

PtG	power to gas
CCU	carbon capture and utilization
ICP-OES	inductively coupled plasma with optical emission spectrometry
IR	infrared
FTIR	Fourier transform infrared spectroscopy
RME	reverse microemulsion
RWGS	reverse water gas shift
SSA	specific surface area
STEM	Scanning transmission electron microscopy
XRD	X-ray diffraction
TCD	thermal conductivity detector
TGA	thermal gravimetric analysis
TPD	temperature programmed desorption
TPR	temperature programmed reduction
XPS	X-ray photoelectron spectroscopy
DFT	density functional theory
OV	Oxygen vacancy

List of symbols

A	pre-exponential factor
CB	carbon balance, %
$C_{CO2,b}$	gas-phase (bulk) CO_2 concentration, mol/m^3
$C_{CO2,s}$	surface CO_2 concentration, mol/m^3
C_{pg}	gas thermal capacity, kJ/(mol K)
D_m	diffusion coefficient, m^2/s
D_{SSA}	SSA-based particle size, nm
D_{XRD}	XRD-based particle size, nm
d_p	particle size, m
$E_{a,rxn}$	activation energy of reaction, kJ/mol
$E_{a,des}$	activation energy of desorption, kJ/mol
E_{rxn}	reaction energy, kJ/mol
E_{x_ads}	adsorption energy of species *x*, kJ/mol
$F_{x,f}$	feed molar flow rate of *x*, mol/s
$F_{x,out}$	outlet molar flow rate of *x*, mol/s
$F_{t,out}$	total outlet molar flow rate, mol/s
fi	CO_2 conversion to species i
$GHSV$	gas hourly space velocity, ml/(h g_{cat})
h	heat transfer coefficient, kJ/(m^2 s K)
k_c	mass transfer coefficient
K	Scherrer equation shape factor
L_{Cu}	Cu loading, wt%
P	absolute pressure, bar
r_p	catalyst particle radius, m
R'_{obs}	observed reaction rate, mol/(kg s)
R_g	ideal gas constant, kJ/(mol K)
S_i	selectivity towards species *i*
STY	space time yield (mol/(g h))
T	temperature, °C
T_{max}	Peak temperature from TPD
T_s	surface temperature, °C
ΔH°_{298}	reaction enthalpy at standard temperature and pressure, kJ/mol
X_{CO2}	CO_2 conversion, %
Y	yield, %
y_i	mole fraction of species *i*

Greek letters

α	H_2/CO_2 feed ratio
β	full weight at half maximum, radians
ε	catalyst void fraction
λ	X-ray wavelength, nm
λ_g	gas thermal conductivity, kJ/(m s k)
λ_s	solid thermal conductivity, kJ/(m s k)
θ	diffraction angle, °
ρ_p	particle density, g/cm^3

Dimensionless numbers

Nu	particle Nusselt number
Pr	Prandtl number
Re	particle Reynolds number
Sc	Schmidt number
Sh	Sherwood number

Chapter 1 Introduction

1.1 Motivation

This research is motivated by two interconnected global challenges that demand urgent attention: the continuous surge in carbon dioxide (CO_2) emissions and the unceasing pursuit of sustainable energy solutions.

In recent decades, the world has awakened to the stark reality of soaring CO_2 emissions and their profound consequences on the environment. [2] The relentless combustion of fossil fuels due to anthropological activities, combined with industrial production and land-use changes, have propelled atmospheric CO_2 concentrations to unprecedented levels. [3] This alarming trend has given rise to global warming, erratic climatic patterns, and a host of ecological crises, underscoring the pressing need to reduce emissions to mitigate their adverse effects. Amidst these pressing concerns lies a transformative vision: CO_2 utilization. This paradigm shift aims to convert CO_2 from a pollutant or natural respiration into a valuable resource—a concept known as carbon capture and utilization (CCU). [4-6] At the core of this endeavor, catalysts and materials emerge as pivotal components since they are essential for the steps from the initial capture and storage of CO_2 to the conversion step which can enhance the reaction efficiency (conversion and selectivity). Catalysts play a foundational role, facilitating the conversion of CO_2 into valuable synthesis gas (syngas) and hydrocarbons. The catalysts employed in the reactions for CO_2 conversion must be carefully designed to optimize reaction conversion, selectivity, and sustainability of the production of the materials utilized for the CO_2 conversion process.

Transition metal-based catalysts have emerged as catalysts for transformative change. Transition metals such as copper (Cu), nickel (Ni), cobalt (Co) and iron (Fe) are commonly used

as catalysts for the hydrogenation of CO_2 to produce chemicals like CO, CH_4 or hydrocarbons and they exhibits great potential facilitating the reduction of CO_2 to these valuable compounds. [7-12] Ceria (CeO_2) is a versatile material used in various catalytic applications due to its unique properties. It is often employed as a support or promoter in catalysts for a wide range of reactions, including oxidation, reduction, and catalytic processes involving hydrogenation and dehydrogenation. [13-17] The catalytic activity of ceria-based catalysts in CO_2 hydrogenation is attributed to oxygen storage capacity, redox properties, and the ability to enhance reaction rates and selectivity. [18, 19] These catalysts, especially integrating multiple metals when used as dopants or bimetallic materials, exhibit unique properties and synergistic effects that elevate their catalytic performance. [20-22] The potential of transition metal and ceria-based catalysts lies in improving the efficiency of CO_2 conversion reactions, offering a pathway to synthesize syngas and hydrocarbons while mitigating the carbon footprint. Despite the laboratory experimental work, conducting the theoretical studies, such as Density Functional Theory (DFT), has the potential in the context of CO_2 conversion and catalyst development which lies in their potential to provide crucial insights and guidance for experimental research. DFT calculations allow for the prediction of catalytic activity, identifying materials that have the potential to be effective catalysts and this aids in the screening of a wide range of candidate materials before conducting time-consuming experimental work.

The method of synthesis is a key point to the catalytic performance for CO_2 conversion since different synthesis methods can lead to various morphology, particle sizes, even altered active phase. This research focuses on an innovative approach—synthesizing multi-metallic transition metal-based catalysts via reverse microemulsions (RME), which is particularly beneficial to synthesis of nano-scale particles with enhanced surface area and leads to superior catalytic

performance. This method provides meticulous control over catalyst composition, particle size, and morphology, aligning with the broader objective of creating sustainable, scalable, and reproducible catalyst synthesis techniques. This is a pivotal step towards realizing the full potential of CO_2 utilization.

In essence, this work aspires to contribute to the development of catalysts and processes that facilitate the conversion of CO_2 into syngas and hydrocarbons. High activity, selectivity and durable non-noble metal catalysts are required for CCU systems; hence, this work aims to explore the advantage of the novel preparation methods and the synergistic effect that the combinations of metals could bring to reverse water gas shift reaction, CO_2 methanation and CO_2 direct hydrogenation to hydrocarbons. The deeper motivation underlying this research converges at the intersection of environmental stewardship and sustainable energy production. It endeavors to bridge the gap between the imperative to reduce CO_2 emissions and the potential to harness CO_2 as a resource for clean and renewable energy generation. By doing so, it addresses the pressing challenges of our time while paving the way toward a more sustainable and energy-efficient future.

1.2 Research hypothesis and objectives

The overarching hypothesis of this thesis is established on that the efficiency of CO_2 conversion processes can be significantly enhanced and approach to the equilibrium conversion limit through the development and improvement of catalyst systems, including Co-Mo carbides and oxides, Fe/Al_2O_3, and CeO_2-based materials. The choice of these materials is based on their unique properties and catalytic potentials. Co-Mo carbides and oxides are known for their exceptional thermal stability and resistance to poisoning, making them suitable for high-temperature reverse water gas shift (RWGS) reaction. [1] Fe is a well-known catalyst for the

Fischer-Tropsch synthesis and CO_2 hydrogenation due to its cost-effectiveness and availability [23]. The ceria (CeO_2), is a support and active material due to its unique oxygen storage capacity and ability to shuttle oxygen, when doped with transition metals it shows improved performance. [13]

It is proposed that by elucidating the underlying mechanisms and interactions at the molecular level, particularly through the advanced synthesis method, synergistic effects of bimetallic compositions and support interactions, one can achieve improved catalytic performance. In this PhD Thesis, the catalytic performance refers to higher CO_2 conversion rates, selectivity towards desired products compared to monometallic materials, and stability under operation conditions. The hypothesis extends to the belief that a detailed understanding of the physiochemical properties of the catalysts, combined with insights from computer-aided materials modeling, can lead to the development of tailored catalysts that are more efficient and environmentally sustainable.

To validate this hypothesis, this research aims to systematically investigate the impact of various synthesis methods, reaction conditions, and doping strategies on the catalytic activity and stability of the selected systems. This involves a comprehensive examination of the structural, electronic, and surface properties of the catalysts and their correlation with catalytic performance. The study hypothesizes that the integration of experimental findings with theoretical insights obtained from first-principles atomistic simulations will uncover near-optimal catalyst structures that promote enhanced CO_2 adsorption, activation, and conversion pathways. Through this holistic approach, this PhD thesis seeks to contribute with novel methodologies and insights to the field of

catalysis, paving the way for the development of next-generation catalysts that offer a viable solution to the challenges posed by CO_2 emissions and the need for sustainable energy sources.

The primary objective of this thesis is to investigate and explore various catalysts for their efficacy and stability in CO_2 thermo-catalytic conversion processes. This thesis aims to provide insights on the impact of synthesis methods on the catalyst structural properties and subsequent activity and selectivity during the CO_2 conversion processes. The specific research objectives pursued in this thesis are as follows:

- Exploration of reverse micro-emulsion method prepared cobalt (Co) and molybdenum (Mo) based bimetallic oxide and carbide catalysts for CO_2 methanation. Assess the characterization and catalytic performance of the CoMo oxide and carbide and determine the carburization process of the bimetallic carbide.

- Synthesis and characterization of Fe/Al_2O_3 catalysts prepared by reverse micro-emulsion method for CO_2 direct reduction to hydrocarbons. Evaluate the catalytic activity of the developed catalyst, and analyze the impact of the synthesis method on morphology and active phase.

- Perform laboratory-scale tests on Cu doped CeO_2 catalysts to assess the catalytic activity for reverse water gas shift reaction, and reveal the synergistic effects caused by introducing Cu to CeO_2 lattice.

- Provide insights on the underlying mechanisms during CO_2 reduction on transition metal-doped CeO_2 surfaces, and screen and identity suitable dopant material for CO_2 reduction with desired catalytic property via DFT analysis and laboratory-scale tests.

By establishing correlations between structural attributes, reaction conditions, and catalytic performance, this PhD thesis aims to provide insightful guidance for the future design and development of advanced CO_2 hydrogenation catalysts, contributing to the broader goal of environmental preservation and sustainable energy.

1.3 Thesis organization

This thesis is structured to provide a comprehensive exploration of the research objectives and findings, addressing the pressing need to mitigate carbon dioxide (CO_2) emissions and develop sustainable energy solutions. The organization is as follows:

Chapter 1 offers an introductory overview of the global CO_2 emissionss problem, highlighting the increasing urgency of addressing this issue, and sets the stage for the subsequent research. Chapter 1 also establishes the foundational aspects of the research, presenting the motivation behind the study and outlining the specific objectives to be achieved throughout the thesis.

Chapter 2 presents an in-depth review of pertinent literature, covering topics such as CO_2 emissionss, utilization, and Power-to-Gas (PtG) technology, while delving into the theoretical underpinnings of CO_2 conversion reactions and heterogeneous catalysis.

Chapter 3 describes the methods employed in this research, encompassing catalyst synthesis, characterization techniques, and the computational tools used to gain insights into the studied reactions.

In Chapter 4, the synthesis, characterization, and performance evaluation of cobalt (Co) and molybdenum (Mo) based bimetallic oxide and carbide catalysts for the reverse water gas shift

(RWGS) reaction are comprehensively discussed, shedding light on their viability for CO_2 conversion. The potential of reverse micro-emulsion synthesis methods in crafting novel cobalt (Co) and molybdenum (Mo) based bimetallic oxide and carbide catalysts designed for CO_2 methanation are analysed.

Chapter 5 centers on the development of iron/aluminum oxide (Fe/Al_2O_3) catalysts using the reverse micro-emulsion technique. This chapter aims to synthesize and characterize Fe/Al_2O_3 catalysts for the direct reduction of CO_2 to hydrocarbons. The catalytic activity of the developed catalyst is evaluated, and the impact of synthesis method on morphology and active phase will be analyzed.

Chapter 6 presents the experimental investigation of copper-doped ceria (Cu/CeO_2) catalysts for RWGS. This chapter provides insights into the synthesis, characterization, and performance evaluation of copper-doped ceria catalysts, particularly their applicability in the reverse water gas shift reaction. The intermediates and the mechanism of CO_2 reduction on Cu/CeO_2 surfaces are also investigated by experimental techniques.

Chapters 7 presents a Density Functional Theory (DFT) analysis to investigate CO_2 adsorption on doped ceria catalysts and the reverse water gas shift reaction on transition metal doped ceria surfaces. This chapter combines DFT calculations and laboratory-scale experiments to screen and identify suitable dopant materials for CO_2 reduction on doped CeO_2 surface, while seeking to understand the factors in terms of electronic properties that influence catalytic stability and performance.

In Chapter 8, the key findings of the research are summarized. Additionally, recommendations for future research avenues are presented, including optimization of catalyst synthesis methods and the potential utilization of machine learning for material screening in CO_2 hydrogenation applications. This chapter serves as a comprehensive conclusion to the thesis, summarises the research's contributions and implications for future endeavors in this field.

Chapter 2 Literature review and theoretical background

2.1 CO_2 emissions, CO_2 utilization, and Power-to-Gas

The role of human activity in global warming is still under discussion. NASA has been tracking the activity of sun over the decades, but the average energy from the sun remained constant [24]. Another justification is that the temperature of the upper layer of the atmosphere experienced a decrease, but the lower layer is becoming warmer because the greenhouse gases are trapping the heat reflected from the earth's surface [25].

The greenhouse gases can be produced by natural processes such as respiration and human activity such as the combustion of fossil fuels. There is plenty of evidence showing that the main reason for global warming is the rising concentration of greenhouse gas in the atmosphere [26], which is mainly caused by anthropological activities, primarily industrial and agriculture. Therefore, the accentuation of the greenhouse effect is the most possible cause of global warming.

Among all the greenhouse gases, water vapour is the richest in the atmosphere, but it can participate into the natural cycle. Carbon dioxide (CO_2) is not a strong greenhouse gas yet an abundant component in the atmosphere but controlling the CO_2 emissions is a critical global issue. The concentration of CO_2 in the atmosphere has increased by one-third since the onset of the Industrial Revolution, and large amounts of CO_2 is still being released into the atmosphere [26].

In Canada, the total greenhouse gas emissions were 716 megatons of CO_2 equivalent (Mt CO_2 eq) in 2017, which is 2.0% lower than the 2005 level [27]. Canada has diligently worked to reduce the emission by various approaches, including switching fuel (e.g. to renewable sources), develop the process to increase efficiency and pricing carbon pollution. [28-30] The biggest

component of GHG emission is energy production, which can be summarized into three sectors, transport, stationary combustion and fugitive. [27]

Renewable energy might replace fossil fuel energy in the long-term future. The proportion of renewable energy has been pushed up gradually in the energy mix. In Canada, renewable energy sources currently provide about 19% of Canada's total primary energy supply [31]. However, most renewable energy sources, such as solar, wind and hydro, are fluctuating and intermittent. For example, wind power is intermittent daily, and the maximum output may appear at night when the consumption of electricity is relatively low. Solar can be considered as a efficient, economical and clean energy, and the advantage of solar energy systems lies in their efficiency, scalability, and potential for aggregation with other processes to generate higher energy outputs, while their disadvantage is their dependency on meteorological factors, which directly impact energy outputs.[32] Biomass is also an attractive direction, particularly through Anaerobic Digestion (AD), is highlighted as an attractive and flexible renewable energy source with the potential to reduce water pollution, generate biogas, and contribute to decarbonizing energy systems by transforming organic materials into valuable fuels and fertilizers. [33-35] With the increasing number of renewable energies being developed, the utility of surplus electricity needs to be considered wisely; hence, advanced computational and prediction tools must be implemented in real-time to improve the efficiency in the operation of these systems when integrated with existing power and CO_2 capture and utilization systems such as chemical looping combustion system (CLC). [36-39]

To avoid waste of the energy generated off-peak, power to gas (PtG) is a promising way to store the electricity in the form of chemical energy inside chemical bonds [40]. The main idea of PtG is to use green electrical power to produce hydrogen by water electrolysis. The resulted hydrogen can be used directly or as the reactant for further conversion. To make this whole process

renewable, the electricity consumed during water electrolysis should come from renewable energy such as surplus electricity as described above. From the utilization of this renewable H_2, the fuels and chemicals generated from CO_2 can also be renewable and eventually leads to fewer net carbon emissions.

A disadvantage that needs to be overcome in the PtG chain is the low efficiency of water electrolysis [41]. The total energy will lose 30% from renewable electricity to compressed hydrogen delivered from the electrolysis. Nowadays, there are three favoured electrolysis approaches, alkaline electrolysis, Proton Exchange Membrane (PEM) electrolysis, and solid oxide electrolysis. Among them, alkaline electrolysis is the most wildly used method for economic reasons. However, if the cost of PEM electrolysis can be cut down by more advanced technologies, PEM will be the most suitable electrolysis method for practical industrial production [41].

2.2 CO_2 conversion to fuels and chemicals

2.2.1 CO_2 hydrogenation reactions

To date, the proportion of renewable energy has been increased gradually in the energy mix. To avoid losses of the renewable energy generated off-peak, [42] power to gas (PtG) is a promising way to store the electricity in the form of chemical energy. [1] One of the concepts of PtG is to use renewable power to produce renewable hydrogen (H_2) via water electrolysis.

This renewable H_2 can be coupled with the captured CO_2 to generate renewable synthetic fuels and chemicals. This pathway leads to lower net carbon emissions through the displacement of fossil fuels via artificial carbon recycle. [40] There are three main pathways for CO_2 reduction: thermocatalytic, photochemical, and electrochemical. Photochemical and electrochemical reduction have certain limitations of efficiency and capacity, as well as several advantages, such as low operation temperature and in situ H_2 generation. [43, 44] Thermocatalytic conversion of

CO_2 is favoured by high reaction rates resulting from the high-temperature reaction conditions, allowing large scale production. Probably the main disadvantage of the thermocatalytic pathway is that it requires gaseous H_2, making reduction of the electrocatalytic H_2 production cost imperative.

Several pathways of thermocatalytic CO_2 conversion have been studied in recent decades. Sabatier reaction (eq. 1-1) [45] is the CO_2 methanation process that can be used for renewable natural gas (RNG) production. On different catalysts and under different reaction conditions, syngas (a mixture of CO and H_2) can be obtained from CO_2 via reverse water gas shift (RWGS, eq. 2-2). [40] Syngas is an essential feed for various downstream processes including CO methanation (eq. 2-3), methanol production (eq. 2-4) [46], and Fischer-Tropsch (FT) synthesis (eq. 2-5). [47]

$$CO_2 + 4H_2 \rightleftharpoons CH_4 + 2H_2O \qquad \Delta H^\circ_{298} = -164 \frac{kJ}{mol} \qquad (2\text{-}1)$$

$$CO_2 + H_2 \rightleftharpoons CO + H_2O \qquad \Delta H^\circ_{298} = +41 \frac{kJ}{mol} \qquad (2\text{-}2)$$

$$CO + 3H_2 \rightleftharpoons CH_4 + H_2O \qquad \Delta H^\circ_{298} = -206 \frac{kJ}{mol} \qquad (2\text{-}3)$$

$$CO + 2H_2 \rightleftharpoons CH_3OH \qquad \Delta H^\circ_{298} = -91 \frac{kJ}{mol} \qquad (2\text{-}4)$$

$$nCO + (2n+1)H_2 \rightarrow C_nH_{2n+2} + nH_2O \qquad \Delta H^\circ_{298} = -165 \frac{kJ}{mol} \qquad (2\text{-}5)$$

2.2.2 Mechanisms of CO_2 conversion using heterogeneous catalysis

i Mechanism of reverse water gas shift

Depending on the conditions, hydrogenation of CO_2 can lead to various products such as CO, methane, methanol, and other valuable chemicals. Methanation of CO_2 (Sabatier reaction) and reforming to methanol are the two most competitive side reactions when it is under the RWGS operation condition. Understanding the underlying mechanism of the reactions is essential to identify attractive materials that can be further optimized thus accelerating the discovery of novel catalyst materials. [48, 49]

Table 2-1 Element reactions of three RWGS mechanisms. [59]

Redox mechanism	Formate mechanism	Carboxyl mechanism
$H_2 + 2* \leftrightarrow H* + H*$	$H_2 + 2* \leftrightarrow H* + H*$	$H_2 + 2* \leftrightarrow H* + H*$
$CO_2 + * \leftrightarrow CO_2*$	$CO_2 + * \leftrightarrow CO_2*$	$CO_2 + * \leftrightarrow CO_2*$
$CO_2* + * \leftrightarrow CO* + O*$	$CO_2* + H_2O* \leftrightarrow HCOO* + OH*$	$CO_2* + H_2O* \leftrightarrow COOH* + OH*$
$H_2O* + O* \leftrightarrow OH* + OH*$	$CO_2* + H* \leftrightarrow HCOO* + *$	$CO_2* + H* \leftrightarrow COOH* + *$
$O* + H* \leftrightarrow OH* + *$	$HCOO* + * \leftrightarrow CO* + OH*$	$COOH* + * \leftrightarrow CO* + OH*$
$H* + OH* \leftrightarrow H_2O* + *$	$H* + OH* \leftrightarrow H_2O* + *$	$H* + OH* \leftrightarrow H_2O* + *$
$H_2O* \leftrightarrow H_2O + *$	$H_2O* \leftrightarrow H_2O + *$	$H_2O* \leftrightarrow H_2O + *$
$CO* \leftrightarrow CO + *$	$CO* \leftrightarrow CO + *$	$CO* \leftrightarrow CO + *$

The mechanism of reverse water gas shift is still under investigation. Depends on different kinds of catalysts, reaction conditions including temperature, pressure and CO_2/H_2 ratio, the pathways and reaction order may differ. [50] Through the studies proposed so far, mechanisms on copper and Pt-based catalysts attracted attention intensively. [51] The mechanism of WGS is often discussed together with RWGS since the elementary reactions can be reversible. As shown Table 2-1, three reaction mechanisms have been widely recognized for the RWGS reaction (i) The CO_2 is reduced by the metal to form a metal oxide and CO while the oxidized metal is further reduced by hydrogen returning to metal state. [52, 53] (ii) A reactive radical intermediate, formate (HCOO) is involved throughout the reaction and split to hydroxyl and CO, as shown in Figure 2-1. [54, 55]

(iii) A relatively new pathway was also reported recently, that a reactive radical intermediate, carboxyl (COOH) is dominant on Cu(111) during the reaction. [56-58]

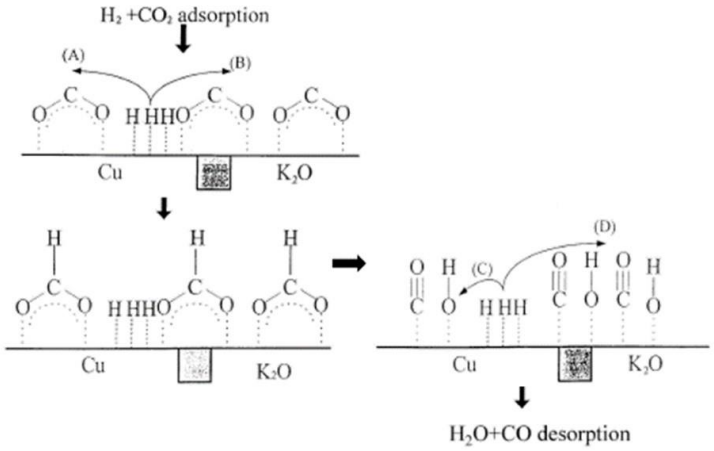

Figure 2-1 RWGS mechanism over K-Cu/SiO_2 catalyst. [55]

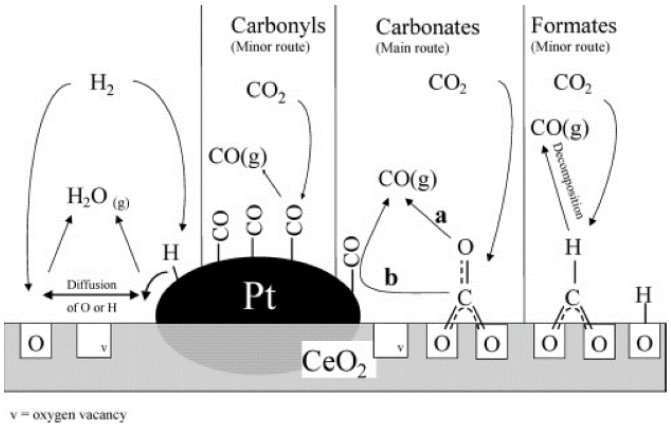

Figure 2-2 RWGS mechanism over Pt/CeO_2 catalyst [53]

Goguet et al, [53] proposed a direct re-oxidation reaction scheme of RWGS on Pt-CeO_2 catalyst. The dominated intermediate was the surface carbonates as shown in Figure 2-2. CO_2 molecules were adsorbed on the CeO_2 support and react with oxygen vacancies to form carbonate species. Then CO was released via two parallel routes, which are directly released by the carbonates or the carbonates can migrate to the platinum-ceria interface and released CO by

forming Pt-bound carbonyl intermediates. Although formate and carbonyls were detected as well, they were all demonstrated not to be the main routes and the CO generated from those two intermediates is limited.

Shido et al. [54] suggested that the intermediate on ZnO during RWGS was bidentate formate and the decomposition of the formate species was highly promoted by the co-adsorption of H_2 but inhibited by the co-adsorption of CO_2. They also claimed that the water gas shift reaction also took place through bidentate formate but at different active sites. RWGS on Cu/SiO_2 promoted by potassium was reported to follow a formate mechanism and the potassium can improve the adsorption ability of CeO_2. [55] As indicated in Figure 2-2, adsorbed hydrogen atoms can spill to the interface between K_2O and copper to form formate and H_2O, followed by releasing CO and H_2O.

Recently, some experimental and DFT studies on water gas shift over Cu and Pt-based catalysts suggested that on some catalysts, even formate species were generated during reaction but they were not involved in the elementary reactions and were more count as spectator species. [56, 58] Moreover, in other studies, formate species were reported to block the active sites instead of being intermediates. Carboxyl (COOH) formed from adsorbed CO_2 and H was identified to be the critical intermediate on the contrary, which was highly reactive yet hard to identify. [58]

ii Mechanism of CO_2 hydrogenation to hydrocarbons

CO_2 can also be hydrogenated to hydrocarbons through direct or indirect pathways. The indirect routes are often RWGS reaction (eq. 2-2) followed by Fischer-Tropsch process (eq. 2-5).

$$CO_2 + CH_4 \rightleftharpoons 2CO + 2H_2 \qquad \Delta H^{\circ}_{298} = +248\frac{kJ}{mol} \qquad \text{(eq. 2-2) [40]}$$

$$CO + 2H_2 \rightleftharpoons (CH_2) + H_2O \qquad \Delta H^{\circ}_{298} = -154.1 \frac{kJ}{mol} \qquad \text{(eq. 2-5)[59]}$$

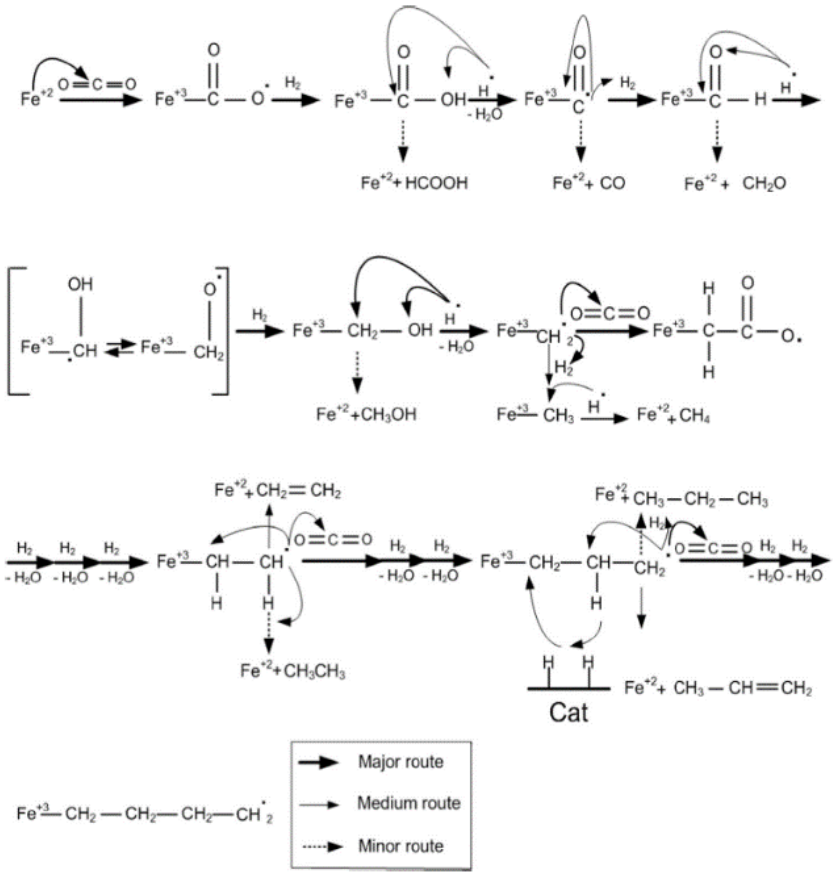

Figure 2-3 Reaction mechanism of CO_2 hydrogenation to hydrocarbons. [60]

Lee et al. [60] proposed a modified mechanism of direct conversion to hydrocarbon on Fe-based catalysts and the deactivation of Fe catalysts was also included (Figure 2-3). Formate species are the intermediates and with the attacking of H, Fe-CH_2 radical can be formed which was the chain growth step. A lower H_2 uptake was proposed to be beneficial to the selectivity towards long-chain hydrocarbons, which means a suitable hydrogen ratio in the feed is crucial to the reaction behaviour.

iii Mechanisms of other CO_2 hydrogenation reactions

The mechanism of CO_2 methanation also remains controversial and the two mainstream opinions are: [61] (i) CO_2 is first converted to CO and the routes are identical as RWGS followed by CO methanation reaction [62] (ii) direct methanation occurs without forming CO as intermediate. [63] Marwood et al. [62] demonstrated that the CO_2 methanation over 2 wt% Ru/TiO_2 experienced a pathway that first forms formate species to produce CO then followed by CO methanation (Figure 2-4). On Pd/ZrO_2 catalyst, the generation pathway of CH_4 was proposed to be the direct hydrogenation of adsorbed surface formate and no CO intermediate was observed. [63]

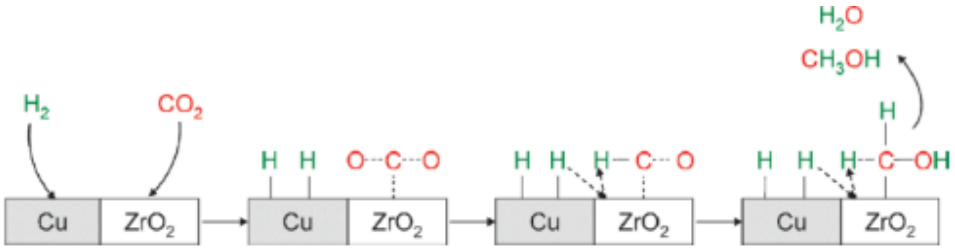

Figure 2-4 Reaction pathway of formation of methanol on Cu/ZrO2 catalyst. [64]

Methanol is also an important product for CO_2 hydrogenation. Two reaction pathways were proposed, [65] formate pathway and hydrocarboxyl (trans-HOCO) pathway. [66] On Cu/ZrO_2 catalyst, methanol can be produced through a dual-site reaction. [64] Figure 2-5 indicates the reaction mechanism that metal-oxide interface was critical for the formation of intermediate formate. The migration of H subsequently resulted in the release of methanol and H_2O.

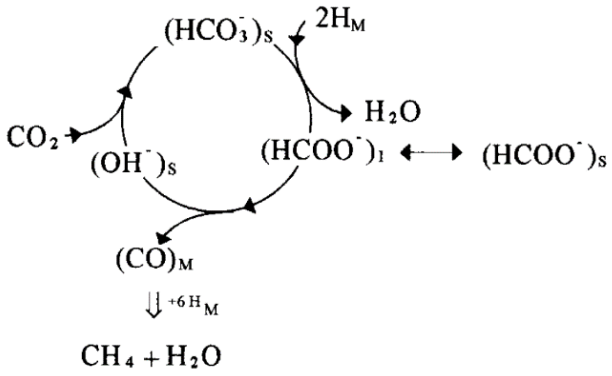

Figure 2-5 Mechanism of CO_2 methanation over 2 wt% Ru/TiO2. [62]

2.3 Heterogeneous catalysts for CO_2 hydrogenation

2.3.1 Catalysts for reverse water gas shift

The most studied materials for RWGS are copper-based catalysts, noble metal catalysts and supported ceria. Copper is advantageous for RWGS to perform activity even at low temperature (~165 °C) and high selectivity towards CO [52]. However, CO_2 is difficult to dissociate on clean copper metal surface when the ratio of H_2/CO_2 is low [67, 68], which leads to numerous studies focused on various supports and promoters cooperating with copper. Copper is also used in the reverse reaction, waster gas shift reaction.

Chen et al. investigated the behaviour of Cu-based catalysts supported on Al_2O_3 and SiO_2 [69-71]. With the increase of H_2/CO_2 ratio, a small amount of methane will start to form from H_2/CO_2ratio is 1 at 500 °C. They emphasised the necessity of hydrogen in the dissociation of CO_2 on the catalyst surface and the formation of intermediates to CO. The mechanism was also proposed in several studies that the key intermediate of RWGS is formate species and the decomposition of formate is the dominated pathway of the reaction [70].

The promotion effect of potassium on Cu/SiO_2 catalysts was studied by Chen et al. as well [55]. At 600 °C, with the presence of potassium, the conversion of CO_2 was doubled compared to

monometallic catalyst Cu/SiO_2. The role of K is to generate new active interfacial sites between K and Cu; hence the adsorbing capacity of CeO_2 is an order of magnitude greater than Cu/SiO_2. Iron can also promote the catalytic performance of Cu [72], as Figure 2-6 depicts, not only to create new active sites but also can strengthen the stability of Cu at higher temperatures, which means preventing sintering and inhibiting the oxidation of Cu.

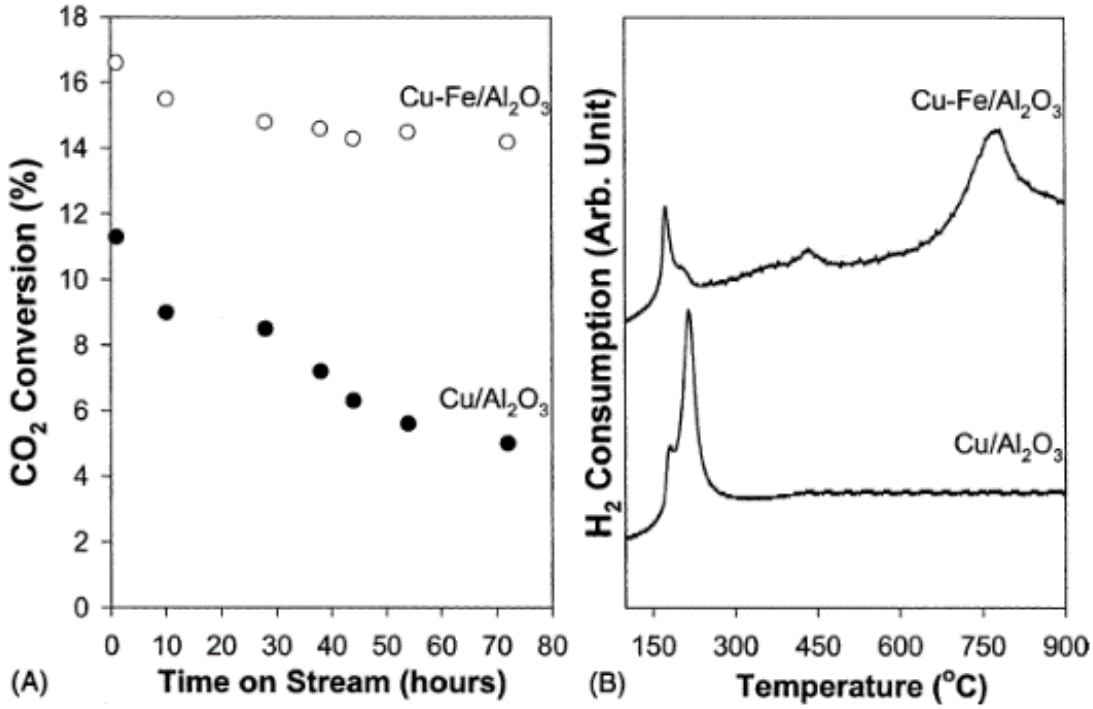

Figure 2-6 The comparison of 10 wt% Cu/Al_2O_3 with and without 0.3wt% Fe: (A) the dependence of CO_2 conversion on reaction time for H_2/CO_2 with 1:1 ratio. [72]

Noble metals (Pt, Pd and Rh) exhibit good stability during the reaction compared to copper catalysts, especially at high temperatures, and the sintering and coking effect is much lower on noble metal catalysts. Nevertheless, the notable weakness of noble metal catalysts lies in their substantially higher cost. Platinum supported on Ceria catalysts were reported to have catalytic activity at low temperature (100-300 °C). On Pt/TiO_2 catalyst, with 1 wt% Pt loading, a 20% conversion of CO_2 and 95% selectivity towards CO can be achieved at 400 °C with a gas hourly

space velocity (GHSV) of 6,000 mL $h^{-1}g_{cat}^{-1}$, $CO_2/H_2/N_2$=45/45/10. Pt-O_v-Ti^{3+} sites are the active sites during the RWGS reaction, while the Pt-CO formed only on Pt particle cannot produce CO at low temperature [73]. K was also reported to promote Pt/mullite catalyst visibly as shown in Figure 2-7. The participation of K between Pt and CO assisted the formation of formate intermediates and the interaction between Pt and K facilitated the decomposition of formate to CO which result in enhancement of CO_2 conversion as well as the selectivity to CO [74].

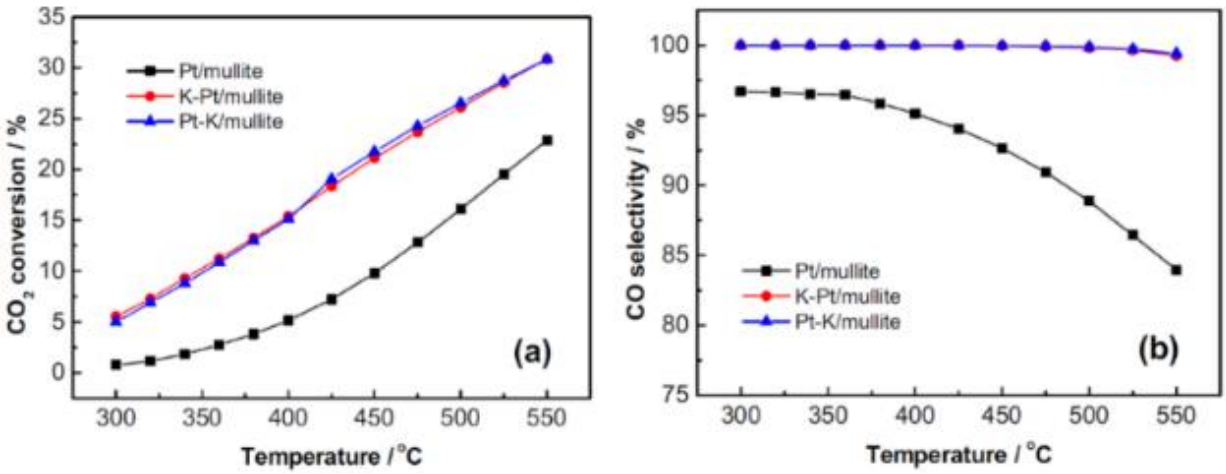

Figure 2-7 Catalyst performance of Pt/TiO2 as a function of temperature. Reaction conditions: GHSV=30,000 mL h-1gcat-1, CO_2/H_2/N2=45/45/10. [74]

Inoue et al. [75] reported the performance of rhodium on various supports (ZrO_2, Nb_2O_5, MgO and TiO_2). Rh/ZrO_2 and Rh/Nb_2O_6 showed the highest activity towards CO_2 methanation while on Rh/TiO_2 CO is produced immediately. However, some studies suggested that on Ru/TiO_2, the formation of CO is not evident and most of the product is methane [76]. The product is highly dependent on the precursor and preparation condition [77]. The combination of Fe and Ru can increase the selectivity to CO on Ru/TiO_2 (around 40%), but still incomparable to Fe/TiO_2 (around 90%) [78].

Transition metals are considered as more valuable catalysts for RWGS since most of them are affordable and can provide similar catalytic activity as some precious metals. Nickel-based catalysts (NiO/CeO_2) with low Ni loading (<3 wt%) were observed to have 100% selectivity towards CO [20]. NiO/CeO_2 was tested by Lu and Kawamoto at atmospheric pressure in a range of 400-900 °C with H_2:CO_2=1, GHSV=14,400 mL $h^{-1}g_{cat}^{-1}$. With the increasing of NiO loading, the conversion of CO_2 increased but the by-product methane started to form when Ni loading was higher than 3 wt%. However, when the temperature continued to rise to 900 °C, the selectivity could reach 100% approximately and the conversion differences are narrowed [20]. Kim et al. [79] reported the performance of Fe-based catalysts. Unsupported Fe oxide was tested for 19 hours, at 600 °C, atmospheric pressure, GHSV=6,000 mL $h^{-1}g_{cat}^{-1}$, H_2:CO_2=1, and the conversion was stabilized at 31%, with 100% selectivity to CO during the reaction which exhibited good activity and stability [79].

Table 2-2 Summary of conversion, TOF and selectivity of Mo catalysts and selected bi-metallic catalysts. [22]

Catalysts	Conversion [%]	TOF [min^{-1}]	CO:CH_4 Ratio
$PtCo/CeO_2$	6.6	14.6	4.5
$PdNi/CeO_2$	2.5	5.6	0.6
Mo_2C	8.7	25.7	14.5
Co-Mo_2C	9.5	16.1	51.3

Molybdenum has been interested for its impact on both H_2 dissociation and CO_2 scission [22]. Mo_2C showed superior performance in RWGS than precious metal based catalysts as

summarized in Table 2-1, $PtCo/CeO_2$ and $PdNi/CeO_2$, which are proposed to be more active than monometallic catalysts, Pt or Pd [22]. The addition of Co to Mo carbide can further promote the performance which will be introduced in part 2.5 in detail. Gao [80] et al. successfully synthesized α-MoC_{1-x} and β-Mo_2C (XRD patterns showed in Figure 2-8) by controlling the preparation conditions and both catalysts performed excellent catalytic activity, selectivity and stability. At 600 °C, 1 atm, GHSV=36,000 mL $h^{-1}g_{cat}^{-1}$, H_2:CO_2=4, the conversion of CO_2 was around 60% which almost approached the equilibrium conversion and no other by-products observed [80].

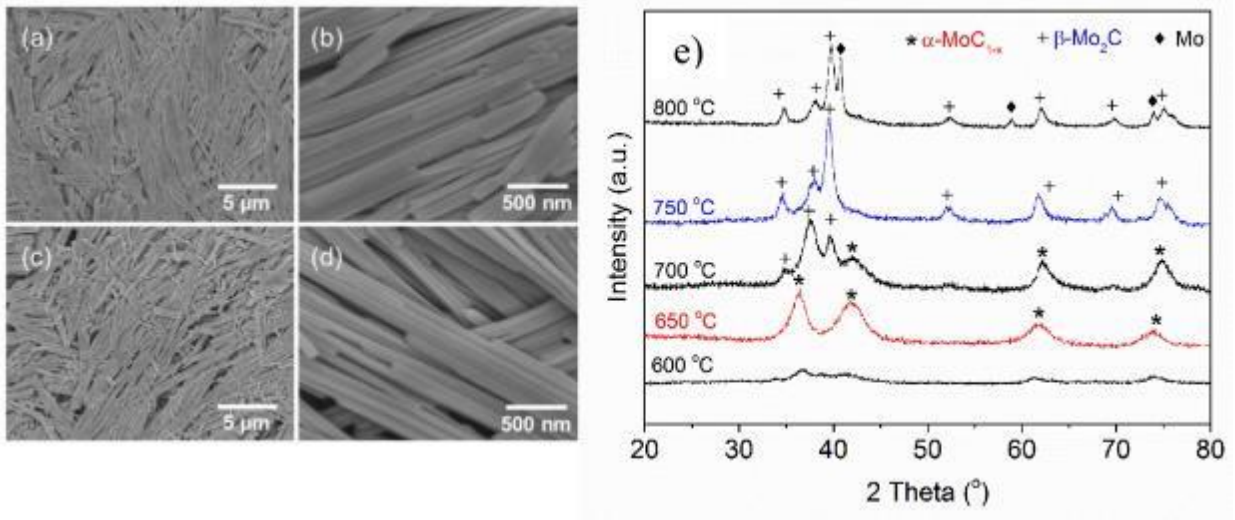

Figure 2-8 TEM images of α-MoC_{1-x} (a and b) and β-Mo_2C (c and d); XRD patterns (e) of Mo_2C samples calcined at different temperatures. [80]

Ceria (CeO_2) is well known in catalysis and widely used as a support material due to its high oxygen storage capacity. Ceria has the ability to reversibly store and release oxygen while switching the cerium charge from Ce^{4+} to Ce^{3+}. The oxygen vacancies formed can act as active sites for catalytic reactions [81, 82]. Ceria can exist in different morphologies (cube, rod and particle) with different crystalline planes exposed on the surface [83]. While the use of ceria as a support or a promoter is well documented, only a few studies have been reported on the RWGS reaction over pure ceria.

Liu et al. [84] explored the properties of ceria nanocubes, nanorods, and nanooctahedra crafted through hydrothermal synthesis techniques. These catalysts uniformly showcased a 100% preference for generating CO, with nanocubes featuring six distinct (100) planes achieving the highest conversion rates. Specifically, a 45% conversion of CO_2 was attained at 800 °C, whereas at a lower temperature of 500 °C, the conversion significantly dropped to 5%. In a related study, Konsolakis et al. [85] documented a 45% conversion of CO_2 and a 90% selectivity for CO when using ceria nanorods and nanocubes, also synthesized hydrothermally, under conditions of 500 °C, 1 atm, and a gas flow rate of 20,000 mL g^{-1} h^{-1} in a quartz fixed bed reactor. The experiments were conducted with a H_2/CO_2 feed ratio of 9. Dai et al. [86] investigated the RWGS reaction using purely synthesized ceria via hard template, complex, and precipitation methods. Tested under 1 atm, with a H_2/CO_2 ratio of 4 and a gas flow rate of 60,000 mL/(g h) across temperatures ranging from 300-580 °C in a quartz reactor, these catalysts demonstrated a perfect CO selectivity and a CO_2 conversion rate varying between 9-16% at 580 °C, compared to the equilibrium conversion of 65%. Mordekovitz et al. [21] studied the effects of gas adsorption on Ca- and Ti-doped CeO_2 surfaces. Their catalytic efficacy was evaluated in a quartz reactor across a temperature range of 450-700 °C, at 1 atm, using a H_2/CO_2 ratio of 1 and a flow rate of 72,000 ml/(g h). The findings revealed that pure CeO_2 reached a peak conversion of 20% at 700 °C, with a 3% conversion observed at 500 °C. A modest enhancement in CO_2 conversion to 23% at 700 °C was seen with $Ce_{0.88}Ti_{0.12}O_2$, attributed to its improved reducibility.

2.3.2 Catalysts for CO_2 hydrogenation to hydrocarbons

Recent studies have proved that at certain conditions and on certain catalysts, CO_2 can be converted directly to hydrocarbons, including alkanes and olefins, which can be regarded to as modified FT process. C2+-based products, namely C_2H_4, C_2H_6, alcohols, CH_3OCH_3 (DME), gasoline, and jet fuel, are of increased energy density, wider application range, and higher

economic value with increasing demand. [87] The design of catalysts for CO_2 hydrogenation to hydrocarbons via thermocatalytic conversion is among the most important challenges to be addressed since an appropriate catalyst must be active for both RWGS (eq. 2) and FT (eq. 5). Moreover, CO_2 and CO methanation are competing reactions, making the selectivity towards C-C bond formation imperative.

Multiple factors may contribute to the catalyst activity and selectivity towards formation of long carbon chains. Increasing amount of literature is devoted to the development of highly selective and cost-effective catalysts (cost considerations are important for practical applications). Various metal-based catalysts have been studied for Fischer-Tropsch synthesis. These catalysts could be typically considered as candidates for modified FT conversion as well. Iron (Fe) have been employed as a conventional FT catalyst for decades, [88-92], and is still the most favoured catalyst for converting CO_2 to hydrocarbons directly. Studies on Fe-based catalysts mainly focuses on various promoters, as well as on different types of supports. Several promoters, including K, Cr, Mo, Zn, and La [93-95] have been reported to enhance the activity; however, the most challenging issue is to improve the selectivity to C2+ hydrocarbons, i.e., reduce the conversion of CO_2 towards CO and CH_4, but promote the C-C coupling reaction which leads to C2+ hydrocarbons. Initial observations from earlier studies have suggested that K is the most prominent promoter. A comprehensive study of Fe-based catalysts doped with various promoters for CO_2 conversion to small hydrocarbons was conducted by Barrios et al. [96] Among 15 promoters investigated, the Cs-promoted Fe catalyst showed the highest conversion with space time yield (STY) of approximately 3.5 mmol g^{-1} h^{-1} at 10 bar and 350 °C, while all promoters studied showed suppression effect on CO_2 conversion. Ding et al. reported the $Fe_{0.30}Co_{0.15}Zr_{0.}30K_{0.10}O_{1.63}$ catalyst

for light olefin production with a STY of 4.93 mmol g^{-1} h^{-1} at 310 °C and 2.0 MPa, and revealed the importance of surface oxygen vacancies and hydroxyl groups for catalytic performance. [97]

Riedel et al. [98] indicated that RWGS is the first step of CO_2 hydrogenation and, subsequently, hydrocarbons are produced via FT reaction on alkalised iron catalysts. Supports also can influence CO_2 conversion, selectivity, and hydrocarbon yields. Riedel et al. observed the highest CO_2 conversion on Al_2O_3 as compared to SiO_2 and TiO_2, due to the increasing amount of adsorbed CO_2, with the selectivity remaining virtually unaffected by the support type. [98] With the addition of K (alkali promotion), not only the CO_2 conversion was increased, but also the carbon product distribution moved significantly to higher hydrocarbons and olefins, which was explained by the facilitating effect of K for Fe carburization under the reaction conditions. [98]

Cu-Fe bimetallic catalysts attracted wide interest because of the synergetic promoting effect, preventing the formation of CH_4 and enhancing the selectivity towards C2+ hydrocarbons. [99] Choi et al. [47] proposed that Cu-Fe catalysts synthesized from delafossite-$CuFeO_2$ precursor enhanced the formation of Hägg carbide (χ-Fe_5C_2), which is considered the primary active phase for Fe-based FT synthesis. K-doped Fe-Co bimetallic catalysts were successfully synthesized through a pore-filling incipient wetness impregnation method by Satthawong et al. [100] The selectivity to C2+ hydrocarbons and the chain growth probability of gas-phase hydrocarbons were significantly improved by the presence of K.

Chen et al. [101] reported the possibility of Mo_2C-supported metal catalysts for C2+ hydrocarbon synthesis. The reaction was carried out at relatively low temperatures (135 °C and 200 °C), and several different metals (Cu, Pd, Co, and Fe) were dispersed onto the Mo_2C support. Cu- and Pd-based catalysts promoted the formation of methanol, while the addition of Co and Fe facilitated the formation of C2+ hydrocarbons.

2.3.3 Catalysts for other CO_2 hydrogenation reactions

RNG can be stored or distributed to end users through pre-existing natural gas infrastructure. Additionally, the system can be utilized to store excess energy from intermitted renewable sources through the power-to-gas (PtG) approach [40]. The technical and economic feasibility of such a system will depend on multiple factors, including the type of catalyst. Proper catalyst selection to achieve high activity, selectivity and stability at low cost is the key. Sabatier reaction is thermodynamically favorable at high pressure and low temperature [102]; however, searching for materials that can result in fast reaction rates at low temperature is challenging. Therefore, there is strong need to develop highly active and stable catalytic materials that selective to CH_4 formation. Normally, elements of group VIII to X of the periodic table can be used to synthesize Sabatier catalysts. Activities and selectivities for different metals have been compared in the literature: Mills et al. ranked the activity towards Sabatier reaction as Ru > Fe > Ni > Co > Mo [103]. In the same study, the selectivity was ranked as follows: Ni > Co > Fe > Ru [103]. Typically, metal oxides such as alumina (Al_2O_3) are used as supports to provide increased surface area [104].

The highest catalytic activity reported thus far was for the Ru-based catalyst. Abe et al. reported 100% CO_2 conversion and selectivity with a 0.8wt% Ru/TiO_2 at 160 °C, but at very low GHSV of 0.24 mL g_{cat}^{-1} h^{-1} [105]. A different study on a 5wt% Ru/Al_2O_3 catalyst found conversion and selectivity to be 55% and 95% respectively at 350 °C [106]. In another study, the performance of Rh-based catalysts was compared while manipulating the support materials. It was found that ZrO_2 had the highest conversion, followed by Al_2O_3 and SiO_2 [107]. Swalus et al. investigated the synergetic effect of mechanically mixed Rh/γ-Al_2O_3 and Ni/C [108]. They found that the mixed catalyst is 100% selective towards CH_4 and observed higher CH_4 production compared to the single catalyst. It was suggested that Rh/γ-Al_2O_3 allows for quick adsorption of CO_2 while H_2 is

adsorbed by the Ni/C, resulting in higher CH_4 production. Xu et al. found that Ru/TiO_2 is more active in CO_2 methanation than Ru/Al_2O_3 (3 times higher reaction rate) [109]. Sharma et al. reported 55% CO_2 conversion with 99% CH_4 selectivity for ceria doped Ru catalyst [110]. Other precious metals, such as Pt and Pd, were studied as well, showing good conversion and selectivity to Sabatier reaction [111, 112]. Martins et al. studied CO_2 methanation over the shape-controlled Pd nanoparticles encapsulated in mesoporous silica [113]. Encapsulation improved the stability of the nano-particles against sintering. However, despite their excellent catalytic properties precious metals are not feasible for industrial, large scale RNG generation systems, simply due to their high cost [104]. Especially considering the fact that RNG is a low-value commodity and its selling price should be comparable, or at least reasonably close to the price of natural gas.

Unlike precious metals, non-noble transition metals are promising candidates for large-scale commercial applications due to their high availability, low cost, and reasonably high catalytic activity [114]. Ni-based catalysts have been studied quite extensively for Sabatier reaction [115]. Garbarino et al. studied CO_2 hydrogenation over a 20wt% Ni/Al_2O_3 catalyst at 400 °C and GHSV of 55,000 mL g_{cat}^{-1} h^{-1} [116]. They obtained 81% CO_2 conversion with 96% CH_4 selectivity. Cai et al. modified the Ni/Al_2O_3 catalyst by the addition of ZrO_2, resulting in better activity and stability [117]. Takano et al. reported 82% CO_2 conversion with 100% CH_4 selectivity over Ni supported on Y-doped ZrO_2 at 350 °C, indicating that the oxygen vacancies formed due to the doping of Y^{+3} to ZrO_2 are responsible for high activity [118]. Rahamani et al. studied the performance of different Ni supported mesoporous Al_2O_3 catalysts [119]. They observed a decrease in specific surface area from 177 to 130 m^2/g as the Ni content increased from 10 to 25wt%, with the 20wt% Ni/Al_2O_3 catalyst showing the highest CO_2 conversion (~79%) with 100% selectivity to CH_4 formation at 350 °C. Tada et el. carried out CO_2 hydrogenation over a sponge

Ni catalyst (the sponge has high thermal conductivity avoiding hot spots) and observed 83% CO_2 conversion at 250 °C and GHSV of 4200 mL g_{cat}^{-1} h^{-1} [120]. However, despite good catalytic activity and selectivity, Ni catalysts are vulnerable to deactivation. At typical operation temperatures of Sabatier reaction (700-800 K), catalyst deactivation is predominately due to carbon deposition on the catalyst surface (coking). Coking further results in surface fouling, blocked active sites and reduction in overall catalyst activity overtime [121].

In several studies non-noble transition metals other than Ni were investigated for their catalytic performance in CO_2 methanation. Alrafei et al. studied CO_2 methanation over alumina-supported Ni-Co catalysts for various loading of Ni and Co. They observed that the presence of Co increased the activity and selectivity towards CH_4 due to its positive effect on Ni reducibility [122]. Primo et al. investigated CO_2 methanation over MoS_2 supported on graphene (MoS_2/G) [123]. The experiments showed promising results for MoS_2/G as a methanation catalyst as compared to bulk MoS_2 that favors the RWGS reaction. Recently, Zhong et al. utilized $LaNi_5H_5$ for CO_2 methanation [124]. $LaNi_5H_5$ plays a dual role, serving as a solid state H_2 source and providing at the same time reduced Ni for catalytic reduction. Despite a considerable amount of work on Sabatier reaction catalysis, most of studies focused on expensive noble metals. Ni-based catalysts are low-cost but vulnerable to deactivation.

2.3.4 Bi-metallic and multi-metallic catalysts

i. Bi-metallic and multi-metallic oxide catalysts

It has been reported that the combination of two or even more metal elements can contribute to the advantages of individual metals such that they provide unique properties that result from the synergy between the metals. The utilization of bi-metallic catalysts has been investigated for various applications. For instance, Jiang et al. [125] studied the Pd-Cu bimetallic catalysts for CO_2

hydrogenation to methanol. The XRD patterns indicated the formation of $CuPdO_2$ after calcination and the bi-metallic oxide was reduced to $PdCu_3$ alloy in the pre-reduction. The synergistic effect was observed on the alloy which led to the promotion of the methanol formation rate which was higher than the sum of the monometallic Cu and Pd catalysts. Huang et al. [126] reported a CoO-NiO-Al_2O_3 system for CO_2 reforming of CH_4. The presence of Co conduced to superior stability than NiO-Al_2O_3 catalyst owing to the mesoporous monometallic alloy from reduction before the reaction.

Regarding RWGS, bi-metallic and multi-metallic catalysts have also made an important contribution to development of RWGS catalysts. It has been reported that the addition of Mo to Fe/γ-Al_2O_3 can improve the activity due to better Fe dispersion and smaller particle size of Fe species. From the TPR patterns (Figure 2-9), it can be seen that the temperature of the H_2 consumption peaks of Fe-Mo/Al_2O_3 are higher than for the monometallic catalysts. The structure of the Fe-O-Mo is monoclinic $Fe_2(MoO_4)_3$ and this bi-metallic oxide is harder to reduce than Fe oxide which provides the enhancement of stability by inhibiting the reduction of the catalyst under reaction condition. [127]

Ye et al. [128] demonstrated that, compared with Pd/SiO_2 catalyst, bi-metallic Pd-In/SiO_2 exhibited lower activity (Figure 2-10) and the number of active sites on the surface for H_2 chemisorption was less, which leads to lower conversion of CO_2. However, the selectivity towards CO at high temperature is much higher than Pd/SiO_2 which because of weaker adsorption of CO on PdIn surface. Ro et al. [129] reported the AuMox/SiO_2 catalysts with different Au/Mo ratios that were synthesized by controlled surface reactions and the performance for RWGS was tested with and without the addition of visible light. It showed that $Au_1Mo_{0.1}/SiO_2$ is the most active catalyst and is 30 times more active than monometallic Au catalyst benefited from the formation

of interfacial sites. Furthermore, the addition of visible light can also increase the activity by around 5 times.

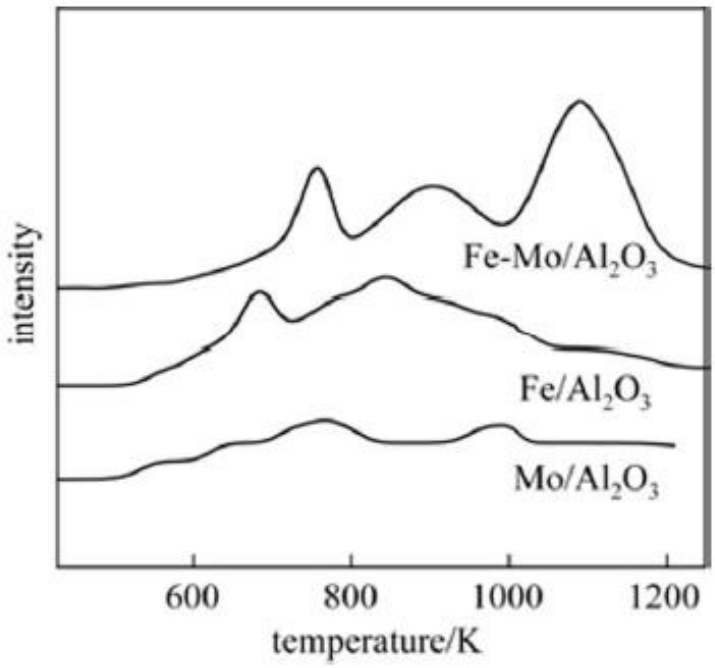

Figure 2-9 The H_2-TPR patterns of calcined Mo/Al_2O_3, Fe/Al_2O_3 and $Fe\text{-}Mo/Al_2O_3$ catalysts. [128]

Barium zirconate-based perovskite-type catalysts have also been tested for RWGS reaction. At 600 °C, Zn- and Y- doped catalyst ($BaZr_{0.8}Y_{0.16}Zn_{0.04}O_3$) showed superior activity but the introduction of Ce into the catalyst can decrease the activity. [130] It was reported that both promotion and restraining effects were caused by vacant oxygen sites. On the one hand, increasing the vacant oxygen sites can be beneficial to the activity, but they can also can decrease the stability of the catalyst during reaction. Mg-Fe-Al-O catalysts were prepared by Dharanipragada et al. [131] and a $MgFeAlO_x$ phase was confirmed in all samples. The presence of the spinel improved the activity also the stability of the Fe catalyst to a great extent. The CO yield obtained on this catalyst

was 10 times higher than 10 wt% Fe_2O_3/Al_2O_3 and was stable throughout over 60 cycles of reduction and re-oxidation between Fe^{3+} to Fe^{2+} at 750 °C.

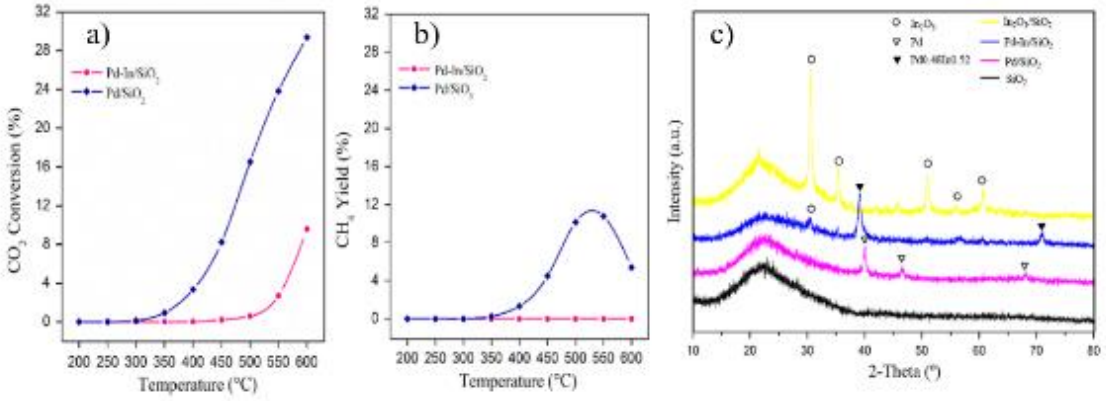

Figure 2-10 Pd–In/SiO_2 and Pd/SiO_2 catalysts catalytic performance and XRD patterns (a) CO_2 conversion (b) CH_4 yield and (c) X-ray diffraction patterns. [128]

ii. Bi-metallic and multi-metallic carbide catalysts

Most of the transition metals can form different carbides and nitrides, except for some second and third-row elements. Recent studies indicated that transition metal carbides have outstanding catalytic performance in terms of activity, selectivity and poisoning resistance. Due to those advantages, transition metal carbides have been investigated on plenty of thermo-catalytic reactions. To modify the catalysts and search for preferable performance, addition of another metal as promoter on the surface or introduce another metal atom into the lattice can modify the catalyst properties, which may contribute to various improvements.

Co_3WO_4 was used as the precursor of Co_6W_6C catalyst after a multi-step carburization process in the mixture of CO_2 and CO. [132] The synthesized Co_6W_6C is a decent heterogeneous catalyst for dry reforming of methane at high temperature. The bi-metallic carbide was not efficient at a range of 500-850 °C, however, when the temperature reaches 850 °C, an active and stable phase which contains Co, WC and C can be formed and was active even at lower temperature. Du

et al. [133] reported Co-Mo carbide catalysts applied in dry reforming of methane. Though no $CoMoC_x$ phase is observed in XRD patterns, they indicated that cobalt incorporated into the Mo_2C carbide by replacing the atoms inside lattice while the framework was not changed significantly. When the loading of the bi-metallic carbide reached 15 wt%, the conversion of CO_2 and CH_4 were both increased significantly with the addition of Co.

Co-W carbides were also investigated in the application of CH_4 partial oxidation and the results showed that the catalytic performance was better than molybdenum carbide. [134] Zhao et al. [135] prepared a series of Ni-Mo carbide catalysts by sol-gel method for CO hydrogenation. For catalysts with Ni/Mo ratio over 0.17, Ni_6Mo_6C might form but for the catalysts with a ratio equalled 0.17, no bimetallic carbide peaks were observed while the catalyst consists of NiO and β-Mo_2C. The highest conversion and selectivity towards alcohol was achieved on $Ni_{0.5}MoC$ sample and the active site for alcohol formation was the Ni_6Mo_6C phase derived from characterization results.

There have been relatively few studies that specifically concentrate on bi-metallic carbides for reverse water gas shift (or water gas shift) reaction. Most of the bi-metallic carbide catalysts developed were one metal dispersed on another type of metal carbide and more often, only small proportion of bi-metallic carbide phase was observed. Most of the studies were based on Mo_2C because of its outstanding properties in RWGS. [50] Various promoters and modifications have been applied to Mo_2C to improve the catalytic performance especially on the activity while the Mo_2C itself exhibited superior stability during the reaction.

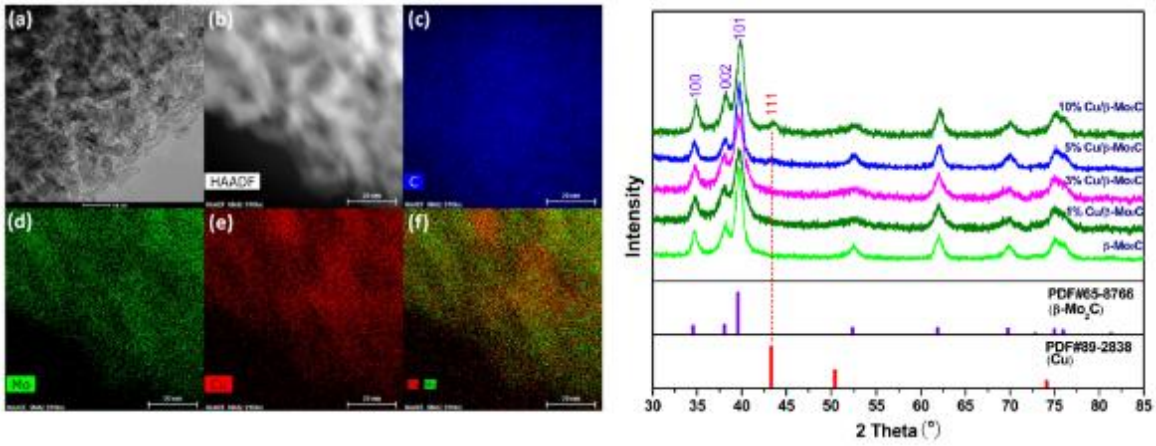

Figure 2-11 Left: Electron microscopic characterizations of 1 wt % Cu/β-Mo_2C sample: (a) TEM image (scale bar, 10 nm) and (b) STEM image. Element mapping of (c) C (d) Mo (e) Cu and (f) Cu + Mo. Right: XRD patterns of Cu-Mo_2C catalysts. [136]

As summarized in Table 2-2, Mo_2C outperforms $PtCo/CeO_2$ and $PdNi/CeO_2$, and with the promotion of Co, the conversion of CO_2 was even higher. [22] The ability of Co-Mo_2C to dissociate CH_4 strengthen the selectivity to CO and Mo_2C was maintained in carbide state by re-carburization effect during the reaction. $CoMoC_yO_z$ was formed and considered to be responsible for the superior performance of RWGS. Zhang et al. [136] synthesized highly dispersed metal copper over β-Mo_2C for RWGS; however, no bi-metallic carbide phase was detected in XRD pattern (Figure 2-11). Copper is highly active for RWGS but can easily deactivate due to aggregation at a high temperature which is required for high conversion for RWGS. With the presence of β-Mo_2C, the dispersion of Cu was enhanced on 1 wt% Cu/β-Mo_2C as the element mapping indicates in Figure 2-11, and no aggregation or sintering of Cu was detected after a 40h RWGS reaction at 600 °C. Moreover, Cu^+ was detected in the sample which revealed the interaction between Cu and Mo_2C, making Cu species more active for CO_2 hydrogenation.

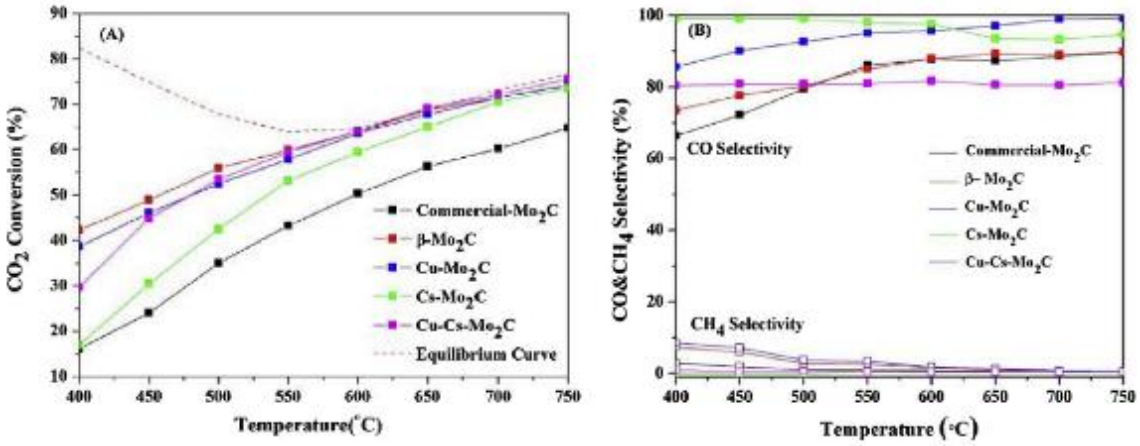

Figure 2-12 (A) CO_2 conversion (B) CO and CH_4 selectivity for the β-Mo_2C, Cu-Mo_2C, Cs-Mo_2C, Cu-Cs-Mo_2C and commercial Mo_2C. [137]

The role of Cs and Cu on Mo_2C catalysts was also proposed by Zhang et al. [137]. The CO_2 conversion on Cu-Mo_2C and Cu-Cs-Mo_2C were quite similar to β-Mo_2C which were close to the equilibrium conversion and Cu-Mo_2C exhibited higher selectivity towards CO (Figure 2-12). Cs-Mo_2C showed relatively lower conversion compared to other counterparts but the selectivity outperformed other catalysts particularly at low temperature which may attribute to the electronic effects of Cs on Mo_2C. Furthermore, the Cs-Mo_2C catalyst showed higher activity (conversion from 54.8% to 66%) after 50 hours on stream and exceeded the conversion on β-Mo_2C (stable at around 60%).

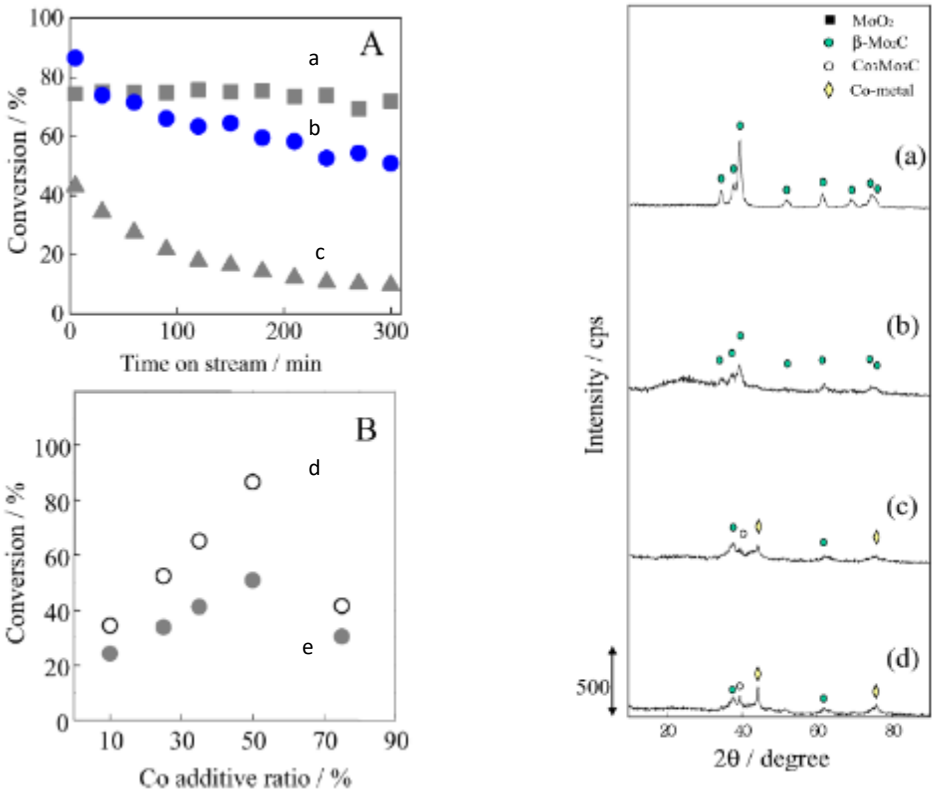

Figure 2-13 Left: (A) Conversion of CO over (a) CuZn catalyst (b) $Co_{0.5}Mo_{0.5}C$, and (c) MoC_x. (B) Conversion of CO at (d) 5 and (e) 300 min over the Co–Mo carbides with various Co/Mo ratios. Right: XRD patterns of catalysts carburized at 875K: (a) Mo_2C, (b) $Co_{0.25}Mo_{0.75}C$, (c) $Co_{0.5}Mo_{0.5}C$, and (d) $Co_{0.75}Mo_{0.25}C$ [1]

Nagai et al. [1] particularly discussed the Co-Mo carbide catalysts for water gas shift with different Co/Mo ratios and Co_3Mo_3C phase was detected when Co/Mo is 1 or higher (Figure 2-13). Co-Mo carbide with Co/Mo ratio of 1 was found to be the most active catalyst among all Co-Mo carbides (Figure 2-13) but the conversion of CO was higher than commercial CuZn catalyst only at the first 5 minutes on the stream but less after. Though Co_3Mo_3C phase was observed in $Co_{0.5}Mo_{0.5}C$, the amorphous Co-Mo oxycarbide was considered as an active phase responsible for the high activity.

Based on the above, the literature indicates that bi-metallic catalysts have been reported to be active and selective to RWGS. While there have been numerous studies on various types of bi-metallic catalysts for different applications, there is a relative scarcity of studies specifically focused on bi-metallic carbides for RWGS or water gas shift reactions. Most of the attention in this field has been on monometallic carbides, particularly Mo_2C, due to their exceptional properties in RWGS. The promising results achieved with Co-Mo carbide catalysts in dry reforming of methane emphasizes the potential for enhanced CO_2 conversion and CH_4 conversion with the addition of Co. [1] These findings suggest that Co-Mo carbides may hold untapped potential for improving RWGS catalysis.

2.4 Density functional theory (DFT) modeling of CO_2 reduction & hydrogenation

2.4.1 Density functional theory simulations of CO_2 hydrogenation reactions

Computational methods have been developed for material property investigation and catalysts design. Density Functional Theory (DFT) is a computational technique widely used in quantum mechanics to model the electronic structure of many-body systems, especially atoms, molecules, and solids. In material science and condensed matter physics, DFT is an indispensable tool for understanding and predicting the properties of materials at the electronic level. For catalyst design, DFT allows the study of surface reactions at the atomic level. It provides insights into the adsorption energy, reaction pathways, and activation energy barriers for different reactants and intermediates. The investigation of catalysts using DFT is an essential part of modern computational catalysis and material science. The main aim is to understand the mechanisms by which a catalyst accelerates a particular reaction, as well as to design new, more efficient catalysts. [138-140]

DFT can be employed to screen various materials like metals, metal alloys, and metal oxides to find candidates that show promising activity for CO_2 hydrogenation. [141] The screening is often performed using descriptors like binding energies or d-band centers that correlate with the catalytic activity. Once a candidate material is identified, DFT can be used to map out the potential energy surface (PES) for the reaction pathway. This includes the estimation of the activation energy barriers and identifying intermediates and transition states. For CO_2 hydrogenation, DFT is particularly useful to elucidate the competing pathways of the conversion of CO_2 to various products (e.g., carbon monoxide, methane, methanol) and identify the rate-limiting steps. DFT can also estimate the adsorption energies of CO_2 and hydrogen on different catalyst surfaces. [142] Strong adsorption energies are often indicative of higher reactivity, but they must be balanced to allow for efficient formation of attractive products, e.g., CO, CH_4 and methanol. DFT is used to calculate the energy barriers for crucial steps in the reaction mechanism, such as CO_2 activation, hydrogen activation, and C-H bond formation. These reaction barriers for the rate limiting steps significantly influence the reaction rate. One of the challenges in CO_2 hydrogenation is the molecule's thermodynamic stability, which makes it difficult to activate. DFT studies can provide insights into how a catalyst can lower the energy barrier for CO_2 activation, a critical step for its hydrogenation. [143]

2.4.2 Density functional theory simulations of CeO_2 (ceria) catalysts for RWGS reaction

As indicated in 2.2.2, studies have proposed two principal mechanisms of RWGS reaction, namely the Surface Redox Mechanism and the Associative Mechanism, which have been elucidated through a combination of reaction kinetics studies, spectroscopy, and density functional theory (DFT) simulations. However, these redox and associative mechanisms have been the subject of intensive DFT studies of RWGS on different materials.

In the RWGS reaction's redox mechanism [52, 53, 144], CO_2 is reduced to CO while the catalyst undergoes direct oxidation. Subsequently, H_2 reduces the catalyst to complete the catalytic turnover. This mechanism relies on two key conditions: (i) the ability of H_2 to reduce the catalyst surface, and (ii) effective reoxidation of the partially reduced catalyst surface under RWGS experimental conditions. Reducible oxide catalysts, easily reducible and oxidizable due to the oxygen provided by the support, predominantly follow this mechanism [145]. For example, in the case of CeO_2, CO adsorbs on a metal surface, oxidized by oxygen atoms from ceria. [146] Catalysts with different supports, such as Pt/CeO_2-TiO_2, have shown that both redox and dissociation mechanisms coexist in the RWGS reaction by DFT simulations. Additionally, the catalytic mechanisms of RWGS on ceria nanocrystals involve oxygen vacancies in ceria. Oxygen vacancy transport through bulk active oxygen was observed in ceria, and the nanostructure of ceria enhanced oxygen-ion conductivity and surface oxygen vacancy density [84, 147], which also opens the direction of using DFT calculations to investigate oxygen vacancy effects. Note that this is an emerging topic that has been widely studied for different applications given their potential to explain enhanced performance in materials' design. [48, 147] In summary, the redox mechanism plays a vital role in the RWGS reaction, particularly with reducible oxide catalysts like CeO_2.

One notable mechanism, termed the "associative mechanism," entails CO_2 adsorption on the catalyst surface, followed by interactions with dissociated hydrogen (H*) to form transitional molecules like formate (*HCOO), carboxyl (*COOH), carbonate (CO_3^{2-}), and bicarbonate (HCO_3^{+}) species. [54-58] These intermediates then undergo transformations, ultimately yielding the final RWGS products, CO and H_2O. Importantly, the decomposition of formates and the carbonate route are both significant pathways in the RWGS reaction. [138] Surface carbonates are considered

reaction intermediates, while formates are termed "minor intermediates" due to their stronger bonding and lower exchange rates. [148]

Based on the above, the redox mechanism emerges as a critical focal point in CO_2 hydrogenation reactions. The CO_2 reduction on the catalyst surfaces will be discussed in Chapter 7 based on this mechanism. This is supported by the fact that the RWGS reaction's redox mechanism, as outlined in previous reports [52, 53, 144], elucidates the interplay of reactions occurring on the catalyst surface. Despite the discussion of mechanism of RWGS, DFT calculation is a powerful tool to explore and benchmark the activity of the material, providing theoretical descriptors of the performance such as adsorption energy of CO_2 and binding energy of surface O to evaluate a catalyst before examining in the laboratory experiments. Section 2.3.1 focused on the discussion of catalysts for RWGS including CeO_2 based catalysts in terms of experimental works, while there are also theoretical studies focus on exploration of effective doped CeO_2 catalysts for RWGS. Metallic Cu [149] and Fe [150] were both reported in DFT studies to have activity for RWGS. [151] Their corresponding oxides were also good catalysts that are theoretically energetically preferred for reverse water gas shift. [151] The best active surface to be CuO among Cu oxides [152, 153] and Fe_3O_4 [154, 155] among Fe oxides. Ni[156] and Co[157] are reported to be active for CO_2 hydrogenation but are more favored for CO_2 methanation with enhanced selectivity towards CH_4. These elements may have the potential to be effective dopants to promote the catalytic activity of CeO_2 since all the candidates exhibit good CO_2 hydrogenation ability. Studies have been conducted to investigate synergistic effects of these transition metals to the performance of CeO_2 system. [158-160] However, a comparison between all these transition metals (Cu, Fe, Co and Ni) using DFT, and their cross validation with experimental results

conducted for consistent synthesized materials and similar transition metal content at same reaction conditions, still require a comprehensive exploration, especially for RWGS reaction.

2.5 Reverse microemulsion (RME) for heterogenous catalysts preparation

2.5.1 Thermodynamic and kinetic properties of reverse microemulsions

In general, the preparation methods of the catalysts often influence catalytic performance. For instance, the particle size may differ from different synthesis methods and normally, smaller particle size and volume to area ratio will lead to higher specific surface area of the material thus providing more active sites which is beneficial to the catalytic performance. Various innovation synthesis methods have been developed and applied to catalyst preparation and one of the common objectives in those methods is to reduce the catalyst particle size and to control the particle size distribution in a limited range.

In the study presented herein, reverse microemulsion (RME) method was implemented with the aim to obtain smaller particle size and narrower size distribution. [161] A microemulsion system consists of the water phase, oil phase and surfactant. The microemulsion looks homogeneous in appearance but at the molecular level, it contains two separate phases. In this study, as shown in Figure 2-14, the continuous phase is the oil phase and small water phase droplets are surrounded by surfactant molecules inside the oil phase. This water in oil system is defined as reverse microemulsion (RME). The hydrophilic heads of the surfactant molecules are attracted by the water phase and point into the water droplet, while their hydrophobic tails extend out of the droplets. Co-surfactant is also introduced to the system to increase stability. During the reaction of different RMEs, the nano-droplets act as micro reactors to limit the amount of reactant to restrain the resulted particle size. When two micelles meet, the surfactant shell may aggregate, and the content inside may react.

RME method is favored by the advantages of the higher specific surface area of the resulting particles. The particle size of the product can be controlled by varying the composition of the RME system, the mole ratio of water to surfactant, etc. RME method was also reported to be a suitable way for bimetallic catalysts synthesis and has its advantages. RME method is applied to obtain core-shell-structure particles which was reported by Yang et al. They coated CdTe particles with SiO_2 by RME method and the particle size was controlled between 45 to 109 nm and the SiO_2 coat also performs decent enhancement towards photostability of the CdTe encapsulated. [162]

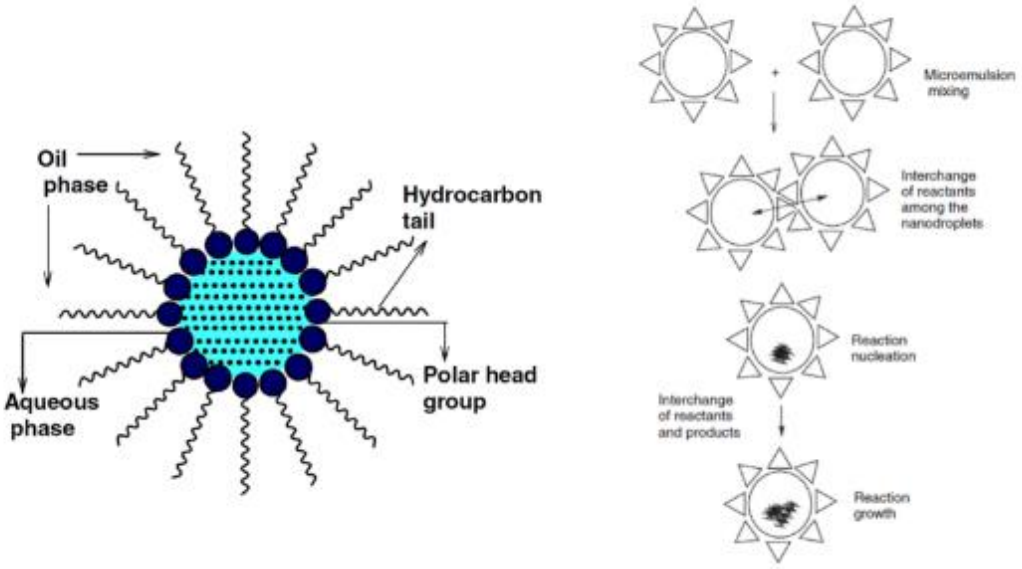

Figure 2-14 RME nano-droplets and reaction sketch. [1]

2.5.2 Applications of reverse microemulsion method to catalyst synthesis

Regarding CO_2 conversion, Park et al. [163] studied the impact of preparation methods on the Pd-Mg/SiO_2 catalytic performance for CO_2 methanation. The Pd-Mg/SiO_2 catalyst prepared by RME showed higher activity and selectivity to methane than traditionally wet impregnation Mg/Pd/SiO_2 catalyst and was stable after 10 hours reaction at the reaction temperature. However,

the particle size before the reaction is ~10 nm while aggregation occurred after the 10 hours reaction leading to an increase to ~20 nm. γ-Al_2O_3 supported NiMg was successfully synthesized by Dieguez [164] and tested for dry reforming of methane and propane. The RME system enhanced the interaction of Mg and Ni phase which resulted in homogeneous and stable bimetallic catalyst phase. Kishida [165] [166] also proposed that the particle size of CO_2 hydrogenation catalyst prepared by RME method, Rh/SiO_2 is 50% smaller than conventional impregnation method.

Santana et al. [167] investigated the effect of synthesis method on Nb-promoted Cu/Zn catalysts for CO_2 hydrogenation to methanol. Among coprecipitation, deposition-precipitation, wet impregnation, and incipient wetness impregnation, small particle size and higher specific surface area were achieved on the catalyst prepared by coprecipitation. Another study focused on CO_2 hydrogenation to methanol indicated the importance of preparation method. [168] The activity (both conversion and selectivity to methanol) of the $Cu/ZnO/Al_2O_3$ catalyst prepared by oxalate-gel coprecipitation was significantly enhanced as compared to the conventional coprecipitation sample. According to a study by Iablokov et al. [169], the regulation of particle size is crucial for CO_2 hydrogenation. It was found that Co nanoparticles within the range of 3-10 nm, obtained through precise control of the synthesis conditions using the hot injection method, exhibited higher turnover frequency compared to larger particles. Sathyamurthy et al. [170] employed the RME method to synthesize polyhedral-shaped CeO_2 nanoparticles with an average size of ca. 5 nm and a surface area of 168.3 m^2/g for use as a UV absorbent. Paschalidou & Theocharis [171] investigated the effect of the tail length of Triton-X surfactants on the surface properties of CeO_2 synthesized via the RME method, resulted in the nanoparticle size distributions in the 2-50 nm range, with the highest specific surface area of 134.8 m^2/g obtained after calcination at 300 ºC. Bumajdad et al. [172] employed the RME method to prepare the nanosized (6-13 nm) cubic CeO_2

for combustion catalysis. The highest obtained surface area before calcination was 250 m^2/g for the RME method compared to 119 m^2/g by thermal decomposition. After the high-temperature calcination at 800 °C, the surface area was reduced to 45-55 m^2/g.

The RME-based catalysts also showed superior catalytic performance which can be explained by the higher specific surface area and the composition of the metal atoms on the support. The increasing radiative forcing caused by accelerating emissions of greenhouse gases is calling attention and becoming a worldwide consensus, and thus heightened interests for controlling greenhouse gases emissions, particularly antropogenic CeO_2. [173-175] Carbon capture and utilization (CCU) has recently attracted attention due to its great potential for reducing CO_2 emissions. As opposed to carbon capture and storage (CCS), the output of captured CO_2 in CCU process is a commercial product, used either as a chemical feedstock or for direct utilization, e.g., for enhanced oil recovery (EOR). [176]

2.6 Summary

Power-to-Gas (PtG) technology is introduced as a promising means of storing surplus electricity through hydrogen production via water electrolysis, potentially leading to reduced carbon emissions. The review on existing reports on various catalysts used in the Reverse Water Gas Shift (RWGS) reaction has highlighted the importance of copper-based catalysts, molybdenum, and ceria in facilitating CO_2 conversion to CO. Also, recent studies has indicated that CO_2 can be directly transformed into hydrocarbons, underscoring the potential of non-noble transition metals as catalysts for these reactions. Additionally, the use of innovative reverse microemulsion (RME) method for catalyst synthesis is key to achieve smaller particle sizes and improved control over size distribution. The use of Density Functional Theory (DFT) modeling to understand and evaluate catalyst performance in CO_2 hydrogenation and RWGS reactions provides

insights into atomic-level mechanisms and offers valuable insights into critical aspects of catalysis, such as adsorption energy, reaction pathways, and activation energy barriers for different reactants and intermediates.

Chapter 3 Experimental and computational methods

3.1 Catalyst synthesis by reverse microemulsion method

3.1.1 Catalyst synthesis

i. Cobalt-molybdenum oxide and carbide catalysts

The RME system, comprising three segments—surfactant, oil, and water in a 2:8:7 ratio—employs a Triton X-100 and Co-surfactant blend, cyclohexane, and a specific salt/alkali solution, respectively. Initial mixing involves the surfactant components, followed by the oil phase, and then gradual inclusion of the aqueous part. Translucency post-mix indicates the need for additional co-surfactant until clarity is regained, with a further 30-minute stir to ensure system stability.

Uniform synthesis of cobalt and molybdenum within the RME system required multiple attempts to perfect composition and procedure. This method promotes the creation of nano-sized, evenly spread bimetallic particles. Instability issues of Ammonium heptamolybdate tetrahydrate (AHM) with cobalt nitrate were resolved by dissolving AHM in excess ammonia, aiding in aluminum and Co precipitation while maintaining RME translucency. Separate RMEs are combined slowly, ensuring no premature reactions and a clear mixture. This blend is then incrementally introduced to RME #3 with continuous stirring for uniform aluminum and cobalt distribution. Despite the system's translucent appearance, the absence of visible particles indicates extremely small precipitate sizes. A final 8-hour stir guarantees thorough reaction completion.

ii. Al_2O_3-supported iron catalysts

Three reverse microemulsions (RME) containing appropriate amounts of ferric nitrate ($Fe(NO_3)_2 \cdot 9H_2O$, Sigma-Aldrich), aluminum nitrate ($Al(NO_3)_3 \cdot 9H_2O$, Fisher Scientific) and

ammonium hydroxide (1M NH_4OH, LabChem Inc.) were prepared by mixing aqueous phase (DI water), surfactant (Triton X-100, Acros Organics), co-surfactant (propanol-2, Sigma-Aldrich), and oil phase (cyclohexane, Sigma-Aldrich). Briefly, aluminum nitrate RME was first mixed with NH_4OH RME (acting as a precipitation agent), and then ferric nitrate RME was added dropwise immediately to prevent precipitation of large particles resulted from the separation of phases. The resulted mixture was mixed using a magnetic stirrer for 8 h and then aged overnight (12 h) for stratification (settle the precipitation for easy separation).

The resulted gel-like precipitate was separated by centrifugation with subsequent washing by a mixture of ethanol and deionized water (3:1). This centrifugation/washing procedure was repeated 4 times. The washed precipitate was collected and dried overnight at 100 °C. K was subsequently added by wet impregnation using a diluted K_2CO_3 solution (0.13 mol/L) as an impregnation medium. After that the precipitate was calcined at 400 °C for 3 h under flow of air. To prepare for reaction, the powder catalysts was pelletized and sieved to 250-425 µm pellets. The catalyst synthesized using the method described above was denoted as RME Fe/Al_2O_3.

Two reference catalysts were prepared for comparison. The Fe/RME-Al_2O_3 catalyst was synthesized by loading Fe via wet (aqueous) impregnation (using $Fe(NO_3)_2{\cdot}9H_2O$) onto the RME γ-Al_2O_3 support. The RME γ-Al_2O_3 support was prepared by the same RME method as described above, but without Fe and K introduction. The Fe/Al_2O_3 catalyst was synthesized via wet (aqueous) impregnation using $Fe(NO_3)_2{\cdot}9H_2O$ as Fe precursor and a commercial support γ-Al_2O_3 (Alfa Aesar). Prior to reaction tests, all powder catalysts were pelletized and sieved to 250-425 µm pellets.

iii. CeO_2-based catalysts

Three reverse microemulsions (RMEs) were synthesized by combining an aqueous phase comprising cerium nitrate (99.5% $Ce(NO3)_3 \cdot 6H_2O$, Alfa Aesar), copper nitrate ($CuNO_3 \cdot 9H_2O$, Sigma-Aldrich), and ammonium hydroxide (28-30% NH_4OH, LabChem Inc.) with a surfactant (Triton X-100, Acros Organics), a co-surfactant (propanol-2, Sigma-Aldrich), and an oil phase (cyclohexane, Sigma-Aldrich) in a proportion of 1:1:4.5:3.5. The RME containing copper nitrate was introduced gradually into the RME with cerium nitrate, while continuously stirring for 4 hours. Subsequently, the RME containing ammonia was incrementally added to the mixture, maintaining a consistent stirring for another 4 hours, until a precipitate emerged. This precipitate was thoroughly rinsed four times using deionized (DI) water and then subjected to centrifugation. Afterward, the cleaned precipitate was left to dry overnight and subsequently calcined at 275℃ for a duration of 4 hours. For catalytic reactions, the resultant powdered catalyst was molded into pellets and sifted to yield pellet sizes ranging from 250-425 µm.

3.2 Catalysts characterization

X-ray diffraction (XRD) patterns of the fresh and spent catalysts were obtained on a powder diffractometer (D8 Discover, Bruker). Temperature programmed reduction (H_2-TPR) of fresh and spent catalysts were carried out under pure hydrogen from 100 °C to 800 °C, with a ramping rate of 10 °C /min with the help of a catalyst characterization instrument (AMI-300Lite). Surface area analysis (SAA) was performed on the same instrument with the single-point BET method. The degree of coking of the spent catalysts will be investigated by thermal gravimetric analysis (TGA) with an in-Line FTIR analyzer (MultiGas™ 2030, MKS Instruments) conducted (referred to In-situ TGA-FTIR). Scanning electron microscope (SEM), scanning electron microscopy coupled energy dispersive spectroscopy (SEM-EDS) and Transmission electron microscopy (TEM)

micrographs will be obtained by a Zeiss microscopy to determine the shape and particle size distribution of as-prepared catalysts.

3.2.1 X-ray powder diffraction (XRD)

To understand the components and the crystal forms of the existing phases, X-ray powder diffraction is a commonly used technology. In 1912, German physicist M. von Laue proposed that crystal lattice can diffract X-rays since the wavelength of X-ray is at the same magnitude as the distance between atoms in the crystal. [177] Constructive interference can be generated when filtered X-rays passes through the crystal phases from many directions. The superposition of the diffracted waves will intensify the signal in some directions and weakened in others then provide a unique "fingerprint" of the sample.

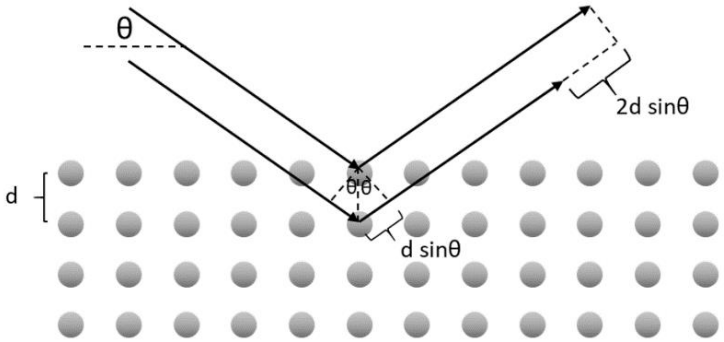

Figure 3-1 Bragg's law schematic.

In 1913, the British physicist Dr. Bragg [178] proposed an equation based on Laue's theory, Brag's law: $2d \sin\theta = n\lambda$. By analyzing the XRD profile obtained on the photographic film, the crystalline structure can be obtained. Each crystal plane will have its own peak positions and intensities. Comparing with the standard JCPDS card, the components can be identified. [179]

3.2.2 Inductively coupled plasma – optical emission spectrometry (ICP-EOS)

ICP-EOS method is applied in this study to determine the composition of the elements in the catalyst samples. An ICP-OES schematic diagram is shown in Figure 3-2. When an atom or ion in the ground state is under the plasma, its extranuclear electrons will be excited to a higher energy level. The unstable extranuclear electron will transit back to the ground and release the energy in the form of electromagnetic wave. Atoms can release various characteristic emission spectra of different wavelengths under the plasma, which will provide the element information. The concentration of an element in the sample can be acquired by comparing the intensity of the waves with the standard curve. In this study, ICP-EOS is capable to analyse the elements including K, Co, Mo, Fe and Al, but some non-metal elements such as C or O are unable to define since they are already included in the acid solution. [180]

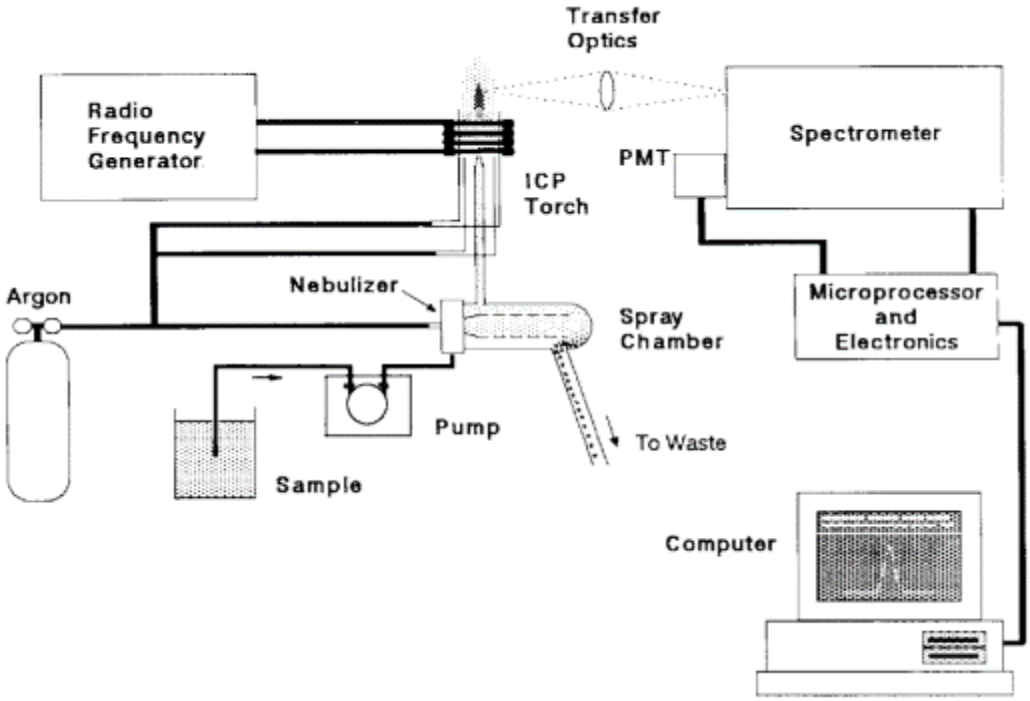

Figure 3-2 ICP-OES schematic diagram. [181]

3.2.3 Temperature-programmed experiments

i. Temperature-programmed reduction (TPR)

The TPR method is a useful experiment to study the reducibility of the catalysts. In a typical TPR experiment setup (Figure 3-3), a certain amount of metal catalyst is fixed in a tube reactor, and a low concentration hydrogen stream is passed through the catalyst with a constant flow rate. At the same time, the reactor is being heated programmatically. The oxide component inside the catalysts will be reduced when the temperature inside the reactor rises. The consumed hydrogen is proportional to the amount of reduced catalyst. H_2 concentration in the outlet steam is continuously detected by a gas thermal conductivity detector (TCD detector), and the recorded data can deduce a TPR curve. Each peak in the curve generally represents the transformation of a reducible species, for example from one type of oxide to another with different oxidation states, or metal. The area integrated is proportional to the amount of consumed hydrogen in the stream. TPR profile can reflect the change of metal oxidation states, the interaction between two metals and the interaction between metal oxide and support.

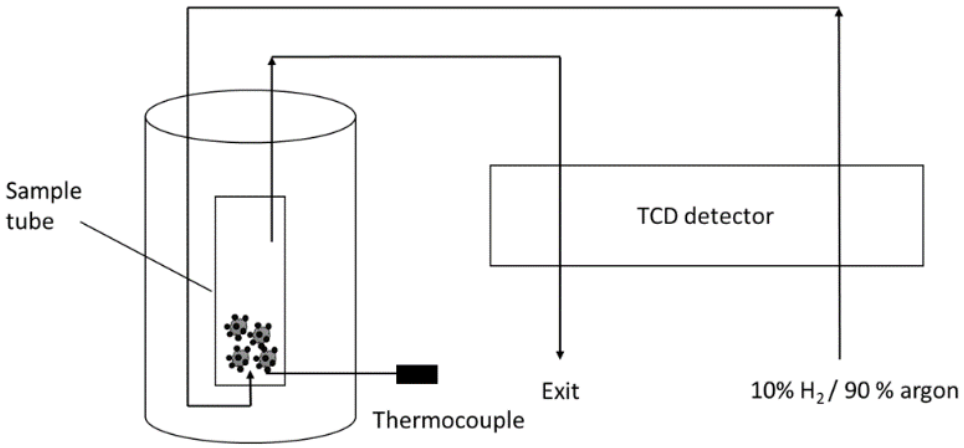

Figure 3-3 Temperature programmed experiments schematic diagram.

i. Temperature-programmed desorption (TPD)

The results of CO_2-TPD could reflect the adsorption strength of CO_2. Before performing TPD, the samples were heated in 30 mL/min 10% H_2/Ar with a ramping rate of 10 °C/min. TPD

adsorption step was conducted at 25 °C after dehydration, with CO_2 flow rate at 25 mL/min, then flushed He at the same temperature for 1 hour to remove gas phase CO_2 in the tube, followed by heating in the same flowrate of He with a ramping rate of 10 °C/min from 25 to 800 °C.

3.2.4 Surface area analysis (SAA)

The specific surface areas of the catalysts are analyzed by one point BET method. Surface area analysis is the application of the BET (Brunauer–Emmett–Teller) theory [182] which describes the physical adsorption of gas molecules on the solid surface. At atmospheric pressure, gas nitrogen molecules can physically adsorb on the surface of the catalyst when the sample is immersed in liquid nitrogen. The specific surface area of the sample can be calculated base on the amount of adsorbed gas. Removing the liquid nitrogen and bring the system back to room temperature will release the adsorbed nitrogen molecules. Usually, the change of the nitrogen in the stream is analyzed by a TCD detector which will generate two peaks in the TCD signal curve. The amount of adsorbed and desorbed molecules can be calculated by the area of the peaks which will rise to two surface area numbers. In this study, the specific surface areas are obtained by taking the average number of adsorption and desorption.

3.2.5 X-ray photoelectron spectroscopy (XPS)

X-ray photoelectron spectroscopy (XPS), also known as electron spectroscopy for chemical analysis (ESCA), is a sophisticated surface analytical technique that reveals the elemental composition, electronic state, and chemical environment of atoms within a material. Based on the photoelectric effect, it measures the kinetic energy of electrons ejected from a sample's surface when irradiated with X-ray photons. Because of its inherent surface sensitivity—typically probing the topmost 1-10 nanometers—XPS is invaluable in various scientific and industrial realms. Specifically, it's instrumental in studying thin film compositions, evaluating surface contamination,

characterizing catalysts, investigating battery materials, and understanding the chemistry of semiconductor interfaces. Its precision offers a comprehensive view of material surfaces, making it pivotal in advancements in nanotechnology, renewable energy, and electronics.

3.2.6 Transmission electron microscopy (TEM)

The morphology of the catalysts is studied by TEM and SEM electron microscopy. Transmission electron microscopy is a high-resolution electro-optical technique that the image is generated by transmitting a beam of focused electrons through the sample. To obtain a clear vision of the sample, the thickness of the sample should be as small as possible to allow the electron to go through. The ideal occasion is that only one layer of atoms is penetrated by the electron beam. TEM consists of an electro-optical system, a power supply and control system, and a vacuum system. The electrons after the sample are received by an imaging system consist of a phosphor screen and after processing and magnification, the information of the material can be provided as pictures. [183]

3.2.7 Scanning Electron Microscope (SEM)

Scanning Electron Microscope (SEM) is an electron microscope developed after TEM. The difference is that the information collected is the reflected signal of the electron beam generated from the source after scanning the surface of the sample point-by-point. [184] A 2-dimensional image of a selected area (usually from 1 cm to 5 microns in width) on the sample surface can be generated. SEM is favoured in generating stereoscopic images, large magnification range, continuous adjustment, high resolution and the sample preparation is simpler than TEM. The dispersion of elements on the surface is also an important characteristic of a catalyst. By combining the SEM and energy-dispersive X-ray spectroscopy (EDS), the element distribution shown as an elemental mapping can be obtained.

3.2.8 Thermogravimetric analysis (TGA)

Thermogravimetric Analysis (TG or TGA) is conducted to analyze the thermal stability, carbon existence and oxidation behaviour of the catalysts. The change of mass along with the temperature can be derived from the experiment. Usually, the sample is heated programmatically in a continuous stream then the relation of weight change and the temperature is recorded. The thermogravimetric method is widely used due to its accuracy measuring the mass change. [185] TGA can analyze processes involving weight change such as sublimation, vaporization, adsorption, desorption.

In this study, the TGA instrument is conducted to execute temperature-programmed oxidation with air as the oxidation gas stream. The weight change in this study is mainly caused by desorption of the water and CO_2, and the oxidation of the deposition carbon or catalysts itself. The outlet stream from the TGA instrument is also analyzed by an FTIR to determine the products released from the sample then the information related to deposition carbon, etc., can be revealed.

3.2.9 Fourier transform infrared spectroscopy (FTIR) for gas composition analysis

Infrared spectroscopy is a technique that analyses the infrared spectrum after the absorption of the sample. The beam contains many frequencies generated from the source and will pass through to the sample at the same time and repeat several times in a short period. The adsorbed infrared wavelengths, intensities and shapes depend on the category of the chemical bond and the atomic weight of the atoms connected at both ends. [186] The chemical bonds that reflect the structure of compounds can be revealed by infrared spectroscopy.

In this study, the outlet stream from a process is measured continuously by in-line FTIR analyzers. Target gases were set up in advance and a single beam infrared goes through specially

designed narrow band-pass optical filters and the energy of the inferred is limited to obtain the specified signal. The adsorption intensity was compared with a standard comparator to measure the concentration quantitatively in the stream.

3.2.10 In-situ FTIR

A transition type in-situ FTIR instrument (Figure 3-4) is also used to determine the intermediates during the reaction. The inferred signal generated from the source transmits the sample pellet, which consists of the mixture of sample catalyst and KBr and then arrives at the detector. When the reactions take place on the catalyst's surface, the adsorbed species, as well as the gas phase in the reactor, can be identified. Spectra at different temperatures and different time-on-stream are obtained to study the possible pathway of reactions. Background spectra are collected at the same temperature as reaction condition in inert gas to eliminate the interference of lab environment.

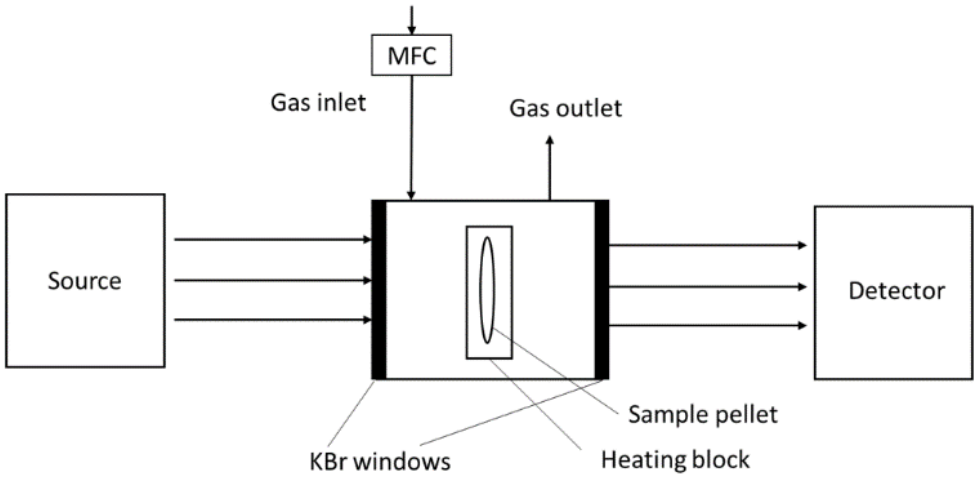

Figure 3-4 in-situ FTIR schematic diagram

3.3 Catalytic performance evaluation

3.3.1 Flow system setup

The flow system conducted to address the catalytic evaluation is demonstrated in

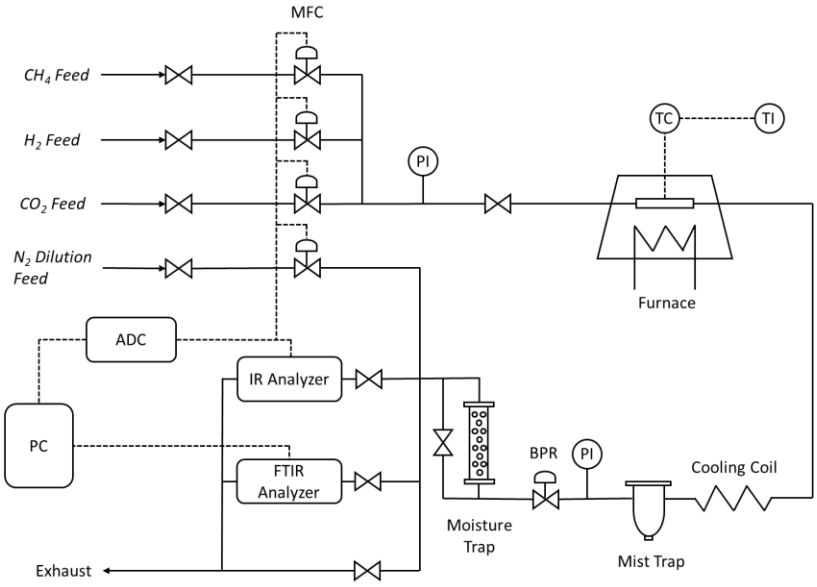

Figure 3-5. Reaction feedstock is regulated by three mass flow controllers connected to the cylinders and the pressure is adjusted by a back pressure regulator (BPR, S01094789B, Swagelok). The reactor is assembled by stainless-steel parts (Swage Lock) and placed inside a programmable furnace (Lindberg/Blue M™ Mini-Mite™, thermo Fisher Scientific). The internal space of a stainless-steel reducer (1/4" to 1/2") is used as the fix bed reactor and the catalysts are fixed between quartz wood. A 1/4" stainless steel tube and a 1/2" tube are attached to the reducer to conduct the flow system. 1/2" tube is applied for a larger opening to load and unload the catalysts. The temperature of the catalyst bed is measured and controlled precisely by a K-type thermocouple (TC, 1/8″, Omega Engineering) installing from the outlet tubing and connected to the controller (UP150, Yokogawa) of the furnace (Lindberg/Blue M™ Mini-Mite™, thermo Fisher Scientific). Moisture in the outlet stream is removed by a mist trap (AFM40-N02-Z-A, SMC Corporation) and a silica gel (Fisher Scientific) column. An IR analyzer (IR-208, Infrared Industries) is applied to

measure the concentration of CO_2, CO and CH_4 in the outlet stream while the data are recorded by an analog-to-digital converter (ADC, USB 6008, National Instruments) and LabView (National Instruments).

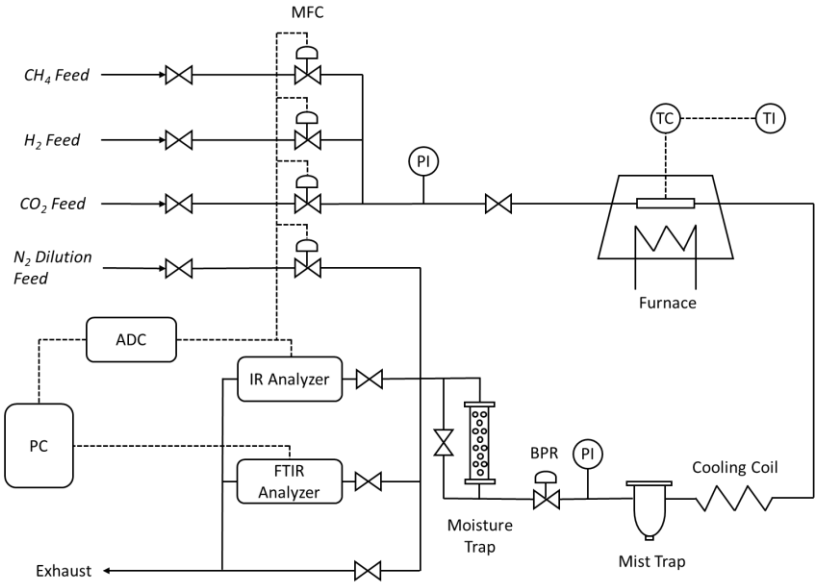

Figure 3-5 and Figure 3-6 indicates the modified flow system setup for hydrocarbon detecting. N_2 purge line was merged into the outlet from the reactor to dilute the concentration of hydrocarbon components (10-fold) for more accurate measuring. FTIR analyzer was conducted to detect products up to C4 hydrocarbons.

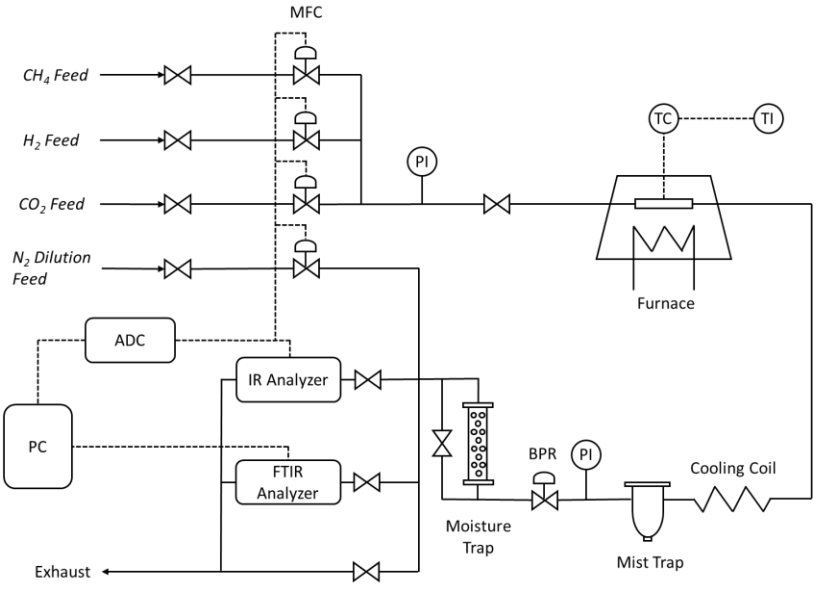

Figure 3-5 Flow system setup. Abbreviations: BPR – back pressure regulator, FTIR – Fourier transform infrared gas analyzer, GC – gas chromatograph, MFC – mass flow controller, PI – pressure indicator, PC – personal computer, TC – thermocouple, TI – temperature TI – temperature indicator, RH – relative humidity sensor.

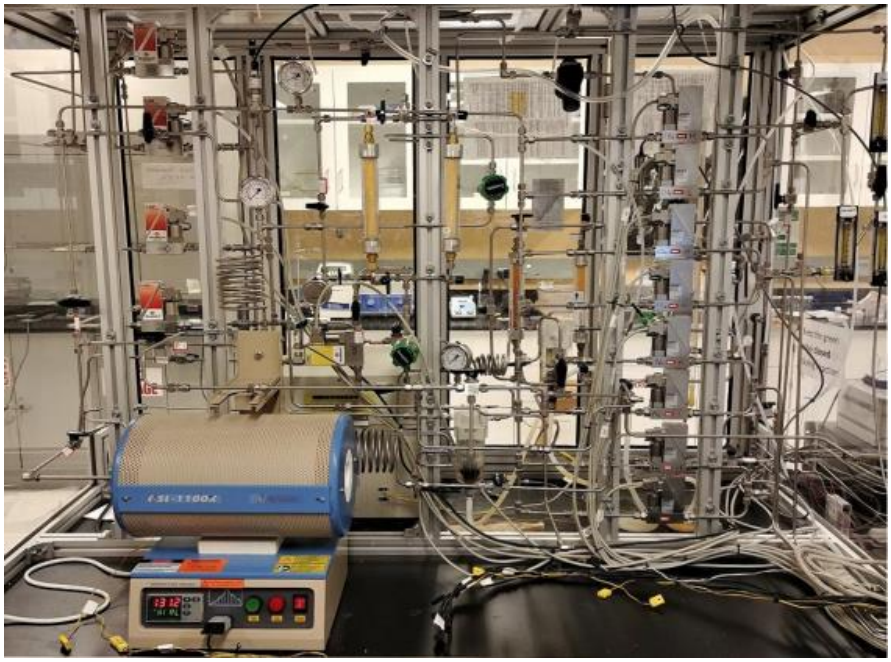

Figure 3-6 Flow system conducted for catalytic performance tests.

3.3.2 Catalytic performance evaluation

The catalytic performance of the prepared catalysts is tested in terms of temperature and pressure, gas hourly space velocity (GHSV), and the stability of the catalysts.

In RWGS reaction tests (in Chapter 4, 6 and 7), the CO_2/H_2 ratio is maintained at 4 by mass flow controllers in all experiments. The temperature effect is evaluated in a range of 300 °C to 600 °C with constant GHSV and pressure. GHSV test will also be carried out from 5,000 mL $h^{-1}g_{cat}^{-1}$ to 200,000 mL $h^{-1}g_{cat}^{-1}$ with other parameter fixed. Before each test, the catalysts are reduced in pure hydrogen f to expose the active site and activate the catalysts. In temperature-dependent test (T-test) and GHSV test, at each reaction condition point, a 2-hour duration is given to reach

the steady state and the interval for staging is 30 min. Detailed reaction conditions of each experiment will be described in Chapter 4, Chapter 5 and Chapter 6.

Gas hourly space velocity (GHSV) is calculated using the following equation:

$$GHSV = {Q_f}/{W_C} \tag{3-1}$$

In eq.3-1 Q_f and W_C are the volumetric flow rate and the weight of the catalysts, respectively. In RWGS reaction, CO_2 conversion and CO selectivity were defined by eq. (3-2) and eq. (3-3) for RWGS. y_{CO_2} , y_{CH_4} and y_{CO} are the mole fraction of CO_2, CH_4, and CO respectively on a dry basis. X is the conversion and S is the selectivity.

$$X_{CO_2} = \frac{y_{CH_4} + y_{CO}}{y_{CO_2} + y_{CH_4} + y_{CO}} \tag{3-2}$$

$$S_{CO} = \frac{y_{CO}}{y_{CH_4} + y_{CO}} \tag{3-3}$$

Carbon balance is defined as the total rate of carbon fed to the reactor divided by the rate of carbon exiting the reactor. Carbon balance (CB) was continuously monitored and recorded in all experiments (using LabVIEW). The carbon balance of the system is given by eq. (3-4), where α is the ratio of H_2/CO_2 in the feed, which is 4 in RWGS. f_i is the conversion towards product i.

$$CB = (y_{CO_2} + y_{CO} + y_{CH_4})(1 + \alpha - f_{CO} - 4 f_{CH_4}) \tag{3-4}$$

$$\alpha = \frac{F_{H_{2,f}}}{F_{CO_{2,f}}} \tag{3-5}$$

$$f_{CO} = \frac{y_{CO}}{y_{CO_2} + y_{CO} + y_{CH_4}} \equiv \frac{F_{CO,out}}{F_{C,out}} = \frac{F_{CO,out}}{F_{CO_2,f}} \tag{3-6}$$

$$f_{CH_4} = \frac{y_{CH_4}}{y_{CO_2} + y_{CO} + y_{CH_4}} \equiv \frac{F_{CH_4,out}}{F_{C,out}} = \frac{F_{CH_4,out}}{F_{CO_2,f}} \tag{3-7}$$

Eq. (3-4) is obtained from the carbon balance definition, Eq. (3-8), using Eq (3-5 to 3-7) and Eq. (3-9) to define the total outlet molar flow rate ($F_{C,out}$ is the outlet molar flow rate of all carbon-containing species, $F_{CO,out}$ and $F_{CH4,out}$ correspond to H_2 consumption in RWGS and methanation, according to reaction stoichiometry):

$$CB = \frac{(y_{CO_2} + y_{CO} + y_{CH_4})F_{t,out}}{F_{CO_2,f}} \tag{3-8}$$

$$F_{t,out} = F_{CO_2,f} + F_{H_2,f} - F_{CO,out} - 4F_{CH_4,out} \tag{3-9}$$

In CO_2 hydrogenation to hydrocarbon reactions, the reaction can be described as:

$$CO_2 + \frac{4x+y}{2x} H_2 = \frac{1}{x} C_x H_y + 2H_2 \tag{3-10}$$

The CO_2/H_2 ratio is controlled from 1 to 4 (in Chapter 5) with a constant GHSV= 3000 mL $h^{-1}g_{cat}^{-1}$. The temperature effect is evaluated in a range of 300 °C to 375°C with a constant GHSV and a pressure of 10 bar. Before each test, the catalysts are reduced in pure hydrogen at 400 ℃ for 3 hours. At each reaction condition point, a 5-hour duration is given to reach the steady state and the interval for staging is 10 min. The hydrocarbon distribution was calculated based on carbon moles and the related calculation equations are listed below.

$$X_{CO_2} = \frac{y_{CH_4} + y_{CO} + \sum x \cdot y_{C_xH_y}}{y_{CO_2} + y_{CH_4} + y_{CO} + \sum x \cdot y_{C_xH_y}} \tag{3-11}$$

$$S_{C_xH_y} = \frac{\sum x \cdot y_{C_xH_y}}{y_{CH_4} + y_{CO} + \sum x \cdot y_{C_xH_y}} \tag{3-12}$$

$$CB = (y_{CO_2} + y_{CO} + y_{CH_4} + \sum x \cdot y_{C_xH_y}) \cdot (1 + \alpha - f_{CO} - 4 f_{CH_4} - \sum \frac{4x+y}{2x} \cdot f_{C_xH_y}) \tag{3-13}$$

Carbon balance is given by eq. (3-14 to 3-18), where α is the H_2/CO_2 ratio in the feed, y_i and f_i is the mole fraction and CO_2 conversion to species i, respectively, and C_{total} is the total mole fraction of carbon-containing species which calculated by the mole fraction of each species multiply by the number of carbon in the corresponding molecule, as shown in eq. (3-15). To calculate the carbon balance, the total carbon mole fraction formula was substituted into eq. (3-16). The conversion to each species was introduced and rearranged to eq. (3-17) and eq. (3-18).

$$CO_2 + \frac{4x+y}{2x} H_2 = \frac{1}{x} C_x H_y + 2H_2O \quad (3\text{-}14)$$

$$C_{total} = y_{CO_2} + y_{CH_4} + y_{CO} + \sum x \cdot y_{C_xH_y} \quad (3\text{-}15)$$

$$CB = C_{total} * (1 + \alpha - \frac{y_{CH_4} + 4y_{CO} + \sum \frac{4x+y}{2x} \cdot y_{C_xH_y}}{C_{total}}) \quad (3\text{-}16)$$

$$CB = C_{total} * (1 + \alpha - f_{CO} - 4f_{CH_4} - \sum \frac{4x+y}{2x} \cdot f_{C_xH_y}) \quad (3\text{-}17)$$

$$CB = (y_{CO_2} + y_{CO} + y_{CH_4} + \sum x \cdot y_{C_xH_y}) \cdot (1 + \alpha - f_{CO} - 4f_{CH_4} - \sum \frac{4x+y}{2x} \cdot f_{C_xH_y}) \quad (3\text{-}18)$$

3.3.3 Mass and heat transfer criterion

The Mears criterion [187] is applied to estimate if mass transfer heat transfer from the bulk gas phase to the catalyst surface can be neglected because of the low reaction rate. Weisz-Prater criterion is used to determine if internal diffusion is limiting the reaction. [187] When Eq 3-19 and 3-22 can be satisfied, the absence of interphase, and intraparticle, mass and heat transfer limitations was confirmed by calculating corresponding [187, 188] criteria (all symbols are in the List of Symbols):

$$\frac{R'_{obs}\rho_b r_p}{k_c C_{CO_2,b}} \ll 0.15 \qquad (\textit{Mears criterion for interphase mass transfer}) \quad (3\text{-}19)$$

$$\frac{|\Delta H_{RWGS}| R'_{obs}\rho_b r_p}{hT} \ll \frac{0.15TR_g}{E_a} \qquad (\textit{Mears criterion for interphase heat transfer}) \quad (3\text{-}20)$$

$$\frac{R'_{obs}\rho_c r_p^2}{D_m C_{CO_2,s}} \ll 1 \qquad (\textit{Weisz-Prater criterion for internal diffusion}) \qquad (3\text{-}21)$$

$$\frac{|\Delta H_{RWGS}| R'_{obs}\rho_b r_p^2}{\lambda_s T_s} \ll \frac{0.75 T_s R_g}{E_a} \qquad (\textit{isothermal pellet criterion}) \qquad (3\text{-}22)$$

Interphase mass and heat transfer coefficients (k_c and h) were calculated using the following correlations:

$$\mathrm{Sh} = \frac{k_c d_p}{D_m} = 2 + 0.6\,\mathrm{Re}^{\frac{1}{2}}\,\mathrm{Sc}^{\frac{1}{3}} \qquad (3\text{-}23)$$

$$\mathrm{Nu} = \frac{h d_p}{\lambda_g} = 2 + 0.6\,\mathrm{Re}^{\frac{1}{2}}\,\mathrm{Pr}^{\frac{1}{3}} \qquad (3\text{-}24)$$

Calculations were conducted for low and high conversions in the 300-375 °C range and for the wide range of activation energies (E_a = 20-200 kJ/mol). In all cases, all transport limitations were completely negligible, as expected for the small size of catalyst pellets (350-425 μm) used in the experiments.

3.4 Computational methods

3.4.1 Model construction

Density Functional Theory (DFT) calculations were carried out using the Vienna Ab Initio Simulation Program (VASP) [189] package. A plane-wave basis set was employed, with a cut-off kinetic energy set at 450 eV. The simulation utilized the Projector-Augmented Wave (PAW) [190] methodology for describing the core-valence interaction, alongside the Perdew–Burke–Ernzerhof (PBE) [191] functional, corrected with the van der Waals Density Functional Theory (vdw-DFT). The spin-polarized Generalized Gradient Approximation plus Hubbard U (GGA+U) [192] method was applied to ceria and transition metals to properly characterize the electronic structure and correct the on-site coulomb repulsion of Ce 4f orbital. [18, 193, 194]

Bulk CeO_2 structure was optimized, and the lattice parameters were carefully confirmed with those reported in the literature. [195] Then (111), (100), and (110) surfaces of the CeO_2 were constructed and optimized. A 15 Å vacuum thickness was introduced between periodic slabs to mitigate interaction between the periodic cells. The periodic cell consist of 3 layers of Ce and the top layer was allowed for relaxation whereas the bottom layers of the structure were fixed at structure optimization to mimic the bulk region. Modifications and doping were performed to the top Ce layer. The convergence criteria were set to 10^{-5} eV for system energy and 0.01 eV/Å for interatomic forces. Due to the relatively large slab cell, Brillouin zone sampling was conducted using a (2 × 2 × 1) Monkhorst–Pack grid, this was chosen since it has been previously reported to achieve an acceptable convergence performance [196].

3.4.2 Calculation of oxygen vacancy formation energy, binding energies and activation energies

The oxygen vacancy formation energy (E_{OV}) on a certain surface can be calculated by the following equation.

$$E_{OV} = E_{slab(OV)} + \frac{1}{2}E_{O2} - E_{slab(stoi)} \qquad (3\text{-}25)$$

Where the $E_{slab(OV)}$, E_{O2} and $E_{slab(stoi)}$ corresponding to the energy of a slab with one oxygen vacancy, energy of gas phase oxygen molecule and energy of a stoichiometric slab without oxygen vacancy.

Binding energies of an adsorbed species were calculated based on the following formula (3-26). Eads, $E_{(slab+ads*)}$, $E_{ads(g)}$ and $E_{slab(OV)}$ represent to the total energy of the adsorbed system, energy of the gas phase adsorbate, and the energy of the bare surface, respectively.

$$E_{ads} = E_{(slab+ads*)} - (E_{ads\ (g)} + E_{slab(OV)}) \qquad (3\text{-}26)$$

Transition states were identified using the Nudged Elastic Band (NEB) method the activation energy (Ea) was calculated using the energy difference between the initial state and transition state and were verified through vibrational frequency calculations by identifying imaginary frequencies. To calculate the free energies of the process, entropy, zero-point energy, and enthalpy correction were determined for all adsorbed structures using statistical thermodynamics. The VASPKIT code was used for post-processing of the VASP calculated data for temperature corrections. [197, 198]

$$E_{act} = E_{TS} - E_{IS} \quad (3\text{-}27)$$

Chapter 4 Cobalt-molybdenum oxide and carbide catalysts for reverse water gas shift

This chapter explores the CoMo-based bimetallic catalysts for CO_2 thermo-catalytic conversion, with a particular focus on their potential for the Reverse Water Gas Shift (RWGS) reaction at 600°C. The investigation including the impact of gas hour space velocity (GHSV), stability assessment, and extensive characterization experiments is considered. As the global pursuit of sustainable energy solutions intensifies, the development of efficient catalysts for CO_2 conversion becomes increasingly imperative. CoMo-based catalysts offer promise in this context, and this chapter aims to unravel their performance, behavior, and underlying mechanisms in the quest for more effective and eco-friendly CO_2 conversion processes.

4.1 Catalyst synthesis

The RME system consists of three parts, surfactant phase, oil phase and water phase in a ratio of 2:8:7. The surfactant phase is a combination of Triton X-100 (Acros Organics), and Co-surfactant (propanol-2, Sigma-Aldrich). Cyclohexane is employed to be the oil phase and the water phase is the solution of demand salt or alkali. Under vigorous stirring, the surfactant and co-surfactant are mixed first and then the oil phase is introduced. After 15 minutes of mixing the surfactant and co-surfactant phase, the aqueous phase is added to the system dropwise. When the solution is completely introduced, the mixture is translucent which demands additional co-surfactant. Extra 2-propanol is added dropwise carefully till the system turns transparent again. RMEs are stirred for extra 30 minutes before mixing with other RMEs to enhance the stability of the system.

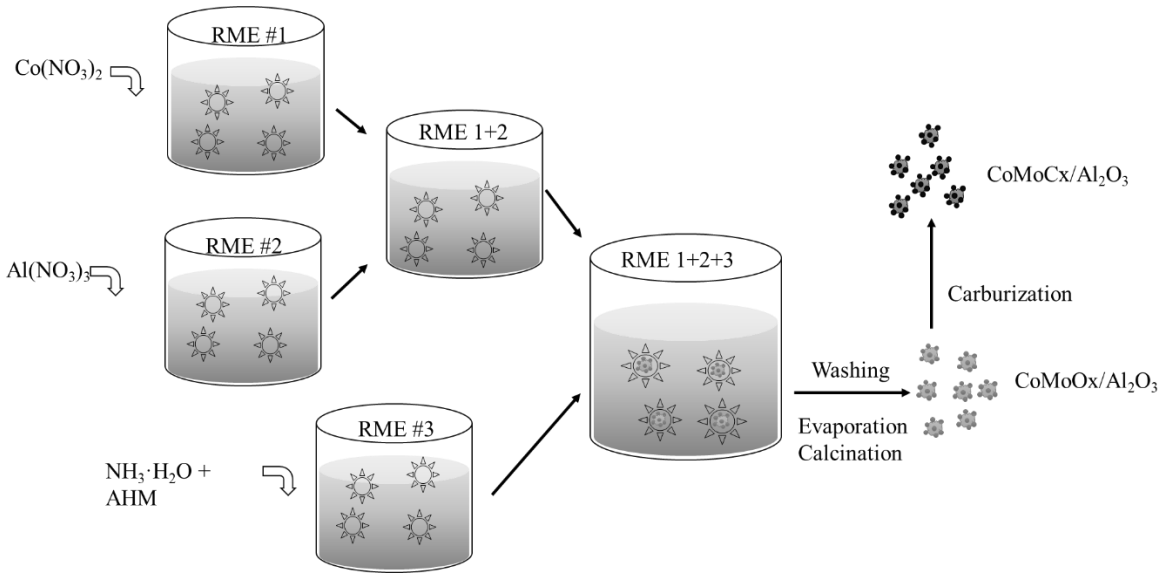

Figure 4-1 Process schematic for synthesizing $CoMoO_x/Al_2O_3$ and $CoMoC_x/Al_2O_3$ catalysts by RME method.

To synthesize a uniform RME system containing both cobalt and molybdenum, several trials of RME composition and mixing order have been made. RME method allows a uniform system that is beneficial to the formation of nanometric and well dispersed bimetallic particles. Since AHM (Ammonium heptamolybdate tetrahydrate) solution can be unstable and tend to precipitate when mixing with cobalt nitrate solution, AHM was dissolved into the excess ammonia, which serves as the precipitator for aluminum and Co. The excess ammonia dilutes the AHM and with the insulation of the RME micelles, AHM RME remains translucent instead of forming chunky precipitates when mixing with cobalt RME.

Table 4-1 RME composition of CoMo catalysts.

RME	**#1. $Co(NO_3)_2$**	**#2. $Al(NO_3)_3$**	**#3. NH_4OH + AHM**	**Volume ratio**
Aqueous phase	0.0826 g cobalt nitrate hexahydrate + 2.25 mL DI	1.499 g aluminium nitrate nonahydrate + 6.65 mL DI	160 mL 1M ammonia + 0.05g AHM	15

Surfactant	1.5 mL Triton X-100	4.45 mL Triton X-100	17.78 mL Triton X-100	10
Co-surfactant	6 mL Propanol-2	17.72 mL Propanol-2	71.1 mL Propanol-2	40
Oil phase	5.5 mL cyclohexane	15.6 mL cyclohexane	62.2 mL cyclohexane	35

The detailed compositions of each RME and the preparation procedure are showed in Table 4-1 and Figure 4-1 separately. Separate RMEs are prepared for mixing and RME #1 and RME #2 were mixed slowly. At this time, no reaction occurs in the RME and a transparent RME mixture is obtained as shown in Figure 4-2. Then the mixture was added into RME #3 dropwise under magnetic stirring to make sure the aluminum and cobalt are dispersed evenly onto the alumina support. The system is translucent (Figure 4-3), but no recognizable particles were observed which means the size of the resulted precipitate is minuscule. The mixture of all RMEs is stirred for 8 hours to allow a complete reaction.

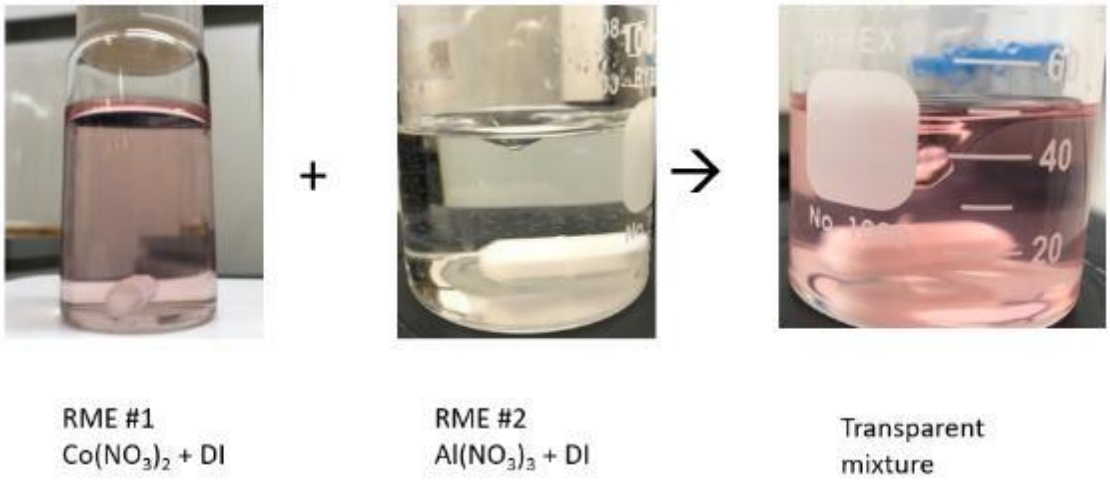

Figure 4-2 RME appearance of RME #1, RME #2 and the mixture

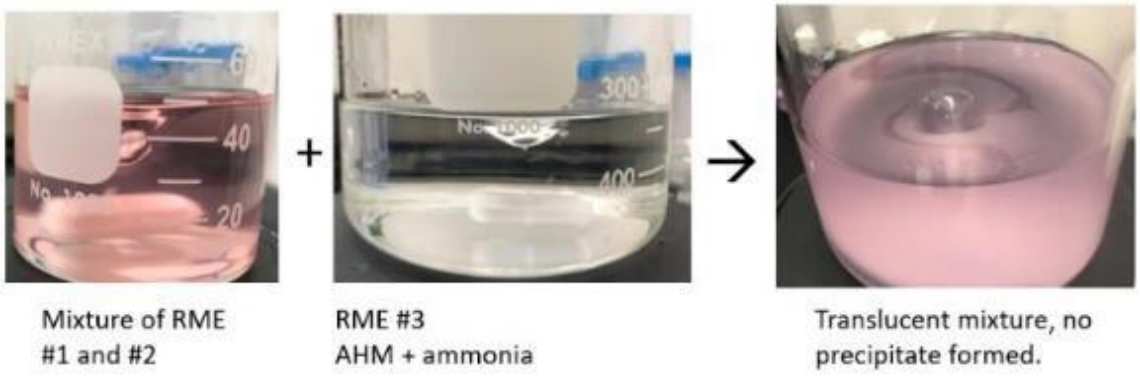

Figure 4-3 RME appearance of RME #3 and the mixture of three RMEs.

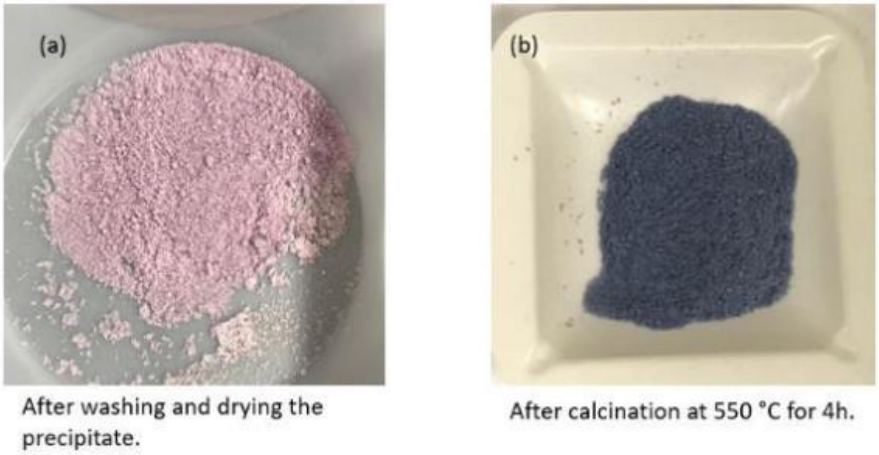

Figure 4-4 CoMo hydroxide precursor (a) and oxide catalysts (b).

After the RMEs are well mixed and precipitated completely, the system is aged overnight to delaminate. The cloudy precipitate is settled at the bottom and the supernatant fluid is removed by centrifugation. The catalyst gel is washed by DI water and ethanol (water : ethanol =1:3) four times to fully removed the surfactant and oil phase. The precipitate is dried at 100 °C overnight and ground to powder and this is the precursor of the CoMo bimetallic oxide. Oxide catalysts are obtained after 4 hours of calcination at 550 °C to remove the water and remaining organic components. The colour of the pink powder transformed to pale blue which indicated the phase change as shown in Figure 4-4. Besides the alumina support, the oxide catalyst contains a mixture

of mono-oxide (cobalt oxide and molybdenum oxide) and bi-metallic oxide which can be identified in the XRD pattern.

To obtain the carbide catalysts, a temperature-programmed carburization process was conducted. The oxide catalysts are placed in a quartz tube under the mixture of CH_4 and H_2 (CH_4: H_2 = 1:4) and the tube is heated with a 1 °C/min ramping rate till 250 °C and hold for 1 hour to remove moisture and the physically adsorbed species inside the sample, and then continue heated to 800 °C. The catalysts are held at 800 °C for 2 hours followed by 1 hour reduction with pure H_2 at the same temperature. The acquired catalysts are pure black. The outlet stream from the system is analyzed by in-line FTIR (MultiGas™ 2030, MKS Instruments). As indicated in Figure 4-5, most of the moisture was removed at 250 ° C and the products detected were CO_2 and CO generated from 500 °C.

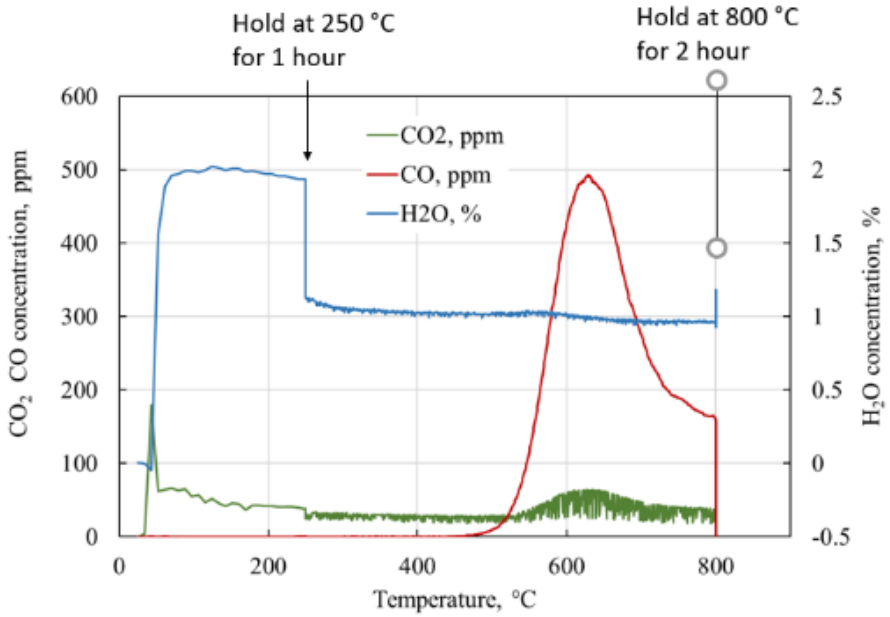

Figure 4-5 Products profile of carburization process.

4.2 Catalyst characterization

4.2.1 Crystallinity

To understand the samples, several characterization techniques were applied. The composition of the catalysts was determined by ICP-OES. Specific surface areas are obtained by one-point BET. XRD patterns were recorded to identify the existing phase. TPR was conducted to study the reducibility. The morphology of the samples was investigated by SEM and TEM microscopy. Specific surface area values are listed in Table 4-2. The calcined oxide catalyst showed extremely high surface area which indicates the success of RME method, however, the specific surface area of the catalyst after the carburization process dropped over 50% which probably due to the sintering effect occurred during the extremely high temperature treatment. This pointed out a potential orientation of future work to optimize the carburization conditions.

The XRD patterns are shown in Figure 4-6. Peaks were unable to identify in CoMoOx sample and the possible reason is that the particles synthesized from RME method were too small also amorphous. After carburization, the alumina, as well as other Co and Mo related phases, can be recognized. A bimetallic carbide Co_3Mo_3C was detected in the fresh carbide samples and a bimetallic oxide $CoMoO_4$ was also identified. The bimetallic oxide is considered as the precursor of the carbide species and remained as a leftover of incomplete carburization.

Table 4-2 Characterization results of CoMo catalysts.

	specific surface area (m^2/g)	Co loading (wt%)	Mo loading (wt%)
Fresh CoMoOx	410.5	12.5	8.4
Fresh CoMoCx	173.2	15.4	9.6

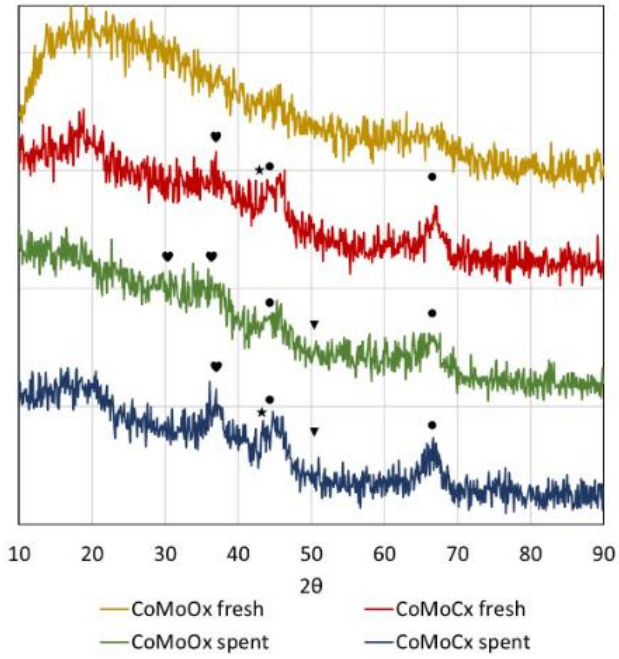

Figure 4-6 XRD patterns of fresh and spent Co/Mo catalysts. (•: γ-Al_2O_3; ▼: Cobalt metal; ♥: $CoMoO_4$; ★:Co_3Mo_3C.)

4.2.2 Reducibility

The reducibility of the two fresh catalysts was studied by temperature-programmed reduction. With the increase of the temperature, the catalysts were reduced by hydrogen and the consumption of the hydrogen was detected by TCD and recorded. Figure 4-7 shows the TPR profiles of the two fresh CoMo catalysts. In general, oxide catalysts can be reduced at higher temperatures than carbides. The peak around 400 °C is related to the reduction of $CoMoO_4$ to another oxide, $CoMoO_3$. Deep reduction to metal alloy happened after 550 °C and mostly around 700 °C, indicating the difficulty of reduction to metal for CoMo oxide.

The CoMo carbide tended to be reduced at a relatively low temperature before 700 °C. The sharp peak showed at 310 °C represented the reduction of oxycarbide species weakly bonded to the alumina support while the peak above 600 °C was a deep reduction of carbide species to metal. It is worth noting that a mild peak appeared at around 400 °C in carbide sample which has the identical position as in the oxide catalyst, corresponding to the reduction of $CoMoO_4$ to $CoMoO_3$, possibly indicating there was still bimetallic oxide in the carbide sample.

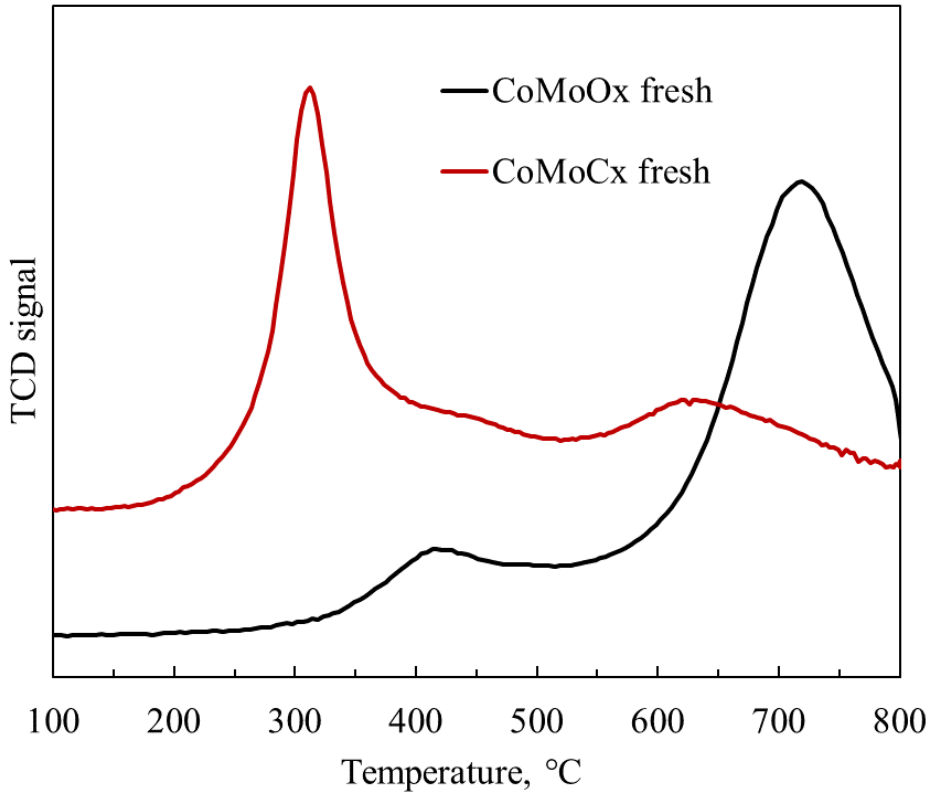

Figure 4-7 TPR patterns of fresh $CoMoO_x$ and $CoMoC_x$.

4.3 Catalytic performance evaluation

The catalytic performance was tested in terms of temperature and time dependence. The CO_2 conversion and selectivity towards CO as a function of temperature are shown in Figure 4-8. The temperature tests were conducted from 300 °C to 600 °C with an interval of 50 °C at 3 bar with

GHSV = 60,000 mL $h^{-1}g_{cat}^{-1}$ (HG4) and GHSV = 10,000 mL $h^{-1}g_{cat}^{-1}$ (LG4). The volumetric ratio of H_2:CH_4 was kept at 4 for all experiments. The catalysts were reduced at 350 °C under 300 ccm H_2 for 2 hours before the introduction of reaction gases. The equilibrium conversion curve (Eq4 in Figure 4-8) of RWGS was added for comparison as well.

CoMo carbide catalyst showed higher conversion than oxide sample at all temperatures but exhibited lower CO selectivity after 450 °C. When the temperature reached 600 °C which is the favoured condition by RWGS, the selectivity increased to 0.9 and 1 at high GHSV and low GHSV, respectively. The oxide sample did not offer distinguishable performance at high GHSV but when the GHSV was 10,000 mL $h^{-1}g_{cat}^{-1}$, the difference of CO_2 conversion between oxide and carbide was degraded. Regarding the selectivity, $CoMoO_x$ showed advantages over $CoMoC_x$ and maintained 1 at all temperatures at high GHSV.

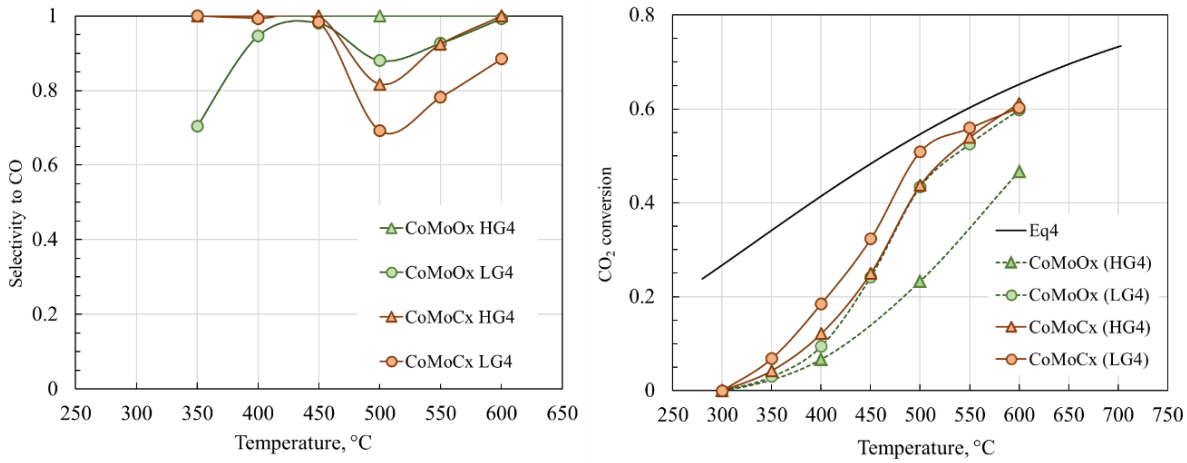

Figure 4-8 CO_2 conversion and CO selectivity of CoMo catalysts as a function of temperature. Reaction condition: P = 3 bar, H_2/CO_2 = 4, GHSV = 60,000 mL h-1gcat-1 (HG4) and GHSV = 10,000 mL h-1gcat-1 (LG4).

Compare to the equilibrium conversion curve, $CoMoC_x$ tested at lower GHSV is the closest one, especially neighbouring 500 °C whereas over 30% of the CO_2 conversion was contributed

from CO_2 methanation instead of CO production. However, if the GHSV is increased to 60,000 mL $h^{-1}g_{cat}^{-1}$ ($CoMoC_x$ HG4), the conversion at 600 °C remained comparable level but the selectivity towards CO surprisingly increased back to 1 which is desired. Overall, $CoMoC_x$ carbide exhibited superior performance than $CoMoO_x$ at a higher temperature and higher GHSV.

4.4 Discussion and concluding remarks

In conclusion, this chapter presents a comprehensive investigation into CoMo-based bimetallic catalysts for CO_2 thermo-catalytic conversion, with a particular focus on their potential for the Reverse Water Gas Shift (RWGS) reaction. The exploration of these catalysts encompasses crucial aspects such as gas hour space velocity (GHSV) impact, stability assessment, and extensive characterization experiments. The catalyst synthesis process involving the RME method is detailed, emphasizing the need for a uniform system to facilitate the formation of well-dispersed bimetallic particles. The subsequent steps, including aging, washing, and calcination, are outlined to obtain both oxide and carbide catalysts. Characterization techniques encompassing ICP-OES, BET surface area analysis, XRD patterns, and TPR profiles are employed to assess catalyst composition, surface area, crystallinity, and reducibility. The catalytic performance evaluation reveals that CoMo carbide catalysts exhibit higher CO_2 conversion rates compared to oxide samples across a range of temperatures. However, CO selectivity decreases in carbides after 450°C, rebounding to desirable levels at 600 °C, particularly at high GHSV. CoMo oxide samples, on the other hand, exhibit better selectivity under certain conditions. In summary, the study underscores the potential of CoMo-based bimetallic catalysts, especially carbides in CO_2 conversion applications, while highlighting the influence of temperature, GHSV, and selectivity. Further research is expected to improve the carburization conditions and deepen the understanding of the catalytic mechanism, which can pave the way for more efficient and sustainable CO_2 conversion processes.

Chapter 5 Al_2O_3-supported iron catalysts for CO_2 hydrogenation to light hydrocarbons

This chapter presents an investigation into CO_2 direct hydrogenation to light hydrocarbons using Fe-based catalysts, aiming to compare the impact of reverse microemulsion method (RME) and reaction conditions. Three catalyst was synthesised for comparison: RME Fe/Al_2O_3, precipitation on RME-synthesized Al_2O_3 ($Fe/RME\text{-}Al_2O_3$), and precipitation Fe/Al_2O_3. Characterization of the catalysts reveals that RME Fe/Al_2O_3 boasts smaller Fe_3O_4 particle sizes, facilitate the generation of χ-Fe_5C_2 phase under reaction condition and superior Fe dispersion on the alumina support. Notably, RME Fe/Al_2O_3 demonstrates outstanding CO_2 conversion and selectivity for C2+ hydrocarbons, with the highest conversion rate observed at 375°C and a maximum conversion of 56%. Investigation of the impact of H_2/CO_2 ration was also conducted. Lowering the H_2/CO_2 ratio results in reduced conversion rates and a 10% decrease in selectivity toward C2+ products while maintaining a comparable space-time yield. Examining spent catalysts confirms the transformation of magnetite to carbides during the reaction, contributing to sustained catalytic activity. The smaller particle size from the RME procedure enhances catalyst activity and stability which highlights RME Fe/Al_2O_3 as a promising candidate for industrial CO_2 hydrogenation applications, particularly for the production of light hydrocarbons.

5.1 Catalyst synthesis

To synthesize γ-Al_2O_3-supported Fe catalyst via the reverse microemulsion (RME) method, three RMEs containing appropriate amounts of ferric nitrate ($Fe(NO_3)_2{\cdot}9H_2O$, Sigma-Aldrich) and aluminum nitrate ($Al(NO_3)_3{\cdot}9H_2O$, Fisher Scientific), and ammonium hydroxide solution (1M NH_4OH, LabChem Inc.) were prepared (target loading was 40wt% Fe in $Fe/\gamma\text{-}Al_2O_3$). RMEs were

obtained by mixing aqueous phase (DI water), surfactant (Triton X-100, Acros Organics), co-surfactant (propanol-2, Sigma-Aldrich), and oil phase (cyclohexane, Sigma-Aldrich) using the 1:1:4.5:3.5volumetric ratio. The prepared RMEs were mixed in the order shown in Supplementary Information (Fig. S1). Briefly, aluminum nitrate RME was first mixed with NH_4OH RME (acting as a precipitation agent), and then ferric nitrate RME was added dropwise immediately to prevent precipitation of large particles resulted from the separation of phases. The resulted mixture was mixed using a magnetic stirrer for 8 h and then aged overnight (12 h) for stratification (settle the precipitation for easy separation).

The resulted gel-like precipitate was separated by centrifugation with subsequent washing by a mixture of ethanol and deionized water (3:1). This centrifugation/washing procedure was repeated 4 times. The washed precipitate was collected and dried overnight at 100 °C. K was subsequently added by wet impregnation using a diluted K_2CO_3 solution (0.13 mol/L) as an impregnation medium (the target value was 5 wt% K in K-Fe/γ-Al_2O_3). After that the precipitate was calcined at 400 °C for 3 h under flow of air. To prepare for reaction, the powder catalysts was pelletized and sieved to 250-425 µm pellets. The catalyst synthesized using the method described above was denoted as RME Fe/Al_2O_3. Two reference catalysts were prepared for comparison. The Fe/RME-Al_2O_3 catalyst was synthesized by loading Fe via wet (aqueous) impregnation (using $Fe(NO_3)_2{\cdot}9H_2O$) onto the RME γ-Al_2O_3 support. The RME γ-Al_2O_3 support was prepared by the same RME method as described above, but without Fe and K introduction. The Fe/Al_2O_3 catalyst was synthesized via wet (aqueous) impregnation using $Fe(NO_3)_2{\cdot}9H_2O$ as Fe precursor and a commercial support γ-Al_2O_3 (Alfa Aesar, 250 m^2/g). Prior to reaction tests, all powder catalysts were pelletized and sieved to 250-425 µm pellets.

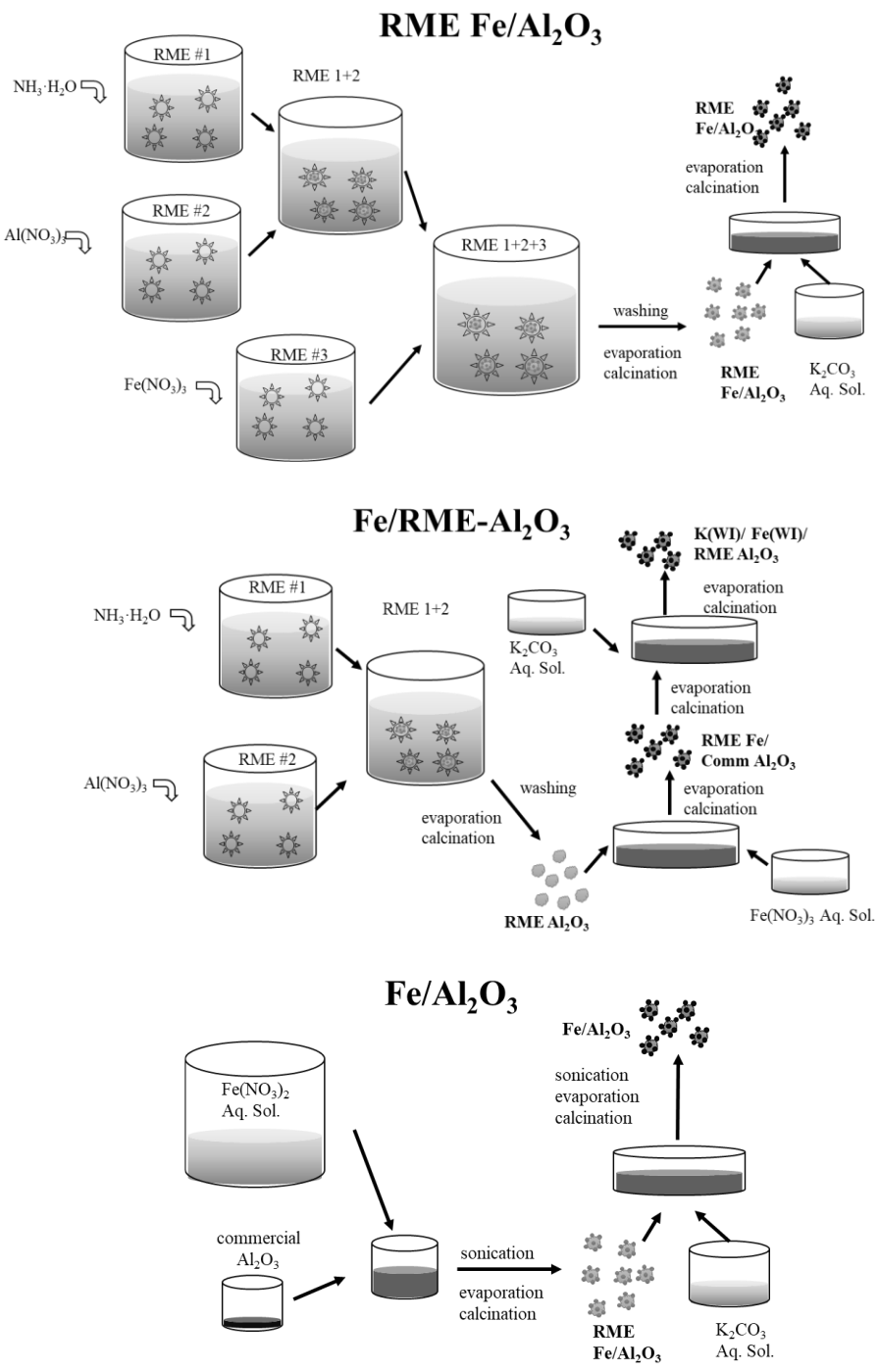

Figure 5-1 Schematic representation of the reverse microemulsion (RME) synthesis (RME Fe/Al_2O_3), combined RME-precipitation method ($Fe/RME\text{-}Al_2O_3$), and direct precipitation synthesis (Fe/Al_2O_3).

5.2 Catalyst characterization

5.2.1 Crystallinity

To investigate elemental composition, crystallinity and morphology, fresh (calcined) and spent (post-reaction) catalysts were characterized via ICP-OES, gas adsorption, XRD, and HRTEM. Elemental composition analysis showed Fe loadings in the 38.3-40.9 wt% range (Table 5-1), with the average value of 39.5 ± 1.31 wt%, i.e., 3.32% standard deviation. The target loading was 40wt% Fe/Al_2O_3 and the average standard deviation between 3 analyzed samples (for each catalyst) was 0.93 wt%. Potassium (K) loading was 4.5wt% and 4.9wt% for Fe/RME-Al_2O_3 and Fe/Al_2O_3, respectively, with the RME Fe/Al_2O_3 sample value deviating by ca. 2wt% (Table 5-1). The target value was 5wt%, and the higher value obtained for the RME method can be attributed to the relatively lower K washout during the centrifugation/washing procedure. It has been reported in the literature that the Fischer-Tropsch catalytic activity of iron catalysts is not enhanced above K/Fe atomic ratio of 0.05 (in the current study K/Fe atomic ration was 0.16-0.25 for 4.5-6.6wt% K loading). [199]

Table 5-1. Specific surface area (SSA), ICP-measured loading (L), and crystallite size calculated from XRD patterns (DXRD) for fresh (calcined) and spent (post-reaction) catalysts. For spent samples, the following reaction conditions were used: T = 300-375 °C, H_2/CO_2 = 3-4, GHSV = 3,000 mL/(g h), P = 10 bar (absolute); the total time-on-stream was 70 h

	SSA, m^2/g		L, wt%		D_{XRD}, nm				
	fresh	spent	Fe	K	fresh		spent		
					Al_2O_3	Fe_2O_3	Al_2O_3	Fe_3O_4	Fe_5C_2
RME Fe/Al_2O_3	219	110	38.3	6.6	3.3	---	---	6.0±1.0	12.7±2.3
Fe/RME-Al_2O_3	199	131	39.3	4.5	3.9	-	---	6.5±1.3	13.0

Fe/Al_2O_3	160	166	40.9	4.8	8.0±1.8	6.1±0.7	6.6	9.6±2.1	---
RME Al_2O_3	299	---	---		3.4	---	---	---	---

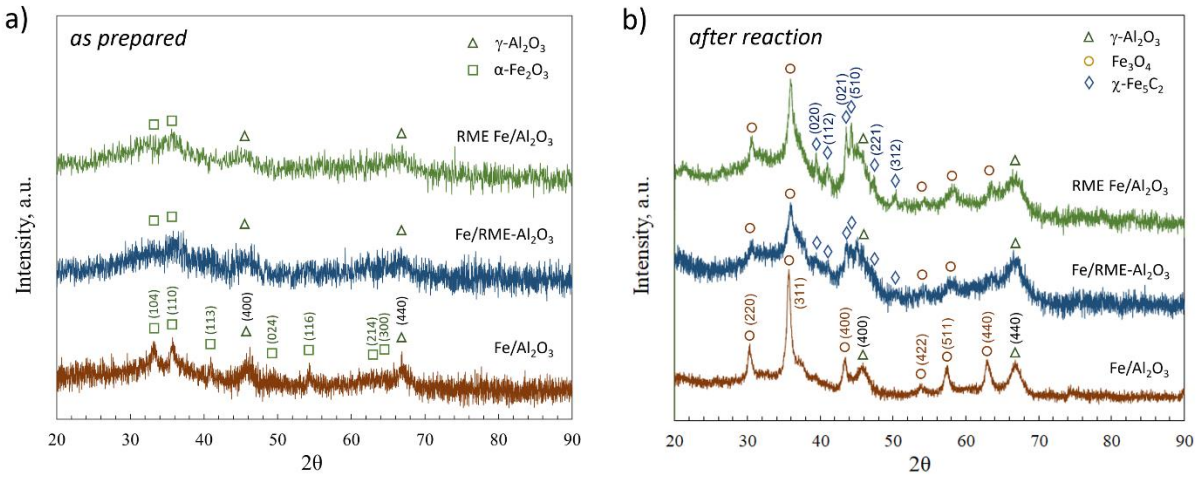

Figure 5-2 XRD patterns of fresh (a) and spent (b) catalysts synthesised by RME method (RME Fe/Al_2O_3), precipitation on RME Al_2O_3 (Fe/RME-Al_2O_3), and precipitation (Fe/Al_2O_3). For spent samples, the following reaction conditions were used: T = 300-375 °C, H_2/CO_2 = 3-4, GHSV = 3,000 mL/(g h), P = 10 bar, time-on-stream = 70 h.

SSA values of as prepared catalysts (after calcination) are listed in Table 2. RME Fe/Al_2O_3 has the highest SSA value (219 m^2/g) that emphasizes the advantage of the RME method in synthesis of high surface area materials. Fe/RME-Al_2O_3 (for which γ-Al_2O_3 support was synthesized via the RME method) also showed higher SSA compared to Fe/Al_2O_3 prepared by wet impregnation on commercial γ-Al_2O_3 (199 m^2/g vs. 160 m^2/g). The obtained values are consistent with the high SSA of the RME-synthesized γ-Al_2O_3 (299 m^2/g, Table 2), which is substantially higher than that for commercial γ-Al_2O_3 (250 m^2/g, see Section 2.1) indicating that the alumina support is also sensitive to the preparation method and will impact the SSA of the catalysts after

Fe_2O_3 was deposited. For spent catalysts after 70 h on stream, there was a significant reduction of SSA for RME-based catalysts, probably attributed to sintering of the high surface area RME-synthesized γ-Al_2O_3. Interestingly, there was no SSA reduction for Fe/Al_2O_3, which is apparently related to high durability of the previously stabilized commercial γ-Al_2O_3. [199]

Fresh (calcined) and spent (post-reaction) catalysts were characterized via XRD to study the phase change behaviour and crystallite size evolution under reaction conditions. K-based phase was not detectable, as expected due to the low K loading. In the fresh Fe/Al_2O_3 sample (Figure 5-2a), diffraction peaks observed at 33.3°, 35.5°, 41.2°, and 54.1° characterise the α-Fe_2O_3 phase (PDF: 33-0664), while the two peaks detected at 45.8° and 66.8° are characteristic of γ-Al_2O_3 (PDF: 29-1486). In fresh RME Fe/Al_2O_3 and Fe/RME-Al_2O_3 (Figure 5-2a), broad peaks were scarcely detectable for α-Fe_2O_3 (33.3° and 35.5°) and γ-Al_2O_3 (45.8° and 66.8°) phases corresponding to the highest intensity peaks . Scherrer equation was used for crystallite size calculation (reported in Table 5-1). Peaks at 45.8° and 66.8° were used for the γ-Al_2O_3 phase and peaks located at 33.3° and 35.5° were used for the α-Fe_2O_3 phase in the Fe/Al_2O_3 sample. For RME Fe/Al_2O_3 and Fe/RME-Al_2O_3 samples, only a peak at 66.8° was relatively clear. The larger crystallite size for γ-Al_2O_3 in the Fe/Al_2O_3 sample is consistent with a smaller SSA value. The α-Fe_2O_3 crystallite size was below 10 nm indicating a relatively good dispersion.

In spent catalysts (Figure 5-2), Fe_2O_3 was transformed to Fe_3O_4 (as expected for highly reducing environment), with the characteristic peaks located at 30.1°, 35.4°, 43.1°, 53.4°, 56.9° and 62.5° (PDF: 19-0629) observed for Fe/Al_2O_3. The γ-Al_2O_3 phase was also clearly detectable for Fe/Al_2O_3 (at 45.8° and 66.8°), and no other phase was detected. For RME Fe/Al_2O_3 and Fe/RME-Al_2O_3, χ-Fe_5C_2 was detected (at 39.4°, 40.9°, 43.5°, 44.2°, 47.3°, and 50.2°; PDF: 36-

1248) in addition to Fe_3O_4 and γ-Al_2O_3. The χ-Fe_5C_2 phase was more defined in the RME Fe/Al_2O_3 sample, while for Fe/RME-Al_2O_3 this phase was scarcely detectable. The absence of the χ-Fe_5C_2 phase in Fe/Al_2O_3 indicates that the RME synthesis promotes the formation of the carbide phase. χ-Fe_5C_2 is widely reported as an active phase in the iron-based FT synthesis, with both Fe_2O_3 and Fe_3O_4 being precursors of χ-Fe_5C_2. [200] The structure evolution of the Fe catalyst starts from the activation of Fe_2O_3 to χ-Fe_5C_2 by CO, oxidation to Fe_3O_4 by CO_2, and regeneration back to χ-Fe_5C_2 by CO. [201] Interestingly, the χ-Fe_5C_2 phase was not detected in the spent Fe/Al_2O_3 catalyst that has a significantly larger Fe_3O_4 crystallite size as compared to the RME-based catalysts (Table 5-1). This observation may indicate that the smaller crystallite size resulted from the RME synthesis facilitated the transformation of magnetite to carbide.

For spent catalysts, the γ-Al_2O_3 crystallite size was only calculated for Fe/Al_2O_3 using a non-overlapping peak located at 66.8°. Note that the γ-Al_2O_3 crystallite size in the spent Fe/Al_2O_3 catalyst is slightly lower than that for fresh Fe/Al_2O_3 (Table 5-1), which is consistent with a slightly higher SSA value for the spent catalyst. The Fe_3O_4 crystallite size was calculated using peaks located at 30.1°, 33.3°, 53.4°, 56.9° and 62.5°, while for the χ-Fe_5C_2 phase the crystallite size was calculated using peaks located at 39.4°, 40.9° and 50.2° for RME Fe/Al_2O_3 and 50.2° for Fe/RME-Al_2O_3, as other peaks were either overlapping or not clear. The χ-Fe_5C_2 crystallite size is relatively large, although it should be emphasized that the related peaks were not clear that can cause significant errors in crystallite size evaluation. Still, qualitatively speaking the χ-Fe_5C_2 peaks are rather sharp (Figure 5-2b), which is indicative of a relatively large crystallite size. It is important to emphasize that, although the SSA for spent RME Fe/Al_2O_3 was relatively small, the calculated Fe_3O_4 particle size still showed the smallest value (6.0 nm, Table 5-1), suggesting that the

reduction in SSA in RME Fe/Al_2O_3 is mainly due to the RME-synthesized γ-Al_2O_3 particle growth and agglomeration under reaction condition.

5.2.2 Reducibility

H_2-TPR results of fresh (calcined) and spent (post-reaction) catalysts are summarized in Figure 5-3. The low temperature peak centered at ca. 350 °C, which was detected for fresh Fe/Al_2O_3 and RME Fe/Al_2O_3 catalysts, corresponds to Fe_2O_3 being reduced to Fe_3O_4. The higher temperature of the $Fe_2O_3 \rightarrow Fe_3O_4$ reduction for Fe/RME-Al_2O_3 (ca. 450 °C) can be attributed to the larger Fe_2O_3 nanoparticle size resulted from the wet impregnation method. The high temperature peak centered at ca. 700 °C, which was observed for all catalysts, indicates the direct reduction of Fe_3O_4 to Fe^0. [202, 203] The intermediate peak that appeared in Fe/Al_2O_3 at 510 °C can be referred to the formation of FeO (Wüstite) that retards the direct reduction of Fe_3O_4 to Fe^0. [202-204] It was reported that Fe_2O_3 reduction to Fe^0 typically follows a three-step route, i.e., $Fe_2O_3 \rightarrow Fe_3O_4 \rightarrow FeO \rightarrow Fe^0$, [202, 204, 205] as it was observed for Fe/Al_2O_3. However, RME Fe/Al_2O_3 and Fe/RME-Al_2O_3 undergo two-step reduction ($Fe_2O_3 \rightarrow Fe_3O_4 \rightarrow Fe^0$), which is evident from the absence of the intermediate-temperature reduction peak. The absence of the $Fe_3O_4 \rightarrow FeO$ step in the RME-based catalysts can be explained by the enhanced dispersion of Fe species on the RME-synthesized γ-Al_2O_3 support resulting in the stronger active phase-support (Fe_3O_4-γ-Al_2O_3) interaction.

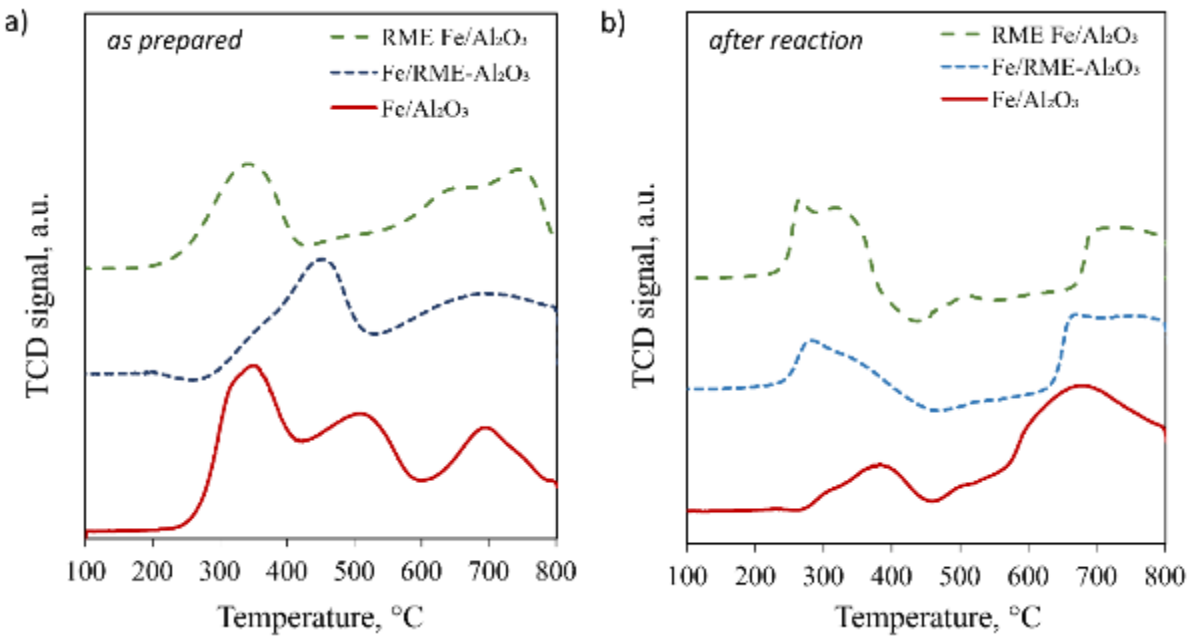

Figure 5-3 H_2-TPR profiles of as prepared, calcined (a) and spent, after 70 h on stream (b) catalysts, comparing the catalysts prepared by the RME method (RME Fe/Al_2O_3), precipitation on RME-synthesized γ-Al_2O_3 (Fe/RME-Al_2O_3), and precipitation on commercial γ-Al_2O_3 (Fe/Al_2O_3).

For spent catalysts, qualitatively similar TPR profiles were obtained, with the two reduction peaks observed, although located at somewhat different temperature range. The first peak located in the 240-450 °C range is related to post-reaction residuals on the catalyst surface (adsorbed CO, CO_2, hydrocarbons, as well as amorphous and polymeric carbon), as it was supported by the TPR off-gas analysis (see Figure 5-15 and *Supplementary Information*). From the same off-gas analysis, it can be seen that the second peak that starts to appear at ca. 550-650 °C (depending on the sample) is first associated with CO, CH_4 and H_2O signals, and then predominantly with the H_2O signal. On the other hand, this peak appears in the similar temperature range as the $Fe_3O_4 \rightarrow Fe^0$ reduction peak in fresh catalysts (Figure 5-2). Therefore, it can be a combination of graphitic carbon hydrogenation (resulting in CH_4 formation) and Fe_3O_4 reduction (leading to H_2O generation). It

has been reported that hydrogenation of χ-Fe_5C_2 occurs above 500 °C [201, 206] but the presence of the post-reaction residuals on the catalyst surface does not allow for deconvolution of this process from hydrogenation of carbonaceous species.

5.2.3 Morphology

Nanomorphology of fresh, calcined catalysts was characterized via STEM, including STEM-HAADF elemental mapping, Figure 5-4 to Figure 5-6. For Fe/Al_2O_3, fresh catalysts show agglomerated nanoparticles. Al_2O_3 nanoparticles with a diameter of 9-20 nm (Figure 5-4b**,c**) and d-spacing of 0.24, 0.193 and 0.14 nm were observable for (311), (400) and (440) facets respectively, while some of the Al_2O_3 phase was in the form of a large crystalline structure with unclear boundaries. Particle size distribution analysis (Figure 5-4a,d) of well defined particles indicated that in the fresh Fe/Al_2O_3 catalyst, the particles primarily comprise Al_2O_3 and Fe_2O_3 with a nanoparticle size of 9.1 ± 1.7 nm (Figure 5-4a). After 70 h on stream, ca. 3 nm growth in the average particle size was observed, resulting in the 10.3 ± 2.8 nm size (Figure 5-4d), with the spent catalyst showing identified phases of Al_2O_3 and Fe_3O_4.

In addition to the relatively uniformly distributed nanoparticles shown in Figure 5-4d, relatively large nanoparticles with a diameter ranging from 50-60 nm were also found in the spent Fe/Al_2O_3 catalyst (Figure 5-4e). This nanoparticles has a core-shell structure that is clearly observable in both STEM images and HAADF mapping (Figure 5-4e,f,g), where the Fe-rich core is surrounded by an amorphous shell enriched with O while K evenly distributed on the Fe containing particle and Al_2O_3 support. From combining the elemental mapping (Figure 5-4g), with d-spacing analysis (Figure 5-4e,f), the core can be ascribed to Fe_3O_4 (d-spacing of 0.25 and 0.49 nm). Interplanar distance analysis indicated that the existing phases are Fe_3O_4 (111) (d = 0.483 Å) and Fe_3O_4 (311) (d = 0.253 Å). This finding agrees with the XRD results (Figure 5-4b) that showed

Fe_3O_4 as the only iron-containing phase in spent Fe/Al_2O_3, while no iron carbide phase was detected.

Nanoparticles in the fresh $Fe/RME\text{-}Al_2O_3$ catalyst after calcination mainly had a particle size of 5.6 ± 1.9 nm (Figure 5-5a). Interestingly, Fe_3O_4 was found as spherical nanoparticles in the fresh catalyst (Figure 5-5b) by d-spacing analysis, which in XRD pattern, only Fe_2O_3 and Al_2O_3 were identified. The nanoparticle size grow to 8.5 ± 3.0 nm for spent $Fe/RME\text{-}Al_2O_3$ catalyst with a slightly decentralized particle size distribution (Figure 5-5c). Similar core-shell structure was also identified in the spent $Fe/RME\text{-}Al_2O_3$ catalyst as in the spent Fe/Al_2O_3 catalyst. However, large Fe-containing nanoparticles over 50 nm as shown in Figure 5-5e were not detected in spent $Fe/RME\text{-}Al_2O_3$, which might be attributed to the enhanced dispersion from the RME synthesized $\gamma\text{-}Al_2O_3$ support. The enhanced dispersion of Fe species on RME Al_2O_3 seems to play a pivotal role in preventing aggregation during the reaction and remain well distributed. This aspect showcases the efficacy of RME alumina in maintaining a favourable particle size distribution even under high temperature, there by contributing to the catalyst's stability and performance.

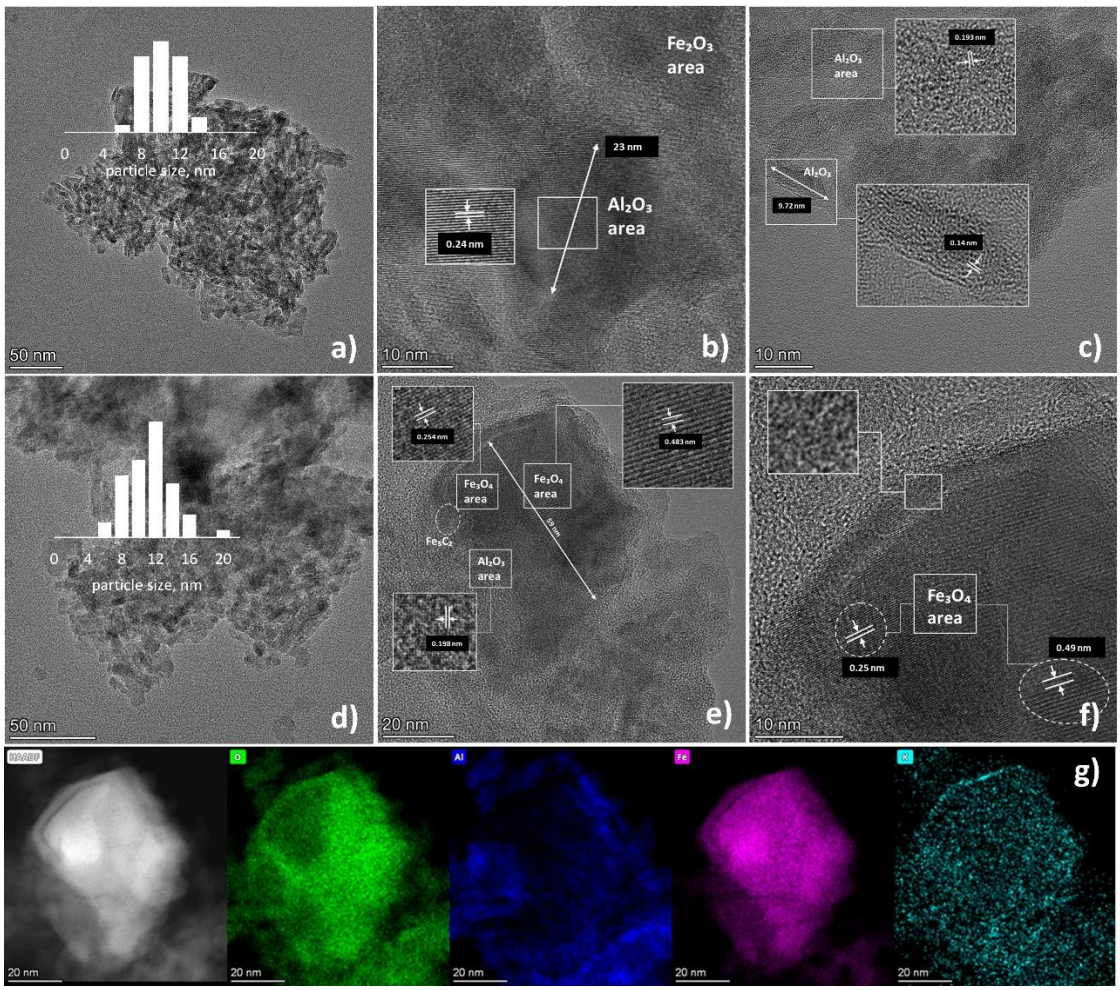

Figure 5-4 STEM images of fresh (a-c) and spent (d-f) Fe/Al_2O_3 catalysts, also showing particle size distribution (a, d) and HAADF (g) elemental mapping of a single particle in the spent Fe/Al_2O_3 catalyst (g).

Fe species in additional to Fe_3O_4, Hägg iron carbide was also identified by d-spacing analysis, with phases of, χ-Fe_5C_2 (510) (d=0.208 Å), χ-Fe_5C_2 (31-2) (d=0.198 Å). Inside the core-shell structure, the carbide phase was well defined and dispersed Fe_3O_4 and Fe_5C_2 particles were also observed in some area on the support without a clear shell. Small amount of Fe^0 particles were also identified on the support which might be the intermediate of the formation of the carbide phase.

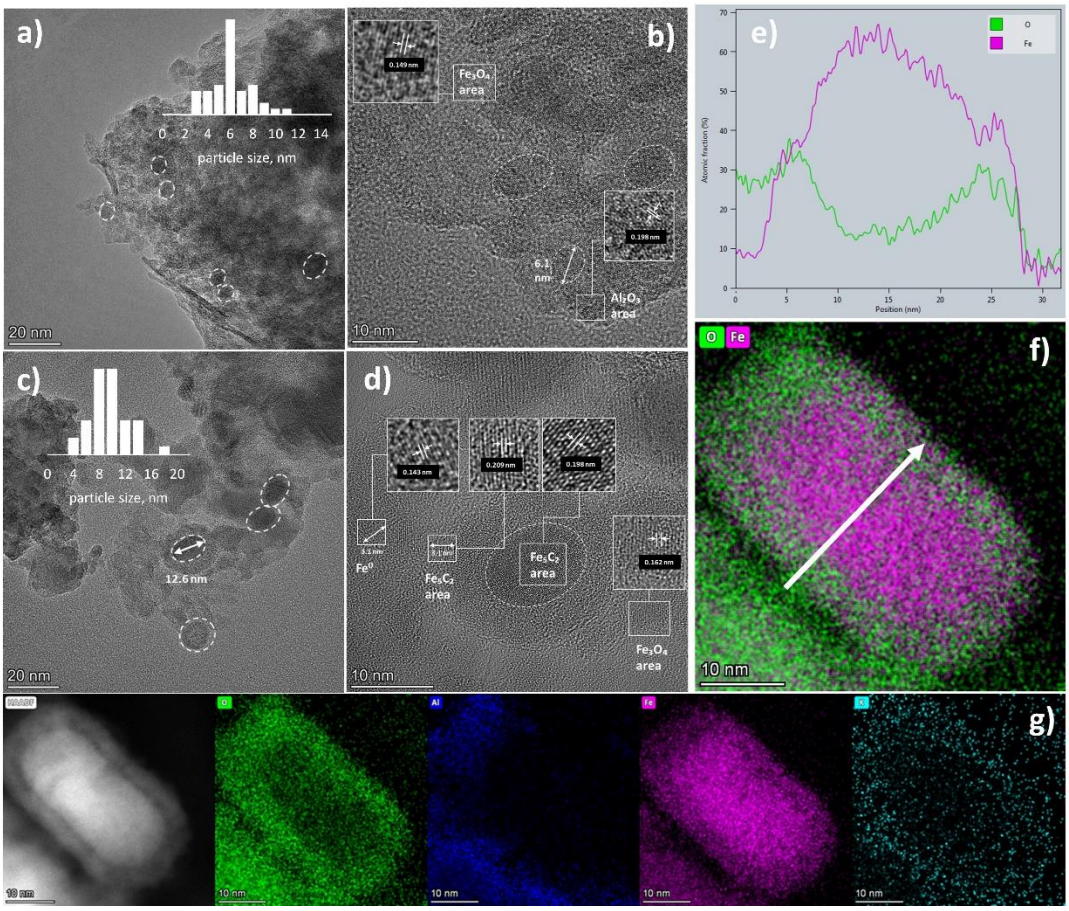

Figure 5-5 STEM images of fresh (a, b) and spent (c, d) Fe/RME-Al_2O_3 catalysts with particle size distribution (a, c), HAADF intensity profile of a typical core-shell nanoparticle in the spent catalyst (e) along the direction pointed in (f), and elemental mapping of this nanoparticle (g).

In the elemental analysis of a single particle (Figure 5-5e,f,g), it can be determined Fe and K are finely distributed and well dispersed on the core-shell structure particle after 70 h on stream. The carbide core was well defined while from the O distribution (Figure 5-5g), although the shell is amorphous, it could be deduced that the shell consists of oxygen-rich oxides. The HAADF intensity profile (Figure 6e) of the particle shown in Figure 5-5f along the direction pointed also indicates the oxygen intensity changes across the particle. The formation of this Fe carbide (code)-oxide (shell) structure may due to the CO dissociation on Fe (110) surface under the reaction

condition which C leads to the formation of carbide and O leads to the oxide shell. [207] d-spacing analysis to the core-shell structure, it was also revealed that χ-Fe_5C_2 and Fe_3O_4 phases can exist in the same core of a core-shell particle which further support the evolution scenario.

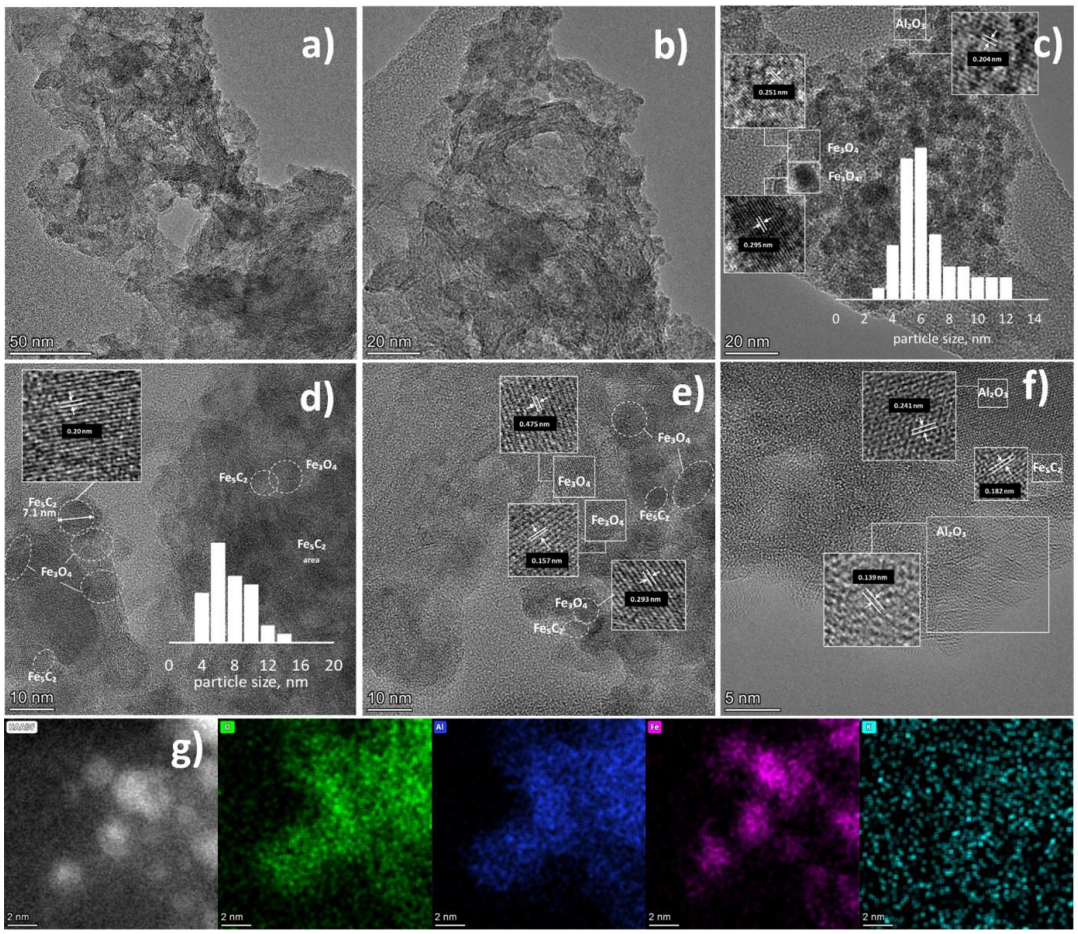

Figure 5-6 STEM images of fresh (a-c) and spent (d-f) RME Fe/Al_2O_3 catalysts with particle size distribution (c, d), and HAADF elemental mapping of the spent RME Fe/Al_2O_3 catalyst (g).

In fresh RME Fe/Al_2O_3, amorphous phase was widely observed (Figure 5-6a,b). In addition, uniform nanoparticles with a relatively narrow particle size distribution were detected (Figure 5-6c), with a nanoparticle size of 6.0 ± 2.1 nm. Nanoparticles under 10 nm are still dominant in the spent RME Fe/Al_2O_3 sample (Figure 5-6d), with the average nanoparticle size of 6.7 ± 3.2 nm.

Spherical χ-Fe_5C_2 and Fe_3O_4 nanoparticles without noticeable oxide shell can be identified in spent RME Fe/Al_2O_3 (Figure 5-6d,e). A slight increase in the average nanoparticle size from 6 to 7 nm was observed. Nanoparticles with d-spacing of 0.20 nm and 0.182 nm (facets (510) and (312), respectively) were assigned to χ-Fe_5C_2, Figure 5-6d,f. Fe_3O_4 was also identified in RME Fe/Al_2O_3, from the d-spacing of 0.475, 0.157 and 0.293 nm, corresponding to (111), (511) and (220) planes, respectively (JCPDS 19-0629). [208]

From the elemental analysis (Figure 5-6g), K was evenly distributed on the surface and that Fe-rich nanoparticles were well-dispersed on the Al_2O_3 support. It is clear that the Fe mapping overlaps with the HHADF images suggesting that the spherical nanoparticles are Fe-rich. Al analysis also indicates that the Fe-rich particles attach to the Al_2O_3 support and potentially interact with the support. From the intensity of the O mapping, O signal was not intensified at Fe-rich region which suggests that O mainly came from the Al_2O_3 support. The existence of iron carbide species was also proved by the TPR-FTIR experiment (Figure 5-15), in which CH_4 and light hydrocarbons desorbed from the catalyst surface when the sample was reduced at high temperature, indicating the possibility of the χ-$Fe_5C_2 + 2H_2 \rightarrow CH_4 + Fe_3C$ reaction. [206]

The STEM analysis unveiled distinct nanomorphology among Fe/Al_2O_3, Fe/RME-Al_2O_3 and RME Fe/Al_2O_3 catalysts. The nanoparticle size of Fe_2O_3 and Al_2O_3 in RME-synthesized fresh samples (RME Fe/Al_2O_3 and Fe/RME-Al_2O_3) was considerably smaller than that for Fe/Al_2O_3 (ca. 6 nm, Figure 5-5a,b and Figure 5-6c), indicating that the RME method enhances active phase dispersion. The fresh Fe/Al_2O_3 catalyst exhibited agglomerated nanoparticles, transitioning to a core-shell structure post-reaction, while the Fe/RME-Al_2O_3 catalyst avoided aggregation due to enhanced Fe dispersion on RME alumina. Conversely, RME Fe/Al_2O_3 displayed an amorphous phase initially, transitioning to χ-Fe_5C_2 and Fe_3O_4 nanoparticles post-reaction without core-shell

structure observed. These findings underscore the alumina support and RME method's impact on Fe species dispersion and stability.

5.2.4 Surface property

In order to analyze the CO_2 adsorption strength, CO_2-TPD was performed on both fresh and spent catalysts. CO_2 desorption peaks are shown in Figure 5-7. Fresh (calcined) catalysts showed a single peak centered at ca. 80 °C for all three methods, corresponding to weak CO_2 adsorption. [209] A relatively small shoulder that appeared at 185 °C for Fe/RME-Al_2O_3 and RME Fe/Al_2O_3 can be attributed to molecular CO_2 with moderate adsorption strength. [209, 210]

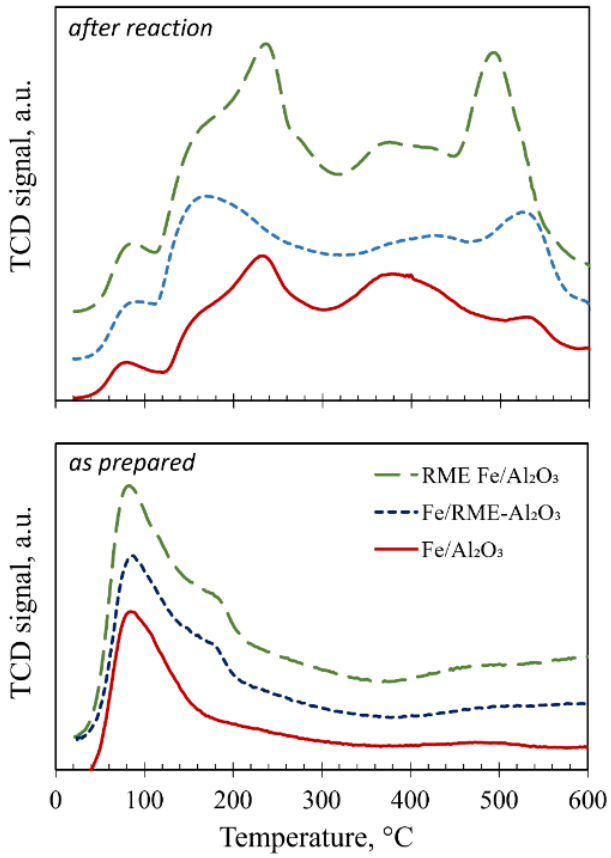

Figure 5-7 CO_2-TPD profiles of as prepared (after calcination) and spent, after reaction (70 h on stream) catalysts.

For spent catalysts after dehydration at 200 °C, TPD profiles were quite complicated. The same peak centered at ca. 90 °C for fresh catalysts, which is associated with weak CO_2 physisorption, was also for all spent catalysts. The second peak at 185 °C was also observed as a shoulder in RME Fe/Al_2O_3 and Fe/Al_2O_3, and as a distinct peak in $Fe/RME\text{-}Al_2O_3$. Notably, in spent catalysts the second peak (at 185 °C) was of significantly higher intensity compared to the first peak (at 80 °C), indicating that the fraction of active sites associated with the molecular CO_2 adsorption with moderate strength has increased significantly after the exposure to reaction conditions for 70 h.

In addition to these two desorption peaks that were also observed in fresh catalysts, three additional peaks were observed in spent catalysts at higher temperatures. The two peaks centered at 232 °C and 375 °C can be ascribed to moderate and strong adsorption of CO_2. [211, 212] The two moderate adsorption peaks cantered 185 and 232 °C may corresponding to the chemisorption of CO_2 at two different active sites and there is a great chance that the active site of the peak at 232 °C is formed in-situ during reaction due to its absence in fresh catalysts. The peak centered at 493 °C for RME Fe/Al_2O_3 and at 535 °C for $Fe/RME\text{-}Al_2O_3$ and Fe/Al_2O_3 may be attributed to the desorption of CO that is generated from the dissociation of surface species such as formates and carbonates adsorbed on the active sites under reaction conditions. [213] Fresh catalysts exhibits weak CO_2 adsorption, while spent catalysts after exposure to reaction condition showed more complex profiles with increased CO_2 adsorption peaks at higher temperatures, suggesting changes in active sites and potential chemisorption of CO_2.

5.3 Catalytic performance evaluation

5.3.1 Effects of operating conditions

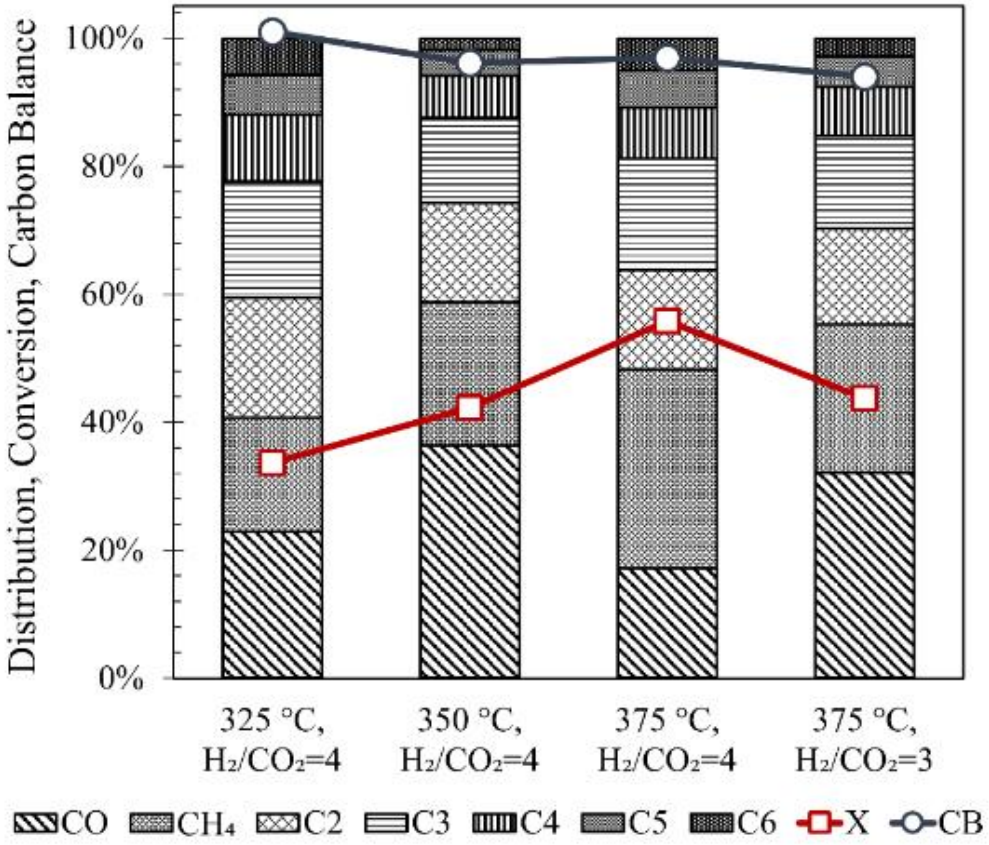

Figure 5-8 Catalytic performance evaluation of RME Fe/Al_2O_3 for T = 325-375 °C and H_2/CO_2 = 3 and 4, showing product distribution, CO_2 conversion (X, squares), and carbon balance (CB, circles). Operating conditions: GHSV = 3,000 mL/(g h), P =10 bar (absolute).

Before reaction tests, the catalysts were reduced at 400 °C, 1 bar, under 300 ccm H_2 for 3 hours to expose the active sites. Since RME Fe/Al_2O_3 is the most promising candidate, reaction tests were performed at various reaction conditions to investigate the effect of temperature and H_2/CO_2 ratio (Figure 5-8). conversion of CO_2 increased along with the temperature when H_2/CO_2 is 4 as expected and the highest selectivity (0.59) was achieved at the lowest temperature 325 ℃ but due to the supressed conversion, the space time yield (STY) was only 5.33 mmol/(g_{cat}·h), while

STY at 375 °C was 7.75 mmol/(g_{cat}·h). H_2/CO_2 was tuned down which aimed for higher selectivity towards C2+ hydrocarbons, the conversion was lower which follows the reaction kinetics, but surprisingly, the selectivity towards C2+ at higher CO_2 mole fraction was lower and.

5.3.2 Comparison between catalysts

The catalytic performance of the three as-prepared catalysts for CO_2 hydrogenation to hydrocarbon reaction were tested under 325-375 °C, pressure of 10 bar, H_2/CO_2=4 or 3, and 3,000 mL/(g h) condition. The conversion, STY and product distribution are summarized in Figure 5-9. RME Fe/Al_2O_3 displayed outstanding catalytic performance with the highest selectivity among these three catalysts at all reaction conditions tested, particularly achieved 0.52 selectivity towards C2+ hydrocarbons at 375 °C, H_2/CO_2=4. It is noteworthy that the superior of RME Fe/Al_2O_3 over the reference catalyst was enlarged at a higher temperature at 375 °C compared to 350 °C in terms of STY and selectivity to C2+ hydrocarbons. The 25 °C of increment in the temperature not only provided a growth of selectivity, 0.11 and 0.02 for RME Fe/Al_2O_3 and Fe/RME-Al_2O_3 respectively, but also pumped up the reaction rates for all catalysts. The conversion of CO_2 increased with the increasing temperature from 350 °C to 375 °C where the highest conversion yet highest growth was both observed on RME Fe/Al_2O_3, from 0.42 to 0.56. Fe/RME-Al_2O_3 showed comparable but slightly lower conversion to RME Fe/Al_2O_3 while the selectivity was unable to exceed the latter, resulting in a lower STY at 375 °C when H_2/CO_2=4. However, comparing to the reference sample Fe/Al_2O_3, RME Fe/Al_2O_3 still have the advantages both in conversion and selectivity. Considering the SSA results, it can be seen that the RME method can enhance the surface area for both Al_2O_3 support as well as the active Fe phase. Interestingly, a positive relationship (Figure 5-9d) was observed which the selectivity towards C2+ hydrocarbon increase with the conversion of CO_2. The

similar trend was observed by Barrios and Liu et al [23, 96] and this may suggest that CO is the primary product while the CH_4 and hydrocarbons are secondary products.

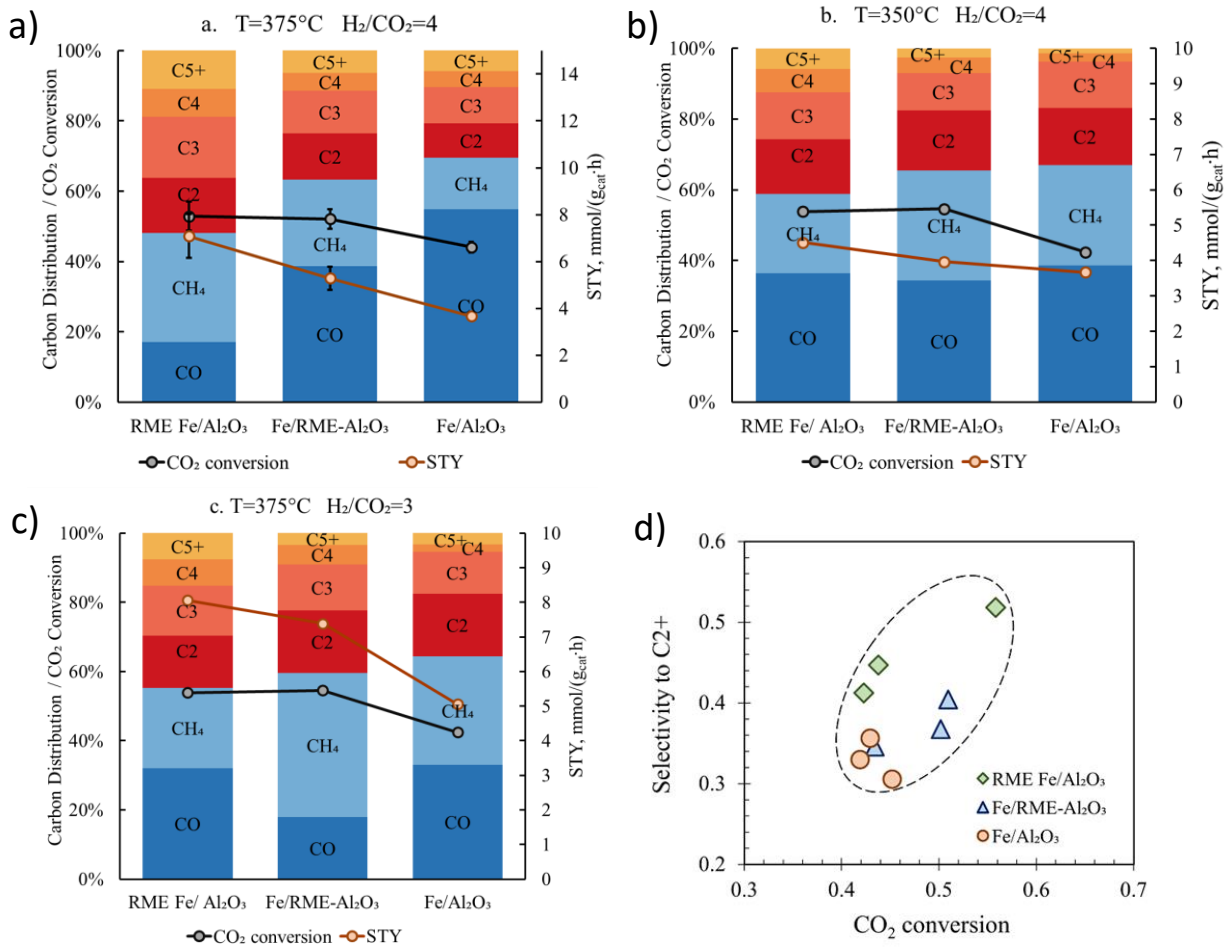

Figure 5-9 Catalytic performance comparison at different operating condition. Product distribution, CO_2 conversion, and space-time yield (STY) are shown for the three catalysts at a) T = 350 °C, H_2/CO_2 = 4, b) T = 375 °C, H_2/CO_2 = 4, and c) T = 375 °C, H_2/CO_2 = 3. Repetition was done to confirm the repeatability and the standard deviation between 2 batches tested at T = 375 °C, H_2/CO_2 = 4 are shown in (a). Selectivity to C2+ vs. CO_2 conversion is shown in (d), for the data reported in (a-c). Operating conditions: GHSV = 3,000 mL/(g h), P = 10 bar (absolute).

The product distribution, conversion, and STY of RME Fe/Al_2O_3 evaluated under conditions ranging from 300-375 °C and H_2/CO_2 ratios of 2-4, are depicted in Figure 5-10a. Note that the

product distribution was quantified based on the FTIR signal with a detection range limited to C1-C4 hydrocarbons. At H_2/CO_2 ratio of 4, the conversion steadily increased with temperature and reached its maximum value at 375 °C, while observing a slight decrease in the selectivity towards C2+ hydrocarbon products. However, when the H_2/CO_2 ratio was decreased at a constant temperature of 375°C, the CO_2 conversion rate decreased due to reaction equilibrium considerations, also resulting in a 10% decrease in the selectivity towards C2+ products.

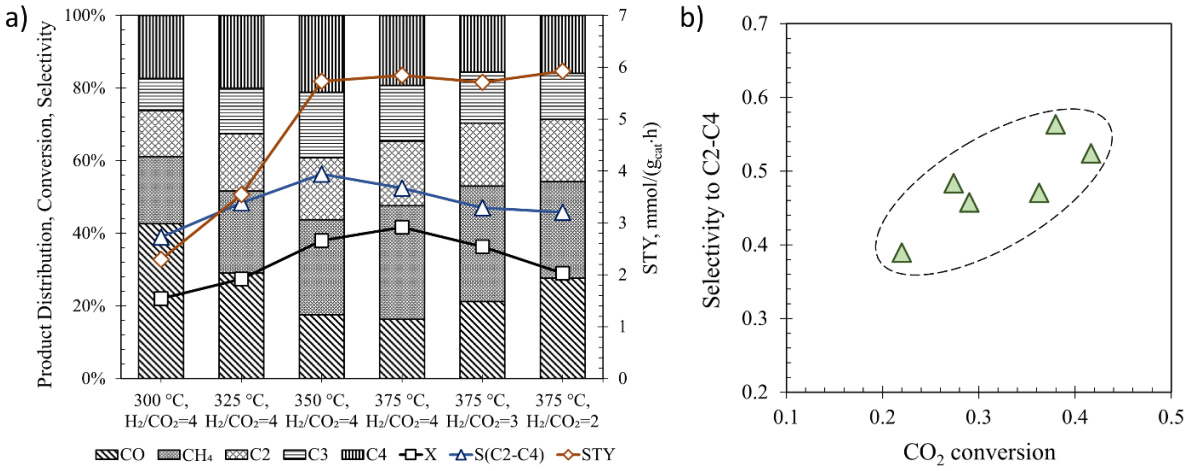

Figure 5-10 Catalytic performance evaluation of RME Fe/Al_2O_3 for T = 300-375 °C and H_2/CO_2 = 2-4, showing product distribution, CO_2 conversion (X, squares), selectivity to C2-C4 (S, triangle), and space-time yield (STY, diamond). Selectivity to C2+ vs. CO_2 conversion is shown in (b), for the data reported in (a). Operating conditions: GHSV = 3,000 mL/(g h), P = 10 bar (absolute).

Despite the reduction in H_2/CO_2 ratio, the STY remained comparable as the GHSV was maintained constant. Figure 5-10b presents the correlation between CO_2 conversion and selectivity towards C2-C4 hydrocarbons. A near linear relationship is observed between these two parameters, which is a considerable improvement as compared to the results depicted in Figure 5-9d, indicating

the linear relationship is observed to be stronger for individual catalysts under different reaction conditions. Table 5-2 summarizes catalysts reported for direct hydrogenation of CO_2 to C2+ hydrocarbons, including this work. Considering the relatively low pressure conducted in this study, the STY of C2+ hydrocarbons on RME Fe/Al_2O_3 catalysts achieved a comparable value with this mild condition of 10 bar since long chain production usually requires high pressure to push the equilibrium. Based on references [99, 100] presented in Table 5-2, it can be observed that the incorporation of additional metals, such as Cu, has the potential to enhance performance. This insight should be taken into account in future work.

Table 5-2 Summary of experimental reports on direct CO_2 hydrogenation to hydrocarbons.

Catalyst	GHSV, mL/(g h)	feed H_2/CO_2	P, bar	T, °C	X(CO_2), %	S(CO), %	S(C2+), %	Product distribution, %			Y(C5+), %	Y(C2+), %	STY(C2+), mol C/(g h)	**Ref**
								C1	C2-C4	C5+				
6.6%K-38.3%RME Fe/Al_2O_3	3000	4	10	375	55.8	17.1	51.8	48.2	40.9	10.9	6.1	28.9	7.7	Current work
$CuFeO_2$	1800	3	10	300	17.3	31.7	66.5	2.7	31.0	66.3	7.8	11.5	2.3	[47]
1.18%Na-Fe_3O_4	2000	3	30	320	40.5	13.5	72.8	15.8	54.1	30.1	10.5	29.5	6.6	[214]
Na-Fe_3O_4/HMCM-22	4000	2	30	320	25.9	17.1	76.3	9.0	10.0	82.0	17.6	19.8	11.8	[215]
Fe_2O_3	1140	3	15	350	40.0	15.0	73.0	14.1	43.5	42.4	14.4	29.2	3.7	[216]
79%Co-21%MnOx	-	1	8	200	15.3	0.4	61.6	46.6	53.4	8.4	-	9.4	-	[217]
Zn-Cr	3000	3	49	400	31.7	85.8	13.2	6.8	68.2	25.0	1.1	4.2	1.4	[218]
Fe-Zn-Zr-HZSM-5-Hbeta	3000	3	50	340	14.9	38.6	60.5	1.5	71.7	26.8	2.5	9.0	3.0	[219]
Fe-Mn-K	2400	3	10	300	38.2	5.6	84.6	10.4	27.7	61.9	22.3	32.3	8.7	[220]
15%Co-6%K/Al_2O_3	1200	3	5	300	42.3	8.2	24.2	73.6	24.3	2.1	0.8	10.2	0.2	[221]
15%Co-8%K/Al_2O_3	1200	3	5	300	12.2	33.5	50.6	23.9	76.1	0.0	0.0	6.2	0.1	
3.8%K-18.4%Fe/MPC	2000	3	25	300	50.6	8.2	76.4	16.8	34.7	48.5	22.5	38.7	8.6	[222]
8.7%K-57.7%Fe-7.5%Cu/Al_2O_3	5000	3	25	300	37.0	9.5	80.0	13.6	33.9	52.5	17.6	29.6	16.5	[223]
0.9%K-13.4%Fe-1.6%Co/TiO_2	3600	3	11	300	23.9	31.0	46.0	33.3	15.9	50.7	8.4	11.0	4.4	[94]
1.3%La-0.9K-1.7%Cu-13.3%Fe/TiO_2	3600	3	11	300	23.1	33.0	54.0	19.4	13.4	67.2	10.4	12.5	5.0	
10%K-13%Fe-2%Co/Zr	7200	3	30	400	42.0	-	52.0	-	32.6	67.4	-	21.8	17.6	[224]
8.7%K-2.6%Co 12.4Fe/Al_2O_3	3600	3	11	300	31.0	18.0	69.0	15.9	84.1	-	-	21.4	8.6	[100]
2.6%K-2.8%Cu 12.2%Fe/Al_2O_3	3600	3	11	300	31.4	16.0	69.0	17.9	82.1	-	-	21.7	8.7	[99]

8.7%K-2.6%Co 12.4%Fe/Al_2O_3	3600	3	11	300	30.9	21.0	64.0	19.0	81.0	-	-	19.8	7.9	

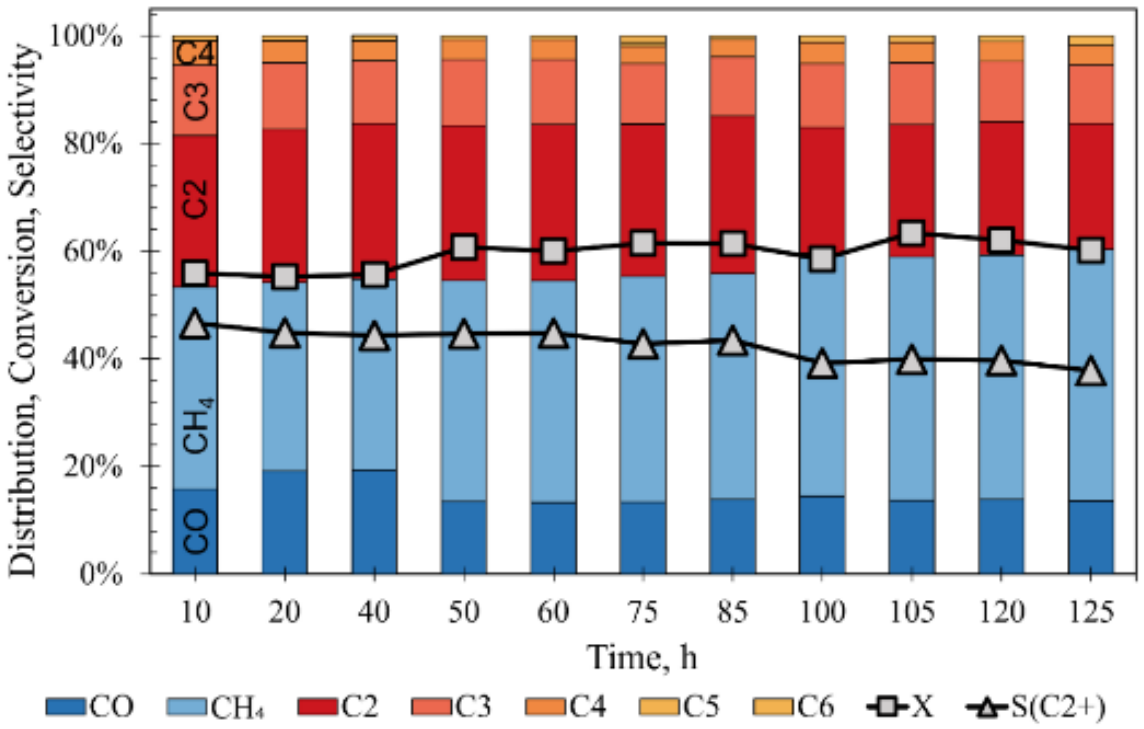

Figure 5-11 Stability test of the RME Fe/Al_2O_3 catalyst, showing product distribution, CO_2 conversion (X, squares), and selectivity to C2+ (triangles). Operating conditions: T = 375 °C, H_2/CO_2 = 4, GHSV = 3,000 mL/(g h), P = 10 bar (absolute).

5.3.3 Stability tests

Since stability is a crucial descriptor to the performance of a catalytic material, RME Fe/Al_2O_3 was tested on stream for over 125 h at the condition with the highest STY (Figure 5-11). Surprisingly the conversion experienced a 9% growth during 40 h to 50 h and maintained at the same level for the rest of the experiments. Nevertheless, the production efficiency of C2+ hydrocarbons decreased gradually which can be revealed from the dropping selectivity. Methane started becoming the dominant product from 50 h but CO fraction remained constant indicating

methane might be the biggest competitor of light hydrocarbons. It was reported that the catalyst phase with high content of χ-Fe_5C_2 might show a gradual increment after a long time on stream. [225, 226]

5.4 Post-reaction characterization

In order to study the phase changes and behavior differences before and after the reaction, characterization technics were also conducted for the spent catalysts. In spent Fe/Al_2O_3, large core-shell particles having size of around 60 nm were widely observed which the diameter was tripled compared to the fresh catalyst (Figure 5-4d). However, in the Fe/RME-Al_2O_3 sample, even though the Fe was loaded to the support by wet impregnation, the Fe particle size (Figure 5-5d) after reaction was still much smaller than Fe/Al_2O_3, and only grew by about 150%, suggesting a superior support not only can provide higher specific surface area but can also prevent the sintering of active phase.

The effect of size to the selectivity (Figure 5-9) is also agree with the observation of Suo et al, [227] the selectivity towards C2+ increases with decreasing particle size. It also has been proposed that the particle size of Fe carbide catalysts is vital to the surface specific activity and the apparent turnover frequency of conversion to hydrocarbons increases with a descending particle size, which was proved in this study as well that smaller particle size corresponding to higher CO_2 conversion and space time yield. [228] A elemental mapping of three catalysts at a smaller resolution were summarized in Figure 5-12 and it can be seen for al samples, Fe and K were well dispersed on the Al_2O_3 support.

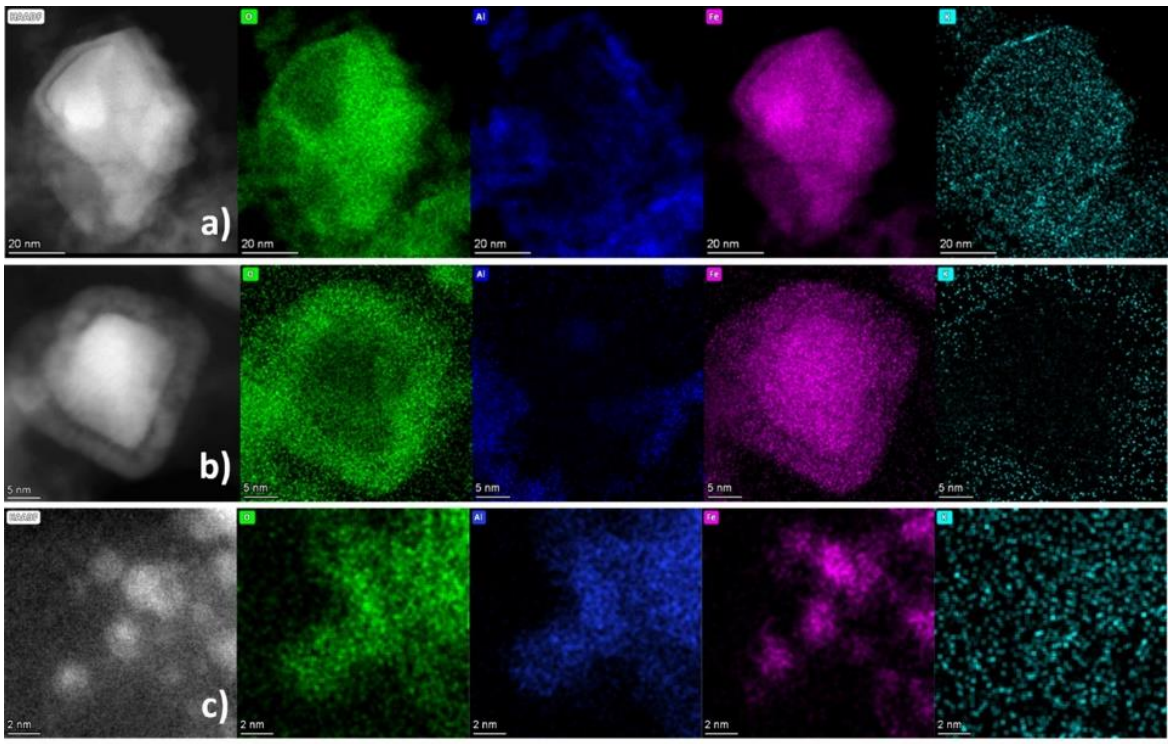

Figure 5-12 HAADF elemental mapping comparison of spent Fe/Al_2O_3 (a), $Fe/RME\text{-}Al_2O_3$ (b), and RME Fe/Al_2O_3 (c) catalysts.

XPS analysis was also conducted to understand the surface chemical nature of the spent catalysts and the Fe 2p and C 1s region for each spent catalyst were shown in Figure 5-13. Peaks around 710.5 and 723.6 eV in all 3 catalysts can be assigned to Fe^{2+} doublet [229] while peaks near 713.9 and 727.3 eV are Fe^{3+} doublets with a satellite peak appeared at 711.5 eV. [230] As shown in Figure 5-13, 295.2 and 292.5 eV are the 2p peaks for K_2O [231] and the peak observed at 284.8 eV was ascribed to Fe-C 1s. [232] Fe_5C_2 appears at ~707 and ~720 eV. Comparing the Fe^{2+} ratio determined from Fe 2p region, RME Fe/Al_2O_3 showed slightly higher content, 80.5%, than $Fe/RME\text{-}Al_2O_3$ (78.1%) and Fe/Al_2O_3 (77.3%). This small discrepancy may not be sufficient to conclude the enhanced catalytic performance of RME Fe/Al_2O_3 was from higher Fe^{2+} or Fe_3O_4

content, the smaller particle sized resulted from RME synthesis is still a more compelling reason of the superiority.

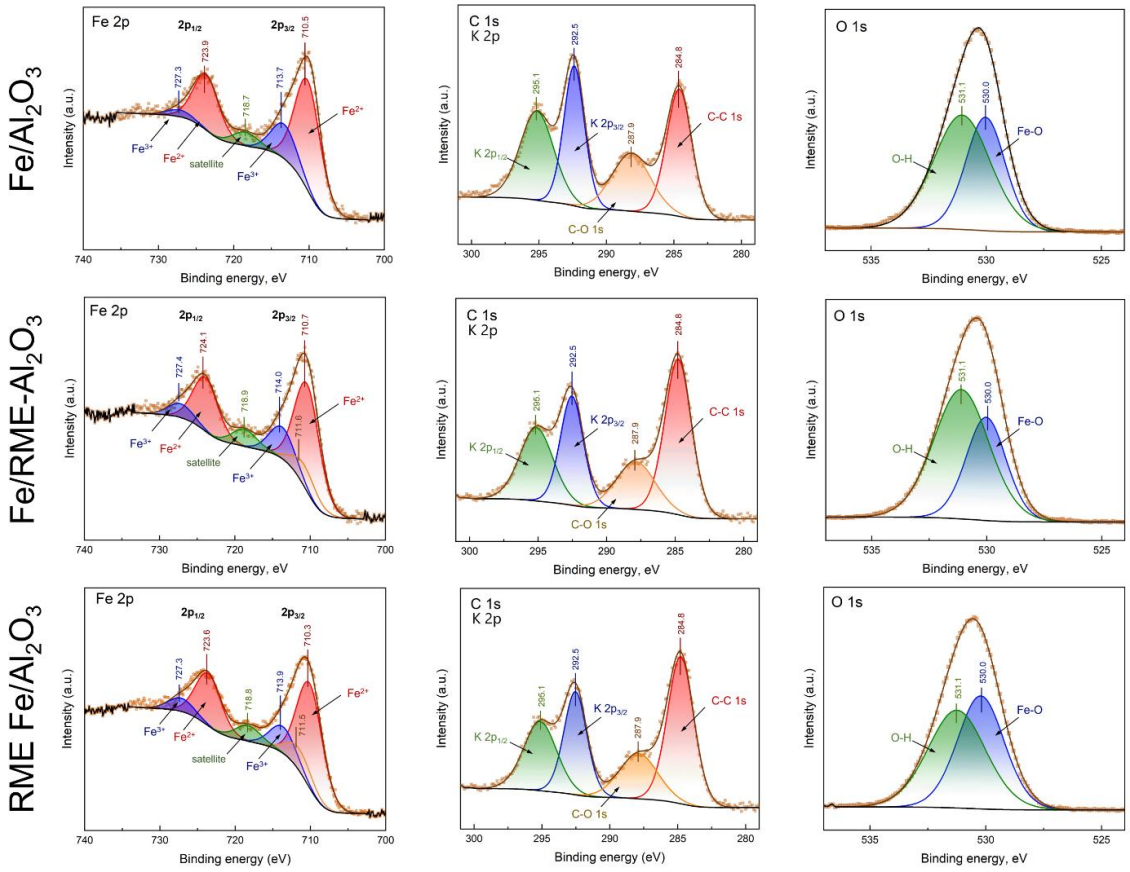

Figure 5-13 XPS patterns of spent Fe/Al_2O_3, $Fe/RME\text{-}Al_2O_3$, and RME Fe/Al_2O_3 catalysts.

The TPO profiles of the catalysts after 70 h time on stream under reaction conditions are shown in Figure 5-14. Three distinct CO_2 peaks represent the presence of three carbonaceous species. The fist peak appeared at around 220 °C (α-peak) corresponds to the reactive carbon, which was determined as the precursor to the hydrocarbonaceous overlayer between the amorphous carbon phase and the Fe carbides phase, as well as the Fe carbide species. [205, 233, 234] The second peak at 355 °C (β-peak) associate with the amorphous hydrocarbon or carbon species deposition on the surface while the third peak at 400 °C (γ-peak) represents the oxidation

of the Fe carbide species. [233, 234] Consider that the total weight loss for all samples during TGA analysis were around 3.5 wt%, the presence and higher content of Fe carbide species in RME Fe/Al_2O_3 and $Fe/RME\text{-}Al_2O_3$ is further supported by the larger intensity of γ-peak, additional to the post-reaction XRD results.

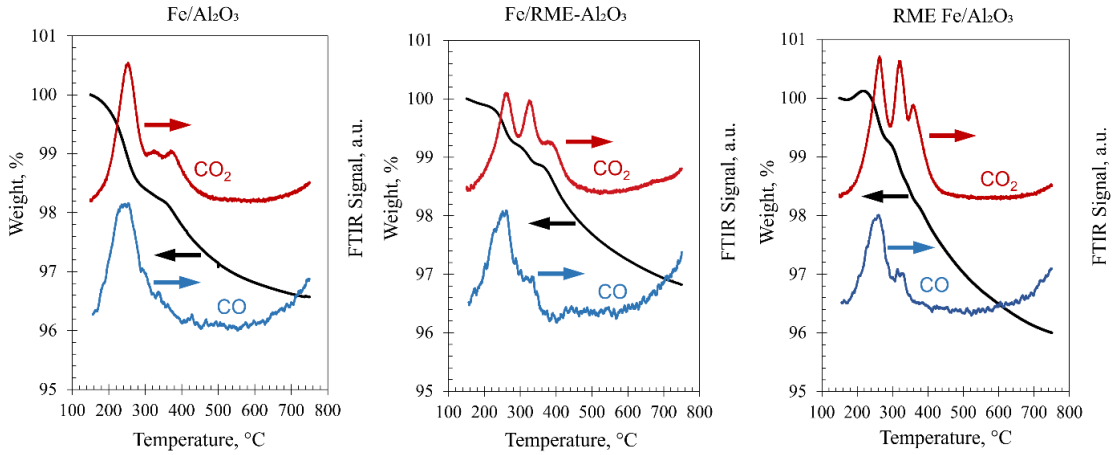

Figure 5-14 TGA-FTIR files of post reaction catalysts (70 h on stream). Stability test conditions: T = 375 °C, H_2/CO_2 = 4, GHSV = 3,000 mL/(g h), P = 10 bar (absolute).

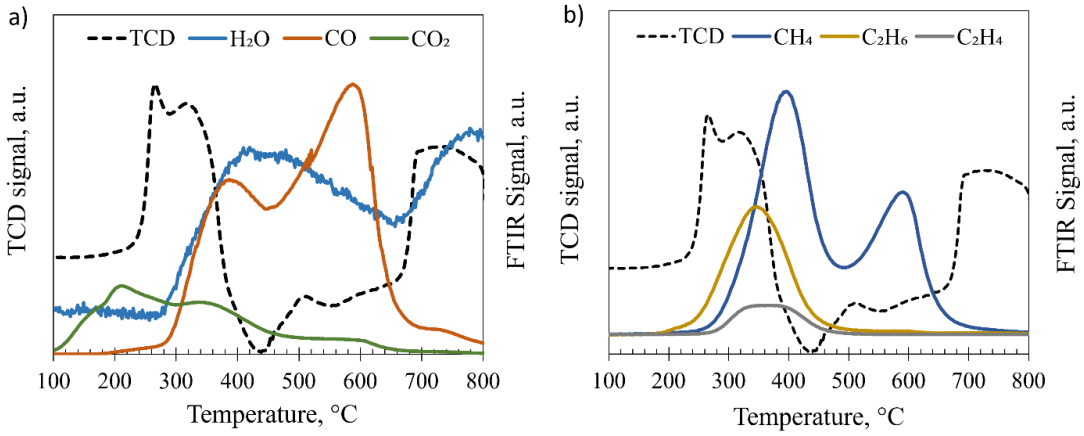

Figure 5-15 TPR-FTIR profiles of the spent RME Fe/Al_2O_3 catalysts (70 h on stream). Stability test conditions: T = 375 °C, H_2/CO_2 = 4, GHSV = 3,000 mL/(g h), P = 10 bar (absolute).

To further confirm the surface carbonaceous species, TPR for spent catalysts was perform and the species in the effluent were analyzed by FTIR as shown in Figure 5-15. Small amount of CO_2 was detected at low temperature range from 260 to 400 °C, which may due to the physical and chemical adsorption on the surface and it was interesting to observe that the CO_2 was reduced to CO starting from 400 °C producing water as by product. The first methane peak at 425 °C could be assigned to the hydrogenation of Fe carbides [206] while the second peak at higher temperature at 630 °C is ascribed to the graphitic carbon deposition. [235]

5.5 Discussion and concluding remarks

The present study sought to investigate the CO_2 hydrogenation reaction over Fe-based catalysts, comparing catalysts prepared by the RME method (RME Fe/Al_2O_3), precipitation on RME-synthesized Al_2O_3 (Fe/RME-Al_2O_3), and precipitation (Fe/Al_2O_3), and to identify the impact of different synthesis methods and reaction conditions. The characterization of fresh catalysts showed that RME Fe/Al_2O_3 exhibited smaller particle sizes of Fe_3O_4 and alumina support, which led to an enhancement in Fe dispersion on the alumina support.

RME Fe/Al_2O_3 showed excellent performance in terms of CO_2 conversion and STY in CO_2 hydrogenation. At H_2/CO_2=4, the highest conversion rate was observed at 375°C, with a maximum conversion of 56%, and the STY was 7.75 mmol/(g_{cat}·h) at this temperature. The selectivity towards C2+ hydrocarbons at his condition was 0.52, which was the highest selectivity achieved among the three tested catalysts. The results also showed that a decrease in the H_2/CO_2 ratio led to a reduction in the conversion rate due to reaction equilibrium considerations, also resulting in a 10% decrease in the selectivity towards C2+ products while maintaining comparable STY.

The core-shell structure observed in the spent Fe/RME-Al_2O_3 and Fe/Al_2O_3 catalysts supported the transformation of magnetite to carbides during the reaction, contributing to the sustained catalytic activity. Moreover, the uniform structure of the core-shell nanoparticles observed in the spent Fe/RME-Al_2O_3 sample suggested that a superior support can prevent the sintering of active phase, leading to better stability. The microscopy results suggested that the smaller particle size resulting from the RME procedure facilitates the transformation of magnetite to carbides, enhancing the activity of the catalyst. The spent RME Fe/Al_2O_3 sample consists primarily of clear spherical χ-Fe_5C_2 and Fe_3O_4 particles with a particle size under 10 nm, and a slight increase in average particle size of 0.8 nm was observed during the analysis, which showed smaller particle size and decelerated growth after 70h on stream compared to Fe/RME-Al_2O_3 and Fe/Al_2O_3. Overall, RME Fe/Al_2O_3 demonstrated excellent performance for CO_2 direct hydrogenation to light hydrocarbons making it a promising candidate for future industrial applications.

Chapter 6 Experimental investigation of copper-doped ceria ($CuCeO_2$) catalysts for reverse water gas shift

This chapter presents a comprehensive exploration of Cu/CeO_2 catalysts synthesized through reverse micro emulsion method, offering insights into their performance, stability, and underlying mechanisms in CO_2 reduction processes. The influence of Cu doping concentration on the catalyst performance is investigated and underscores the balance between Cu loading and catalyst integrity, as confirmed by XPS and XRD analyses. Long-term stability tests reveal minimal degradation over 110 hours, highlighting resistance to coking and sintering. In-situ FTIR analysis unveils the crucial role of oxygen vacancies generated by Cu doping, facilitating CO_2 adsorption and activation. The findings emphasize the potential of Cu/CeO_2 catalysts in CO_2 reduction applications, while also highlighting the importance of Cu doping levels. Insights into the reaction mechanism and the dynamic nature of surface adsorbates offer valuable guidance for catalyst design, with room for further computational studies to deepen mechanistic understanding and catalyst development.

6.1 Catalyst synthesis

Three reverse microemulsions (RMEs) were synthesized by combining an aqueous phase comprising cerium nitrate (99.5% $Ce(NO_3)_3 \cdot 6H_2O$, Alfa Aesar), copper nitrate ($CuNO_3 \cdot 9H_2O$, Sigma-Aldrich), and ammonium hydroxide (28-30% NH_4OH, LabChem Inc.) with a surfactant (Triton X-100, Acros Organics), a co-surfactant (propanol-2, Sigma-Aldrich), and an oil phase (cyclohexane, Sigma-Aldrich) in a proportion of 1:1:4.5:3.5. The RME containing copper nitrate was introduced gradually into the RME with cerium nitrate, while continuously stirring for 4 hours. Subsequently, the RME containing ammonia was incrementally added to the mixture, maintaining

a consistent stirring for another 4 hours, until a precipitate emerged. This precipitate was thoroughly rinsed four times using deionized (DI) water and then subjected to centrifugation. Afterward, the cleaned precipitate was left to dry overnight and subsequently calcined at 275 ℃ for a duration of 4 hours. For catalytic reactions, the resultant powdered catalyst was molded into pellets and sifted to yield pellet sizes ranging from 250-425 µm.

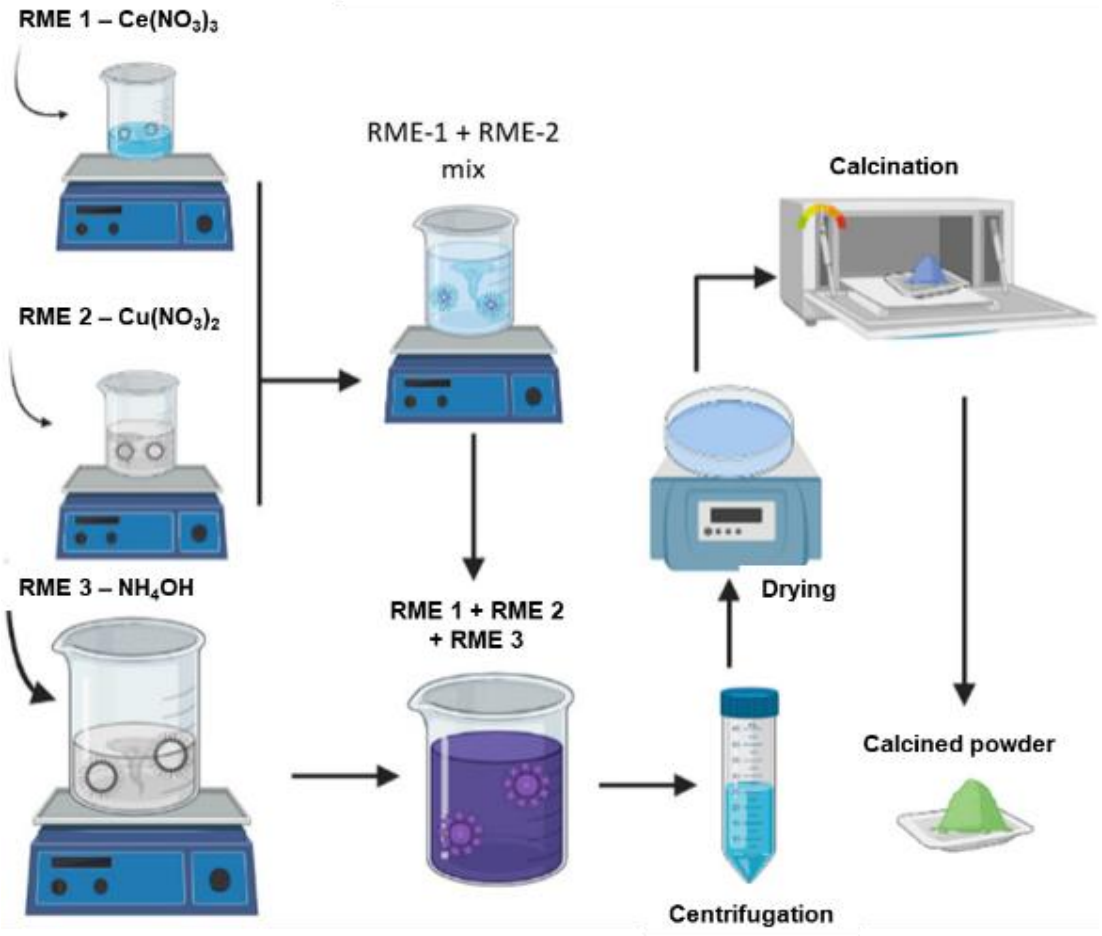

Figure 6-1 RME Synthesis schematic for Cu/CeO_2 catalyst preparation

6.2 Catalyst characterization

6.2.1 Crystallinity

Figure 6-2 presents the XRD patterns of both newly calcined and used (post-reaction) catalysts. The specified percentages (0, 0.62, 1.17, 5.36, 10.20, and 26.54%) correspond to atomic

percentages (at%) computed as Cu/(Ce+Cu) on a molar basis, as verified by ICP-OES (refer to Table 6-1). For fresh catalysts, the diffraction peaks are notably broad, suggesting the presence of small nanocrystallites. In contrast, the spent catalysts display distinct, sharp peaks. The XRD patterns of both fresh and spent catalysts match the CeO_2 fluorite structure (PDF 00-034-0394). Importantly, no additional crystalline phases of Cu or Cu oxides (such as CuO or Cu_2O) were observed in all XRD patterns, indicating that Cu is primarily integrated into the CeO_2 lattice, replacing Ce ions. It's also plausible that sub-nanometric clusters of Cu or Cu oxides exist on the surface, although these clusters would remain undetected by XRD. This high level of Cu doping observed aligns with findings from previous studies. [236]

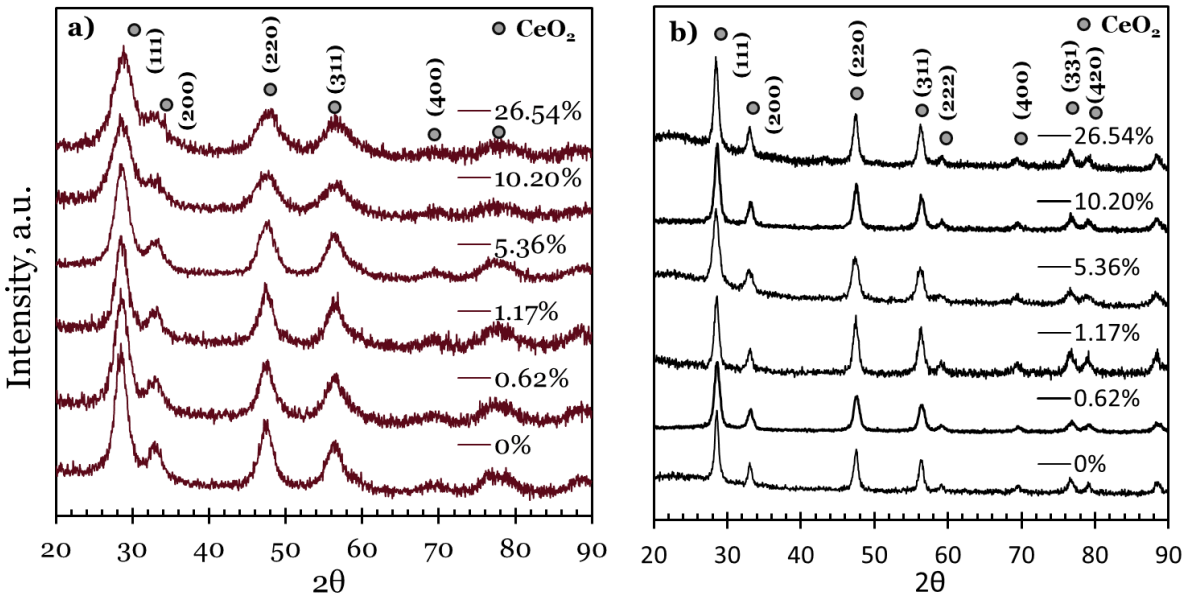

Figure 6-2. XRD patterns of as prepared, calcined catalysts (a) and of catalysts after 20 h under reaction conditions (b).

Table 6-1 illustrates the sizes of crystallites derived from XRD patterns using the Scherrer formula. Peaks of (111), (220), and (311) (of highest intensity) were utilized to compute the mean crystallite size. Deviations reported in Table 6-1 refer to standard deviations between the three

values. The findings indicate that in fresh catalysts, the size of the nanocrystallites decrease with the increase of Cu doping, stabilizing after reaching 10.20 at%.

Table 6-1: Cu loading (Cu/(Ce+Cu) at% as determined by ICP-OES), BET-measured specific surface area (SSA), and crystallite size as determined from XRD patterns (D_{XRD}).

Cu loading, at%	SSA, m^2/g		D_{XRD}, nm	
	fresh	spent	fresh	spent
0	115	15	5.2	15.1
0.62	-	-	4.2	11.2
1.17	143	20	5.3	12.0
5.36	143	32	4.2	9.8
10.20	127	13	3.3	11.1
26.54	127	12	3.1	12.7

The behavior of crystallite sizes in spent catalysts deviates from that observed in fresh catalysts. The alteration in crystallite size can be attributed to two primary factors: the replacement of larger Ce^{4+} ions with smaller Cu^{2+} ions, reducing crystallite size, and the creation of oxygen vacancies due to Cu doping, which could potentially expand the lattice. [237] These competing effects result in a more complex relationship between Cu doping level and nanocrystallite size in spent catalysts. Additionally, the observed variations in crystallite sizes may be influenced by other factors, as lattice size is not directly proportional to nanocrystallite size. Surface area measurements through BET analysis, using N_2 adsorption, indicated that lower Cu doping concentrations yield higher SSA in fresh catalysts, though this trend reverses at higher Cu concentrations (10.20 and 26.54 at%).

6.2.2 Surface property

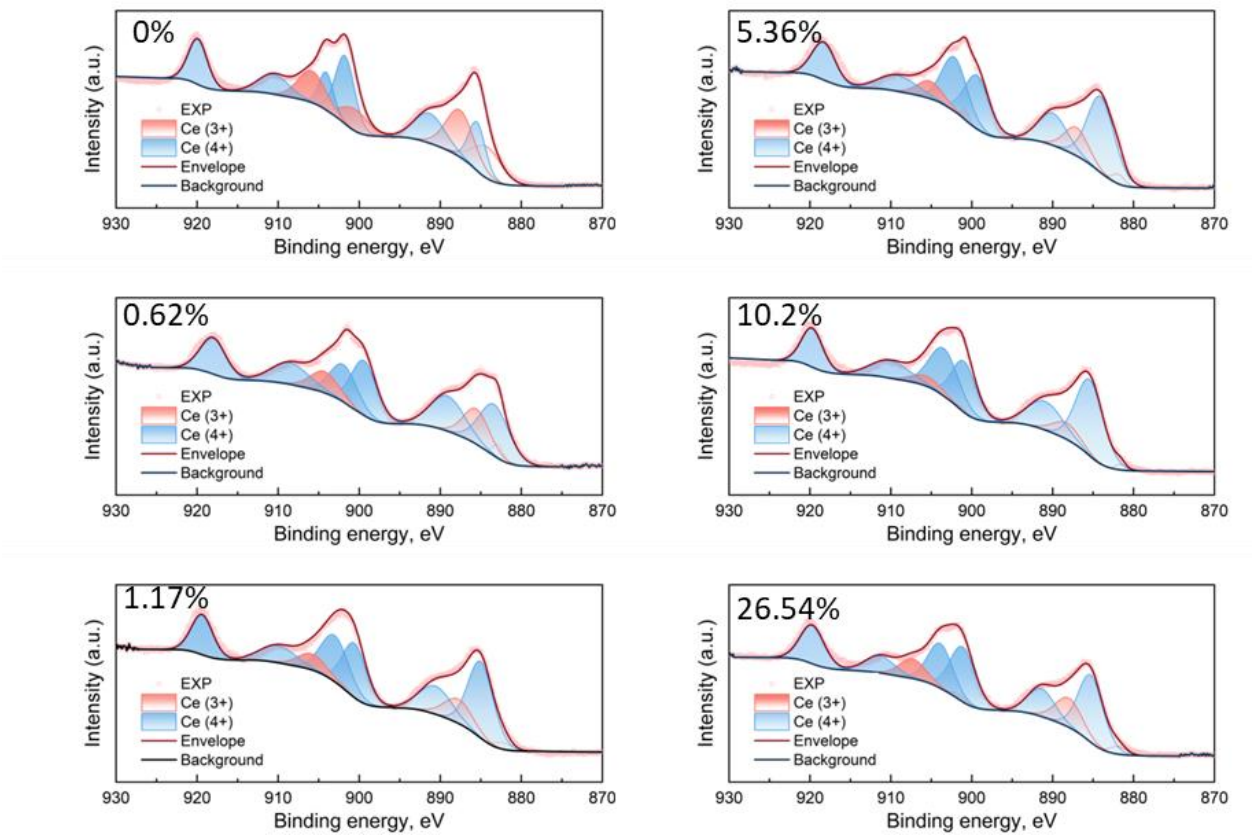

Figure 6-3. XPS spectra of fresh (calcined) catalysts showing Ce 3d region for pure CeO_2 (0 at%) and Cu-doped CeO_2 (0.62-26.54 at%).

Surface elemental composition and chemical states were evaluated through XPS (Figure 6-3). Analysis of the Ce 3d subshell, comprising five orbitals in two spin states ($3d_{5/2}$ and $3d_{3/2}$), revealed 10 well-defined peaks. Peak fitting criteria were established for all samples, resulting in a consistent 3:2 peak area ratio between the $3d_{5/2}$ and $3d_{3/2}$ doublet peaks. [238] 10 well fitted peaks were obtained for all samples: u_o, u, u', u'', u''', v_o, v, v', v'', v''' (u represents peaks associated with the $3d_{5/2}$ spin state, while v associated with the $3d_{3/2}$ spin state). Concentration of Ce^{3+} and Ce^{4+} states can be calculated as follows (with eq. 6-3 representing the fraction of Ce^{3+} ions)

$$Ce^{3+} = u_0 + u' + v_0 + v' \quad (6\text{-}1)$$

$$Ce^{4+} = u + u'' + u''' + v + v'' + v''' \quad (6\text{-}2)$$

$$Ce^{3+} = \frac{Ce^{3+}}{Ce^{3+} + Ce^{4+}} \tag{6-3}$$

The Ce^{3+} and Ce^{4+} states were identified by summing the areas of peaks associated with each oxidation state. Figure 6-4 demonstrates a correlation between the concentration of Ce^{3+} and the Cu doping level, revealing a significant decrease in Ce^{3+} with increasing Cu, except at the highest Cu loading. This suggests Cu substitution at Ce^{3+} sites near the surface, as XPS primarily probes the few subsurface atomic layers of the nanoparticles. It is widely recognized that elevated levels of Ce3+ are associated with an increased presence of oxygen vacancies, which typically form in proximity to the Ce^{3+} ion [239]. Consequently, a decrease in the Ce^{3+} concentration leads to a corresponding reduction in oxygen vacancies. Conversely, the introduction of Cu^{2+} ions can create additional oxygen vacancy sites, thereby augmenting the overall concentration of oxygen vacancies as a result of Cu doping. This substitution of Ce^{3+} with Cu^{2+} markedly increases the number of oxygen vacancy sites, which in turn enhanced the chemisorption capacity for CO_2. Interestingly, at a 26.54 at% Cu doping level, there is a notable increase in the Ce^{3+} concentration, although it remains significantly lower compared to the concentration in pure CeO_2.

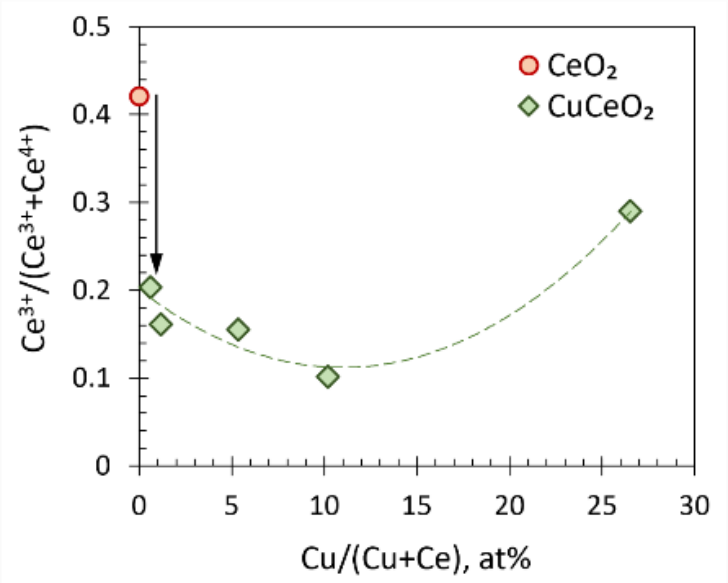

Figure 6-4. XPS-measured $Ce^{3+}/(Ce^{3+} + Ce^{4+})$ chemical state ratio vs. Cu/(Cu+Ce) atomic ratio as determined by ICP-OES.

Figure 6-5 displays the CO_2 temperature-programmed desorption (TPD) profiles for both unreduced and reduced catalysts. In these profiles, two distinct peaks, labeled α and β, are observed at relatively low temperatures, along with a higher-temperature peak designated γ. These three desorption peaks correspond to distinct CO_2 adsorption sites/configurations, indicative of weak, moderate, and strong CO_2 adsorption strengths, respectively. For the unreduced samples, the α-peak consistently appears around 90-100 °C across all doping levels, including the pure CeO_2 sample, which is associated with the weak adsorption of CO_2 species on the surface. The α-peak is likely related to bicarbonate desorption due to its weak interaction with the surface. Upon reduction, the α-peak becomes more pronounced, maintaining its temperature position. The β-peak that related to the moderate adsorption, while less discernible for the 26.54 at% sample, shows a slight shift to higher temperatures, ranging from approximately 150 °C to around 170 °C at intermediate Cu doping levels. However, the β-peak exhibits a notable shift to substantially higher temperatures, especially at increased Cu loadings, ranging from about 190 °C to approximately 300 °C. In contrast, the γ-peak is situated at approximately 410-420 °C for all samples. The γ-peak consistently shifts to temperatures above 500 °C for all samples. Conversely, the β and γ-peaks are possibly linked to monodentate or bidentate desorption configurations, which are characterized by stronger surface binding. [240]

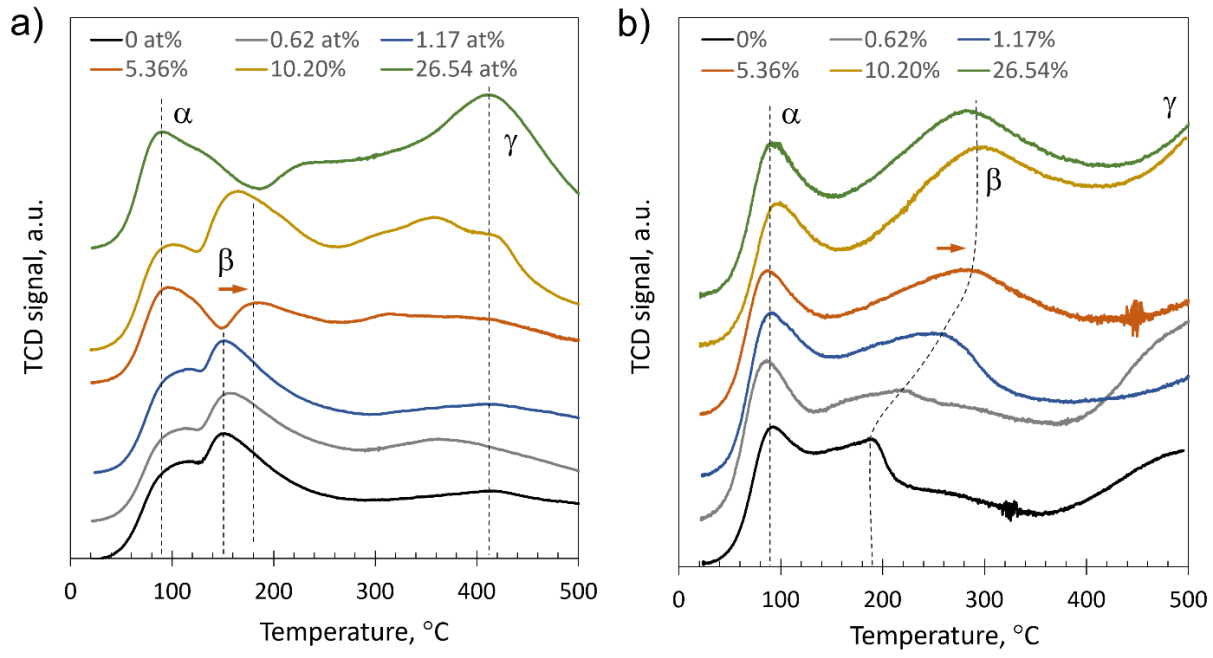

Figure 6-5. CO_2 TPD profiles obtained for unreduced (fresh, after calcination) samples (a) and samples after reduction at 400 °C (b).

Additionally, the activation energy of desorption ($E_{a,des}$) was calculated from the obtained TPD profiles by Polanyi-Wigner equation and showed in Figure 6-6. The $E_{a,des}$ values for the α-peak remained relatively consistent across all samples, both unreduced and reduced, with the notable exception of a marked decrease at a Cu loading of 10.20 at% in the reduced sample. In the case of the β-peak, a slight rise in $E_{a,des}$ was noted for the unreduced samples, although this was not applicable for the 26.54 at% loading due to detection challenges. Contrastingly, in the reduced samples, there was a distinct increase in $E_{a,des}$ values at lower Cu doping levels, which eventually plateaued between 5.36 at% and 26.54 at%. Overall, a significant escalation in $E_{a,des}$ was observed in the reduced catalyst, escalating from 145 kJ/mol at 0 at% to 173 kJ/mol at a Cu loading of 26.54 at%. The observed elevation in the activation energy for CO_2 desorption associated with the β-peak suggests that this specific adsorption site or configuration may be linked to the presence of

surface oxygen vacancies, which are likely formed as a result of Cu incorporation. These sites are potentially responsible for the enhanced adsorption of CO_2. It is important to note that the XPS findings indicated an increased concentration of oxygen vacancies, which could be a consequence of substituting Ce^{3+} ions with Cu^{2+} ions, as detailed in Figure 6-4.

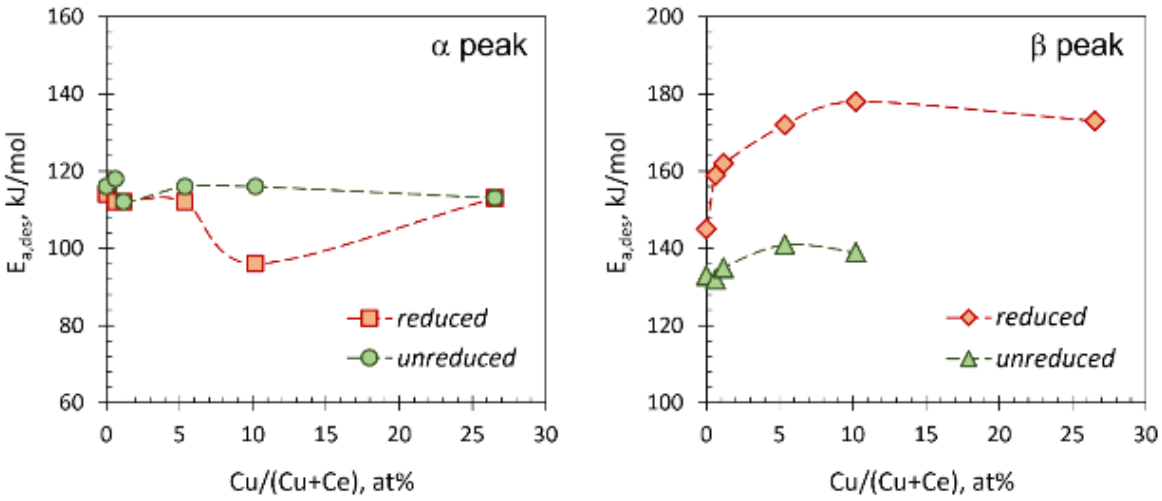

Figure 6-6. Activation energy of desorption (Ea,des) vs. Cu loading (Cu/(Cu+Ce)) for α-peak (left panel) β-peak (right panel); α- and β-peaks correspond to CO_2 TPD peaks presented in Figure 6-5.

6.3 Catalyst performance evaluation

The performance of the synthesized catalysts was thoroughly evaluated in terms of CO_2 conversion and CO selectivity. This assessment was conducted through reaction tests over a temperature range of 300-600 °C, with a gas hourly space velocity (GHSV) set at 60,000 ml/(g h). Prior to these tests, all catalysts underwent a reduction process using pure H_2 at 600 °C for two hours, ensuring an optimal state and activation for reacting with the feed gases. Figure 6-7a illustrates the CO_2 conversion (X) and CO selectivity (S) across various temperatures for the Cu/CeO_2 samples. Remarkably, all samples demonstrated complete selectivity to CO. A closer

examination of CO_2 conversion revealed detectable levels starting at 400 °C for doping concentrations ranging from 0 to 1.13 at%. Pure CeO_2 exhibited a relatively poor performance, achieving a maximum conversion of only 40% at 600 °C. In contrast, doping concentrations of 1.13 at% and 5.2 at% achieved higher conversion rates of 47% and 49%, respectively, at 600 °C. Notably, a significant enhancement in catalytic performance was observed for samples with 10.2 at% and 26.54 at% Cu doping, even at lower temperatures. At 400 °C, these samples showed a twofold improvement in conversion, reaching approximately 20%, compared to pure CeO_2. Furthermore, at higher temperatures, their conversion rates approached equilibrium values, nearly 60% at 600 °C. Intriguingly, the catalytic performance of 10.2 at% and 26.54 at% Cu loadings was similar, indicating a saturation point in copper doping beyond which further increases do not significantly enhance performance. This observation is in agreement with the results obtained from XPS and XRD analyses.

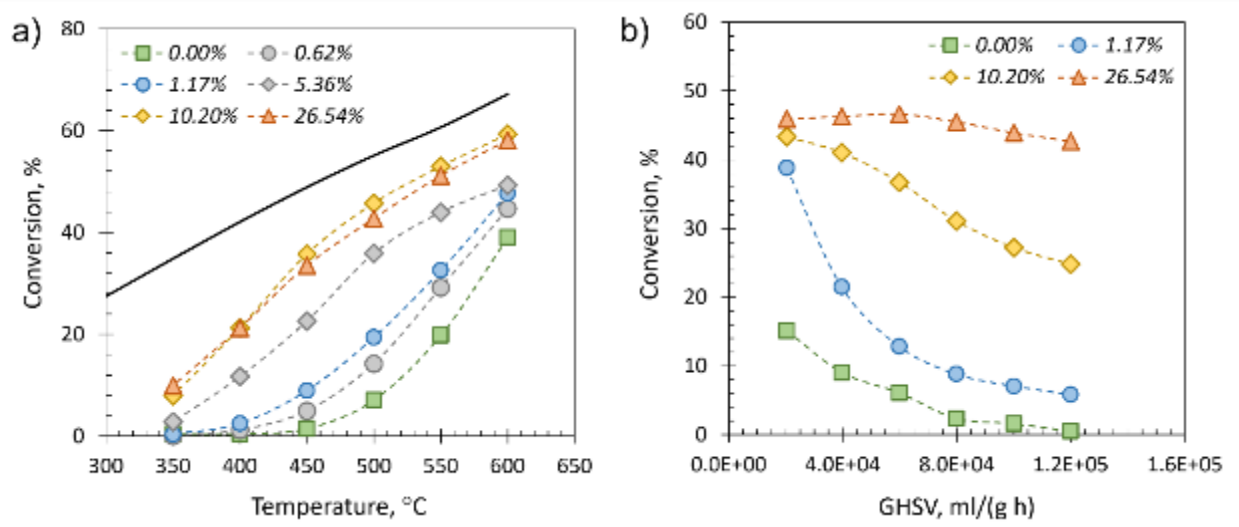

Figure 6-7. a) Catalytic performance evaluation of all samples of Cu/CeO_2 catalyst as a function of temperature (300-600 °C) b) Catalytic performance evaluation of all samples of Cu/CeO_2 catalyst as a function of GHSV (20,000 – 120,000 ml/(g h)). The solid black line

represents RWGS equilibrium. Parameters: P = 3 bar, H_2/CO_2 = 3 (feed), a) GHSV = 60,000 mL/(g h) b) T = 500 °C.

To extend the evaluation of catalytic performance, GHSV tests were carried out at 500℃, spanning a range of space velocities from 20,000 ml/(g h) to 120,000 ml/(g h) with the results presented in Figure 6-8b. It was observed that all catalysts exhibited superior performance at lower GHSV, likely due to the increased residence time allowing for more effective reaction dynamics. CeO_2 continued to show limited effectiveness, with its conversion dropping to zero at the highest GHSV of 120,000 ml/(g h). In comparison, the Cu-doped catalysts demonstrated significantly better performance, particularly at the lowest GHSV of 20,000 ml/(g h), where conversion rates for Cu loadings of 1.17 at% to 24.54 at% ranged between 38-45%. Interestingly, the performance drop for a doping concentration of 1.4 at% was more pronounced and stabilized as GHSV increased. However, this trend was less evident at higher Cu concentrations (10.2 at% and 26.54 at%), suggesting that higher doping levels might reduce the rate of sintering, thereby enhancing performance in terms of GHSV.

Arrhenius plot, shown in Figure 6-8a, was used to estimate the activation energy of reaction ($E_{a,rxn}$). Eq. 6-4 and 6-5 were used to calculate the CO generation rate and activation energy, respectively.

$$R_{CO} = \frac{F_{CO_{2,f}} \times X_{CO_2}}{W_C} \tag{6-4}$$

$$\ln(R) = \ln(A) - \frac{E_a}{R_g T} \tag{6-5}$$

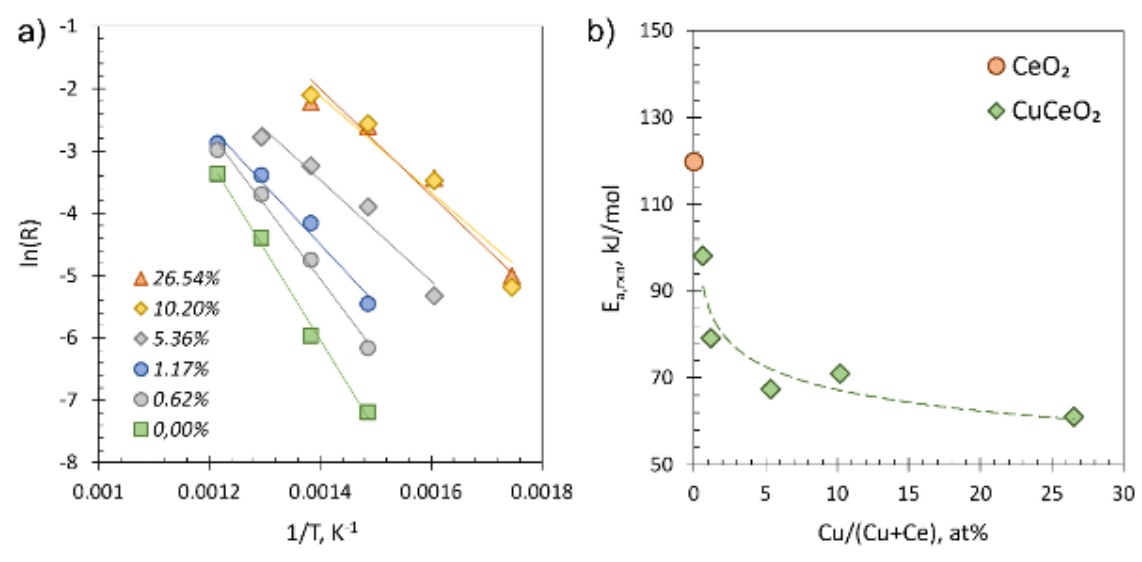

Figure 6-8. a) Arrhenius plot (ln(R) vs 1/T) of all samples b) Activation energy of reaction ($E_{a,rxn}$) vs atomic ratio (Cu/(Cu+Ce)) of all samples.

The CO generation rate and activation energy were calculated using equations 6-4 and 6-5, respectively. To ensure the validity of the results, $E_{a,rxn}$ was evaluated at temperatures below 550℃, where the CO_2 conversion for all catalysts remained below 20%. Figure 6-8b reveals that the $E_{a,rxn}$ for CeO_2 was the highest at 119 kJ/mol. Significantly, there was a marked decrease in $E_{a,rxn}$ values from CeO_2 to 60 kJ/mol for the 26.54 at% Cu/CeO_2, following a decreasing trend indicative of an inverted power law relationship.

Notably, the activation energy plateaued as the Cu doping concentration reached 26.54 at%, reinforcing the observed doping limit in copper, as indicated by XPS, XRD, and reaction test results. The decrease in $E_{a,rxn}$ in Cu-doped CeO_2 can be attributed to the formation of oxygen vacancies, a consequence of Cu doping, which enhances CO_2 adsorption and activation. Consequently, as Cu doping increases, the $E_{a,rxn}$ decreases, leading to improved catalytic performance.

6.4 Mechanistic study of CO_2 reduction on copper-doped ceria surface

The adsorption behavior of CO_2 and reaction mechanism were investigated by in-situ FTIR techniques. Comparing pure CeO_2 and Cu doped CeO_2 stoichiometric surface (Figure 6-9), similar species were identified on the surface with no distinguish peak position, revealing that the adsorption behaviour on stoichiometric CeO_2 and Cu/CeO_2 are similar. Peaks centred at 1508, 1369, 1298 cm^{-1} corresponding to the frequencies of C-O bond in the unidentate carbonate denoted as 1.21 in [241], in which the three integers indicate that the carbonate is bound by three oxygen. The integer 2 in the middle indicates that the highest coordinate of the three oxygen atoms is 2 and meanwhile the other two oxygen atoms are coordinated to one Ce cation, while the point represents that one of the oxygen is coordinated to a neighbor Ce but not the 2 Ce atoms in the highest coordinate. Previous DFT calculation also suggested that this carbonate configuration is one of the most stable CO_2 adsorption configurations on the CeO_2 surface with oxygen vacancy. [241]

Reaction test was also conducted with in-situ FTIR measurement. Figure 6-10 indicates the comparison of the in-situ FTIR profile between reduced CeO_2 and Cu doped CeO_2 at 300 °C under CO_2 and H_2 mixture. Only carbonates were detected as carbonaceous species at 15 min after introducing the reaction mixture, and CO peak also proves the occurrence of RWGS reaction. Moreover, no noticeable difference was detected between the two samples which suggest that the intermediate species and reaction mechanism did not change with Cu doping.

To further investigate the relation of adsorbed species and the intermediates, in-situ FTIR with reaction gases ($2\%CO_2/8\%H_2/Ar$) was tested for 10.2% Cu/CeO_2 at three temperature from 100-300 °C and the spectra are shown in Figure 6-11. The OH peaks are visible at 1214 and 1389 cm^{-1}, indicating some hydrogen carbonates on the surface of the catalysts. However, as the catalyst

was heated up to 200 °C, the hydrogen carbonate disappeared and only carbonate species are detectable.

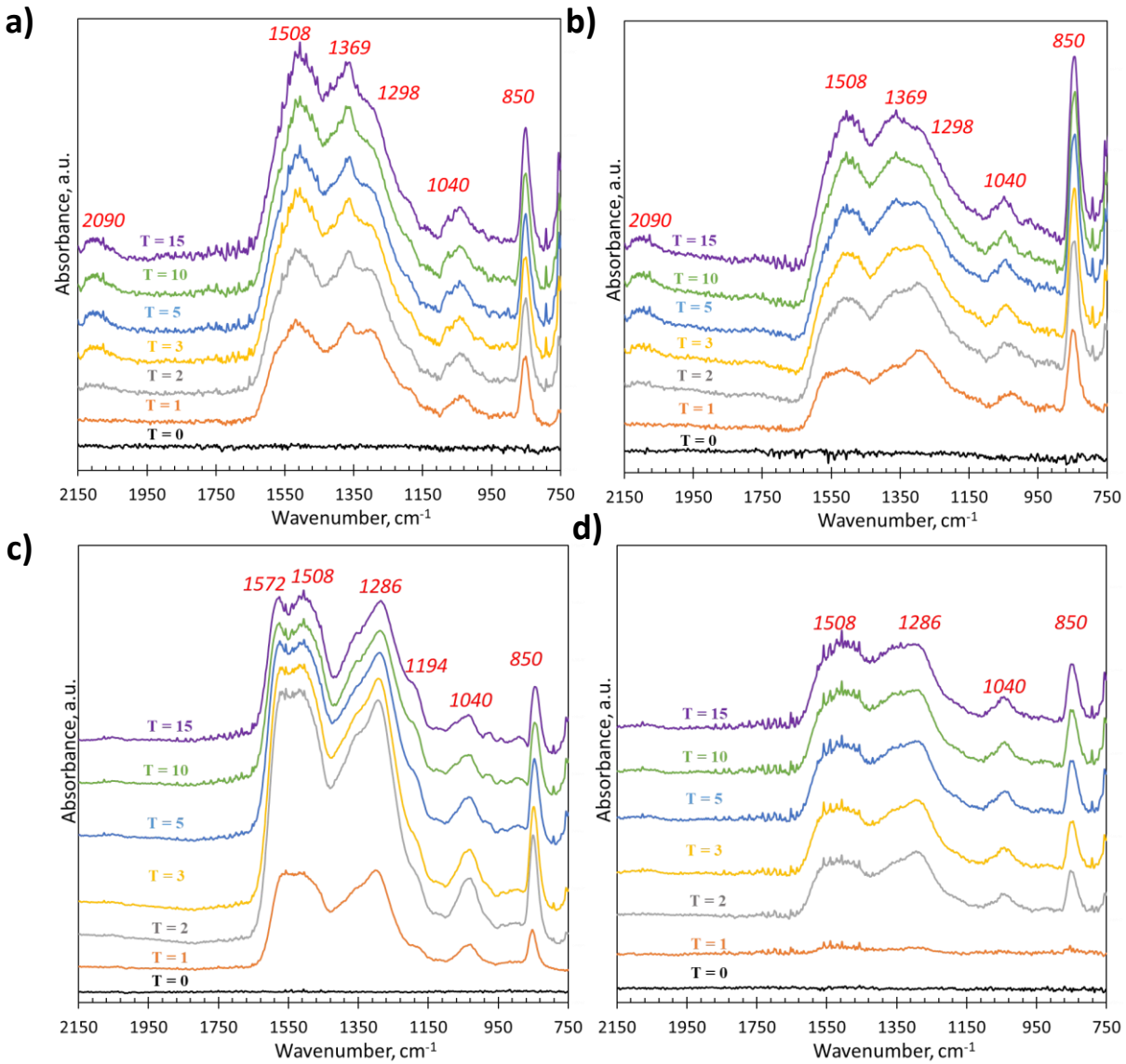

Figure 6-9 In-situ FTIR profiles of a) reduced CeO_2 catalyst, b) reduced 10.2 wt% Cu/CeO_2, c) unreduced CeO_2 catalyst and d) unreduced 10.2 wt% Cu/CeO_2 at 300 °C under 5% CO_2/He flow.

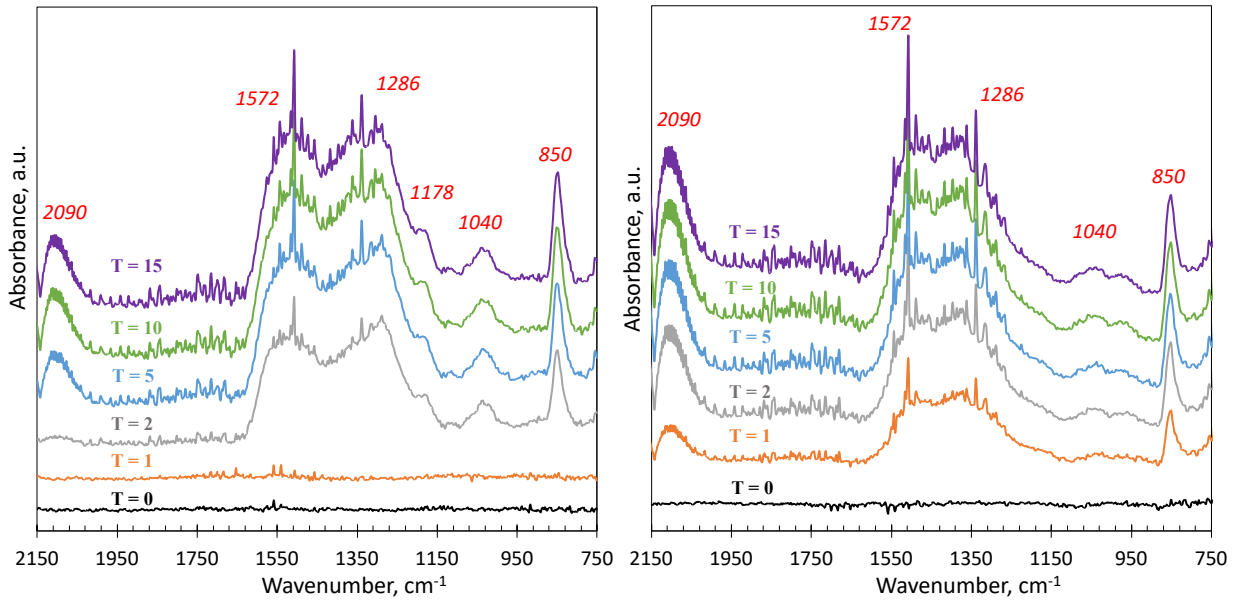

Figure 6-10 In-situ FTIR profiles of left, CeO_2 catalyst; right, 10.2 % Cu/CeO_2 at 300 °C under 2% CO_2/8%H_2/He flow.

To investigate the impact of the reduction pre-treatment, in-situ FTIR of unreduced CeO_2 and 10.2 at% Cu/CeO_2 were performed and the results are shown in Figure 6-9,d. It is obvious that on the reduced surface, signal of CO was detected at 2090 cm^{-1}, while the peak is negligible on the unreduced surface. This observation indicates that the reduction with H_2 before introducing the reaction gas mixture exposed more oxygen vacancy and CO_2 can be adsorbed on the vacancy site and reduced to CO. On the unreduced CeO_2 surfaces in which the oxygen vacancy concentration are lower than the reduced slabs, a new peak at 1572 cm^{-1} was identified which is assigned to another CO_2 adsorption configuration (1.3.1 type) carbonate. This carbonate species is also reported to be the adsorption configuration near oxygen vacancy site which may indicates that there are multiple kinds of oxygen vacancy site on the unreduced catalysts while the reduction procedure might reconstruct the surface vacancy and the CO_2 adsorption might also transformed

from 1.3.1 type to 1.21 type. A shoulder was also identify in Figure c) at 1194 cm^{-1} and can be considered as bidentate carbonate on the reduced surface, however this configuration can potentially adsorbed at Ce^{4+} site. [241] However, when Cu was introduced, after reduction, this 1.3.1 type carbonate was not detected and might suggest that the unidentate configuration is favored on Cu doped surfaces.

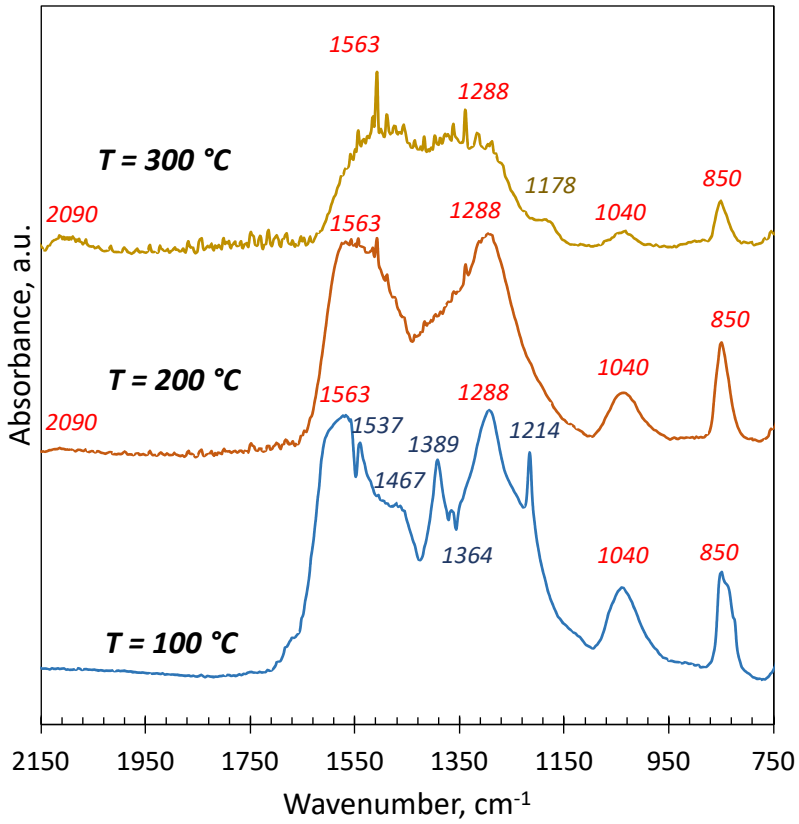

Figure 6-11 In-situ FTIR profiles of 10.2 % Cu/CeO_2 at 300 °C under 2% CO_2/8%H_2/He flow.

One possible reason of the absence of hydrogen carbonates is the hydrogenated carbonates are less stable compared to carbonates and desorbed at higher temperature, and another possible reason is that the hydrogen carbonates are highly active at reaction condition, while transformed

to products immediately before detected by the FTIR. The mechanism of the RWGS on the CeO_2 and Cu/CeO_2 is still under debating but some computational calculation indicated that hydrogen is involved in the reaction interacting with CO_2 but not only reduce the surface oxygen on Cu/CeO_2 surface. [138] Further investigation will be discussed in Chapter 7.

6.5 Discussion and concluding remarks

In the comprehensive study of Cu/CeO_2 catalysts, significant insights were gained into the catalyst's performance, stability, and underlying mechanisms during CO_2 reduction processes. The catalysts demonstrated remarkable CO_2 conversion and CO selectivity, particularly evident within a temperature ambit of 300-600°C. A striking observation was that all samples were 100% selective to CO, emphasizing the potential efficiency of these catalysts in CO_2 conversion processes. The performance of the catalysts was significantly influenced by Cu doping concentration. CeO_2 alone exhibited limited activity, but the introduction of Cu drastically improved CO_2 conversion, especially at concentrations of 10.2 at% and 26.54 at%, where the conversion rates approximated equilibrium values (60% at 600°C). Interestingly, there seems to be an optimal limit to Cu doping, beyond which no significant enhancements in activity were observed. This plateau suggests a balance between Cu incorporation and the catalyst's structural and functional integrity, confirming findings from XPS and XRD analyses.

Stability was another critical focus. Long-term stability tests, especially for the 1.4 at% Cu/CeO_2 catalyst, demonstrated minimal performance degradation over 110 hours, even when subjected to stepwise changes in GHSV and temperature elevation up to 800°C. TGA-FTIR analyses of the spent catalyst post-stability test revealed negligible carbon deposition, indicating the catalyst's high resistance to coking and sintering under the reaction conditions.

Investigating the reaction mechanism via in-situ FTIR highlighted the role of oxygen vacancies generated by Cu doping, facilitating CO_2 adsorption and activation. Both reduced and unreduced catalysts exhibited distinct behaviors, with the presence of Cu altering the adsorption dynamics and possibly the surface reaction pathways. The absence of hydrogen carbonates at higher temperatures suggests their transient nature in the reaction mechanism, potentially evolving rapidly into reaction intermediates or products.

The findings underscore the potential of Cu/CeO_2 catalysts in CO_2 reduction applications, particularly in achieving high CO selectivity, conversion rates, and stability. However, the results also point towards an optimal range of Cu doping for maximized performance, beyond which no additional benefits are apparent. The insights into the reaction mechanism, particularly the role of oxygen vacancies and the dynamic nature of surface adsorbates, provide valuable information for the future design of more efficient and robust catalysts for environmental applications. Continued research is essential, especially computational studies, to unravel deeper mechanistic details and optimize catalyst designs further.

Chapter 7 Density functional theory simulations of CO_2 reverse water gas shift on doped CeO_2 catalysts

Chapter 7 explores the intricate relationship between CO_2 adsorption energies and the concentration of transition metals doped onto CO_2 surfaces, offering valuable insights into catalyst design for CO_2 conversion. The introduction of Cu atoms significantly enhances CO_2 adsorption, and the investigations will extend to other transition metals, revealing varied adsorption behaviors for Fe, Co, and Ni. This chapter also underscores the pivotal role of transition metal doping in catalytic enhancement for CO_2 reduction on CeO_2 based catalysts surfaces, particularly Cu and Fe. Furthermore, near-linear Brønsted-Evans-Polanyi (BEP) relationship observed between adsorption energies, reaction activation energies of CO_2 direct reduction to CO, and oxygen vacancy formation energies further confirms the typical behavior observed for CO_2 dissociative reactions on heterogeneous catalysts.

7.1 CO_2 adsorption on doped CeO_2 catalysts

7.1.1 Construction of bulk CeO_2 unit cell and doped (111) CeO_2 surfaces

The optimized of bulk CeO_2 by GGA formalism has been shown to yield accurate results. The bulk lattices parameters of CeO_2 was optimized as 5.44 A, which is in good agreement with the reported simulation and experimental value of 5.41 A. [242, 243]

Since CeO_2(111) was reported to be the most energetically stable, [244, 245] stoichiometric surface and the corresponding surfaces with one oxygen vacancy were optimized and investigated. The adsorption energy of CO_2 was calculated on both reduced and stoichiometric surfaces. Stoichiometric and reduced CeO_2(111) surfaces are optimized with the top atomic layer relaxed and the bottom 2 layer fixed during optimization. Oxygen vacancy formation energies (E_{OV}) were

calculated as the removal of the first oxygen and the reduced surfaces shown in Figure 7-2 corresponding to 1 OV surfaces, and the calculated E_{OV} are listed in Table 7-1. It has been previously reported that oxygen vacancy formation is favored at the nearest neighbor (1NN) of the doping position and the oxygen vacancy was calculated based on the removal of the top layer oxygen by equation 3-26. [246, 247] The stoichiometric CeO_2(111) surface and surfaces with 1 oxygen vacancy is shown in Figure 7-2.

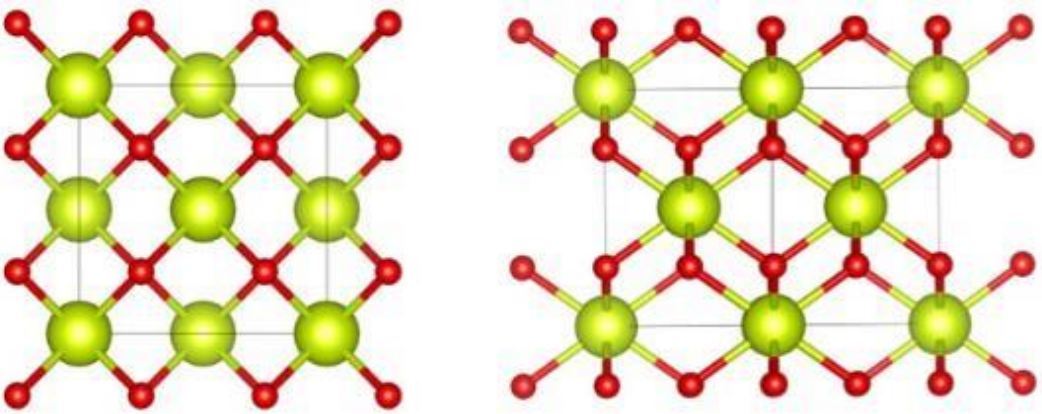

Figure 7-1 Top and side view of the optimized bulk structure of CeO_2 unit cell.

Metals that are widely used for CO_2 hydrogenation were selected as dopants. These were introduced by replacing Ce atom with the desired atoms before relaxation. Usually, there are three ways that the CeO_2 surface can be modified with the transition metals reported, [248], i.e., adsorption, insertion and substitution. Adsorption and insertion represent that additional dopant atoms are introduced to the surface or inside the lattice, while substitution means the cerium atoms being replaced by transition metal ions, which is a widely acceptable method to study doped CeO_2 catalysts at low dopant concentrations. Due to the lack of time and demanding computational cost, only replacement is considered in this study, while insertion and adsorption of the dopants are outside the scope of this study. The surfaces with one oxygen vacancy are shown in Figure 7-2

(Noted as M-CeO_{2-x}). Note that the configuration of some dopants and some facets only changes slightly after structure configuration and minor deformation around the doping atom was observed.

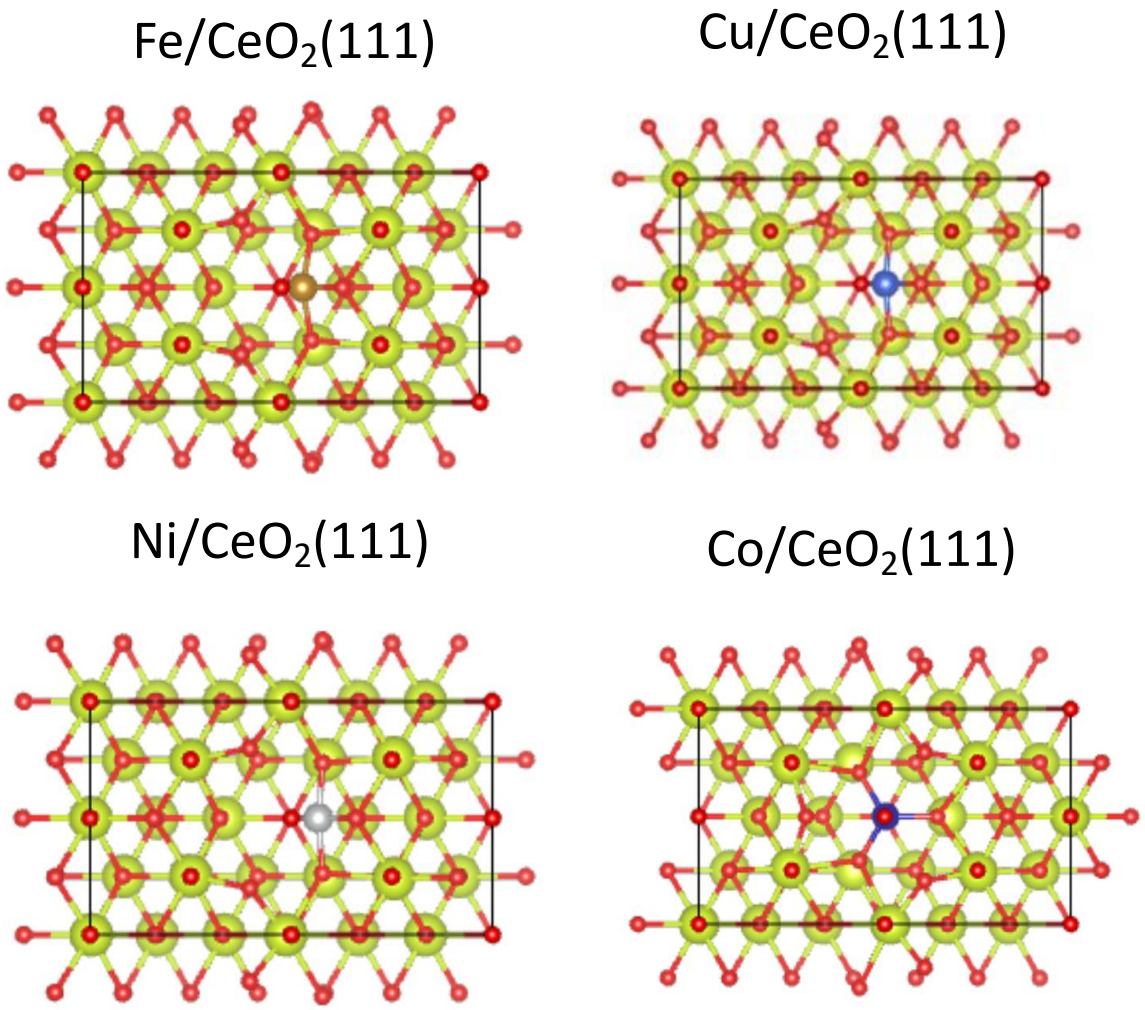

Figure 7-2 Optimized structure of M/CeO_{2-x}(111) surfaces.

7.1.2 CO_2 adsorption on doped (111) CeO_2 surfaces

i. CO_2 adsorption on Cu-doped CeO_2 surfaces

The adsorption of CO_2 on stoichiometric and reduced surfaces are investigated and the effect of loading of Cu on the top layer was studied. Figure 7-3 indicates the surfaces with 1, 2 or 3 top-layer Ce being replaced by Cu atoms (nCu/CeO_2, n=1,2,3) and the corresponding reduced surface

with CO_2 as adsorbates (nCu/CeO_{2-x}, n=1,2,3). The energies that are required to form the oxygen vacancy are listed in Table 7-1. The energy to form an OV on stoichiometric CeO_2 surface is 3.15 eV, which is a relatively high value compared to the Cu doped surface, while the energies required on nCu/CeO_{2-x}, n=1,2,3 surfaces are all negative values indicating that the formation of OV on the surface are all spontaneous. Notably, as indicated in Figure 7-4, the formation of OV is even more favorable when the loading of Cu increases and a near linear relationship was observed between the OV formation energy and Cu loading on the surface. This observation supports the state and the observation in Chapter 6 that the introduction of Cu into the lattice could enhance the reducibility of the surface and facilitate the removal of surface oxygen to form more OV sites, potentially improve the catalytic performance of the catalysts.

Table 7-1 Oxygen vacancy formation energies and the corresponding CO_2 adsorption energies on $M/CeO_{2-x}(111)$ surfaces.

surfaces	E_{OV}	E_{ads_CO2}
CeO_2	3.15	-0.71
$1Cu/CeO_{2-x}(111)$	-0.02	-0.88
$2Cu/CeO_{2-x}(111)$	-0.82	-1.37
$3Cu/CeO_{2-x}(111)$	-3.49	-1.01
$1Fe/CeO_{2-x}(111)$	2.24	-0.66
$2Fe/CeO_{2-x}(111)$	2.04	-1.11
$3\ Fe/CeO_{2-x}(111)$	1.49	-1.55
$1Co/CeO_{2-x}(111)$	0.84	-0.43
$1Ni/CeO_{2-x}(111)$	1.69	-0.55

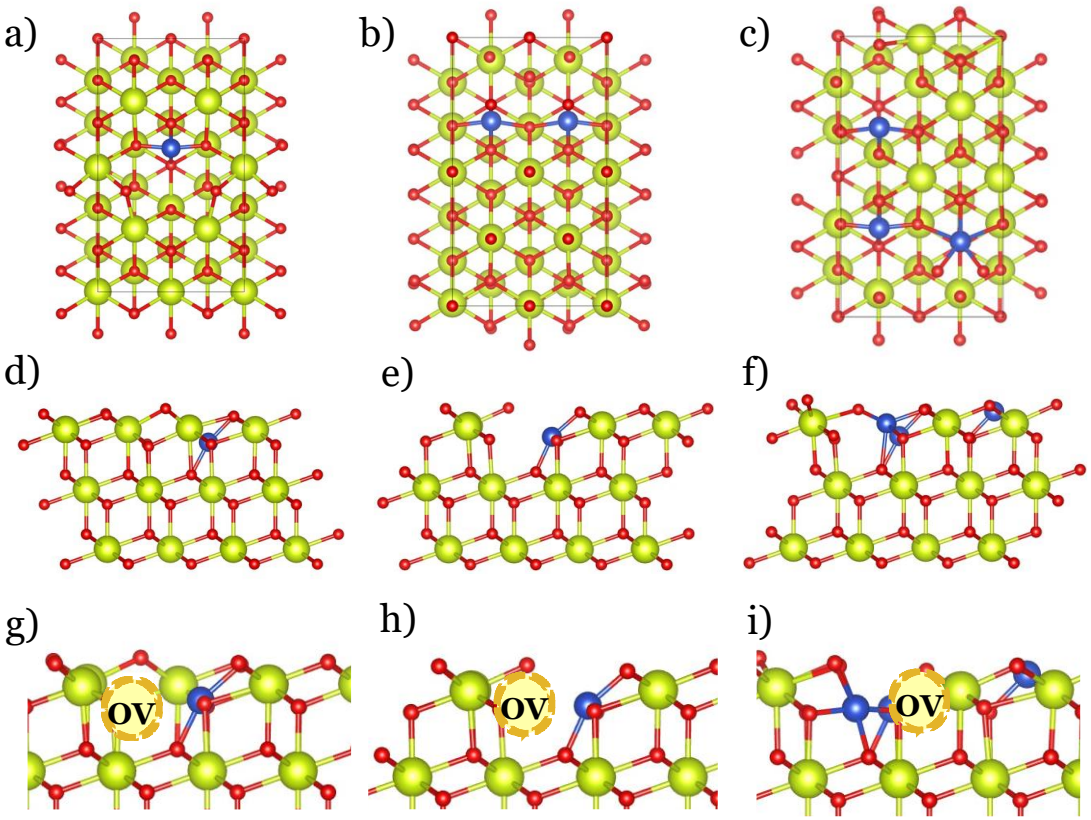

Figure 7-3 Optimized structure of $Cu/CeO_2(111)$ and $Cu/CeO_{2-x}(111)$ surfaces. a-c) Top view of the stoichiometric surfaces of different Cu loading and d-f) corresponding side view. g-i) Side view of the reduced surfaces and the oxygen vacancy position are indicated.

The adsorption energies of CO_2 are listed in Table 7-1 and the configurations of adsorbed CO_2 on the surface are shown in Figure 7-5. As depicted in Figure 7-5a, it is clear that the CO_2 molecule undergoes deformation that switched from a linear structure to a banded configuration adsorbed as monodentate carbonate or bidentate carbonate species. The stable adsorption configuration on stoichiometric Cu/CeO_2 surface all exhibits monodentate carbonate configuration, as illustrated in Figure 7-5. In $1Cu/CeO_2$ (Figure 7-5a), the bond length of the intramolecular C-O bond expanded to 1.275 Å from 1.16 Å, which also indicates the occurrence of chemisorption on the surface. The C-O bond length between the carbon in CeO_2 and the surface O in $1Cu/CeO_2$ is

1.31 Å, which is at the same level of partial double bond suggesting the charge transfer between the adsorbate and surface O indicating strong interfacial bonds. Compared to the 1 Cu doped surface, the length of intramolecular C-O bond, 1.274 Å, in $2Cu/CeO_2$ is almost the same as 1Cu doped surface while the C-O_{surf} is 1.37 Å. This indicates that CO_2 molecule is activate on those sites.

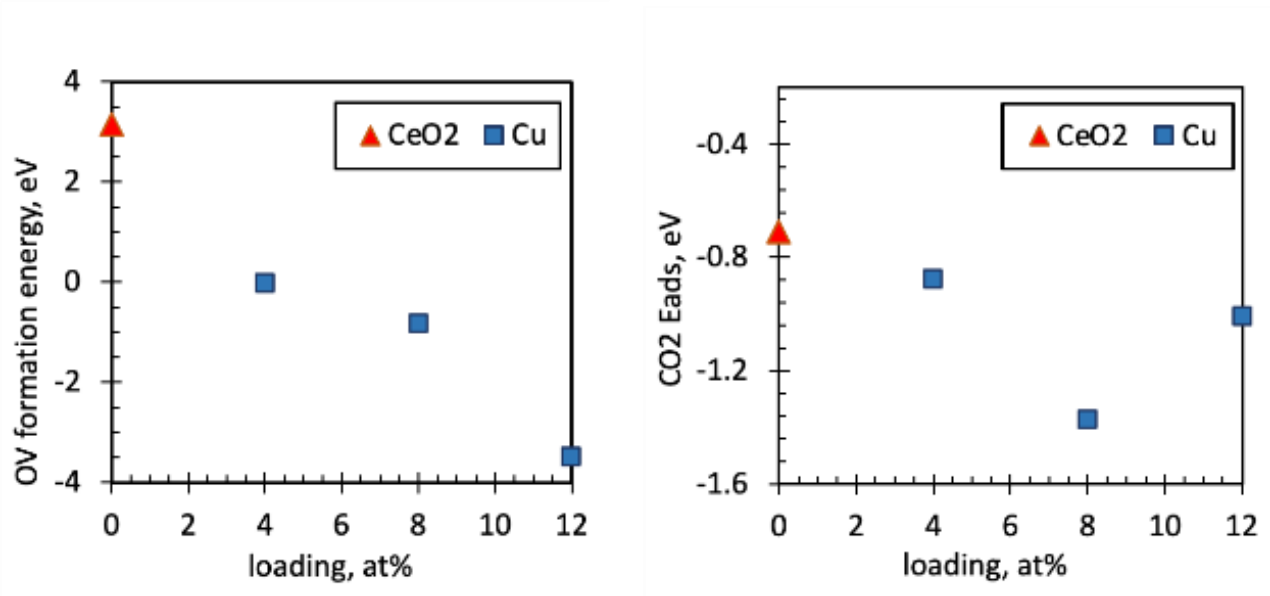

Figure 7-4 OV formation energy (left) and CO_2 adsorption energy (right) as a function of Cu loading.

The adsorption energies of the stable CO_2 adsorption configuration as a function of Cu loading on CeO_2 are shown in Figure 7-4a). Compared to the pure CeO_2 without Cu doping, the adsorption energy of CO_2 decreases with the introduction of Cu into the top surface and the highest CO_2 adsorption energy was observed on the $2Cu/CeO_{2-x}$(111) surface with a binding energy of -1.37 eV while the binding energy of CO_2 on pure CeO_2(111) surface is -0.71 eV, which indicate the presence of Cu enhances the interaction and electron transfer of carbon and the surface oxygen.

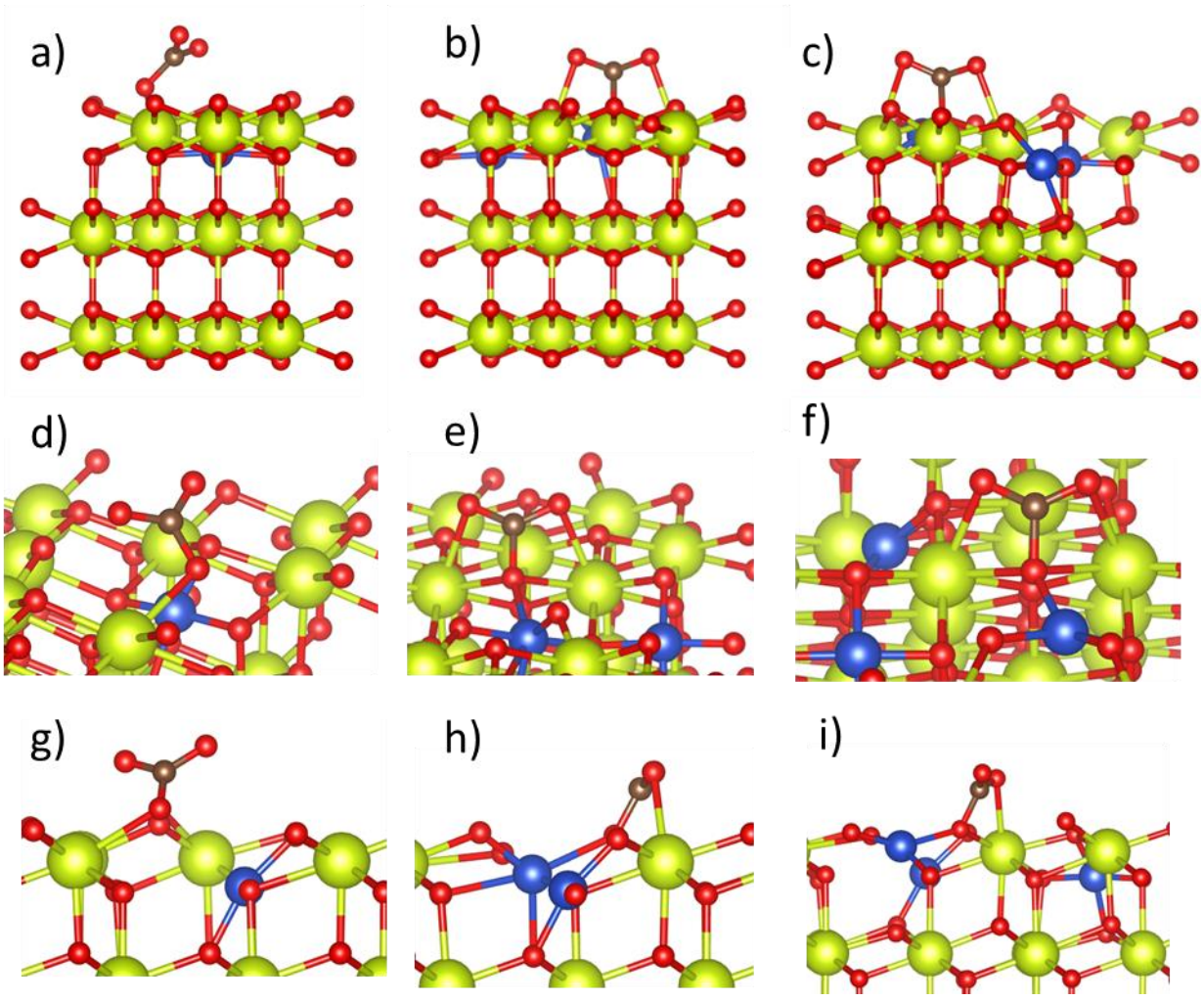

Figure 7-5 Optimized structure of CO_2 adsorbed on $Cu/CeO_{2-x}(111)$ surfaces. a-c) Side view of the surfaces of 4.2, 8.3, and 12.5 at% (1,2 and 3)Cu/(Cu+Ce) loading and d-f) corresponding top view. g-i) Side view of the zoomed in CO_2 adsorption configuration.

Note that the stable configurations of the CO_2 adsorbed on the $2Cu/CeO_{2-x}(111)$ and $3Cu/CeO_{2-x}(111)$ agree with the in-situ FTIR results discussed in Chapter 6, Figure 6-9. Peaks centred at 1508, 1369, 1298 cm^{-1} identified from in-situ FTIR are assigned to C-O bond in the carbonate adsorbed on the surface [241], in which the carbonate is bound with the three oxygens. From the DFT calculations, the monodentate carbonate is the most favorable structure which the

surface O in carbonate coordinated by two surface Ce and each of the other two O are coordinated by one surface Ce near the surface O. However, the posture of the carbonate is not the 1.21 type carbonate that was reported on CeO_{2-x}(111) surface but the 1.2.1 type reported in [241], which may due to the introduction of the Cu atoms to the lattice. Since the neighborhood Ce is replaced by one or multiple Cu atoms, it is unfavorable for the formation of a O-$metal_{surf}$ bond thus the 1.2.1 type carbonate is more stable, where each of the two O of the CO_2 are attached to one Ce that are the first and second nearest Ce from the C, respectively. On the other hand, in the case of 1.21 type carbonate, one of the O in CO_2 is attached to the third nearest Ce whereas the other O is attached to the first nearest Ce.

ii. CO_2 adsorption on Fe/CeO_2 surfaces

Expanding the scope beyond Cu, CO_2 adsorption on other transition metals, namely Fe, Co, and Ni, was also examined to glean insights into CO_2 activation on reduced surfaces. The attention is first drawn to Figure 7-6, showcasing CO_2 adsorption configurations on nFe/CeO_{2-x}(111) surfaces, with corresponding binding and OV formation energies detailed in Table 7-1. Despite requiring higher energy for surface vacancy formation compared to nCu/CeO_{2-x}(111), nFe/CeO_{2-x}(111) surfaces still register lower than pure CeO_{2-x}(111). A notable observation surfaces with increased Fe doping; the formation energy diminishes to 1.49 eV for 3Fe/CeO_{2-x}(111), an indication that Fe atoms might be activating the 1NN surface oxygen, weakening the O-Ce bond, and consequently lowering the OV formation energy thus promoting more active sites for the CO_2 reduction to CO.

CO_2 adsorption configurations on nFe/CeO_{2-x}(111) show different behavior compared with nCu/CeO_{2-x}(111). The stable structure of CO_2 on 1Fe/CeO_{2-x}(111) is the 1.2.1 type carbonate at

the oxygen 1NN from the Fe atom. However, on $2Fe/CeO_{2-x}(111)$, the most stable configuration is carboxylate, in which the carbon directly attached to the surface Fe, and the two oxygen pointing to the surface vacancy. Carboxylate was reported to be weak adsorption on CeO_2 surfaces [249, 250], and the adsorption of carboxylate on $nCu/CeO_{2-x}(111)$ surfaces are weaken than carbonates from the investigation in section 7.1.2 A more stable configuration was identified on $3Fe/CeO_{2-x}(111)$, which is a "flat-lying" 1.2.1 type carbonate but almost parallel to the slab. Flat-lying carbonates was reported on 100 surface as tridentate carbonate [251] but in this case, the carbonate remained as bidentate carbonate without attaching to the third surface metal.

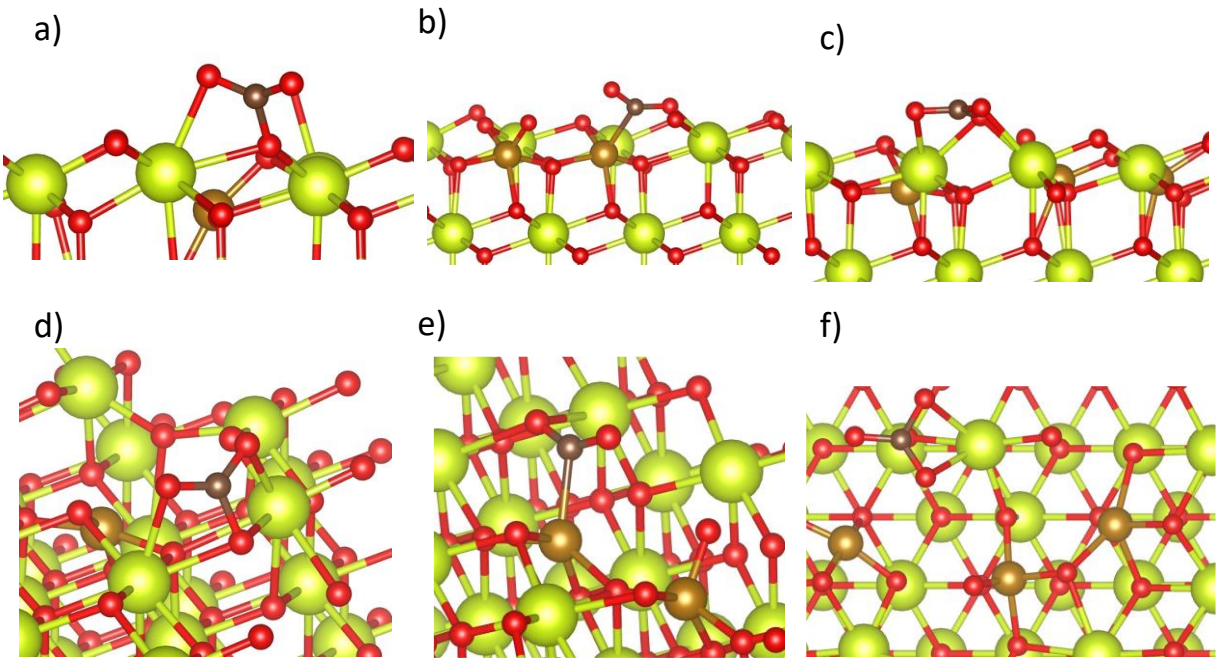

Figure 7-6 Optimized structure of CO_2 adsorbed on $nFe/CeO_{2-x}(111)$ surfaces. a-c) Side view of the surfaces of 4.2, 8.3, and 12.5 at% (1,2 and 3) Fe/(Fe+Ce) loading and d-f) corresponding top view.

iii. CO_2 adsorption on Co and Ni surfaces

Transitioning to Co and Ni, Figure 7-7 reveals the optimized structures of CO_2 adsorbed on $1Co/CeO_{2-x}(111)$ and $1Ni/CeO_{2-x}(111)$ alongside the OV formation energies. These surfaces show that the formation of surface OV is not spontaneous, yet the energy required is comparatively lower than on $1Fe/CeO_{2-x}(111)$. Notably, CO_2 maintains its linear molecule structure on both surfaces, albeit with a slight bending observed in the C=O=C bond, measured at 178.79° (Figure 7-7a,c) and 178.15° (Figure 7-7b,d) for $1Co/CeO_{2-x}(111)$ and $1Ni/CeO_{2-x}(111)$, respectively. This deformation, along with the recorded adsorption energies of -0.43 eV and -0.55 eV, indicates a chemisorption of CO_2. Yet, it is evident that CO_2 experiences more substantial activation on $1Cu/CeO_{2-x}(111)$ and $nFe/CeO_{2-x}(111)$ surfaces, as inferred from the carbonate or carboxylate configuration and the larger binding energy of CO_2 on these surfaces compared to $1Co/CeO_{2-x}(111)$ and $1Ni/CeO_{2-x}(111)$.

In light of these findings, it becomes apparent that while Cu and Fe-doped CeO_2 surfaces demonstrate enhanced CO_2 adsorption capabilities, there's a nuanced interplay between the type of transition metal used, the concentration, and the resulting CO_2 adsorption energy and configuration. However, a pivotal aspect that warrants further exploration is the activity of the surfaces. Higher adsorption energy, while indicative of strong binding, also poses potential challenges for desorption in certain catalytic mechanisms. Therefore, subsequent studies should endeavor to unravel this aspect, since higher adsorption energy also exacerbates the difficulty of desorption in certain mechanisms.

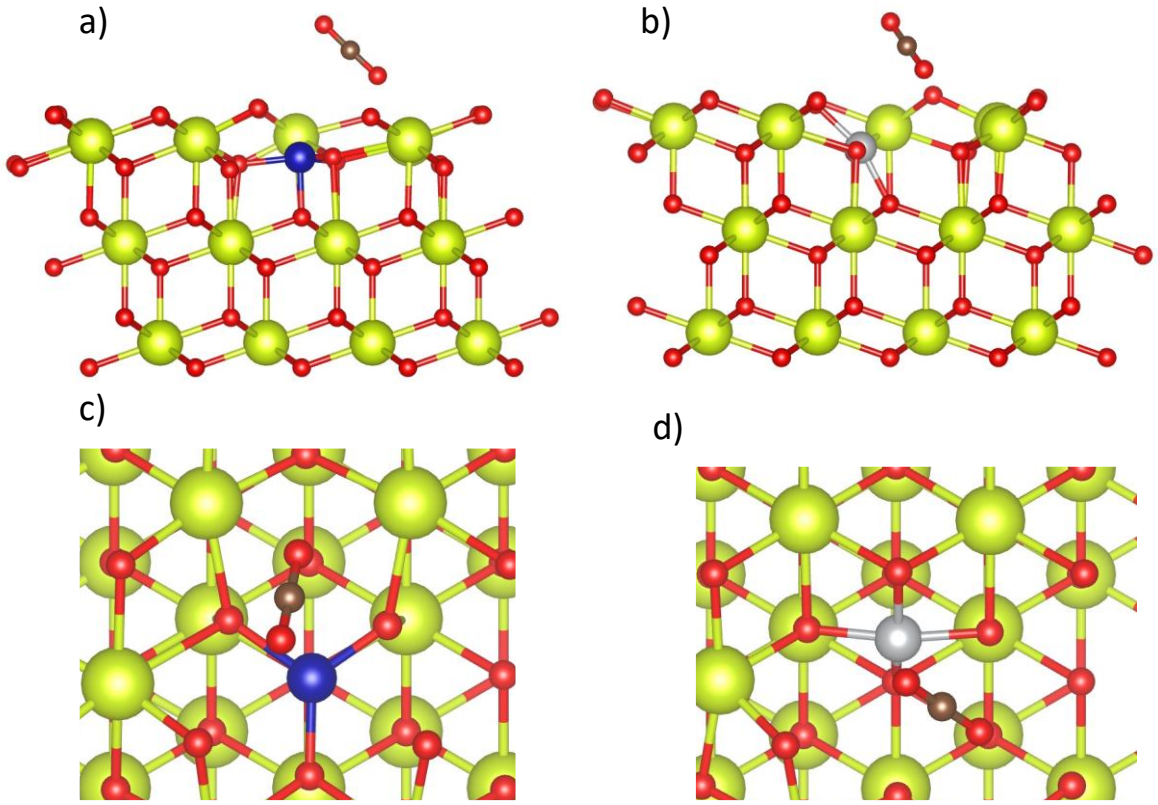

Figure 7-7 Optimized structure of CO_2 adsorbed on $1Co/CeO_{2-x}(111)$ surfaces (a,c), and $1Ni/CeO_{2-x}(111)$ surfaces (b,d).

7.2 DFT calculations of reverse water gas shift reaction on doped CeO_2 catalysts

In this section, the behavior of CO_2 reduction on $M/CeO_{2-x}(111)$ calculated from DFT analysis will be discussed and the results compared to laboratory experiments conducted in this research. To keep the consistency between the samples, all of the samples are prepared by co-precipitation method but not RME method that was mentioned in the previous chapters. As discussed in Chapter 2, RME method can lead to smaller particles and higher surface area, which will promote the catalytic performance, at the expense of high cost in terms of catalyst preparation period and chemical usage. Co-precipitation may result in larger particles and lower conversion

but is a widely reported and conventional synthesis method, which has been implemented for the preparation of CeO_2-based catalysts. [252-254]

7.2.1 CO_2 direct reduction to CO on metal doped CeO_2 surface

It was widely reported that the CO_2 reduction on the CeO_2 based catalysts pathway might be the direct reduction of the adsorbed CO_2 molecule on the surface OV, so that the catalytic performance is highly related to the surface vacancy. CO_2 reduction on the reduced $M/CeO_{2-x}(111)$ surfaces was studied in this section. It should be emphasized that the transition states calculated in this section are with the premises that the reaction energy, i.e., the free energy difference between final state (FS) and initial state (IS), should be lower than 2.0 eV for further activation energy calculations, which is within the interested domain. For elemental reactions that the FS free energy is higher that IS, reaction energy is the minimum energy required by the reaction, which reflects the ease with which the reaction may happen on those sites. Pairs of IS and FS with reaction energies higher than this threshold value (2 eV) will be excluded from the investigation. However, discussing these less important pairs remains essential for gaining insights into the impact of reaction energies, adsorption energies, and OV formation energies to the activation energy of the reaction, and establish the BEP relationship between reaction energy and activation energy.

Figure 7-8 illustrates the energy profile of CO_2 hydrogenation to CO with detailed energy value listed in Table 7-2. The CO_2 molecule first adsorbed on the surface, near the 1NN OV site (Figure 7-6), and the corresponding adsorption energies are reported in Table 7-1. From the insets of Figure 7-8, it can be seen that the final state of CO_2 reduction to CO revealing two types of stable configuration: one where the CO from dissociated CeO_2 is adsorbed above the Ce ion and another where it is adsorbed on the Fe ion. For $1Fe/CeO_{2-x}(111)$ surface, the adsorption of the CO on the 1NN Ce ion is the favored site with a CO_2 dissociative adsorption energy of 1.57 eV, but

on 2Fe/CeO_{2-x}(111), adsorption of CO on top of Fe at 1NN is the most stable structure, while the adsorption energy (1.76 eV) is comparable of that on 1Fe/CeO_{2-x}(111). The adsorption of CO on 3Fe/CeO_{2-x}(111) where 3 surface Ce ions were replaced by Fe ions is not stable when compared to the lower loading surface; this indicates that the large deformation of the surface is unfavourable for the adsorption of CO.

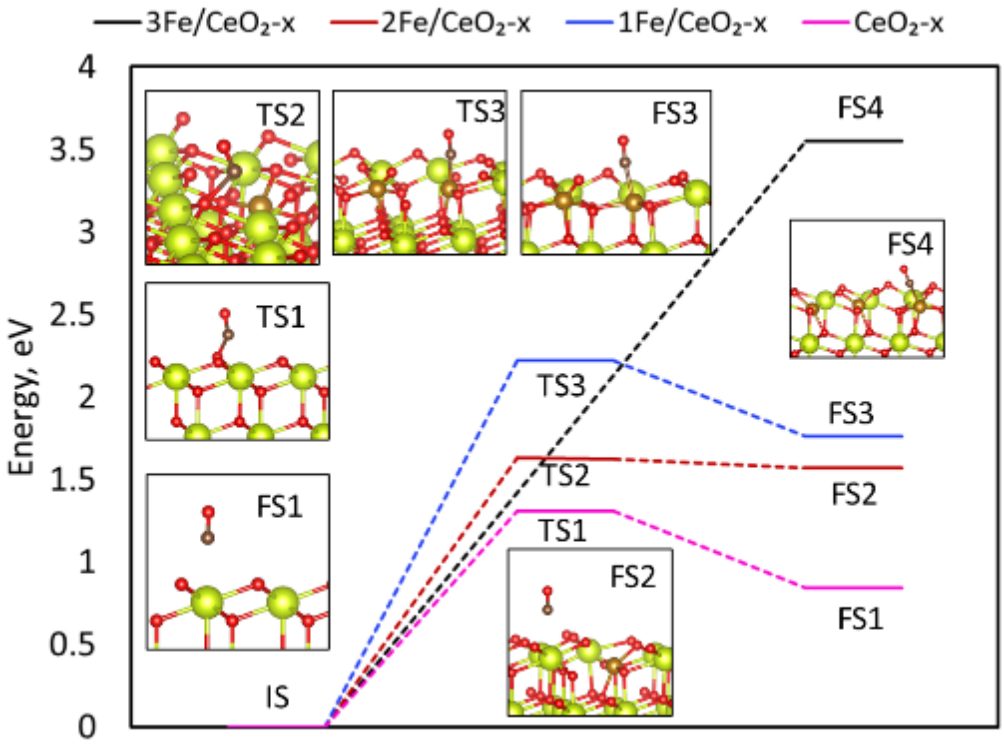

Figure 7-8 Energy profile of CO_2 reduction to CO on Fe/CeO_{2-x}(111) surfaces. Transition state energies are with reference to the energies of the initial state (IS) of adsorbed CO_2 on the surfaces. The insets represent the side views of transition states (TS) and final states (FS).

Table 7-2 Adsorption energies and transition state energies of CO_2 direction reduction to CO.

	E_{CO2_ads}	$E_{CO\_O\_ads}$	E_{rxn}	E_{act}
		M/CeO_{2-x}(111)		
CeO_{2-x}(111)	-0.48	0.37	0.84	1.31
1Cu/CeO_{2-x}(111)	-0.88	3.55	4.42	
2Cu/CeO_{2-x}(111)	-1.37	4.20	5.57	
3Cu/CeO_{2-x}(111)	-0.71	2.82	3.52	
1Fe/CeO_{2-x}(111)	-0.48	1.28	1.76	2.22
2Fe/CeO_{2-x}(111)	-0.22	1.35	1.57	1.63
3Fe/CeO_{2-x}(111)	-0.78	2.77	3.55	
3Fe/CeO_{2-x}(111)	-0.73	1.40	2.13	
1Ni/CeO_{2-x}(111)	-0.51	1.80	2.31	2.69
1Co/CeO_{2-x}(111)	-0.42	1.68	2.10	
		M/CeO_{2-x}(110)		
CeO_{2-x}(110)	-1.41	0.81	2.22	2.76
1Fe/CeO_{2-x}(110)	-0.45	2.21	2.67	
1Fe/CeO_{2-x}(110)	-0.40	1.71	2.11	3.50
1Cu/CeO_{2-x}(110)	-0.42	3.38	3.80	
1Cu/CeO_{2-x}(110)	-0.40	2.74	3.14	
1Co/CeO_{2-x}(110)	-0.35	2.67	3.02	
1Ni/CeO_{2-x}(110)	-0.51	3.23	3.74	

The activation energy of CO_2 dissociation on CeO_{2-x}(111) was calculated as 1.31 eV by comparing the transition state energy with the initial state energy, [255] but with the presence of Fe as dopant, the Fe/CeO_{2-x}(111) did not exhibit kinetic advantages in terms of activation energy (E_{act}), as shown in Table 7-2. The activation energy of CO_2 reduction were 1.63 and 2.22 eV for 1Fe/CeO_{2-x}(111) and 2Fe/CeO_{2-x}(111), respectively, which are both higher than pure CeO_2. As indicated in Table 7-2, the 2Fe/CeO_{2-x}(111) showed superior performance (activation energy of 1.63 eV) than 1Fe/CeO_{2-x}(111) (activation energy of 2.22 eV) with a 0.59 eV lower activation energy. This observation agree with the experimental results that have shown that Fe/CeO_2

catalysts with higher loading at 5.7% exhibits higher conversion of CO_2 than that of 1.7% in the test temperature range.

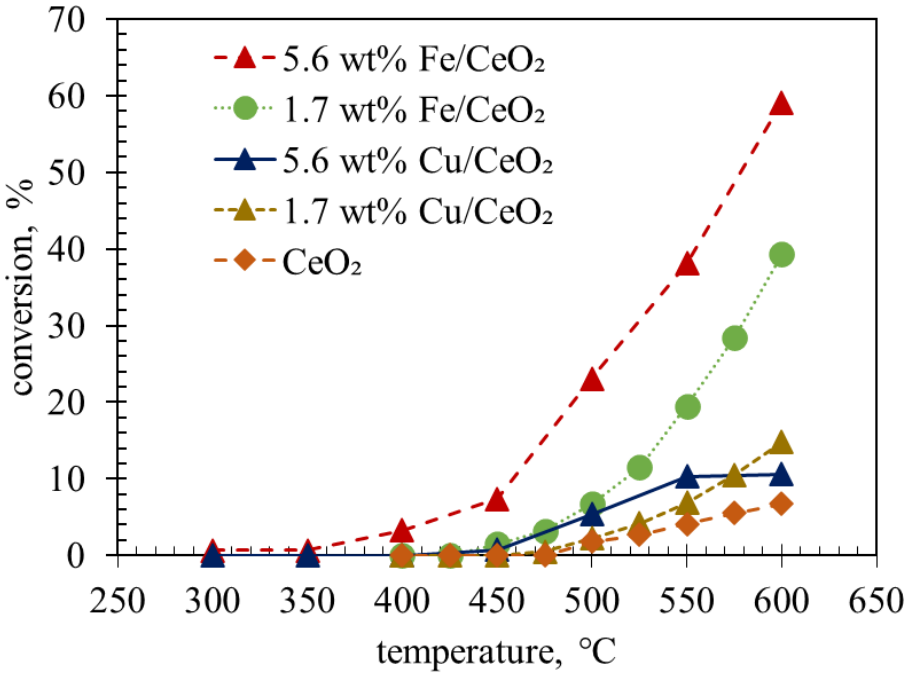

Figure 7-9 conversion of CO_2 as a function of temperature tested in laboratory experiments. Reaction condition: P = 3 bar, H_2/CO_2 = 3 (feed), GHSV = 60,000 mL/(g h) T = 300-600 °C, reduction in 75 ml/min H_2 are performed period to reaction.

However, laboratory experiments indicates that the Fe dopant promotes the conversion of CO_2 indeed, even though nFe/CeO_{2-x}(111) have lower activation energy than CeO_{2-x}(111). Figure 7-9 indicates the conversion of CO_2 to CO as a function of temperature on nFe/CeO_{2-x}(111). During the reaction, CO was the only product observed in the outlet stream and the selectivity towards CO was 100%, while CO_2 hydrogenation on bulk Fe catalysts usually generate methane and even hydrocarbons. This finding is consistent to the previous observation of pure CeO_2 in the lab, which suggests that the introduction of Fe will not modify the superior selectivity of CeO_2 to the CO.

Compared to the pure CeO_2 without doping in Figure 7-9, Fe/CeO_2 showed higher conversion at all temperatures, 5 wt% Fe/CeO_2 with larger Fe loading exhibited higher conversion of CO_2 compared to 1% Fe/CeO_2 as well, which agree with the simulation results.

7.2.2 Correlations between adsorption energies and reaction activation energies

To understand the relationship between adsorption energy of the species involved in the reaction, the activation energy of the CO_2 direct reduction reaction to CO was calculated for the pairs of IS and FS having energy difference lower than 2 eV. The correlation between electron energies (adsorption energy of CO, CO_2 molecule and dissociated CO_2) and the activation energy of CO_2 dissociation on the relevant configurations (discussed in section 7.1) is shown in Figure 7-10 a). Note that the dissociative adsorption energy of CO_2 ($E_{CO\_O\_ads}$) is the final state of the CO_2 reduction and the configurations are shown in the inset denoted as FS in Figure 7-8. As shown in Figure 7-10a, there is a near linear relationship between activation energy (E_{act}) and the reaction energy (E_{rxn}), which is a typical Brønsted-Evans-Polanyi (BEP) behaviour for dissociative reactions on heterogeneous catalysts. [159, 256, 257]

To further investigate the scaling relationship between activation energy and adsorption energies, the relationships among the activation energy of reaction (denoted as E_{act}), dissociative adsorption energy of CO_2 after reduction ($E_{CO\_O\_ads}$), adsorption energy of CO_2 as carbonates or carboxylates (E_{CO2_ads}) and adsorption energy of CO (E_{CO_ads}) that fall in the interested domain were plotted and indicated in Figure 7-10 b, c and d, respectively. $E_{CO\_O\_ads}$ exhibits a near linear relationship with activation energy, however the CO_2 adsorption energy and the CO adsorption energy did not show any visible correlation with the activation energy. This observation emphasized that the adsorption stability of dissociated CO_2 on the surface is the key point of the performance in terms of transition state energy since the linear correlation shown in Figure 7-10b

indicates that there is a positive relationship. A stable CO_2 dissociative adsorption configuration on the surface leads to lower activation energy, which is kinetic favoured by the reaction. This dissociative adsorption energy of CO_2 could be divided into two parts for further discussion, which are the binding energy of O on the OV site, and the binding energy of CO at the ion site. From Figure 7-10 d), the E_{CO_ads} did not show obvious relationship with activation energy which brings the focus of the study to the investigation to the properties of the OV sites on the surfaces.

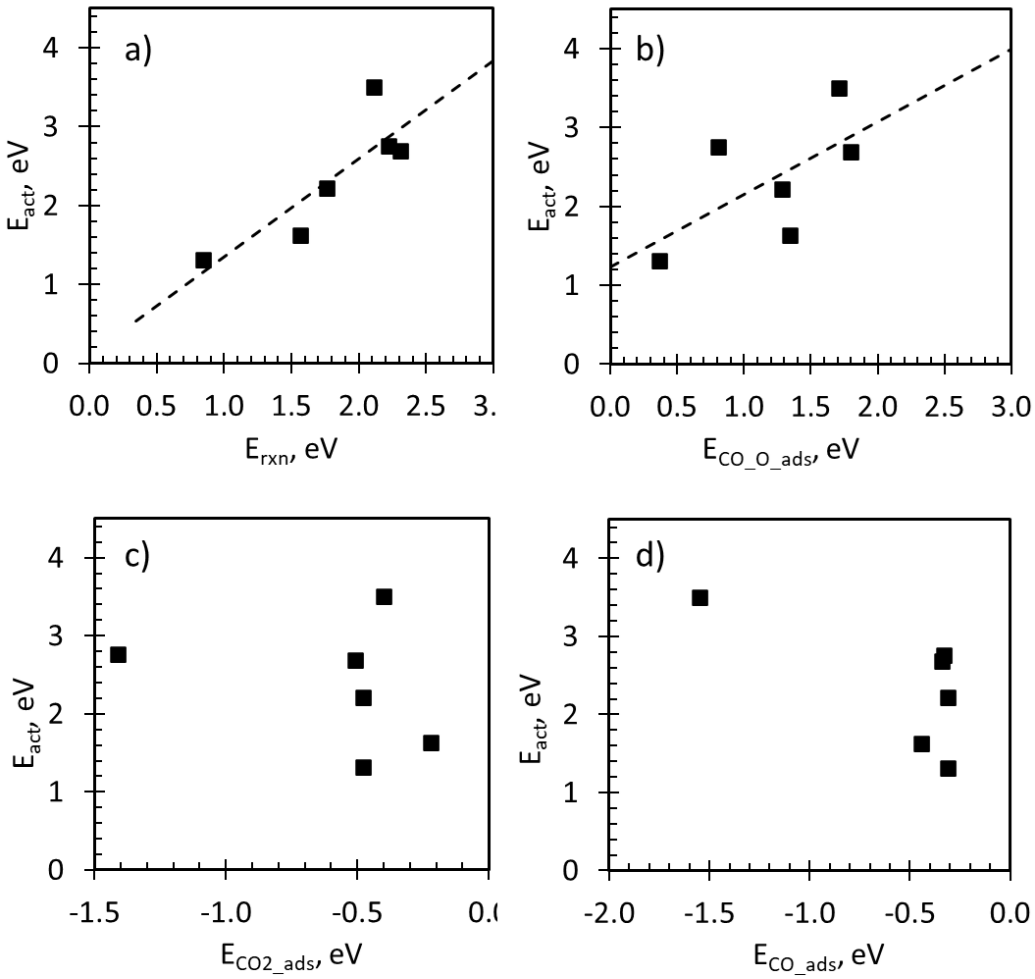

Figure 7-10 BEP and scaling relationship between activation energy of CO_2 dissociation and a) reaction energy, b) CO_2 dissociative adsorption energy, c) CO_2 adsorption energy, d) CO adsorption energy.

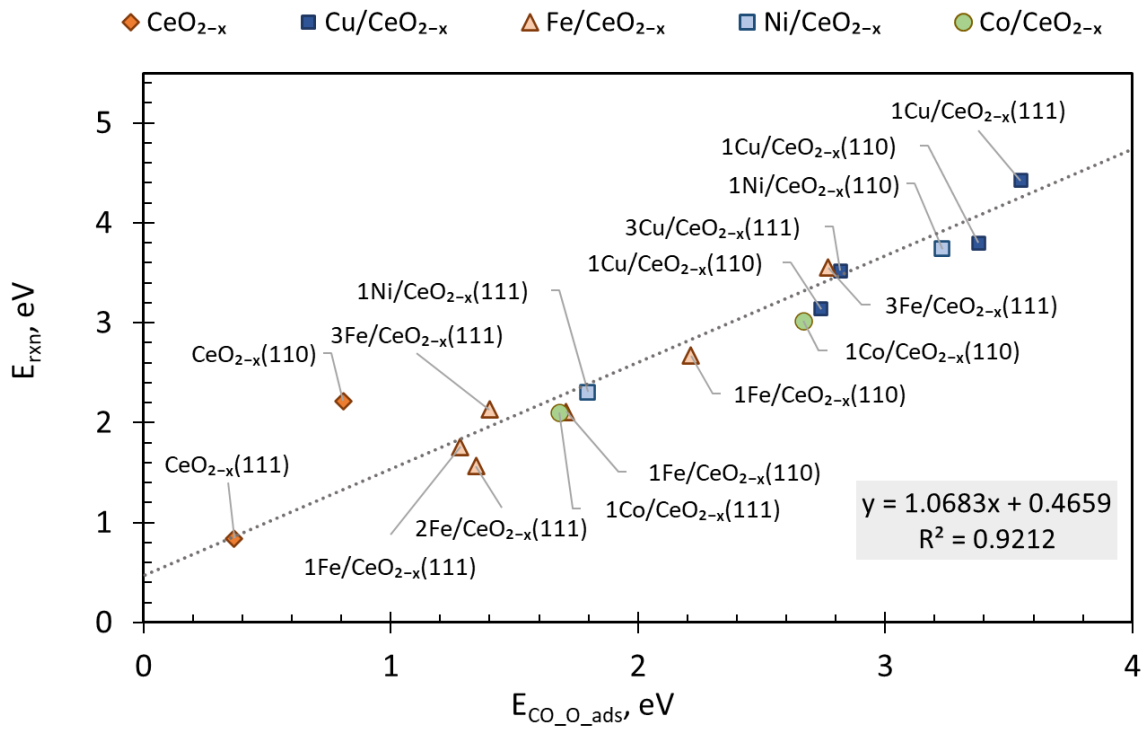

Figure 7-11 Reaction energy (E_{rxn}) as a function of CO_2 dissociative adsorption energy ($E_{CO\_O\_ads}$) on metal doped CeO_{2-x} slabs.

After establishing the BEP relationship between activation energy and reaction energy, the E_{rxn} can be an informative descriptor for the surfaces, which is especially useful to filtering out the pairs of IS and FS that are out of the interest domain and qualitatively evaluate the surfaces. As indicated in Figure 7-11, a linear relationship between E_{rxn} and $E_{CO\_O\_ads}$ was observed with a coefficient of determination R^2 of 0.92 calculated by eq (7-1), which additionally underlines that $E_{CO\_O\_ads}$ is highly related to the reaction energy and activation energy. However, pure CeO_{2-x} surfaces shows the lowest $E_{CO\_O\_ads}$ and relatively lower activation energy, but as illustrated in Figure 7-9, laboratory results indicated pure CeO_{2-x} did not exhibit advances performance, i.e., higher conversion than doped CeO_{2-x}, thus further investigations and discussions are crucial for

understanding the properties and performance. The next section will provide a more elaborate discussion on this topic.

$$R^2 = 1 - \frac{sum\ squared\ regression}{total\ variation} \qquad \text{eq. 7-1}$$

7.2.3 Correlations between oxygen vacancy formation energies and reaction energies

Oxygen vacancies on the surface have been intensively investigated; various dopants are able to lower the energy required to remove the 1NN oxygen (E_{OV}) thus facilitating the formation of surface vacancy. [18, 19, 258] The presence of the oxygen vacancy also provide active sites for the reduction of CO_2 adsorbed near the OV and accept the dissociated O from C=O bond. [258] To study the effect of dopants on the energy of OV formation, $E_{CO\_O\_ads}$ and E_{rxn} was plotted as a function of the E_{OV} and are shown in Figure 7-12 and Figure 7-13. As the E_{OV} increases, i.e., more difficult for the OV site to generate, the dissociative adsorption energy of CO_2 tends to be more stable on the surfaces, which according to the linear correlation defined in Figure 7-11, will correspond to a lower reaction energy. However, pure CeO_2 that have high E_{OV} and low E_{rxn} are approved to be less active than other metal doped surface, suggesting the formation of surface oxygen vacancy is essential to the activity of the surfaces. However, Figure 7-13 shows the relationship between E_{OV} and E_{rxn}, revealing that when the reaction energy is low, which is favoured by the reaction, the energy required to form OV, i.e., the active site where reaction takes place, is more difficult. The process of OV formation followed by CO_2 dissociation that are important to the activity can be expressed as the following formula:

$$Slab \overset{H_2}{\Leftrightarrow} Slab^* + O^* \qquad 7\text{-}2$$

$$Slab^* + CO_2(g) \Leftrightarrow Slab^* + {CO_2}^* \qquad 7\text{-}3$$

$$Slab^* + {CO_2}^* \Leftrightarrow Slab + CO^* \qquad 7\text{-}4$$

where Slab, Slab*, O*, CO_2(g), CO_2*and CO* represent the stoichiometric slab, slab with 1 OV, removed O by reductant, gas phase CO_2 molecule, adsorbed CO_2 as carbonates or carboxylates, and CO adsorbed at 1NN metal site, respectively. The adsorption energy of CO_2 molecule on the surface does not show a clear relationship with the activation energy as indicated in Figure 7-10c. The reduction of the catalyst surfaces (eq 7-3) and the reduction of CO_2 (eq 7-4) are the two critical steps that affect the total performance instead of the adsorption of CO_2 on the reduced surfaces (eq 7-2), thus the descriptor of both two important steps, OV formation energy (E_{OV}) and CO_2 dissociative adsorption energy ($E_{CO\_O\_ads}$) are important for determine the activity of the materials. Based on the experimental and computational results, the next step in performance benchmarking involves determination of the optimal range of values or region for E_{OV} and $E_{CO\_O\_ads}$.

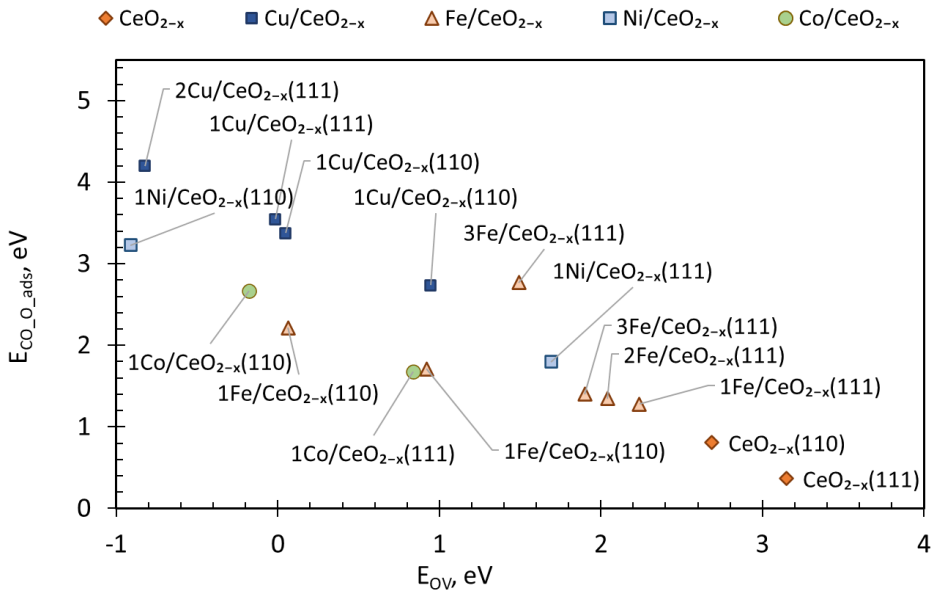

Figure 7-12 Adsorption energy of dissociative CO_2 ($E_{CO\_O\_ads}$) as a function of oxygen vacancy formation energy (E_{OV}).

The ideal OV site should not only require moderate energy for the surface to be reduced but also should provide strong interaction with the surface metal such that it promotes C-O bond scission reaction. Strengthening bridge OV site oxygen-metal allows more electrons to contribute to the formation of the bond which may switch the bond from ionic to covalent. Since more electrons have been withdraw from the metal to O, after O is transferred from carbonaceous species to the OV site, CO is more likely the be adsorbed on the metal cation site near the OV, which corresponds to lower energy and more stable configuration.

From Figure 7-9, the highest conversion at all temperatures were obtained from laboratory experiments for Fe/CeO_2 catalysts, which correspond to the $nFe/CeO_{2-x}(111)$ catalysts; the computational calculations revealed that the most kinetic favored $nFe/CeO_{2-x}(111)$ surfaces for CO_2 reduction are $1Fe/CeO_{2-x}(111)$ and $2Fe/CeO_{2-x}(111)$, with E_{OV} of 2.24 and 2.04 eV, $E_{CO\_O\_ads}$ of 1.28 and 1.35eV, and E_{act} of 2.22 and 1.63 eV, respectively. The activation energies and reaction energy on $1Fe/CeO_{2-x}(111)$ and $2Fe/CeO_{2-x}(111)$ calculated from DFT method also are the lowest numbers among the materials investigated in this study. Both the experimental results and the DFT calculations indicate that the Fe/CeO_2 catalysts exhibit favorable properties for CO_2 reduction. The DFT calculations provide detailed numerical values that support the experimental findings by showing that these catalyst surfaces have lower activation energies and reaction energies compared to other materials studied. Therefore, the DFT results align with and provide a theoretical basis for the experimental observations, suggesting that the Fe/CeO_2 catalysts are indeed promising for CO_2 reduction. A preliminary conclusion can be deduced that the desired E_{OV} for CO_2 scission is around 2.0-2.5 eV and the $E_{CO\_O\_ads}$ range where the materials have great potential lands in 1.0-1.5 eV. This is concluded form the values of Fe/CeO_2 that exhibits the highest conversion and lowest

activation energy calculated from DFT. These descriptors can guide the experimental reach of promising catalysts, which can also be the goal of high-throughput screening using Machine Learning technics.

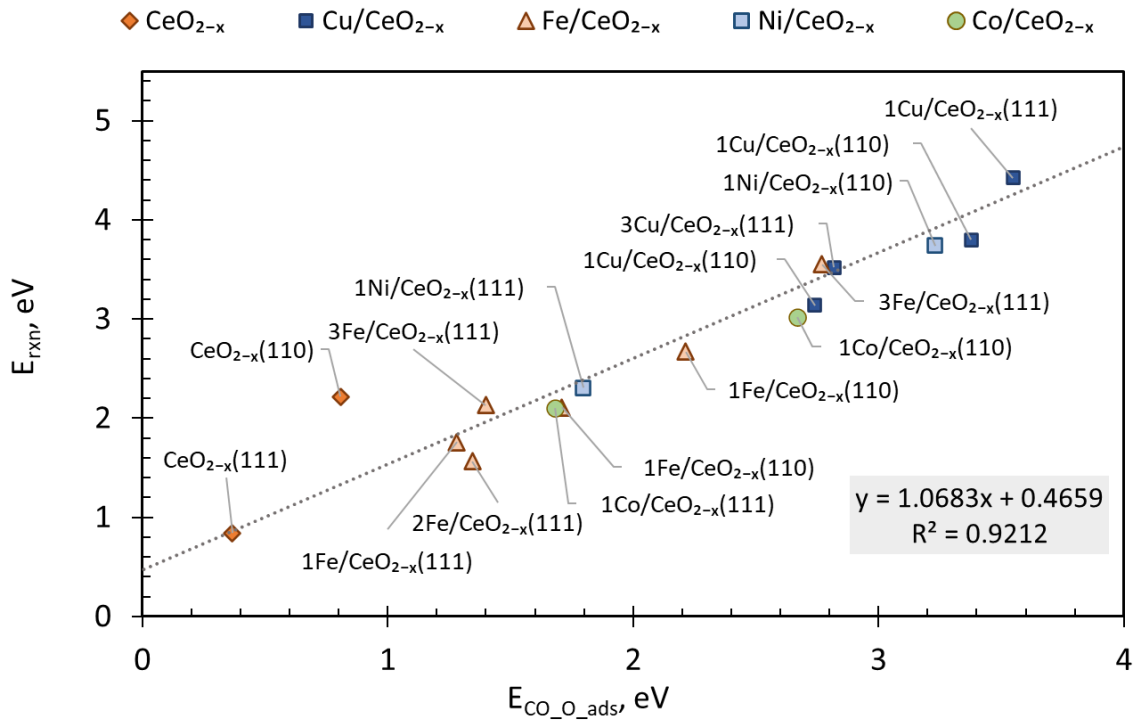

Figure 7-13 Reaction energy (E_{rxn}) as a function of oxygen vacancy formation energy (E_{OV}).

7.3 Discussion and concluding remarks

In summary, this chapter elucidates the intricate relationship between CO_2 adsorption energies and the concentration of various transition metals doped on CeO_2 surfaces. The introduction of Cu atoms notably enhances CO_2 adsorption, evidenced by a substantial decrease in adsorption energy compared to pure CeO_2 surfaces. Specifically, the $2Cu/CeO_{2-x}(111)$ surface manifests the highest adsorption energy. The investigations also extend to other transition metals, including Fe, Co, and Ni. Notably, Fe doping shows varied adsorption behaviors depending on the

concentration, with notable structural differences in CO_2 adsorption configurations. However, Co and Ni surfaces present relatively lower CO_2 activation, indicated by the preservation of CO_2 linear molecular structure and lower adsorption energies.

The present analysis underscores the significance of transition metal doping in enhancing CO_2 adsorption on CeO_2 surfaces, with Cu and Fe showing particularly promising results. Note that only 1Co/CeO_{2-x}(111) and 1Ni/CeO_{2-x}(111) were investigated in this study and the influence of metal content on these two surfaces still requires further investigation. A critical facet of this research hinges on the direct reduction of CO_2 to CO on metal-doped CeO_2 surfaces, emphasizing the integral role of surface oxygen vacancies (OVs) in influencing the catalytic performance. Notably, the final state of CO_2 reduction reveals two types of stable configurations, contingent upon whether the dissociated CO from CO_2 is adsorbed above the Ce or on the Fe ion. Despite that the addition of Fe as a dopant does not lower the activation energy compared to pure CeO_2, laboratory experiments showed that the Fe dopant indeed promotes the conversion of CO_2. This is owing to the reduced OV formation energy of Fe doped CeO_2 surfaces compared to the pure CeO_2 surface, which increases the number of active sites on the surface and eventually leads to a higher conversion. This agreement between theoretical predictions and experimental results highlights the complexities of heterogeneous catalytic processes and the challenges in predicting catalyst behavior solely based on theoretical calculations.

The correlations established between adsorption energies, reaction activation energies, and OV formation energies are critical to gain insights on catalytic performance. The near-linear Brønsted-Evans-Polanyi (BEP) relationship observed between activation energy and reaction energy underscores typical behavior for dissociative reactions on heterogeneous catalysts. Furthermore, the study accentuates that the adsorption stability of dissociated CO_2 on the surface

is paramount in determining the performance in terms of transition state energy. Drawing upon the computational and experimental data, this work suggests an optimal E_{OV} value or region, indicating that the ideal OV site should balance between moderate energy requirement for surface reduction and strong interaction with the surface metal to promote C-O bond scission. These descriptors are instrumental in guiding future experimental exploration of catalysts and also stand as valuable metrics for high-throughput screening via Machine Learning techniques.

Chapter 8 Conclusions and Future Work

To address the critical challenges associated with enhancing CO_2 conversion and hydrogenation processes, this thesis has explored various catalyst systems and their underlying mechanisms including Co-Mo carbides and oxides, Fe/Al_2O_3 system, and CO_2 based materials. From the evaluation of Co-Mo oxide and carbide catalysts for reverse water gas shift (RWGS) reactions to the examination of Al_2O_3-supported Fe catalysts for CO_2 hydrogenation, and the comprehensive analysis of ceria-based catalysts for RWGS, this thesis has contributed with invaluable insights. The combined experimental investigations with theoretical approaches, has unveiled promising avenues for catalytic advancements in CeO_2-based materials. This chapter outlines the key findings from this research study, and outline recommendations for future research endeavors.

8.1 Conclusions

8.1.1 Cobalt-molybdenum oxide and carbide catalysts for reverse water gas shift

CoMo-based bimetallic catalysts exhibit promising activity for CO_2 thermo-catalytic conversion in the RWGS reaction, particularly at 600 °C and a GHSV of 60,000 mL $h^{-1}gcat^{-1}$. However, comprehensive investigations into these catalysts are still necessary, specifically regarding the impact of GHSV, stability, and further characterization due to initial time constraints. Future work will also address the optimization of the synthesis procedure, concentrating on the carburization process to minimize carbon deposition and enhance the formation of carbide phases.

Current XRD patterns suggest incomplete carburization, evident from the detectable bi-metallic oxide in the carburized catalyst. The existing carburization method involves a meticulous heating protocol under a methane-hydrogen mixture, followed by a reduction in hydrogen and a

nitrogen cool-down phase. Optimization strategies include adjusting the temperature ramping rate and the final temperature. Preliminary data indicate the onset of carburization around 500 °C, with a CO peak at 650 °C, negating the need to elevate the final carburization temperature beyond 800 °C. To ensure complete carburization without compromising the alumina support's integrity, future efforts will focus on decreasing the ramping rate from 1 to 0.5 °C while maintaining the final temperature.

8.1.2 Al_2O_3-supported iron catalysts for CO_2 hydrogenation to light hydrocarbons

This study evaluated CO_2 hydrogenation over various Fe-based catalysts, focusing on the synthesis methods' impact and reaction conditions. RME Fe/Al_2O_3, prepared via the RME method, showcased superior performance, attributable to the smaller Fe_3O_4 and alumina support particles enhancing Fe dispersion. Notably, RME Fe/Al_2O_3 achieved the highest CO_2 conversion and STY during CO_2 hydrogenation. Optimal performance was observed at 375°C with a H_2/CO_2 ratio of 4, yielding a 56% conversion rate and an STY of 7.75 mmol/(g_{cat}·h). This catalyst also recorded the highest selectivity towards C2+ hydrocarbons at 0.52. A lower H_2/CO_2 ratio, however, decreased both the conversion rate and C2+ selectivity by 10%, owing to reaction equilibrium dynamics, while maintaining a similar STY.

Post-reaction analysis revealed a core-shell structure in spent Fe/RME-Al_2O_3 and Fe/Al_2O_3 catalysts, indicating magnetite's transformation to carbides, which underpins sustained activity. The RME method's advantage was evident, as the uniform nanoparticle structure in spent Fe/RME-Al_2O_3 prevented active phase sintering, thereby enhancing stability. This structural integrity, coupled with the facilitated magnetite-to-carbide transition due to smaller particles, underscores the high efficiency of RME Fe/Al_2O_3. With primarily χ-Fe_5C_2 and Fe_3O_4 particles under 10 nm,

and minimal growth after prolonged use, RME Fe/Al_2O_3 emerges as a robust candidate for industrial CO_2 hydrogenation processes.

8.1.3 Ceria-based catalysts for reverse water gas shift

The comprehensive research into CeO_2-based catalysts for the reverse water-gas shift reaction reveals critical insights into the system's performance, particularly when enhanced with transition metals like Cu and Fe.

Cu/CeO_2 catalysts demonstrate remarkable efficiency in CO_2 conversion, maintaining 100% selectivity to CO within a 300-600°C range. The performance hinges significantly on the Cu doping level, indicating an optimal concentration beyond which no further benefits are observed. This balance is crucial to maintaining the catalyst structural and functional integrity. Transition metal doping, especially with Cu and Fe, significantly enhances CO_2 adsorption on CeO_2 surfaces. Cu notably improves adsorption, while Fe shows varied behaviors, and other metals like Co and Ni present lesser impacts. This finding indicates the necessity for further studies into reaction kinetics and desorption processes, considering the potential challenges posed by higher adsorption energies. DFT computations, paired with laboratory experiments, offer a nuanced understanding of CO_2 reduction on metal-doped CeO_2. Despite theoretical predictions, Fe-doped catalysts enhance CO_2 conversion the most, emphasizing the complex nature of catalytic processes. The research establishes a direct correlation between activation energies, reaction energies, and oxygen vacancy formation, providing a benchmark for future catalyst design and development.

The complex relationship between CO_2 adsorption energy and the loading of transition metals doped onto CeO_2 surfaces emphasizes the effect of dopants on the modification of the property of CeO_2. Specifically, the introduction of Cu atoms significantly enhances CO_2

adsorption, with the $2Cu/CeO_{2-x}(111)$ surface displaying the highest adsorption energy. Other transition metals, such as Fe, Co, and Ni, were also investigated, revealing varied adsorption behaviors. Cu and Fe doping show particularly promising results in enhancing CO_2 adsorption. However, higher adsorption energies may pose challenges in certain catalytic mechanisms, thus necessitating of future exploration of kinetic aspects for CO_2 reduction reactions. Future work, therefore, should also explore the kinetic aspects to balance adsorption capacity and regeneration efficiency, critical for practical applications in environmental remediation and sustainable energy processes.

This research combines Density Functional Theory (DFT) calculations with laboratory experimental to gain further insights into CO_2 reduction on metal-doped CeO_2 surfaces. The study emphasizes the role of surface oxygen vacancies (OVs) on catalytic performance. The relationship between adsorption energies, reaction activation energies, and OV formation energies is critical, highlighting a near-linear Brønsted-Evans-Polanyi (BEP) relationship between activation energy and reaction energy. Notably, despite pure CeO_2 surfaces having lower activation energy and more stable CO_2 adsorption, metal-doped CeO_{2-x} surfaces still outperform the former. This study suggests optimal E_{OV} values and ranges for efficient CO_2 scission, providing valuable guidelines for future experimental exploration and high-throughput screening using Machine Learning techniques.

In summary, the detailed analysis of CeO_2-based catalysts for RWGS reactions highlights the pivotal role of transition metal doping in enhancing catalytic performance. The research underscores the importance of a balanced approach, considering both theoretical computations and experimental data. The findings on optimal doping, catalyst stability, and energy interplays present

a robust foundation for developing more efficient and resilient catalysts for RWGS reactions, contributing vitally to sustainable energy initiatives.

8.2 Recommendations for Future work

8.2.1 Optimizing preparation conditions of reverse microemulsion method

Optimizing catalyst preparation using the reverse microemulsion method necessitates precise manipulation of various factors. Paramount is the surfactant and cosurfactant concentration, vital for stabilizing the emulsion and controlling nanoparticle size. Equally crucial is the oil-to-water ratio, influencing the size and quantity of nanoreactors, thus dictating nanoparticle characteristics. The concentration of metal precursors must be carefully managed to avoid particle agglomeration or insufficient yield. Reaction conditions, such as temperature and duration, require careful calibration to ensure adequate nanoparticle formation without triggering sintering or agglomeration. Post-synthesis treatments, including washing, drying, and calcination, are pivotal, affecting the final catalyst attributes like crystallinity and phase composition. Ensuring reproducibility through rigorous control of all variables is essential, often demanding high-precision equipment. Finally, the synthesized catalyst must undergo thorough testing under application-specific conditions to assess performance metrics like activity, selectivity, and stability, guiding further refinement of synthesis parameters.

8.2.2 Bimetallic and Multimetallic material

The synergistic effects have shown great potential when one material is modified with other metals, which could elevate their catalytic performance. In this PhD thesis, to further improve the performance of Fe/Al_2O_3 material for CO_2 hydrogenation to hydrocarbons, an additional promoter could be introduced besides K. The materials that have been reported to be active for RWGS could potentially be effective promoters to increase the selectivity towards CO since RWGS is

considered to be the first step for hydrocarbon production and CO is the preliminary product. Metallic Cu [149] was reported to be active for RWGS and the 100% selectivity towards CO making it a promising promoter for CO_2 Fischer–Tropsch process. [151] Its corresponding oxides were also suitable catalysts that show high CO_2 conversion and are energetically preferred for RWGS [151]. Other transition metals such as Ni[156] and Co[157] are reported to be active for CO_2 hydrogenation but are more favored for CO_2 methanation with enhanced selectivity towards CH_4. However, lower loading of Co and Ni could lead to high selectivity of Co if utilized as promoter with low loading. These transition metals mentioned above could be the potential promoters for Fe/Al_2O_3 to improve the conversion of CO_2 and selectivity towards hydrocarbons. Future research could focus on investigating the role of secondary promoters mentioned above and their synergistic effects with the Fe catalyst, which could lead to enhanced CO_2 conversion and improved selectivity towards hydrocarbons.

A range of transition metals for CeO_2 modifications have been explored for RWGS in this thesis and the potential and limitations regarding the materials selected were also discussed (see section 7.2). The challenge of the development of RWGS catalysts is achieving high CO_2 conversion and maintain high selectivity towards CO and suppress the competing reaction, i.e., CO_2 methanation. The selection of suitable dopant for CeO_2 should consider the impact of these performance parameters. To explore the combination of transition metals as promoters for CeO_2, multi-metallic materials should be considered and investigate the synergy effect between dopant by performing experimental lab work and DFT analyses.

8.2.3 Machine learning-assisted material screening for CO_2 hydrogenation

Searching for the transition states, or the reaction barrier of every elementary step in RWGS in the presence of a doped Ceria using DFT can be time consuming. Since adsorption energy on

heterogeneous catalysts can be engaged as a descriptor of the catalytic evaluation through BEP relation, the activation energy calculation can be avoided. Moreover, computer-aided materials design using intensive DFT calculations combined with ML algorithms have recently shown potential to guide the experimental development of new materials that can result in the specification of products with desirable properties in short turnaround times. [38, 48] This study aims to predict the adsorption energies of species involved in RWGS. The next research phase will pivot from traditional, time-intensive DFT methods to the identification of transition states in RWGS reactions with doped Ceria in short turnaround times.

Moreover, the predictive power of adsorption energy as a catalyst performance descriptor should be emphasized, based on the established BEP relation, circumventing the need for the direct calculation of the activation energy. DFT combined with ML can provide a framework for identifying a desired catalytic formulation for a particular reaction of interest. Finetuning combined with improvement and optimization of the vector embedding of ML algorithms showed potential for predicting on a new dataset of interests that is outside of the main training set and efficient implementation of the materials selection framework. By refining the vector presentation in the 3D graph, further optimization will be performed to improve the model aiming for higher accuracy of prediction and elevated efficiency of material screening.

References

[1] M. Nagai, K. Matsuda, Low-temperature water–gas shift reaction over cobalt–molybdenum carbide catalyst, Journal of Catalysis, 238 (2006) 489-496.
[2] V. Masson-Delmotte, P. Zhai, A. Pirani, S.L. Connors, C. Péan, S. Berger, N. Caud, Y. Chen, L. Goldfarb, M. Gomis, Climate change 2021: the physical science basis, Contribution of working group I to the sixth assessment report of the intergovernmental panel on climate change, 2 (2021).
[3] R. Newell, D. Raimi, S. Villanueva, B. Prest, Global energy outlook 2021: Pathways from Paris, Resources for the Future, 8 (2021).
[4] S.A. Usas, L. Ricardez-Sandoval, An optimal sustainable planning strategy for national carbon capture deployment: A review on the state of CO_2 capture in Canada, The Canadian Journal of Chemical Engineering, https://doi.org/10.1002/cjce.25249.
[5] M.F. Hasan, E.L. First, F. Boukouvala, C.A. Floudas, A multi-scale framework for CO_2 capture, utilization, and sequestration: CCUS and CCU, Computers & Chemical Engineering, 81 (2015) 2-21.
[6] J. Farfan, M. Fasihi, C. Breyer, Trends in the global cement industry and opportunities for long-term sustainable CCU potential for Power-to-X, Journal of Cleaner Production, 217 (2019) 821-835.
[7] M. Cokoja, C. Bruckmeier, B. Rieger, W.A. Herrmann, F.E. Kühn, Transformation of carbon dioxide with homogeneous transition‐metal catalysts: a molecular solution to a global challenge?, Angewandte Chemie International Edition, 50 (2011) 8510-8537.
[8] F. Franco, C. Rettenmaier, H.S. Jeon, B.R. Cuenya, Transition metal-based catalysts for the electrochemical CO_2 reduction: from atoms and molecules to nanostructured materials, Chemical Society Reviews, 49 (2020) 6884-6946.
[9] A. Tortajada, F. Juliá‐Hernández, M. Börjesson, T. Moragas, R. Martin, Transition‐metal‐catalyzed carboxylation reactions with carbon dioxide, Angewandte Chemie International Edition, 57 (2018) 15948-15982.
[10] J. Ma, N. Sun, X. Zhang, N. Zhao, F. Xiao, W. Wei, Y. Sun, A short review of catalysis for CO_2 conversion, Catalysis Today, 148 (2009) 221-231.
[11] K. Huang, C.-L. Sun, Z.-J. Shi, Transition-metal-catalyzed C–C bond formation through the fixation of carbon dioxide, Chemical Society Reviews, 40 (2011) 2435-2452.
[12] S. Liang, L. Huang, Y. Gao, Q. Wang, B. Liu, Electrochemical Reduction of CO_2 to CO over Transition Metal/N‐Doped Carbon Catalysts: The Active Sites and Reaction Mechanism, Advanced Science, 8 (2021) 2102886.
[13] P. Ebrahimi, A. Kumar, M. Khraisheh, A review of CeO_2 supported catalysts for CO_2 reduction to CO through the reverse water gas shift reaction, Catalysts, 12 (2022) 1101.
[14] D.P. Tran, M.-T. Pham, X.-T. Bui, Y.-F. Wang, S.-J. You, CeO_2 as a photocatalytic material for CO_2 conversion: A review, Solar Energy, 240 (2022) 443-466.
[15] F. Wang, M. Wei, D.G. Evans, X. Duan, CeO_2-based heterogeneous catalysts toward catalytic conversion of CO_2, Journal of Materials Chemistry A, 4 (2016) 5773-5783.
[16] T. Montini, M. Melchionna, M. Monai, P. Fornasiero, Fundamentals and catalytic applications of CeO_2-based materials, Chemical reviews, 116 (2016) 5987-6041.
[17] Q. Li, L. Song, Z. Liang, M. Sun, T. Wu, B. Huang, F. Luo, Y. Du, C.-H. Yan, A review on CeO_2‐based electrocatalyst and photocatalyst in energy conversion, Advanced Energy and Sustainability Research, 2 (2021) 2000063.
[18] M. Nolan, S.C. Parker, G.W. Watson, The electronic structure of oxygen vacancy defects at the low index surfaces of ceria, Surface Science, 595 (2005) 223-232.

[19] M. Nolan, J.E. Fearon, G.W. Watson, Oxygen vacancy formation and migration in ceria, Solid State Ionics, 177 (2006) 3069-3074.
[20] B. Lu, K. Kawamoto, Preparation of mesoporous CeO_2 and monodispersed NiO particles in CeO_2, and enhanced selectivity of NiO/CeO_2 for reverse water gas shift reaction, Materials Research Bulletin, 53 (2014) 70-78.
[21] Y. Mordekovitz, L. Shelly, B.A. Rosen, S. Hayun, Surface properties of Ca, Ti - doped CeO_2 and their influence on the reverse water - gas shift reaction, Journal of the American Ceramic Society, 104 (2021) 2337-2347.
[22] M.D. Porosoff, X. Yang, J.A. Boscoboinik, J.G. Chen, Molybdenum carbide as alternative catalysts to precious metals for highly selective reduction of CO_2 to CO, Angewandte Chemie International Edition, 53 (2014) 6705-6709.
[23] J. Liu, G. Zhang, X. Jiang, J. Wang, C. Song, X. Guo, Insight into the role of Fe_5C_2 in CO_2 catalytic hydrogenation to hydrocarbons, Catalysis Today, 371 (2021) 162-170.
[24] M. Lockwood, Solar change and climate: an update in the light of the current exceptional solar minimum, Proceedings of the Royal Society A: Mathematical, Physical Engineering Sciences, 466 (2010) 303-329.
[25] H. Shaftel, The Causes of Climate Change, in: H. Shaftel (Ed.)NASA Global Climate Change, 2020.
[26] H.R.a.M. Roser, CO_2 and Greenhouse Gas Emissions, Our World in Data, 2020.
[27] E. Canada, National Inventory Report 1990–2017: Greenhouse gas sources and sinks in Canada, Environment Canada, Greenhouse Gas Division Ottawa, 2019.
[28] S.M. Jordaan, E. Romo-Rabago, R. McLeary, L. Reidy, J. Nazari, I.M. Herremans, The role of energy technology innovation in reducing greenhouse gas emissions: A case study of Canada, Renewable and Sustainable Energy Reviews, 78 (2017) 1397-1409.
[29] R. Elias, M. Yuan, M. Wahab, N. Patel, Quantifying saving and carbon emissions reduction by upgrading residential furnaces in Canada, Journal of Cleaner Production, 211 (2019) 1453-1462.
[30] K. Toffolo, S. Meunier, L. Ricardez-Sandoval, Optimal operation of a large-scale packed bed chemical-looping combustion process using nonlinear model predictive control, Fuel, 357 (2024) 129876.
[31] About Renewable Energy, Government of Canada, Natural Resources Canada, 2017.
[32] D. Chaffart, L.A. Ricardez-Sandoval, Optimization and control of a thin film growth process: A hybrid first principles/artificial neural network based multiscale modelling approach, Computers & Chemical Engineering, 119 (2018) 465-479.
[33] K. Toffolo, S. Meunier, L. Ricardez-Sandoval, Reactor network modelling for biomass-fueled chemical-looping gasification and combustion processes, Fuel, 366 (2024) 131254.
[34] T.A. Mendiola-Rodriguez, L.A. Ricardez-Sandoval, Robust control for anaerobic digestion systems of Tequila vinasses under uncertainty: A Deep Deterministic Policy Gradient Algorithm, Digital Chemical Engineering, 3 (2022) 100023.
[35] T.A. Mendiola-Rodriguez, L.A. Ricardez-Sandoval, Integration of design and control for renewable energy systems with an application to anaerobic digestion: A deep deterministic policy gradient framework, Energy, 274 (2023) 127212.
[36] G.D. Patrón, K. Toffolo, L. Ricardez-Sandoval, Economic model predictive control for packed bed chemical looping combustion, Chemical Engineering and Processing-Process Intensification, (2024) 109731.
[37] G.D. Patrón, L. Ricardez-Sandoval, An integrated real-time optimization, control, and estimation scheme for post-combustion CO_2 capture, Applied Energy, 308 (2022) 118302.
[38] D. Rangel-Martinez, K. Nigam, L.A. Ricardez-Sandoval, Machine learning on sustainable energy: A review and outlook on renewable energy systems, catalysis, smart grid and energy storage, Chemical Engineering Research and Design, 174 (2021) 414-441.

[39] M.H. Sahraei, L. Ricardez-Sandoval, Controllability and optimal scheduling of a CO_2 capture plant using model predictive control, International Journal of Greenhouse Gas Control, 30 (2014) 58-71.
[40] D.S. Simakov, Renewable synthetic fuels and chemicals from carbon dioxide: fundamentals, catalysis, design considerations and technological challenges, Springer2017.
[41] M. Götz, J. Lefebvre, F. Mörs, A.M. Koch, F. Graf, S. Bajohr, R. Reimert, T. Kolb, Renewable Power-to-Gas: A technological and economic review, Renewable Energy, 85 (2016) 1371-1390.
[42] A. Mazza, E. Bompard, G. Chicco, Applications of power to gas technologies in emerging electrical systems, Renewable and Sustainable Energy Reviews, 92 (2018) 794-806.
[43] B. Hu, C. Guild, S.L. Suib, Thermal, electrochemical, and photochemical conversion of CO_2 to fuels and value-added products, Journal of CO_2 Utilization, 1 (2013) 18-27.
[44] P. Yaashikaa, P.S. Kumar, S.J. Varjani, A. Saravanan, A review on photochemical, biochemical and electrochemical transformation of CO_2 into value-added products, Journal of CO_2 Utilization, 33 (2019) 131-147.
[45] C. Vogt, M. Monai, G.J. Kramer, B.M. Weckhuysen, The renaissance of the Sabatier reaction and its applications on Earth and in space, Nature catalysis, 2 (2019) 188-197.
[46] M.J. da Silva, Synthesis of methanol from methane: Challenges and advances on the multi-step (syngas) and one-step routes (DMTM), Fuel Processing Technology, 145 (2016) 42-61.
[47] Y.H. Choi, Y.J. Jang, H. Park, W.Y. Kim, Y.H. Lee, S.H. Choi, J.S. Lee, Carbon dioxide Fischer-Tropsch synthesis: A new path to carbon-neutral fuels, Applied Catalysis B: Environmental, 202 (2017) 605-610.
[48] Y. Guan, D. Chaffart, G. Liu, Z. Tan, D. Zhang, Y. Wang, J. Li, L. Ricardez-Sandoval, Machine learning in solid heterogeneous catalysis: Recent developments, challenges and perspectives, Chemical Engineering Science, 248 (2022) 117224.
[49] Y. Yuan, H. You, L. Ricardez-Sandoval, Recent advances on first-principles modeling for the design of materials in CO_2 capture technologies, Chinese Journal of Chemical Engineering, 27 (2019) 1554-1565.
[50] Y.A. Daza, J.N. Kuhn, CO_2 conversion by reverse water gas shift catalysis: comparison of catalysts, mechanisms and their consequences for CO_2 conversion to liquid fuels, RSC Advances, 6 (2016) 49675-49691.
[51] S. Saeidi, S. Najari, F. Fazlollahi, M.K. Nikoo, F. Sefidkon, J.J. Klemeš, L.L. Baxter, Mechanisms and kinetics of CO_2 hydrogenation to value-added products: A detailed review on current status and future trends, Renewable Sustainable Energy Reviews, 80 (2017) 1292-1311.
[52] S.-I. Fujita, M. Usui, N. Takezawa, Mechanism of the reverse water gas shift reaction over Cu/ZnO catalyst, Journal of Catalysis, 134 (1992) 220-225.
[53] A. Goguet, F.C. Meunier, D. Tibiletti, J.P. Breen, R. Burch, Spectrokinetic investigation of reverse water-gas-shift reaction intermediates over a Pt/CeO_2 catalyst, The Journal of Physical Chemistry B, 108 (2004) 20240-20246.
[54] T. Shido, Y. Iwasawa, The effect of coadsorbates in reverse water-gas shift reaction on ZnO, in relation to reactant-promoted reaction mechanism, Journal of Catalysis, 140 (1993) 575-584.
[55] C.-S. Chen, W.-H. Cheng, S.-S. Lin, Study of reverse water gas shift reaction by TPD, TPR and CO_2 hydrogenation over potassium-promoted Cu/SiO_2 catalyst, Applied Catalysis A: General, 238 (2003) 55-67.
[56] A.A. Gokhale, J.A. Dumesic, M. Mavrikakis, On the mechanism of low-temperature water gas shift reaction on copper, Journal of the American Chemical Society, 130 (2008) 1402-1414.
[57] L.C. Grabow, A.A. Gokhale, S.T. Evans, J.A. Dumesic, M. Mavrikakis, Mechanism of the water gas shift reaction on Pt: First principles, experiments, and microkinetic modeling, The Journal of Physical Chemistry C, 112 (2008) 4608-4617.
[58] R.J. Madon, D. Braden, S. Kandoi, P. Nagel, M. Mavrikakis, J.A. Dumesic, Microkinetic analysis and mechanism of the water gas shift reaction over copper catalysts, Journal of Catalysis, 281 (2011) 1-11.

[59] P.M. Maitlis, What is Fischer–Tropsch?, Greener Fischer-Tropsch Processes for Fuels and Feedstocks, (2013) 1-15.
[60] S.-B.a.K. Lee, Seong-Il and Lee, Won-Young and Lee, Kyu-Wan and Choi, Myoung-Jae, Product Distribution Analysis for Catalytic Reduction of CO_2 in a Bench Scale Fixed Bed Reactor, Studies in Surface Science and Catalysis, 153 (2004) 73-78.
[61] W. Wei, G. Jinlong, Methanation of carbon dioxide: an overview, Frontiers of Chemical Science Engineering, 5 (2011) 2-10.
[62] M. Marwood, R. Doepper, A. Renken, In-situ surface and gas phase analysis for kinetic studies under transient conditions. The catalytic hydrogenation of CO_2, Applied Catalysis A: General, 151 (1997) 223-246.
[63] C. Schild, A. Wokaun, A. Baiker, On the mechanism of CO and CO_2 hydrogenation reactions on zirconia-supported catalysts: A diffuse reflectance FTIR study: Part II. Surface species on copper/zirconia catalysts: Implications for methanoi synthesis selectivity, Journal of Molecular Catalysis, 63 (1990) 243-254.
[64] F. Arena, G. Italiano, K. Barbera, S. Bordiga, G. Bonura, L. Spadaro, F. Frusteri, Solid-state interactions, adsorption sites and functionality of Cu-ZnO/ZrO_2 catalysts in the CO_2 hydrogenation to CH_3OH, Applied Catalysis A: General, 350 (2008) 16-23.
[65] X. Tao, J. Wang, Z. Li, Q. Ye, Theoretical study on the reaction mechanism of CO_2 hydrogenation to methanol, Computational Theoretical Chemistry, 1023 (2013) 59-64.
[66] Y.-F. Zhao, Y. Yang, C. Mims, C.H. Peden, J. Li, D. Mei, Insight into methanol synthesis from CO_2 hydrogenation on Cu (1 1 1): complex reaction network and the effects of H_2O, Journal of Catalysis, 281 (2011) 199-211.
[67] C. Liu, T.R. Cundari, A.K. Wilson, CO_2 reduction on transition metal (Fe, Co, Ni, and Cu) surfaces: In comparison with homogeneous catalysis, The Journal of Physical Chemistry C, 116 (2012) 5681-5688.
[68] S.-G. Wang, X.-Y. Liao, D.-B. Cao, C.-F. Huo, Y.-W. Li, J. Wang, H. Jiao, Factors controlling the interaction of CO_2 with transition metal surfaces, The Journal of Physical Chemistry C, 111 (2007) 16934-16940.
[69] C.S. Chen, J.H. Wu, T.W. Lai, Carbon dioxide hydrogenation on Cu nanoparticles, The Journal of Physical Chemistry C, 114 (2010) 15021-15028.
[70] C.-S. Chen, W.-H. Cheng, S.-S. Lin, Mechanism of CO formation in reverse water–gas shift reaction over Cu/Al_2O_3 catalyst, Catalysis Letters, 68 (2000) 45-48.
[71] C.-S. Chen, W.-H. Cheng, Study on the mechanism of CO formation in reverse water gas shift reaction over Cu/SiO_2 Catalyst by pulse reaction, TPD and TPR, Catalysis Letters, 83 (2002) 121-126.
[72] C.-S. Chen, W.-H. Cheng, S.-S. Lin, Study of iron-promoted Cu/SiO_2 catalyst on high temperature reverse water gas shift reaction, Applied Catalysis A: General, 257 (2004) 97-106.
[73] X. Chen, X. Su, H. Duan, B. Liang, Y. Huang, T. Zhang, Catalytic performance of the Pt/TiO_2 catalysts in reverse water gas shift reaction: controlled product selectivity and a mechanism study, Catalysis Today, 281 (2017) 312-318.
[74] B. Liang, H. Duan, X. Su, X. Chen, Y. Huang, X. Chen, J.J. Delgado, T. Zhang, Promoting role of potassium in the reverse water gas shift reaction on Pt/mullite catalyst, Catalysis Today, 281 (2017) 319-326.
[75] T. Inoue, T. Iizuka, K. Tanabe, Hydrogenation of carbon dioxide and carbon monoxide over supported rhodium catalysts under 10 bar pressure, Applied Catalysis A: General, 46 (1989) 1-9.
[76] F. Solymosi, A. Erdőhelyi, T. Bánsági, Methanation of CO_2 on supported rhodium catalyst, Journal of Catalysis, 68 (1981) 371-382.
[77] T. Szailer, É. Novák, A. Oszkó, A. Erdőhelyi, Effect of H_2S on the hydrogenation of carbon dioxide over supported Rh catalysts, Topics in Catalysis, 46 (2007) 79-86.

[78] M.R. Gogate, R.J. Davis, Comparative study of CO and CO_2 hydrogenation over supported Rh–Fe catalysts, Catalysis Communications, 11 (2010) 901-906.
[79] D.H. Kim, S.W. Han, H.S. Yoon, Y.D. Kim, Reverse water gas shift reaction catalyzed by Fe nanoparticles with high catalytic activity and stability, Journal of Industrial Engineering Chemistry, 23 (2015) 67-71.
[80] J. Gao, Y. Wu, C. Jia, Z. Zhong, F. Gao, Y. Yang, B. Liu, Controllable synthesis of α-MoC1-x and β-Mo_2C nanowires for highly selective CO_2 reduction to CO, Catalysis Communications, 84 (2016) 147-150.
[81] B. Bulfin, A.J. Lowe, K.A. Keogh, B.E. Murphy, O. Lübben, S.A. Krasnikov, I.V. Shvets, Analytical Model of CeO_2 Oxidation and Reduction, J. Phys. Chem. C, 117 (2013) 24129-24137.
[82] L. Chen, P. Fleming, V. Morris, J.D. Holmes, M.A. Morris, Size-related lattice parameter changes and surface defects in ceria nanocrystals, J. Phys. Chem. C, 114 (2010) 12909-12919.
[83] M. Kovacevic, B.L. Mojet, J.G. van Ommen, L. Lefferts, Effects of morphology of cerium oxide catalysts for reverse water gas shift reaction, Catalysis Letters, 146 (2016) 770-777.
[84] Y. Liu, Z. Li, H. Xu, Y. Han, Reverse water–gas shift reaction over ceria nanocube synthesized by hydrothermal method, Catalysis Communications, 76 (2016) 1-6.
[85] M. Konsolakis, M. Lykaki, S. Stefa, S.A. Carabineiro, G. Varvoutis, E. Papista, G.E. Marnellos, CO_2 hydrogenation over nanoceria-supported transition metal catalysts: role of ceria morphology (nanorods versus nanocubes) and active phase nature (Co versus Cu), Nanomaterials, 9 (2019) 1739.
[86] B. Dai, S. Cao, H. Xie, G. Zhou, S. Chen, Reduction of CO_2 to CO via reverse water-gas shift reaction over CeO_2 catalyst, Korean Journal of Chemical Engineering, 35 (2017) 421-427.
[87] S.C. Mandal, A. Das, D. Roy, S. Das, A.S. Nair, B. Pathak, Developments of the heterogeneous and homogeneous CO_2 hydrogenation to value-added C2+-based hydrocarbons and oxygenated products, Coordination Chemistry Reviews, 471 (2022) 214737.
[88] Q. Zhang, J. Kang, Y. Wang, Development of novel catalysts for Fischer–Tropsch synthesis: tuning the product selectivity, ChemCatChem, 2 (2010) 1030-1058.
[89] H. Schulz, Comparing Fischer-Tropsch synthesis on iron-and cobalt catalysts: The dynamics of structure and function, Studies in surface science and catalysis, Elsevier2007, pp. 177-199.
[90] B.H. Davis, Fischer–Tropsch synthesis: reaction mechanisms for iron catalysts, Catalysis Today, 141 (2009) 25-33.
[91] M.D. Shroff, D.S. Kalakkad, K.E. Coulter, S.D. Kohler, M.S. Harrington, N.B. Jackson, A.G. Sault, A.K. Datye, Activation of precipitated iron Fischer-Tropsch synthesis catalysts, Journal of Catalysis, 156 (1995) 185-207.
[92] S. Abelló, D. Montané, Exploring Iron‐based Multifunctional Catalysts for Fischer–Tropsch Synthesis: A Review, ChemSusChem, 4 (2011) 1538-1556.
[93] S.-S. Nam, S.-J. Lee, H. Kim, K.-W. Jun, M.-J. Choi, K.-W. Lee, Catalytic conversion of carbon dioxide into hydrocarbons over zinc promoted iron catalysts, Energy Conversion and Management, 38 (1997) S397-S402.
[94] N. Boreriboon, X. Jiang, C. Song, P. Prasassarakich, Fe-based bimetallic catalysts supported on TiO_2 for selective CO_2 hydrogenation to hydrocarbons, Journal of CO_2 Utilization, 25 (2018) 330-337.
[95] Y. Souma, M. Fujiwara, R. Kieffer, H. Ando, Q. Xu, Hydrocarbon synthesis from CO_2 over composite catalysts, Studies in Surface Science and Catalysis, 114 (1998) 327-332.
[96] A.J. Barrios, D.V. Peron, A. Chakkingal, A.I. Dugulan, S. Moldovan, K. Nakouri, J. Thuriot-Roukos, R. Wojcieszak, J.W. Thybaut, M. Virginie, Efficient Promoters and Reaction Paths in the CO_2 Hydrogenation to Light Olefins over Zirconia-Supported Iron Catalysts, ACS Catalysis, 12 (2022) 3211-3225.
[97] J. Ding, L. Huang, W. Gong, M. Fan, Q. Zhong, A.G. Russell, H. Gu, H. Zhang, Y. Zhang, R.-p. Ye, CO_2 hydrogenation to light olefins with high-performance Fe0.30Co0.15Zr0.45K0.10O1.63, Journal of Catalysis, 377 (2019) 224-232.

[98] T. Riedel, M. Claeys, H. Schulz, G. Schaub, S.-S. Nam, K.-W. Jun, M.-J. Choi, G. Kishan, K.-W. Lee, Comparative study of Fischer–Tropsch synthesis with H_2/CO and H_2/CO_2 syngas using Fe-and Co-based catalysts, Applied Catalysis A: General, 186 (1999) 201-213.
[99] W. Wang, X. Jiang, X. Wang, C. Song, Fe–Cu bimetallic catalysts for selective CO_2 hydrogenation to olefin-rich C2+ hydrocarbons, Industrial Engineering Chemistry Research, 57 (2018) 4535-4542.
[100] R. Satthawong, N. Koizumi, C. Song, P. Prasassarakich, Bimetallic Fe–Co catalysts for CO_2 hydrogenation to higher hydrocarbons, Journal of CO_2 Utilization, 3 (2013) 102-106.
[101] Y. Chen, S. Choi, L.T. Thompson, Low temperature CO_2 hydrogenation to alcohols and hydrocarbons over Mo_2C supported metal catalysts, Journal of Catalysis, 343 (2016) 147-156.
[102] D. Sun, D.S.A. Simakov, Thermal management of a Sabatier reactor for CO_2 conversion into CH_4: Simulation-based analysis, Journal of CO_2 Utilization, 21 (2017) 368-382.
[103] G.A. Mills, F.W. Steffgen, Catalytic methanation, Catalysis Reviews - Science and Engineering, 8 (1974) 159-210.
[104] W. Wang, S. Wang, X. Ma, J. Gong, Recent advances in catalytic hydrogenation of carbon dioxide, Chemical Society Reviews, 40 (2011) 3703-3727.
[105] T. Abe, M. Tanizawa, K. Watanabe, A. Taguchi, CO_2 methanation property of Ru nanoparticle-loaded TiO_2 prepared by a polygonal barrel-sputtering method, Energy & Environmental Science, 2 (2009) 315-321.
[106] J.H. Kwak, L. Kovarik, J.n. Szanyi, CO_2 reduction on supported Ru/Al_2O_3 catalysts: cluster size dependence of product selectivity, ACS Catalysis, 3 (2013) 2449-2455.
[107] T. Iizuka, Y. Tanaka, K. Tanabe, Hydrogenation of CO and CO_2 over rhodium catalysts supported on various metal oxides, Journal of Catalysis, 76 (1982) 1-8.
[108] C. Swalus, M. Jacquemin, C. Poleunis, P. Bertrand, P. Ruiz, CO_2 methanation on $Rh/\gamma\text{-}Al_2O_3$ catalyst at low temperature: “In situ” supply of hydrogen by Ni/activated carbon catalyst, Applied Catalysis B: Environment and Energy, 125 (2012) 41-50.
[109] J. Xu, Q. Lin, X. Su, H. Duan, H. Geng, Y. Huang, CO_2 methanation over TiO_2–Al_2O_3 binary oxides supported Ru catalysts, Chinese Journal of Chemical Engineering, 24 (2016) 140-145.
[110] S. Sharma, Z. Hu, P. Zhang, E.W. McFarland, H. Metiu, CO_2 methanation on Ru-doped ceria, Journal of Catalysis, 278 (2011) 297-309.
[111] W.-J. Shen, M. Okumura, Y. Matsumura, M. Haruta, The influence of the support on the activity and selectivity of Pd in CO hydrogenation, Applied Catalysis A: General, 213 (2001) 225-232.
[112] M.A. Vannice, C. Twu, S. Moon, SMSI effects on CO adsorption and hydrogenation on Pt catalysts: I. Infrared spectra of adsorbed CO prior to and during reaction conditions, Journal of Catalysis, 79 (1983) 70-80.
[113] J. Martins, N. Batail, S. Silva, S. Rafik-Clement, A. Karelovic, D.P. Debecker, A. Chaumonnot, D. Uzio, CO_2 hydrogenation with shape-controlled Pd nanoparticles embedded in mesoporous silica: Elucidating stability and selectivity issues, Catalysis Communications, 58 (2015) 11-15.
[114] G.D. Weatherbee, C.H. Bartholomew, Hydrogenation of CO_2 on group VIII metals: I. Specific activity of $NiSiO_2$, Journal of Catalysis, 68 (1981) 67-76.
[115] T. Bligaard, J.K. Nørskov, S. Dahl, J. Matthiesen, C.H. Christensen, J. Sehested, The Brønsted–Evans–Polanyi relation and the volcano curve in heterogeneous catalysis, Journal of Catalysis, 224 (2004) 206-217.
[116] G. Garbarino, D. Bellotti, P. Riani, L. Magistri, G. Busca, Methanation of carbon dioxide on Ru/Al_2O_3 and Ni/Al_2O_3 catalysts at atmospheric pressure: Catalysts activation, behaviour and stability, International Journal of Hydrogen Energy, 40 (2015) 9171-9182.
[117] M. Cai, J. Wen, W. Chu, X. Cheng, Z. Li, Methanation of carbon dioxide on $Ni/ZrO_2\text{-}Al_2O_3$ catalysts: Effects of ZrO_2 promoter and preparation method of novel $ZrO_2\text{-}Al_2O_3$ carrier, Journal of Natural Gas Chemistry, 20 (2011) 318-324.

[118] H. Takano, Y. Kirihata, K. Izumiya, N. Kumagai, H. Habazaki, K. Hashimoto, Highly active Ni/Y-doped ZrO_2 catalysts for CO_2 methanation, Applied Surface Science, 388 (2016) 653-663.
[119] S. Rahmani, M. Rezaei, F. Meshkani, Preparation of highly active nickel catalysts supported on mesoporous nanocrystalline γ-Al_2O_3 for CO_2 methanation, Journal of Industrial and Engineering Chemistry, 20 (2014) 1346-1352.
[120] S. Tada, S. Ikeda, N. Shimoda, T. Honma, M. Takahashi, A. Nariyuki, S. Satokawa, Sponge Ni catalyst with high activity in CO_2 methanation, International Journal of Hydrogen Energy, 42 (2017) 30126-30134.
[121] C. Bartholomew, Catalyst deactivation and regeneration, 2000.
[122] B. Alrafei, I. Polaert, A. Ledoux, F. Azzolina-Jury, Remarkably stable and efficient Ni and Ni-Co catalysts for CO_2 methanation, Catalysis Today, (2019).
[123] A. Primo, J. He, B. Jurca, B. Cojocaru, C. Bucur, V.I. Parvulescu, H. Garcia, CO_2 methanation catalyzed by oriented MoS_2 nanoplatelets supported on few layers graphene, Applied Catalysis B: Environmental, 245 (2019) 351-359.
[124] D. Zhong, L. Ouyang, J. Liu, H. Wang, Y. Jia, M. Zhu, Metallic Ni nanocatalyst in situ formed from $LaNi_5H_5$ toward efficient CO_2 methanation, International Journal of Hydrogen Energy, (2019).
[125] X. Jiang, N. Koizumi, X. Guo, C. Song, Bimetallic Pd–Cu catalysts for selective CO_2 hydrogenation to methanol, Applied Catalysis B: Environmental, 170 (2015) 173-185.
[126] X. Huang, C. Ji, C. Wang, F. Xiao, N. Zhao, N. Sun, W. Wei, Y. Sun, Ordered mesoporous CoO-NiO-Al_2O_3 bimetallic catalysts with dual confinement effects for CO_2 reforming of CH_4, Catalysis Today, 281 (2017) 241-249.
[127] A.G. Kharaji, A. Shariati, M.A. Takassi, A novel γ-Alumina supported Fe-Mo bimetallic catalyst for reverse water gas shift reaction, Chinese Journal of Chemical Engineering, 21 (2013) 1007-1014.
[128] J. Ye, Q. Ge, C.-j. Liu, Effect of PdIn bimetallic particle formation on CO_2 reduction over the Pd–In/SiO_2 catalyst, Chemical Engineering Science, 135 (2015) 193-201.
[129] I. Ro, R. Carrasquillo-Flores, J.A. Dumesic, G.W. Huber, Intrinsic kinetics of plasmon-enhanced reverse water gas shift on Au and Au–Mo interfacial sites supported on silica, Applied Catalysis A: General, 521 (2016) 182-189.
[130] D.H. Kim, J.L. Park, E.J. Park, Y.D. Kim, S. Uhm, Dopant effect of barium zirconate-based perovskite-type catalysts for the intermediate-temperature reverse water gas shift reaction, ACS Catalysis, 4 (2014) 3117-3122.
[131] N.A. Dharanipragada, L.C. Buelens, H. Poelman, E. De Grave, V.V. Galvita, G.B. Marin, Mg–Fe–Al–O for advanced CO_2 to CO conversion: carbon monoxide yield vs. oxygen storage capacity, Journal of Materials Chemistry A, 3 (2015) 16251-16262.
[132] H. Shao, E.L. Kugler, W. Ma, D.B. Dadyburjor, Effect of temperature on structure and performance of in-house cobalt–tungsten carbide catalyst for dry reforming of methane, Industrial Engineering Chemistry Research, 44 (2005) 4914-4921.
[133] X. Du, L. France, V. Kuznetsov, T. Xiao, P. Edwards, H. AlMegren, A. Bagabas, Dry reforming of methane over ZrO_2-supported Co–Mo carbide catalyst, Applied Petrochemical Research, 4 (2014) 137-144.
[134] T.-c. Xiao, A. Hanif, A.P. York, M.L. Green, Methane partial oxidation to synthesis gas over bimetallic cobalt/tungsten carbide catalysts and integration with a Mn substituted hexaaluminate combustion catalyst, Catalysis Today, 147 (2009) 196-202.
[135] L. Zhao, K. Fang, D. Jiang, D. Li, Y. Sun, Sol–gel derived Ni–Mo bimetallic carbide catalysts and their performance for CO hydrogenation, Catalysis Today, 158 (2010) 490-495.
[136] X. Zhang, X. Zhu, L. Lin, S. Yao, M. Zhang, X. Liu, X. Wang, Y.-W. Li, C. Shi, D. Ma, Highly dispersed copper over β-Mo_2C as an efficient and stable catalyst for the reverse water gas shift (RWGS) reaction, ACS Catalysis, 7 (2017) 912-918.

[137] Q. Zhang, L. Pastor-Pérez, W. Jin, S. Gu, T. Reina, Understanding the promoter effect of Cu and Cs over highly effective β-Mo_2C catalysts for the reverse water-gas shift reaction, Applied Catalysis B: Environmental, 244 (2019) 889-898.
[138] L. Xue, C. Zhang, J. Wu, Q.-Y. Fan, Y. Liu, Y. Wu, J. Li, H. Zhang, F. Liu, S. Zeng, Unveiling the reaction pathway on Cu/CeO_2 catalyst for electrocatalytic CO_2 reduction to CH_4, Applied Catalysis B: Environmental, 304 (2022) 120951.
[139] A.E. Mattsson, P.A. Schultz, M.P. Desjarlais, T.R. Mattsson, K. Leung, Designing meaningful density functional theory calculations in materials science—a primer, Modelling and Simulation in Materials Science and Engineering, 13 (2004) R1.
[140] I. Obot, D. Macdonald, Z. Gasem, Density functional theory (DFT) as a powerful tool for designing new organic corrosion inhibitors. Part 1: an overview, Corrosion Science, 99 (2015) 1-30.
[141] D. Cheng, F.R. Negreiros, E. Aprà, A. Fortunelli, Computational approaches to the chemical conversion of carbon dioxide, ChemSusChem, 6 (2013) 944-965.
[142] Á. Morales‐García, F. Viñes, J.R. Gomes, F. Illas, Concepts, models, and methods in computational heterogeneous catalysis illustrated through CO_2 conversion, Wiley Interdisciplinary Reviews: Computational Molecular Science, 11 (2021) e1530.
[143] Z. Tian, C. Priest, L. Chen, Recent progress in the theoretical investigation of electrocatalytic reduction of CO_2, Advanced Theory and Simulations, 1 (2018) 1800004.
[144] K.-J. Kim, Y.-L. Lee, H.-S. Na, S.-Y. Ahn, J.-O. Shim, B.-H. Jeon, H.-S. Roh, Efficient waste to energy conversion based on Co-CeO_2 catalyzed water-gas shift reaction, Catalysts, 10 (2020) 420.
[145] S.S. Kim, H.H. Lee, S.C. Hong, A study on the effect of support's reducibility on the reverse water-gas shift reaction over Pt catalysts, Applied Catalysis A: General, 423 (2012) 100-107.
[146] L.-C. Wang, M.T. Khazaneh, D. Widmann, R.J. Behm, TAP reactor studies of the oxidizing capability of CO_2 on a Au/CeO_2 catalyst–A first step toward identifying a redox mechanism in the Reverse Water–Gas Shift reaction, Journal of catalysis, 302 (2013) 20-30.
[147] B. Ren, J. Li, G. Wen, L. Ricardez‐Sandoval, E. Croiset, First-principles based microkinetic modeling of CO_2 reduction at the Ni/SDC cathode of a solid oxide electrolysis cell, The Journal of Physical Chemistry C, 122 (2018) 21151-21161.
[148] Y. Zhang, L. Liang, Z. Chen, J. Wen, W. Zhong, S. Zou, M. Fu, L. Chen, D. Ye, Highly efficient Cu/CeO_2-hollow nanospheres catalyst for the reverse water-gas shift reaction: Investigation on the role of oxygen vacancies through in situ UV-Raman and DRIFTS, Applied Surface Science, 516 (2020) 146035.
[149] J. Yoshihara, C.T. Campbell, Methanol synthesis and reverse water–gas shift kinetics over Cu (110) model catalysts: structural sensitivity, Journal of Catalysis, 161 (1996) 776-782.
[150] H.-J. Li, J.-J. Ho, Density functional calculations on the hydrogenation of carbon dioxide on Fe (111) and W (111) surfaces, The Journal of Physical Chemistry C, 114 (2010) 1194-1200.
[151] E. Pahija, C. Panaritis, S. Gusarov, J. Shadbahr, F. Bensebaa, G. Patience, D.C. Boffito, Experimental and Computational Synergistic Design of Cu and Fe Catalysts for the Reverse Water–Gas Shift: A Review, ACS Catalysis, 12 (2022) 6887-6905.
[152] A.M. Bahmanpour, F. Héroguel, M. Kılıç, C.J. Baranowski, L. Artiglia, U. Röthlisberger, J.S. Luterbacher, O. Kröcher, Cu–Al spinel as a highly active and stable catalyst for the reverse water gas shift reaction, ACS Catalysis, 9 (2019) 6243-6251.
[153] H. Wu, N. Zhang, H. Wang, S. Hong, Adsorption of CO_2 on Cu_2O (1 1 1) oxygen-vacancy surface: First-principles study, Chemical Physics Letters, 568 (2013) 84-89.
[154] T. Yang, X.-D. Wen, C.-F. Huo, Y.-W. Li, J. Wang, H. Jiao, Structure and energetics of hydrogen adsorption on Fe_3O_4 (1 1 1), Journal of Molecular Catalysis A: Chemical, 302 (2009) 129-136.
[155] X. Li, J. Paier, Vibrational properties of CO_2 adsorbed on the Fe_3O_4 (111) surface: Insights gained from DFT, The Journal of Chemical Physics, 152 (2020).

[156] D. Li, X. Ding, X. Liu, J. Cheng, Z. Jiang, Y. Guo, CO_2 hydrogenation to methane over Ni/ZrO_2 and Ni/CeO_2 catalysts: experimental and DFT studies, Journal of Materials Science, 58 (2023) 12584-12595.
[157] M. Wang, G. Zhang, J. Zhu, W. Li, J. Wang, K. Bian, Y. Liu, F. Ding, C. Song, X. Guo, Unraveling the tunable selectivity on cobalt oxide and metallic cobalt sites for CO_2 hydrogenation, Chemical Engineering Journal, 446 (2022) 137217.
[158] H. Wang, G. Tsilomelekis, Catalytic performance and stability of Fe-doped CeO_2 in propane oxidative dehydrogenation using carbon dioxide as an oxidant, Catalysis Science & Technology, 10 (2020) 4362-4372.
[159] A. Michaelides, Z.-P. Liu, C. Zhang, A. Alavi, D.A. King, P. Hu, Identification of general linear relationships between activation energies and enthalpy changes for dissociation reactions at surfaces, Journal of the American Chemical Society, 125 (2003) 3704-3705.
[160] H. Shen, Y. Dong, S. Yang, Y. He, Q. Wang, Y. Cao, W. Wang, T. Wang, Q. Zhang, H. Zhang, Identifying the roles of Ce3+− OH and Ce− H in the reverse water-gas shift reaction over highly active Ni-doped CeO_2 catalyst, Nano Research, 15 (2022) 5831-5841.
[161] S. Eriksson, U. Nylén, S. Rojas, M. Boutonnet, Preparation of catalysts from microemulsions and their applications in heterogeneous catalysis, Applied Catalysis A: General, 265 (2004) 207-219.
[162] Y. Yang, L. Jing, X. Yu, D. Yan, M.J.C.o.m. Gao, Coating aqueous quantum dots with silica via reverse microemulsion method: toward size-controllable and robust fluorescent nanoparticles, Chemistry of Materials, 19 (2007) 4123-4128.
[163] J.-N. Park, E.W. McFarland, A highly dispersed Pd–Mg/SiO_2 catalyst active for methanation of CO_2, Journal of Catalysis, 266 (2009) 92-97.
[164] M. García-Diéguez, C. Herrera, M.Á. Larrubia, L.J. Alemany, CO_2-reforming of natural gas components over a highly stable and selective NiMg/Al_2O_3 nanocatalyst, Catalysis Today, 197 (2012) 50-57.
[165] M. Kishida, K. Umakoshi, J.-i. Ishiyama, H. Nagata, K. Wakabayashi, Hydrogenation of carbon dioxide over metal catalysts prepared using microemulsion, Catalysis Today, 29 (1996) 355-359.
[166] M. Kishida, T. Fujita, K. Umakoshi, J. Ishiyama, H. Nagata, K. Wakabayashi, Novel preparation of metal-supported catalysts by colloidal microparticles in a water-in-oil microemulsion; catalytic hydrogenation of carbon dioxide, Journal of the Chemical Society, Chemical Communications, (1995) 763-764.
[167] C.S. Santana, L.S. Shine, L.H. Vieira, R.J. Passini, E.A. Urquieta-González, E.M. Assaf, J.F. Gomes, J.M. Assaf, Effect of the synthesis method on physicochemical properties and performance of Cu/ZnO/Nb2O5 catalysts for CO2 hydrogenation to methanol, Industrial & Engineering Chemistry Research, 60 (2021) 18750-18758.
[168] Y. Liu, Y. Zhang, T. Wang, N. Tsubaki, Efficient conversion of carbon dioxide to methanol using copper catalyst by a new low-temperature hydrogenation process, Chemistry Letters, 36 (2007) 1182-1183.
[169] V. Iablokov, S.K. Beaumont, S. Alayoglu, V.V. Pushkarev, C. Specht, J. Gao, A.P. Alivisatos, N. Kruse, G.A. Somorjai, Size-controlled model Co nanoparticle catalysts for CO2 hydrogenation: synthesis, characterization, and catalytic reactions, Nano letters, 12 (2012) 3091-3096.
[170] S. Sathyamurthy, K.J. Leonard, R.T. Dabestani, M.P. Paranthaman, Reverse micellar synthesis of cerium oxide nanoparticles, Nanotechnology, 16 (2005) 1960.
[171] P. Paschalidou, C.R. Theocharis, Surface properties of ceria synthesised using Triton-X based reverse microemulsions, RSC Advances, 9 (2019) 7025-7031.
[172] A. Bumajdad, M.I. Zaki, J. Eastoe, L. Pasupulety, Microemulsion-based synthesis of CeO_2 powders with high surface area and high-temperature stabilities, Langmuir, 20 (2004) 11223-11233.
[173] I.C. Change, The physical science basis, Contribution of working group I to the fifth assessment report of the intergovernmental panel on climate change, 1535 (2013) 2013.

[174] P. Forster, V. Ramaswamy, P. Artaxo, T. Berntsen, R. Betts, D.W. Fahey, J. Haywood, J. Lean, D.C. Lowe, G. Myhre, Changes in atmospheric constituents and in radiative forcing. Chapter 2, Climate change 2007. The physical science basis2007.
[175] Z. Mi, J. Zheng, J. Meng, H. Zheng, X. Li, D.M. Coffman, J. Woltjer, S. Wang, D. Guan, Carbon emissions of cities from a consumption-based perspective, Applied Energy, 235 (2019) 509-518.
[176] R.M. Cuéllar-Franca, A. Azapagic, Carbon capture, storage and utilisation technologies: A critical analysis and comparison of their life cycle environmental impacts, Journal of CO_2 utilization, 9 (2015) 82-102.
[177] M. Eckert, Max von Laue and the discovery of X‐ray diffraction in 1912, Annalen der Physik, 524 (2012) A83-A85.
[178] A. Monshi, M.R. Foroughi, M.R. Monshi, Modified Scherrer equation to estimate more accurately nano-crystallite size using XRD, World Journal of Nano Science Engineering, 2 (2012) 154-160.
[179] D.M. Moore, R.C. Reynolds Jr, X-ray Diffraction and the Identification and Analysis of Clay Minerals, Oxford University Press (OUP)1989.
[180] J.W. Olesik, Elemental analysis using ICP-OES and ICP/MS, Analytical Chemistry, 63 (1991) 12A-21A.
[181] B. Charles, K.J. Fredeen, Concepts, instrumentation and techniques in inductively coupled plasma optical emission spectrometry, Perkin Elmer Corporation, (1997).
[182] R.B. Anderson, Modifications of the Brunauer, Emmett and Teller equation1, Journal of the American Chemical Society, 68 (1946) 686-691.
[183] B. Fultz, J.M. Howe, Transmission electron microscopy and diffractometry of materials, Springer Science & Business Media2012.
[184] D. Stokes, Principles and practice of variable pressure/environmental scanning electron microscopy (VP-ESEM), John Wiley & Sons2008.
[185] C.D. Doyle, Kinetic analysis of thermogravimetric data, Journal of Applied Polymer Science, 5 (1961) 285-292.
[186] B. Stuart, Infrared spectroscopy, Kirk‐Othmer Encyclopedia of Chemical Technology, (2000).
[187] H.S. Fogler, Elements of chemical reaction engineering, Pearson2020.
[188] D.E. Mears, Tests for transport limitations in experimental catalytic reactors, Industrial & Engineering Chemistry Process Design Development, 10 (1971) 541-547.
[189] G. Kresse, J. Furthmüller, Efficient iterative schemes for ab initio total-energy calculations using a plane-wave basis set, Physical review B, 54 (1996) 11169.
[190] P.E. Blöchl, Projector augmented-wave method, Physical review B, 50 (1994) 17953.
[191] J.P. Perdew, K. Burke, M. Ernzerhof, Generalized gradient approximation made simple, Physical review letters, 77 (1996) 3865.
[192] M.P. Teter, M.C. Payne, D.C. Allan, Solution of Schrödinger's equation for large systems, Physical Review B, 40 (1989) 12255.
[193] Y. Jiang, J.B. Adams, M. Van Schilfgaarde, Density-functional calculation of CeO_2 surfaces and prediction of effects of oxygen partial pressure and temperature on stabilities, The Journal of chemical physics, 123 (2005).
[194] M. Nolan, S. Grigoleit, D.C. Sayle, S.C. Parker, G.W. Watson, Density functional theory studies of the structure and electronic structure of pure and defective low index surfaces of ceria, Surface Science, 576 (2005) 217-229.
[195] E. Kümmerle, G. Heger, The structures of C–$Ce_2O_{3+\delta}$, Ce_7O_{12}, and Ce_1O_{20}, Journal of Solid State Chemistry, 147 (1999) 485-500.
[196] J.-F. Jerratsch, X. Shao, N. Nilius, H.-J. Freund, C. Popa, M.V. Ganduglia-Pirovano, A.M. Burow, J. Sauer, Electron localization in defective ceria films: A study with scanning-tunneling microscopy and density-functional theory, Physical review letters, 106 (2011) 246801.

[197] V. Wang, N. Xu, J.C. Liu, G. Tang, W.-T. Geng, VASPKIT: a pre-and post-processing program for VASP code, arXiv preprint arXiv:1908.08269, (2019).
[198] V. Wang, N. Xu, J.-C. Liu, G. Tang, W.-T. Geng, VASPKIT: A user-friendly interface facilitating high-throughput computing and analysis using VASP code, Computer Physics Communications, 267 (2021) 108033.
[199] M. Luo, R.J. O'Brien, S. Bao, B.H. Davis, Fischer–Tropsch synthesis: induction and steady-state activity of high-alpha potassium promoted iron catalysts, Applied Catalysis A: General, 239 (2003) 111-120.
[200] C. Yang, H. Zhao, Y. Hou, D. Ma, Fe_5C_2 nanoparticles: a facile bromide-induced synthesis and as an active phase for Fischer–Tropsch synthesis, Journal of the American Chemical Society, 134 (2012) 15814-15821.
[201] Y. Zhang, C. Cao, C. Zhang, Z. Zhang, X. Liu, Z. Yang, M. Zhu, B. Meng, J. Xu, Y.-F. Han, The study of structure-performance relationship of iron catalyst during a full life cycle for CO_2 hydrogenation, Journal of Catalysis, 378 (2019) 51-62.
[202] R. Warringham, N.G. Hamilton, I.P. Silverwood, C. How, P.B. Webb, R.P. Tooze, W. Zhou, C.D. Frost, S.F. Parker, D. Lennon, The application of inelastic neutron scattering to investigate a hydrogen pre-treatment stage of an iron Fischer–Tropsch catalyst, Applied Catalysis A: General, 489 (2015) 209-217.
[203] A. Kadkhodayan, A. Brenner, Temperature-programmed reduction and oxidation of metals supported on γ-alumina, Journal of Catalysis, 117 (1989) 311-321.
[204] W. Jozwiak, E. Kaczmarek, T. Maniecki, W. Ignaczak, W. Maniukiewicz, Reduction behavior of iron oxides in hydrogen and carbon monoxide atmospheres, Applied Catalysis A: General, 326 (2007) 17-27.
[205] R. Warringham, A.R. McFarlane, D.A. MacLaren, P.B. Webb, R.P. Tooze, J. Taylor, R.A. Ewings, S.F. Parker, D. Lennon, The application of inelastic neutron scattering to explore the significance of a magnetic transition in an iron based Fischer-Tropsch catalyst that is active for the hydrogenation of CO, The Journal of Chemical Physics, 143 (2015) 174703.
[206] J. Xu, C.H. Bartholomew, Temperature-programmed hydrogenation (TPH) and in situ Mössbauer spectroscopy studies of carbonaceous species on silica-supported iron Fischer− Tropsch catalysts, The Journal of Physical Chemistry B, 109 (2005) 2392-2403.
[207] L. Niu, X. Liu, X. Zhou, C. Huo, J. Xu, X. Wen, J. Niemantsverdriet, Y. Yang, Y. Li, Genesis of an Fe_5C_2@ Fe_3O_4 core/shell structure during CO carburization of metallic iron nanoparticles, Journal of Catalysis, 407 (2022) 97-103.
[208] Y. Tuo, G. Liu, B. Dong, J. Zhou, A. Wang, J. Wang, R. Jin, H. Lv, Z. Dou, W. Huang, Microbial synthesis of Pd/Fe_3O_4, Au/Fe_3O_4 and PdAu/Fe_3O_4 nanocomposites for catalytic reduction of nitroaromatic compounds, Scientific reports, 5 (2015) 13515.
[209] M. Niemelä, M. Nokkosmäki, Activation of carbon dioxide on Fe-catalysts, Catalysis today, 100 (2005) 269-274.
[210] C.-l. Zhang, S. Li, L.-j. Wang, T.-h. Wu, S.-y. Peng, Studies on the decomposing carbon dioxide into carbon with oxygen-deficient magnetite: II. The effects of properties of magnetite on activity of decomposition CO_2 and mechanism of the reaction, Materials chemistry and physics, 62 (2000) 52-61.
[211] H.-J. Wan, B.-S. Wu, C.-H. Zhang, H.-W. Xiang, Y.-W. Li, B.-F. Xu, F. Yi, Study on Fe–Al_2O_3 interaction over precipitated iron catalyst for Fischer–Tropsch synthesis, Catalysis Communications, 8 (2007) 1538-1545.
[212] C.-H. Zhang, Y. Yang, B.-T. Teng, T.-Z. Li, H.-Y. Zheng, H.-W. Xiang, Y.-W. Li, Study of an iron-manganese Fischer–Tropsch synthesis catalyst promoted with copper, Journal of Catalysis, 237 (2006) 405-415.
[213] R. Satthawong, N. Koizumi, C. Song, P. Prasassarakich, Light olefin synthesis from CO_2 hydrogenation over K-promoted Fe–Co bimetallic catalysts, Catalysis Today, 251 (2015) 34-40.

[214] J. Wei, J. Sun, Z. Wen, C. Fang, Q. Ge, H. Xu, New insights into the effect of sodium on Fe_3O_4-based nanocatalysts for CO_2 hydrogenation to light olefins, Catalysis Science & Technology, 6 (2016) 4786-4793.
[215] J. Wei, R. Yao, Q. Ge, Z. Wen, X. Ji, C. Fang, J. Zhang, H. Xu, J. Sun, Catalytic hydrogenation of CO_2 to isoparaffins over Fe-based multifunctional catalysts, ACS Catalysis, 8 (2018) 9958-9967.
[216] M. Albrecht, U. Rodemerck, M. Schneider, M. Bröring, D. Baabe, E.V. Kondratenko, Unexpectedly efficient CO_2 hydrogenation to higher hydrocarbons over non-doped Fe_2O_3, Applied Catalysis B: Environmental, 204 (2017) 119-126.
[217] Z. He, M. Cui, Q. Qian, J. Zhang, H. Liu, B. Han, Synthesis of liquid fuel via direct hydrogenation of CO_2, Proceedings of the National Academy of Sciences, 116 (2019) 12654-12659.
[218] M. Fujiwara, R. Kieffer, H. Ando, Y. Souma, Development of composite catalysts made of Cu-Zn-Cr oxide/zeolite for the hydrogenation of carbon dioxide, Applied Catalysis A: General, 121 (1995) 113-124.
[219] X. Wang, G. Yang, J. Zhang, S. Chen, Y. Wu, Q. Zhang, J. Wang, Y. Han, Y. Tan, Synthesis of isoalkanes over a core (Fe–Zn–Zr)–shell (zeolite) catalyst by CO_2 hydrogenation, Chemical Communications, 52 (2016) 7352-7355.
[220] B. Yao, T. Xiao, O.A. Makgae, X. Jie, S. Gonzalez-Cortes, S. Guan, A.I. Kirkland, J.R. Dilworth, H.A. Al-Megren, S.M. Alshihri, Transforming carbon dioxide into jet fuel using an organic combustion-synthesized Fe-Mn-K catalyst, Nature communications, 11 (2020) 1-12.
[221] P.R. Khangale, R. Meijboom, K. Jalama, CO_2 hydrogenation to liquid hydrocarbons via modified Fischer–Tropsch over alumina-supported cobalt catalysts: effect of operating temperature, pressure and potassium loading, Journal of CO_2 Utilization, 41 (2020) 101268.
[222] S.-M. Hwang, C. Zhang, S.J. Han, H.-G. Park, Y.T. Kim, S. Yang, K.-W. Jun, S.K. Kim, Mesoporous carbon as an effective support for Fe catalyst for CO_2 hydrogenation to liquid hydrocarbons, Journal of CO_2 Utilization, 37 (2020) 65-73.
[223] S.-M. Hwang, S.J. Han, J.E. Min, H.-G. Park, K.-W. Jun, S.K. Kim, Mechanistic insights into Cu and K promoted Fe-catalyzed production of liquid hydrocarbons via CO_2 hydrogenation, Journal of CO_2 Utilization, 34 (2019) 522-532.
[224] W. Li, A. Zhang, X. Jiang, M.J. Janik, J. Qiu, Z. Liu, X. Guo, C. Song, The anti-sintering catalysts: Fe–Co–Zr polymetallic fibers for CO_2 hydrogenation to C2=–C4=–rich hydrocarbons, Journal of CO_2 Utilization, 23 (2018) 219-225.
[225] J. Zhang, M. Abbas, W. Zhao, J. Chen, Enhanced stability of a fused iron catalyst under realistic Fischer–Tropsch synthesis conditions: insights into the role of iron phases (χ-Fe_5C_2, θ-Fe_3C and α-Fe), Catalysis Science & Technology, (2022).
[226] S. Lyu, L. Wang, Z. Li, S. Yin, J. Chen, Y. Zhang, J. Li, Y. Wang, Stabilization of ε-iron carbide as high-temperature catalyst under realistic Fischer–Tropsch synthesis conditions, Nature communications, 11 (2020) 1-8.
[227] H. Suo, S. Wang, C. Zhang, J. Xu, B. Wu, Y. Yang, H. Xiang, Y.-W. Li, Chemical and structural effects of silica in iron-based Fischer–Tropsch synthesis catalysts, Journal of catalysis, 286 (2012) 111-123.
[228] H.M. Torres Galvis, J.H. Bitter, T. Davidian, M. Ruitenbeek, A.I. Dugulan, K.P. de Jong, Iron particle size effects for direct production of lower olefins from synthesis gas, Journal of the American Chemical Society, 134 (2012) 16207-16215.
[229] T. Yamashita, P. Hayes, Analysis of XPS spectra of Fe2+ and Fe3+ ions in oxide materials, Applied surface science, 254 (2008) 2441-2449.
[230] F. Kong, Y. Qie, Y. Liu, Z. Yang, Z. Shi, H. Yang, Magnetic properties and electrocatalytic properties of Fe_5C_2 particles with different morphologies, Journal of Materials Science: Materials in Electronics, 33 (2022) 884-893.

[231] R. Sawyer, H. Nesbitt, R. Secco, High resolution X-ray Photoelectron Spectroscopy (XPS) study of K_2O–SiO_2 glasses: Evidence for three types of O and at least two types of Si, Journal of Non-Crystalline Solids, 358 (2012) 290-302.
[232] Z. Ye, Y. Qie, Z. Fan, Y. Liu, Z. Shi, H. Yang, Soft magnetic Fe_5C_2–Fe_3C@ C as an electrocatalyst for the hydrogen evolution reaction, Dalton Transactions, 48 (2019) 4636-4642.
[233] A.L. Davidson, P.B. Webb, S.F. Parker, D. Lennon, Hydrogen partitioning as a function of time-on-stream for an unpromoted iron-based Fischer–Tropsch synthesis catalyst applied to CO hydrogenation, Industrial & Engineering Chemistry Research, 59 (2019) 52-60.
[234] R. Warringham, A.L. Davidson, P.B. Webb, R.P. Tooze, R.A. Ewings, S.F. Parker, D. Lennon, Examining the temporal behavior of the hydrocarbonaceous overlayer on an iron based Fischer–Tropsch catalyst, RSC advances, 9 (2019) 2608-2617.
[235] Y. Zhang, D. Fu, X. Liu, Z. Zhang, C. Zhang, B. Shi, J. Xu, Y.F. Han, Operando spectroscopic study of dynamic structure of iron oxide catalysts during CO_2 hydrogenation, ChemCatChem, 10 (2018) 1272-1276.
[236] K. Mužina, S. Kurajica, G. Dražić, P. Guggenberger, G. Matijašić, True doping levels in hydrothermally derived copper-doped ceria, Journal of Nanoparticle Research, 23 (2021) 1-14.
[237] R. Si, J. Raitano, N. Yi, L. Zhang, S.-W. Chan, M. Flytzani-Stephanopoulos, Structure sensitivity of the low-temperature water-gas shift reaction on Cu–CeO_2 catalysts, Catalysis Today, 180 (2012) 68-80.
[238] Jolm F. Moulder, William F. Stickle, Peter E.'Sobol, K.D. Bomben, Handbook of X-ray Photoelectron Spectroscopy, Perkin-Elmer Corporation, United States of America, 1992.
[239] J. Han, J. Meeprasert, P. Maitarad, S. Nammuangruk, L. Shi, D. Zhang, Investigation of the facet-dependent catalytic performance of Fe_2O_3/CeO_2 for the selective catalytic reduction of NO with NH_3, The Journal of Physical Chemistry C, 120 (2016) 1523-1533.
[240] S. Ewald, O. Hinrichsen, On the interaction of CO_2 with Ni-Al catalysts, Applied Catalysis A: General, 580 (2019) 71-80.
[241] G.N. Vayssilov, M. Mihaylov, P.S. Petkov, K.I. Hadjiivanov, K.M. Neyman, Reassignment of the vibrational spectra of carbonates, formates, and related surface species on ceria: a combined density functional and infrared spectroscopy investigation, The Journal of Physical Chemistry C, 115 (2011) 23435-23454.
[242] T. Désaunay, A. Ringuedé, M. Cassir, F. Labat, C. Adamo, Modeling basic components of solid oxide fuel cells using density functional theory: Bulk and surface properties of CeO_2, Surface Science, 606 (2012) 305-311.
[243] C. Schilling, A. Hofmann, C. Hess, M.V. Ganduglia-Pirovano, Raman spectra of polycrystalline CeO_2: a density functional theory study, The Journal of Physical Chemistry C, 121 (2017) 20834-20849.
[244] Z. Yang, T.K. Woo, M. Baudin, K. Hermansson, Atomic and electronic structure of unreduced and reduced CeO_2 surfaces: A first-principles study, The Journal of chemical physics, 120 (2004) 7741-7749.
[245] Y. Choi, H. Abernathy, H.T. Chen, M.-C. Lin, M. Liu, Characterization of O_2–CeO_2 interactions using in situ Raman spectroscopy and first‐principle calculations, ChemPhysChem, 7 (2006) 1957-1963.
[246] K. Ahn, Y.-C. Chung, K.J. Yoon, J.-W. Son, B.-K. Kim, H.-W. Lee, J.-H. Lee, Lattice-strain effect on oxygen vacancy formation in gadolinium-doped ceria, Journal of Electroceramics, 32 (2014) 72-77.
[247] D.A. Andersson, S.I. Simak, N.V. Skorodumova, I.A. Abrikosov, B. Johansson, Optimization of ionic conductivity in doped ceria, Proceedings of the National Academy of Sciences, 103 (2006) 3518-3521.
[248] D. Tian, K. Li, Y. Wei, X. Zhu, C. Zeng, X. Cheng, Y. Zheng, H. Wang, DFT insights into oxygen vacancy formation and CH_4 activation over CeO_2 surfaces modified by transition metals (Fe, Co and Ni), Physical Chemistry Chemical Physics, 20 (2018) 11912-11929.
[249] K.R. Hahn, M. Iannuzzi, A.P. Seitsonen, J.r. Hutter, Coverage effect of the CO_2 adsorption mechanisms on CeO_2 (111) by first principles analysis, The Journal of Physical Chemistry C, 117 (2013) 1701-1711.

[250] K. Yoshikawa, M. Kaneeda, H. Nakamura, Development of Novel CeO_2-based CO_2 adsorbent and analysis on its CO_2 adsorption and desorption mechanism, Energy Procedia, 114 (2017) 2481-2487.
[251] P.M. Albrecht, D.-e. Jiang, D.R. Mullins, CO_2 adsorption as a flat-lying, tridentate carbonate on CeO_2 (100), The Journal of Physical Chemistry C, 118 (2014) 9042-9050.
[252] G. Li, L. Hu, J.M. Hill, Comparison of reducibility and stability of alumina-supported Ni catalysts prepared by impregnation and co-precipitation, Applied Catalysis A: General, 301 (2006) 16-24.
[253] G. Qi, R.T. Yang, R. Chang, MnOx-CeO_2 mixed oxides prepared by co-precipitation for selective catalytic reduction of NO with NH_3 at low temperatures, Applied Catalysis B: Environmental, 51 (2004) 93-106.
[254] P. Djinović, J. Batista, J. Levec, A. Pintar, Comparison of water–gas shift reaction activity and long-term stability of nanostructured CuO-CeO_2 catalysts prepared by hard template and co-precipitation methods, Applied Catalysis A: General, 364 (2009) 156-165.
[255] J. Hafner, Ab‐initio simulations of materials using VASP: Density‐functional theory and beyond, Journal of computational chemistry, 29 (2008) 2044-2078.
[256] J. Bronsted, Acid and Basic Catalysis, Chemical Reviews, 5 (1928) 231-338.
[257] J. Shorter, Correlation analysis in organic chemistry: an introduction to linear free-energy relationships, 1973.
[258] Z. Hu, H. Metiu, Effect of dopants on the energy of oxygen-vacancy formation at the surface of ceria: Local or global?, The Journal of Physical Chemistry C, 115 (2011) 17898-17909.

Appendix

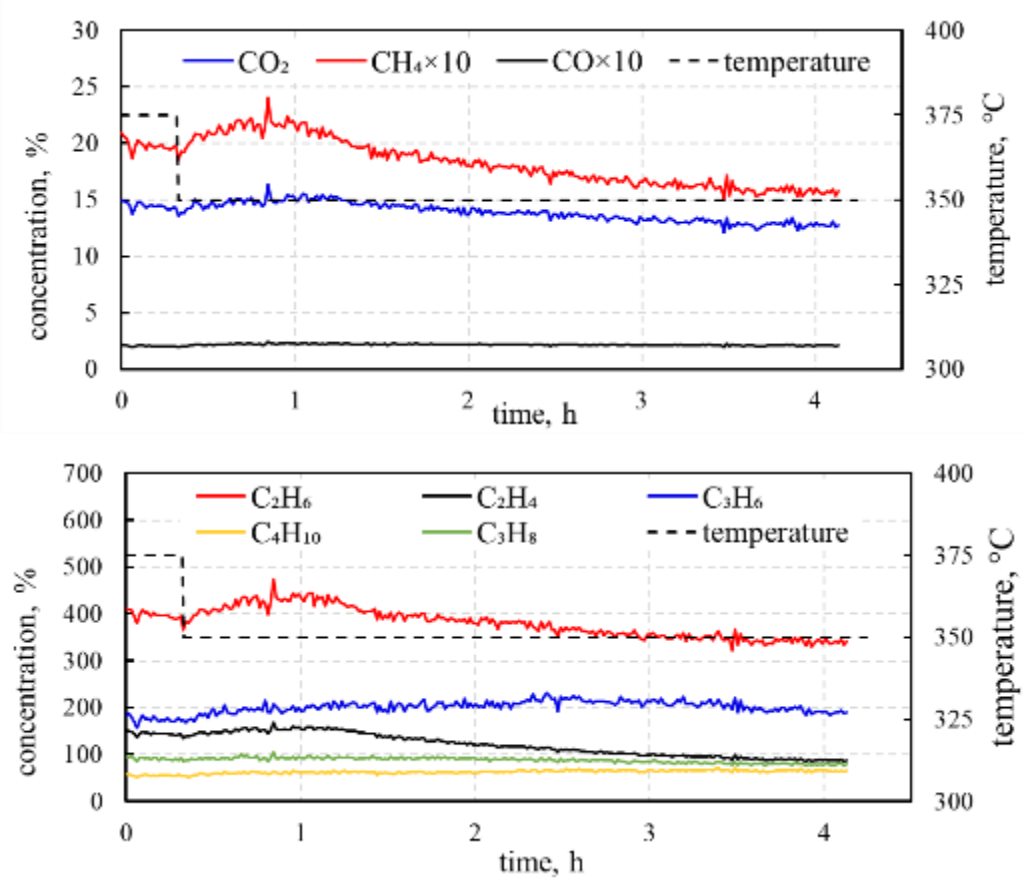

Figure S1: Time dependent concentration profile of carbon-based species recorded during the reaction test. Catalyst: Fe/Al_2O_3; operating conditions: GHSV = 3,000 mL/(g h), P = 10 bar, $H_2/CO_2 = 4$.

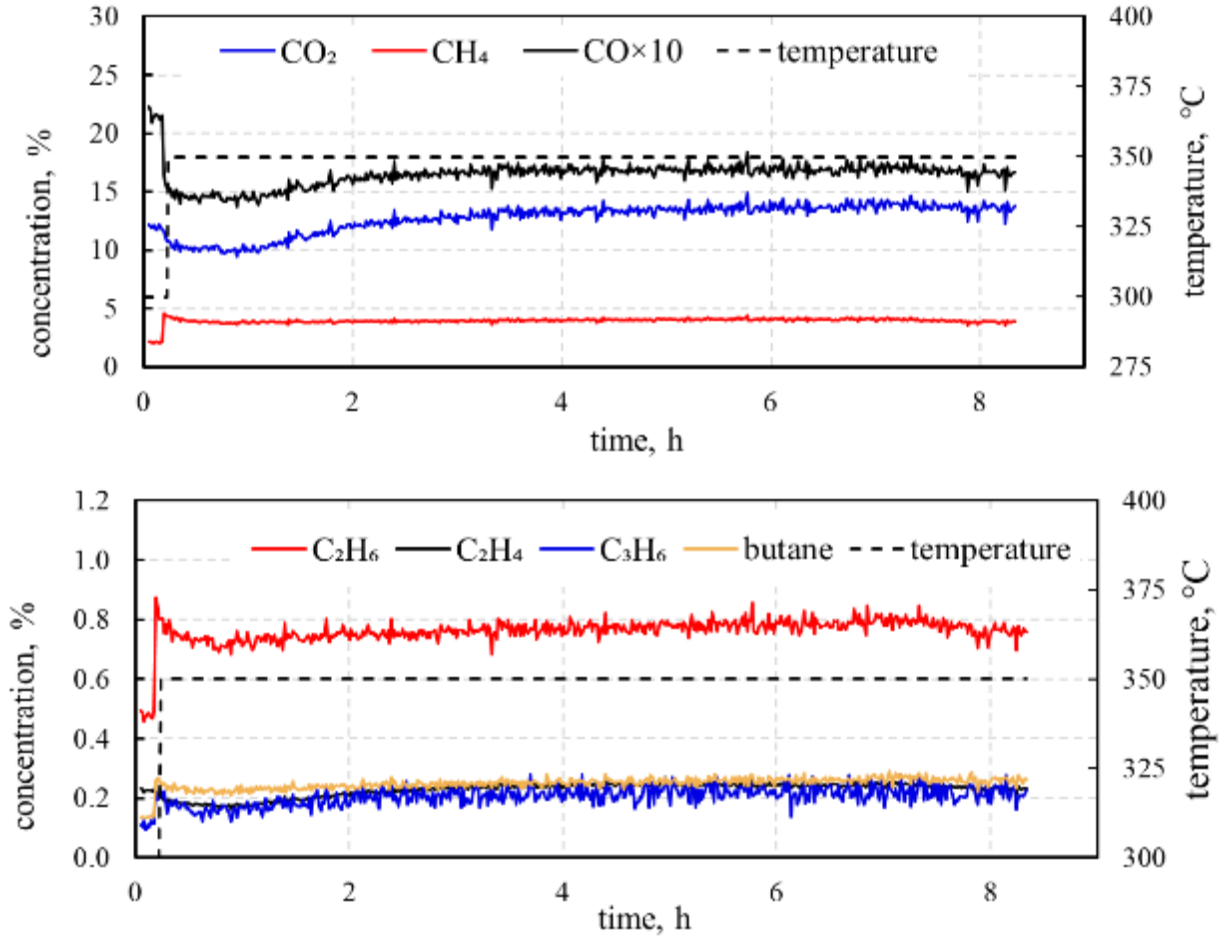

Figure S2: Time-dependent concentration profiles of carbon-based species recorded during the reaction test after increasing temperature to 350 °C. Catalyst: Fe/RME-Al_2O_3; operating conditions: GHSV = 3,000 mL/(g h), P = 10 bar, H_2/CO_2 = 4.

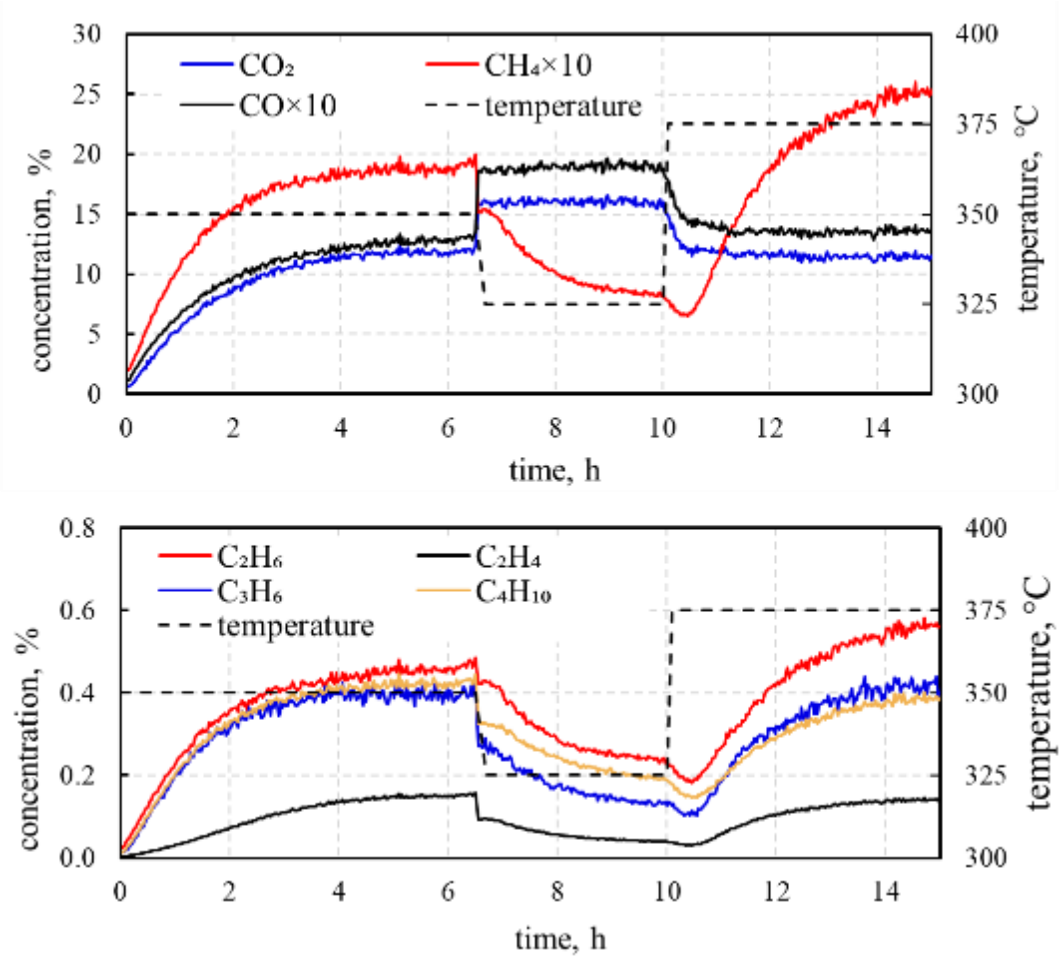

Figure S3: Time-dependent concentration profiles of carbon-based species recorded during the reaction test with varying temperature. Catalyst: RME Fe/Al_2O_3; operating conditions: GHSV = 3,000 mL/(g h), P = 10 bar, H_2/CO_2 = 4.

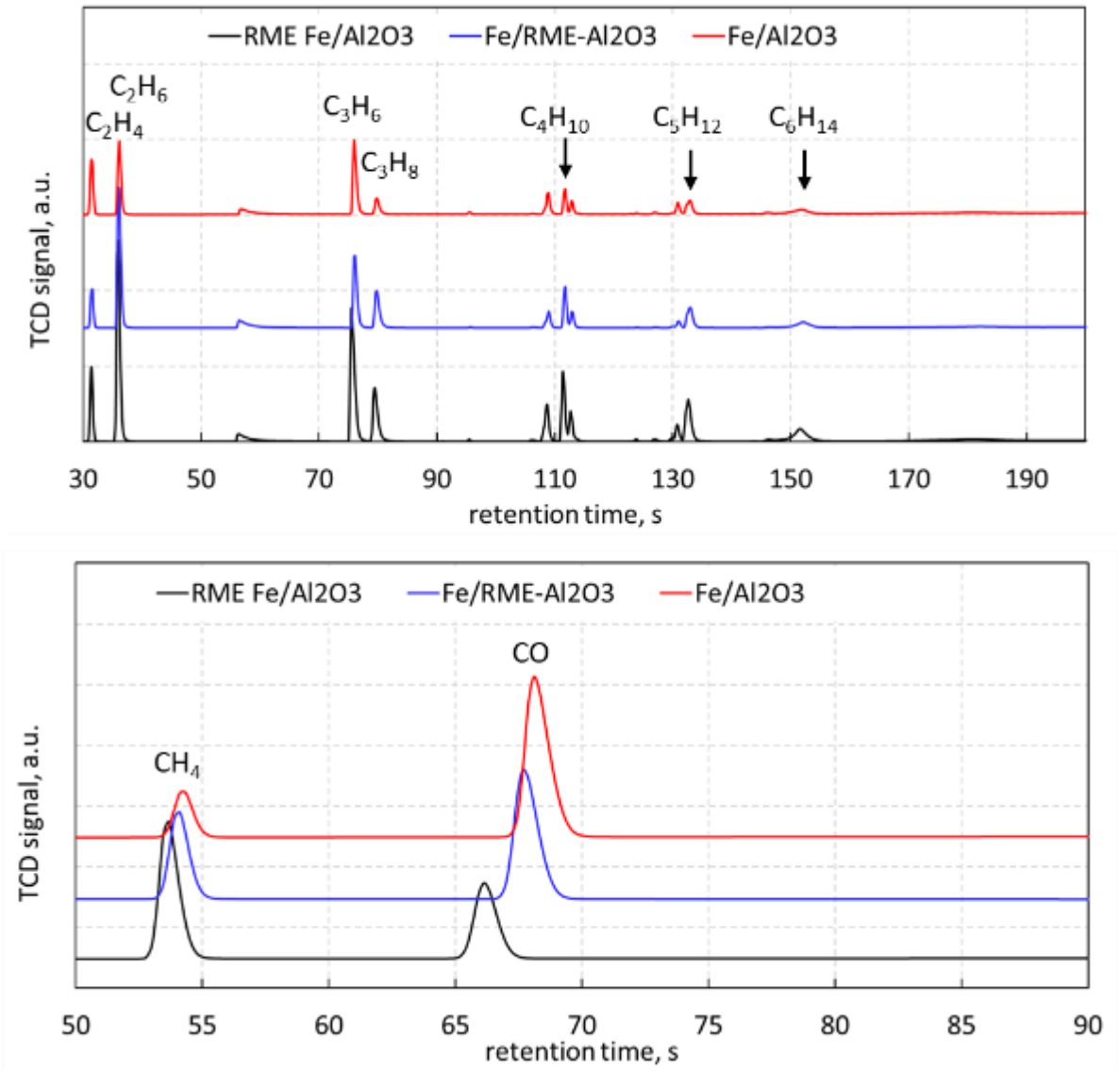

Figure S4: GC spectra of carbon-based species recorded during the reaction test. Operating conditions: GHSV = 3,000 mL/(g h), P = 10 bar, H_2/CO_2 = 4, T = 375 °C.

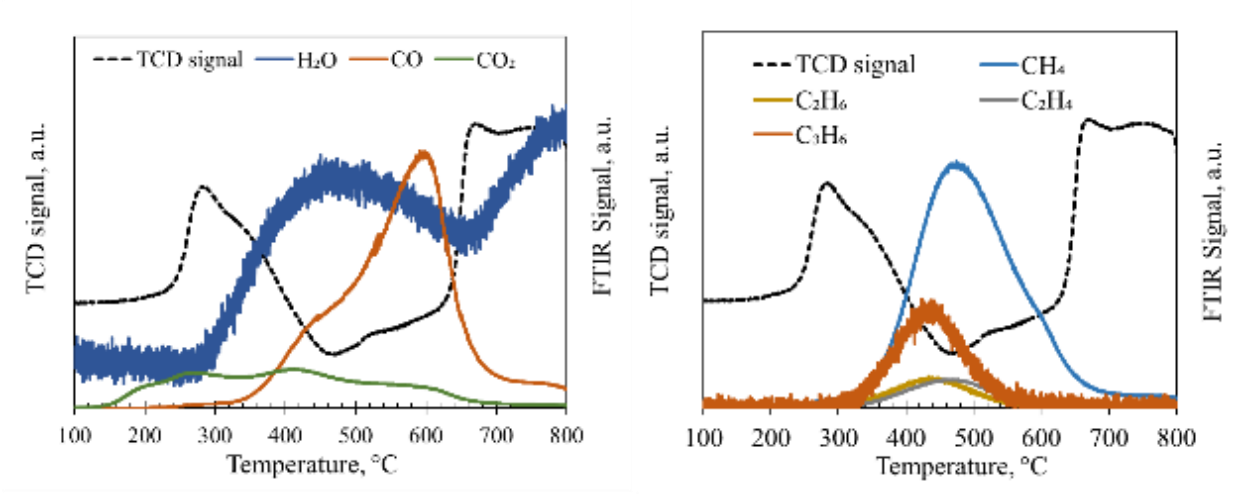

Figure S5: TPR-FTIR files of post reaction on Fe/RME-Al_2O_3 catalysts (70 h on stream). Stability test conditions: T = 375 °C, H_2/CO_2 = 4, GHSV = 3,000 mL/(g h), P = 10 bar (absolute).

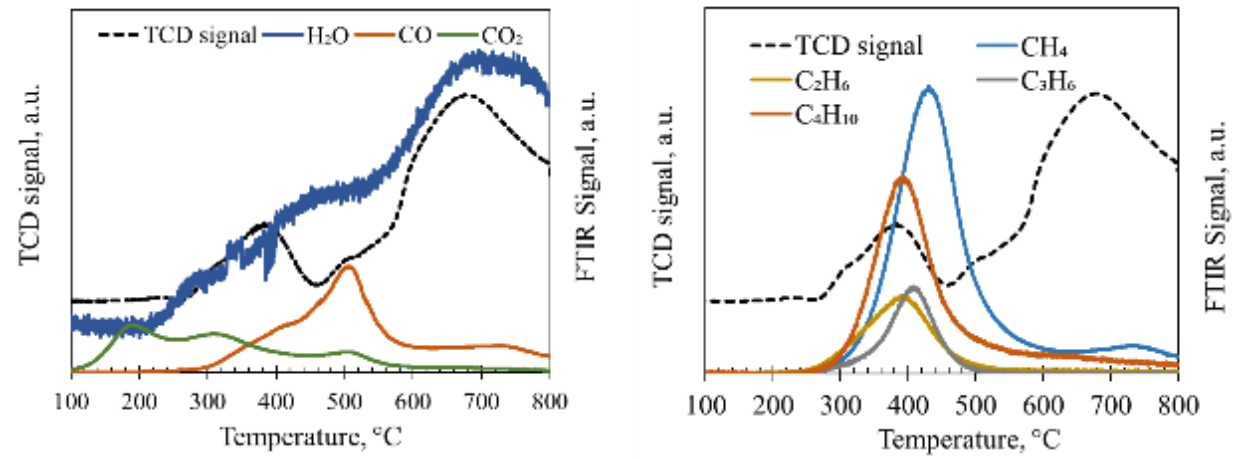

Figure S6: TPR-FTIR files of post reaction on Fe/Al_2O_3 catalysts (70 h on stream). Stability test conditions: T = 375 °C, H_2/CO_2 = 4, GHSV = 3,000 mL/(g h), P = 10 bar (absolute).

XRD Pattern of RME γ-Al_2O_3

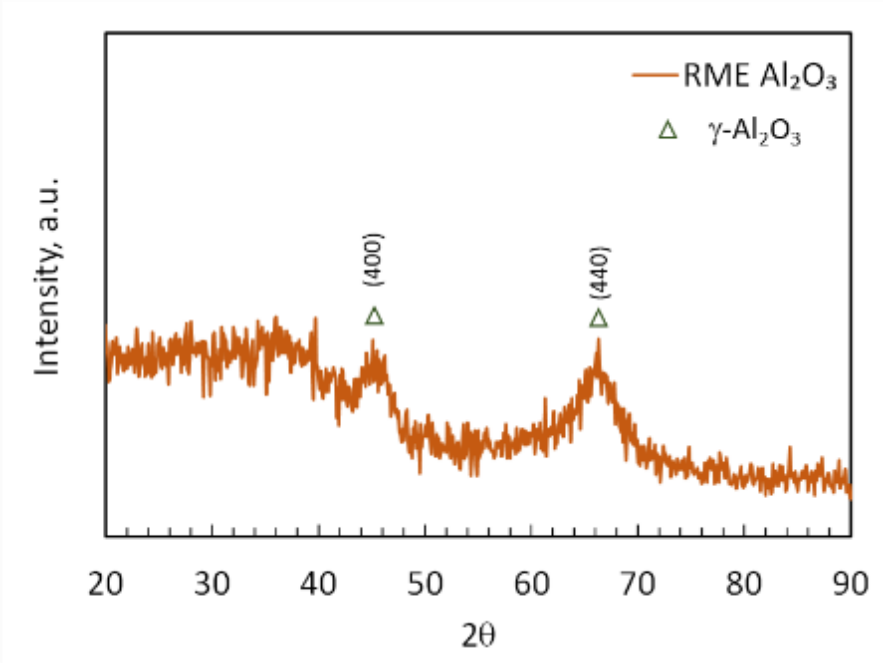

Figure S7 XRD Pattern of RME γ-Al_2O_3